Lawrence Berkeley Laboratory
UNIVERSITY OF CALIFORNIA

THE ATTENUATED RADON TRANSFORM: THEORY AND APPLICATION IN MEDICINE AND BIOLOGY

Grant Theodore Gullberg
(Ph. D. thesis)

June 1979

Prepared for the U. S. Department of Energy
under Contract W-7405-ENG-48

TABLE OF CONTENTS

THE ATTENUATED RADON TRANSFORM: THEORY AND APPLICATION IN MEDICINE AND BIOLOGY

Grant Theodore Gullberg

ABSTRACT

A detailed analysis is given of the properties of the attenuated Radon transform and of how increases in photon attenuation influence the numerical accuracy and computation efficiency of iterative and convolution algorithms used to determine its inversion. The practical applications for this work involve quantitative assessment of the distribution of injected radiopharmaceuticals and radionuclides in man and animals for basic physiological and biochemical studies as well as clinical studies in nuclear medicine. The theorems and numerical results presented are applicable to other fields in which computed tomography is used to reconstruct information about an internal source of unknown strength using projection data wherein the source strength, position and intervening attenuation are unknown. This problem is mathematically and practically quite different from the well known methods in transmission computed tomography (TCT) where both the source strength and source position are known and only the attenuation is unknown.

A mathematical structure is developed using function theory and the theory of linear operators on Hilbert spaces which leans itself to better understanding the spectral properties of the attenuated

Radon transform. A generalization of the single angle projection operator for the attenuated Radon transform gives an N-fold projection operator which maps $L^2(\Omega,\tilde{a})$ into $L^2(\Omega_{\theta_1},\hat{\chi}_{\mu,\theta_1}) \oplus \ldots \oplus L^2(\Omega_{\theta_N},\hat{\chi}_{\mu,\theta_N})$ where Ω is a bounded open set in $\mathbb{R}^2$, $\tilde{a}(x,y)$ is the maximum of the attenuation factors $a(x,y,-x\sin\theta_i+y\cos\theta_i,\theta)$ for N angles, Ω_{θ_i} is the θ_i-silhouette of Ω, and $\hat{\chi}_{\mu,\theta_i}$ is the attenuated Radon transform of the characteristic function χ with support Ω.

The continuous attenuated Radon transform reduces to a matrix operator for discrete angular and lateral sampling, and the reconstruction problem reduces to a system of linear equations. For the situation of variable attenuation coefficient frequently found in nuclear medicine applications of imaging the heart and chest, the procedure developed in this thesis involves iterative techniques of performing the generalized inverse. Simulations indicate that the iterative algorithms adequately converge for ^{201}Tl (μ = .18 cm^{-1}) cross-sectional images of the heart but increasing attenuation above μ = .18 cm^{-1} for a 30 cm object decreases the rate of convergence, so that at μ = .60 cm^{-1} the result does not converge within an acceptable error criterion after 30 iterations. Errors which are the result of using TCT to calculate the attenuation coefficients increase the errors in the emission reconstruction. The percent root-mean-square uncertainty of computed tomograms of a distributed source in a 20 cm diameter region with μ = .15 cm^{-1} cannot be better than 9.8% even with infinite statistics if the attenuation coefficients are determined using an incident transmission beam of 1000 photons per projection ray (4.2×10^6 total photons).

For constant attenuation coefficient less than .15 cm^{-1}, convolution methods can reliably reconstruct a 30 cm object with .5 cm resolution. The convolution method of reconstruction is appealing because of its computational efficiency and because it requires very little computer memory. The convolvers are determined 1) by a least-squares fit of the attenuated back-projection of the convolver to a desired point response function; 2) by a power series expansion which gives an analytical expression of the convolution function; 3) by defining window functions which filter the projections in frequency space. However, for high attenuation coefficients or for the situation where there is variable attenuation such as reconstruction of distribution of isotopes in the heart, iterative techniques developed in this thesis give the best results.

SYMBOLS AND DEFINITIONS

ECT	- Emission computed tomography
TCT	- Transmission computed tomography
A_μ	- The attenuated Radon transform
$\hat{x} = (x,y)$	- Position vector in $\mathbb{R}^2$
$\rho(\hat{x})$	- The concentration distribution of the radionuclide in counts/Area
$\mu(\hat{x})$	- The distribution of the linear attenuation coefficients in $(\text{length})^{-1}$
$p_\gamma(\xi,\theta)$	- Single-photon projections at lateral sampling ξ and angle θ.
$\underset{\sim}{\theta} = (-\sin\theta, \cos\theta)$	- The unit directional vector along which projection are sampled
$\underset{\sim}{\theta}^{\perp} = (\cos\theta, \sin\theta)$	- The unit directional vector along which projection line integrals are integrated
$\langle \hat{x}, \underset{\sim}{\theta} \rangle$	- The inner product between the vectors $\hat{x}$ and $\underset{\sim}{\theta}$.
$\delta(x)$	- Dirac delta function
$\mathcal{R}$	- The Radon transform
$p(\xi,\theta)$	- Transmission and unattenuated emission projection data at lateral sampling ξ and angle θ
$\mathcal{B}$	- The back-projection operator
$\mathcal{F}$	- Fourier transform operator
$\mathcal{F}^{-1}$	- Inverse Fourier transform
$\tilde{p}(R,\theta) = \mathcal{F}_1[p(\xi,\theta)]$	- The one-dimensional Fourier transform of $p(\xi,\theta)$
$\tilde{c}(R)$	- Frequency space filter
$w(R)$	- Window function
$\mathbb{C}$	- A subset in $\mathbb{R} \times [0,2\pi)$
$c(\xi)$	- Real space convolution function

$\hat{f}$	- Estimate of f
$I(\xi,\theta)$	- The number of transmitted photons in TCT
$I_o(\xi,\theta)$	- The number of incident photons in TCT
τ	- The photoelectric linear attenuation coefficient in $(\text{length})^{-1}$
σ_{coh}	- The coherent linear attenuation coefficient in $(\text{length})^{-1}$
σ	- The Compton linear attenuation coefficient in $(\text{length})^{-1}$
π	- The pair production linear attenuation coefficient in $(\text{length})^{-1}$
$p_{\gamma\gamma}(\xi,\theta)$	- Positron projections at lateral sampling ξ and angle θ
$a(x,y,\xi,\theta)$	- The attenuation function for the attenuated Radon transform
A_μ	- The modified attenuated Radon transform
$p(\xi,\theta)$	- Modified projections at lateral sampling ξ and angle θ
$S^\perp$	- Orthogonal complement of S
$\overline{S}$	- The closure of S
$R(A_\mu)$	- Range space of the attenuated Radon transform
$N(A_\mu)$	- Null space of the attenuated Radon transform
A_μ^*	- The adjoint operator of the operator $A_\mu: L^2(\mathbb{R}^2,W) \to L^2(\mathbb{R}\times[0,2\pi),w)$
A_μ^G	- The generalized inverse of the attenuated Radon transform
$\langle \rho,\rho' \rangle_{\Omega,W}$	- The inner product with respect to the weight function W in the Hilbert space of concentration functions defined on $\Omega \subseteq \mathbb{R}^2$
$[p,g]_{\mathbb{C},w}$	- The inner product with respect to the weight function w in the Hilbert space of projection functions defined on $\mathbb{C} \subseteq \mathbb{R}\times[0,2\pi)$

$L^2(\Omega,W)$ - The space of square integrable functions with respect to the weight function W defined on $\Omega \subseteq \mathbb{R}^2$, i.e., $\iint_{\mathbb{R}^2} |\rho(x,y)|^2 W(x,y)dxdy < \infty$

$L^2(\mathbb{C},w)$ - The space of square integrable functions with respect to the weight function w defined on $\mathbb{C} \subseteq \mathbb{R} \times [0,2\pi)$ i.e., $\iint_{\mathbb{C}} |\rho(\xi,\theta)|^2 \; w(\xi,\theta)d\xi d\theta < \infty$

$K(x',y'|x,y)$ - Kernel of the Fredholm integral of the first kind for the operator $A_\mu^* A_\mu$

$I(\xi,\theta|\xi',\theta')$ - Kernel of the Fredholm integral of the first kind for the operator $A_\mu A_\mu^*$

$(\psi_i,\phi_i;\lambda_i)$ - Singular system for the operator A_μ composed of eigenfunctions of $A_\mu A_\mu^*$ and $A_\mu^* A_\mu$ corresponding to the eigenvalue λ_i

$A\{\rho,\mu;\xi,\theta\}$ - The attenuated Radon transform of ρ for the attenuation distribution μ calculated at ξ and θ

$(A_\mu\rho)(\xi,\theta)$ - The attenuated Radon transform of ρ evaluated at ξ and θ

B_μ - The attenuated back-projection operator

$\mathcal{B}_\mu$ - The modified attenuated back-projection operator

$(A_{\mu,\theta}\rho)(\xi)$ - The attenuated Radon transform of ρ for a fixed angle θ evaluated at ξ, i.e., $(A_{\mu,\theta}\rho)(\xi) = (A_\mu\rho)(\xi,\theta)$

$A_{\mu,N}\rho = (A_{\mu,\theta_1}\rho, A_{\mu,\theta_2}\rho,\ldots,A_{\mu,\theta_N}\rho)$ - The N-fold projection operator which maps the function ρ into the N-tuple of single angle projections

$L^1(\mathbb{R}^2,a)$ - The space of functions such that $\rho \in L^1(\mathbb{R}^2,a)$ if and only if $\iint_{\mathbb{R}^2} |p(x,y)|\, a(x,y,-x\sin\theta+y\cos\theta,\theta)dxdy < \infty$

$\|A_\mu\| = \sup_{\|\rho\| \leq 1} \|A_\mu\rho\|$ - The norm of the operator A_μ

$A_{\mu,\theta}^*$ - The adjoint of the operator $A_{\mu,\theta}: L^2(\mathbb{R}^2) \to L^2(\mathbb{R})$

B_θ - The adjoint of the operator $A_{\mu,\theta}: L^1(\mathbb{R}^2,a) \to L^1(\mathbb{R})$

χ - Characteristic function for some $\Omega \subseteq \mathbb{R}^2$, i.e., $\chi(x,y) = 1$ if $(x,y) \in \Omega$, 0 otherwise

$\hat{\chi}_\theta$ - The attenuated Radon transform of χ, i.e., $\hat{\chi}_\theta = A_{\mu,\theta}\chi$

M_f - Multiplication operator, $(M_f g)(x,y) = f(x,y)g(x,y)$

Ω - A subset of $\mathbb{R}^2$

$\hat{\Omega}_\theta$ - The θ-silhouette of Ω, $\hat{\Omega}_\theta = \{\langle \hat{x}, \underset{\sim}{\theta} \rangle \mid \hat{x} \in \Omega\}$

$\Omega_{\xi,\theta}$ - The intersection of the line $\xi+\sin\theta-y\cos\theta = 0$ and the set Ω

$R_{\mu,\theta}$ - The projection operator: $R_{\mu,\theta} = M_{(\hat{\chi}_\theta)^{-1}} A_{\mu,\theta}$

$R^*_{\mu,\theta}$ - The adjoint operator: $R^*_{\mu,\theta} = M_\chi B_\theta$

$L^2(\Omega,a)$ - For a fixed θ and weight function a, the space of square integrable functions defined on Ω, i.e., $\iint_\Omega |\rho(x,y)|^2 \, a(x,y,-x\sin\theta+y\cos\theta,\theta)dxdy < \infty$

$L^2(\hat{\Omega}_\theta, \hat{\chi}_{\mu,\theta})$ - For a fixed θ and weight function $\hat{\chi}_{\mu,\theta}$, the space of square integrable functions defined on $\hat{\Omega}_\theta \subseteq \mathbb{R}$, i.e., $\int_{\hat{\Omega}_\theta} |\rho(\xi)|^2 \, \hat{\chi}_{\mu,\theta}(\xi)d\xi < \infty$

$P_{\mu,\theta}$ - Projection operator which for any $\rho \in L^2(\Omega,a)$ maps $L^2(\Omega,a)$ onto the subspace $\rho + N(R_{\mu,\theta})$

$\underline{h} = (h_1, h_2, \ldots h_N)$ - N-tuple of real valued functions defined on $\mathbb{R}$

$A^*_{\mu,N}$ - The adjoint of the operator $A_{\mu,N}: L^2(\mathbb{R}^2) \to L^2(\mathbb{R}) \oplus \ldots \oplus L^2(\mathbb{R})$

$[\underline{g},\underline{h}]_{L^2_N(\mathbb{R})} = \frac{1}{N} \sum_{j=1}^{N} \int_{\mathbb{R}} g_j(\xi) \, h_j(\xi)d\xi$ - The inner product for the space $L^2_N(\mathbb{R}) = L^2(\mathbb{R}) \oplus \ldots \oplus L^2(\mathbb{R})$

$$[\underline{g},\underline{h}]_{L^2_N(\hat{\chi}_\mu)} = \frac{1}{N}\sum_{j=1}^{N}\int_{\hat{\Omega}_{\theta_j}} g_j(\xi)\, h_j(\xi)\, \hat{\chi}_{\mu,\theta_j}(\xi)d\xi$$

- The inner product for the space $L^2_N(\hat{\chi}_\mu) = L^2(\hat{\Omega}_{\theta_1},\hat{\chi}_{\mu,\theta_1}) \oplus \ldots \oplus L^2(\hat{\Omega}_{\theta_N},\hat{\chi}_{\mu,\theta_N})$

$$\tilde{a}(x,y) = \max_{i=1,N} \{a(x,y,-x\sin\theta_i+y\cos\theta_i,\theta_i)\}$$

- The maximum of the attenuation functions for the angles θ_i i=1,..N

$$R_{\mu,N}\rho = (R_{\mu,\theta_1}\rho,\ R_{\mu,\theta_2}\rho,\ldots,R_{\mu,\theta_N}\rho)$$

- The N-fold projection operator which maps the function ρ into the N-tuple of single angle projections.

$R^*_{\mu,N}$ - The adjoint of the operator $R_{\mu,N}:L^2(\Omega,\tilde{a}) \to L^2_N(\hat{\chi}_\mu)$

$G_\mu(\xi,\theta)$ - The integral of the attenuation coefficients between the central axis and ∞

$a(x,y,\xi,\theta)$ - The attenuation function for the modified attenuated Radon transform

A^*_μ - The adjoint of the operator $A_\mu:L^2(\mathbb{R}^2,W) \to L^2(\mathbb{C},w)$

K - Kernel of the Fredholm integral of the first kind for the operator $A^*_\mu A_\mu$

I - Kernel of the Fredholm integral of the first kind for the operator $A_\mu A^*_\mu$

T_n - Tchebycheff polynomial of the first kind

U_n - Tchebycheff polynomial of the second kind

H_n - Hermite polynomial

c_{μ} - The convolution function for constant attenuation

D_{ij} - Rectangular pixels in $\mathbb{R}^2$

χ_{ij} - Characteristic function with support D_{ij}

s_{ij} - The attenuated Radon transform of χ_{ij}, i.e., $s_{ij} = A\{\chi_{ij}(x,y),\mu(x,y); \xi,\theta\}$

δ_{ij} - The modified attenuated Radon transform of χ_{ij}, i.e., $\delta_{ij} = A\{\chi_{ij}(x,y),\mu(x,y); \xi,\theta\}$

A - The discrete matrix operator for the attenuated Radon transform

A - The discrete matrix operator for the modified attenuated Radon transform

A^T - The transpose of the matrix operator A

A^G - The generalized inverse of the matrix operator A

$tr(A)$ - The trace of the matrix A equal to the sum of the diagonal elements.

P - Matrix of projection samples for the attenuated Radon transform

P - Matrix of projection samples for the modified Radon transform

$\chi^2(\rho)$ - The least-squares function

$m_{\rho}(\hat{x})$ - Mean value function for the random field ρ

$\sigma^2_{\rho}(\hat{x})$ - The variance of the random field ρ at $\hat{x}$

$R_{\rho\rho}(\hat{x}_1,\hat{x}_2)$ - The autocorrelation function for the random field ρ

$C_{\rho\rho}(\hat{x}_1,\hat{x}_2)$ - The autocovariance function for the random field ρ

$C_{\rho\mu}(\hat{x}_1,\hat{x}_2)$ - The cross correlation function for the two random fields ρ and μ

$S_{\rho\rho}(\hat{W})$ - The spectral density of a homogeneous random field

$\overline{\rho}$ - Spatial average for the mean

$R(\alpha,\beta)$ - Spatial average for the autocorrelation

$Cov(\rho)$ - Covariance matrix for the least-squares estimate of ρ

$\sigma^2(\rho_j)$ - The variance for the estimate of the jth element of ρ

$\sigma^2(\rho)$ - The spatial average for the variance of a subset of ρ

RMS - Root-mean-squared

$h(\hat{r})$, $h(\hat{x})$ - Point spread function

J_0 - Zeroth order Bessel function

J_1 - First order Bessel function

$E\{p(\xi,\theta)\}$ - The expectation of p at ξ and θ

$\sigma^2\{p(\xi,\theta)\}$ - The variance of p at ξ and θ

$\mathbb{R}^2$ - The Euclidean plane

1. INTRODUCTION

The inversion of the attenuated Radon transform has the important application in single-photon emission computed tomography (ECT) of quantitating the three-dimensional distribution of gamma emitting radiopharmaceuticals in the body. ECT is a field of nuclear medicine which uses radiopharmaceutical distribution data collected using scintillation detectors at different angles to reconstruct cross-sectional images of the internal organs of the body. The application of ECT gives the physician a more accurate way of seeing inside the human body and permits a noninvasive procedure for studying function of biological processes in health and disease. The instrumentation and strategies of ECT are divided into two major categories -- 1) single-photon counting using either multiple detector arrays or scintillation cameras for the detection of radionuclides such as ^{99m}Tc, and ^{131}I; and 2) coincidence detection of annihilation photons from positron emitting radionuclides such as ^{11}C, ^{13}N, and ^{15}O. The reconstruction procedures used with single-photon counting techniques invert the attenuated Radon transform by various methods (Budinger and Gullberg, 1977).

The major impetus for emission computed tomography is to use the various radiopharmaceuticals to make quantitative measurements of *in vivo* biochemical and hemodynamic functions. This is in contrast to x-ray transmission computed tomography (TCT) which has as its major emphasis the anatomic description of the cross section of body organs. The major difference lies in the fact that ECT seeks to describe the location and intensity of sources of emitted photons in an attenuating

medium whereas TCT seeks to determine the density distribution of the attenuating medium (Fig. 1.1). Not only does the biological objective of ECT differ from TCT; but single-photon ECT as exemplified by the attenuated Radon transform differs from both TCT and positron ECT in the mathematical procedures required to reconstruct the cross-sectional images. Methods for inverting the attenuated Radon transform present a mathematical challenge. However, iterative and convolution methods can be developed which adequately quantitate the distribution of single-photon radiopharmaceuticals which are useful in depicting non-invasively the spatial and temporal distribution of biological processes in healthy and diseased tissue.

Tomography (which comes from the Greek work "tomo" meaning slice) is the process of imaging a single plane through an object. In the past tomographic images in diagnostic radiology and nuclear medicine were produced by employing the principles of longitudinal tomography which utilizes optical devices to obtain an image of a plane parallel to the face of the detector (Anger, 1973; Anger, 1974). Today the term computerized tomography usually refers to transaxial tomography which uses digital computers and mathematical algorithms to give an image of a plane perpendicular to the face of the detector.

The first clinically useful x-ray TCT machine was invented by G. N. Hounsfield of EMI, Ltd. in 1970. Since that time x-ray TCT has made a major impact on diagnostic radiological procedures. Even before the EMI scanner, the principles of ECT were worked out by Kuhl and Edwards (1963). However, the clinical application of ECT has lagged far behind x-ray

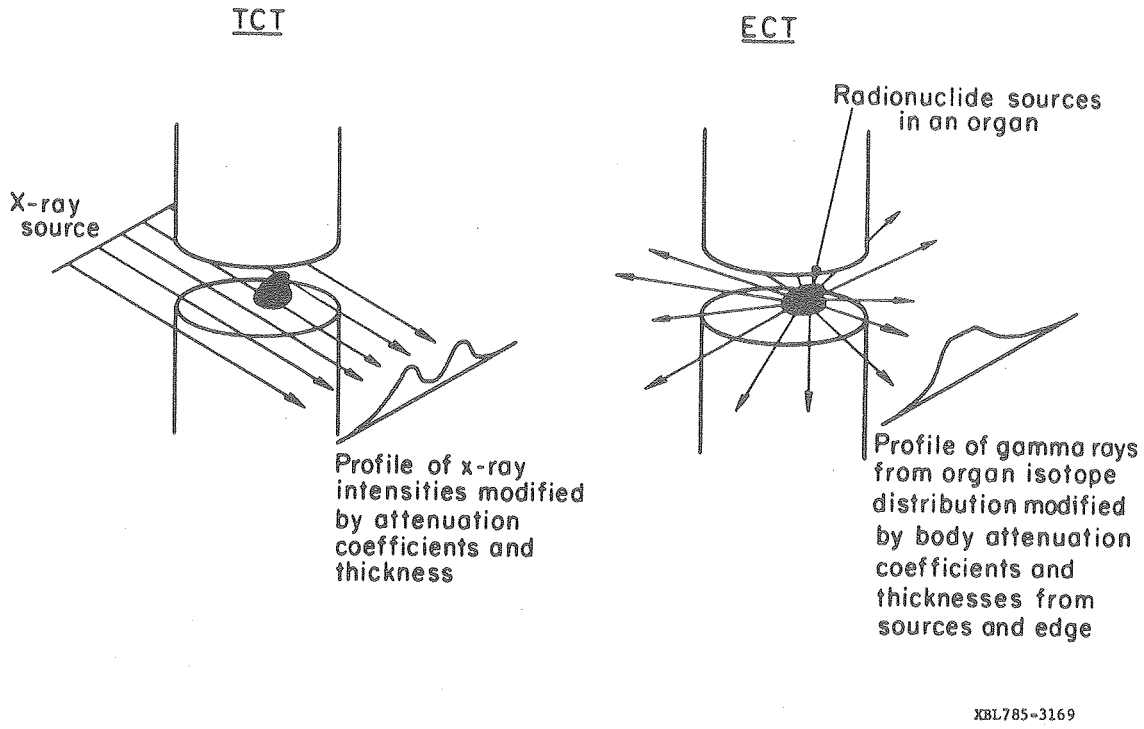

Figure 1.1. The basic physical difference between TCT and ECT is that both the source and the attenuation functions are unknown in ECT, whereas only the attenuation function is unknown in TCT.

TCT primarily due to the attenuation problem which has made it difficult to quantitate the distribution of radiopharmaceuticals. In the last 10 years, researchers have investigated different ways of reconstructing radiopharmaceutical distributions by developing new instruments and algorithms for inverting the attenuated Radon transform. These advances are reviewed in (Ter-Pogossian, 1977; Phelphs, 1977; Brownell, Correia, and Zamenhof, 1978; Budinger, Gullberg, and Huesman, 1979).

The methods of three-dimensional reconstruction are not unique to transmission and emission computed tomography but are used in many other disciplines. These disciplines include radioastronomy (Bracewell and Riddle, 1967; Weiler and Seielstad, 1972), electron microscopy (Klug and Crowther, 1972), nondestructive testing, holographic interferometry (Sweeney and Vest, 1973), and zeumatography (Lauterbur, 1973; Singer, 1978). Much of the current activity is directed toward digital reconstruction because of its flexibility. However analog methods using optical and acoustic devices are also applied to the reconstruction problem. There are mathematical similarities among reconstruction problems in these varied disciplines. However emission computed tomography especially single-photon imaging offers some of the most difficult mathematics of all the disciplines due to the attenuation problem. The attenuation problem also occurs in zeugmatography which reconstructs the strength of magnetic resonance signals using the techniques of nuclear magnetic resonance (NMR).

To illustrate the concepts of single-photon emission computed tomography, consider the example of a physician who is trying to detect

small lesions in a patient's liver. The patient is injected with a radiopharmaceutical such as ^{99m}Tc sulfur colloid which localizes by phagocytosis in the Kupffer cells of the liver and other cells of the reticuloendothelial system which involves organs such as the liver, spleen, lymph nodes and bone marrow. In the liver the ^{99m}Tc sulfur colloid is phagocytized only by healthy Kupffer cells (Sheppard, et al., 1951; Dobson and Jones, 1952; Root, et al., 1954) and cancer invasion results in a failure of the diseased area to concentrate the colloidial particles.

A gamma scintillation camera (Anger, 1966a; Anger, 1966b; Anger, 1972) is used to detect those photons emitted by the radionuclide ^{99m}TC. The scintillation camera consists of a crystal which converts the high energy gamma photons into light, and photomultiplier tubes which convert the light scintillation into an electronic signal. By electronic circuitry these electrical signals are used to display an image on an oscilloscope or are converted from analog to digital signals and stored in a computer for display as a digital image.

The images show an intensity directly proportional to the concentration of the radiopharmaceutical. Therefore a neoplastic lesion in the liver would show up on the images as a low intensity region surrounded by higher intensity from the normally functioning tissue. Since the image from the scintillation camera represents the projection of the liver, overlying and underlying tissues, and other organs such as the spleen; small lesions will be obliterated by the projection of these surrounding tissues onto the image plane.

In order to visualize the liver better, it is necessary to obtain images at different angles in which the internal organs appear in different relationships to one another. If the information from a cross-section of body through the liver is projected onto a plane perpendicular to an axis of rotation (Fig. 1.2) a single one-dimensional line is recorded on the gamma camera image. Taking this line for each angle and digitally processing the data, the desired two-dimensional cross section is reconstructed. To obtain a full three-dimensional picture the various cross-sections can be stacked. This procedure of three-dimensional reconstruction separates the overlying and underlying tissue and allows the physician to quantitate the spatial distribution of the sulfur colloid sequestered by the liver. The lesions such as the one shown in Fig. 1.2 can be detected with better quantitation, better resolution and greater contrast than is possible with any of the projected images.

The reconstruction of the cross-sectional image is complicated by the attenuation of the emitting photons. The scintillation detector can only detect those unattenuated photons projected along rays intersecting the camera face. The degree with which these photons are attenuated will depend upon the energy of the emitted photons and the density of the tissue interposed between the emitting source and the detector. For example, of the 140 keV photons emitted from ^{99m}Tc radionuclides, 78% will be absorbed in passing through 10 cm of tissue. Therefore only 22% of the photons emitted will actually be recorded.

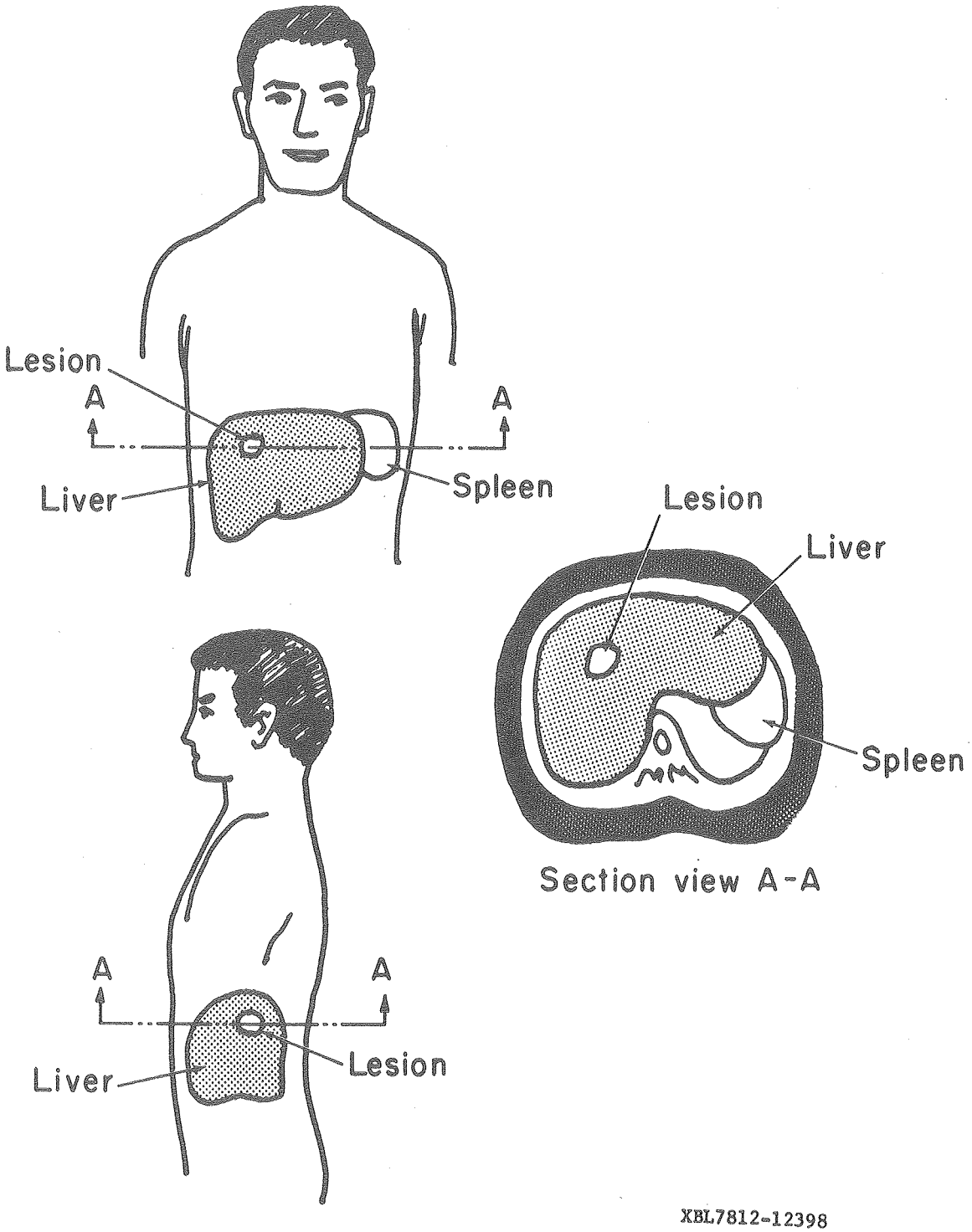

Figure 1.2. Illustration of a transverse section through the liver and spleen as one would view it looking from the feet toward the head. The anterior and left lateral views show the projected image of the lesion shown in the transverse section.

This presents a difficult problem for quantitating the actual distribution in any cross-sectional image.

If mathematical algorithms appropriate for TCT are applied to projection data obtained from a scintillation camera using a homogeneous distribution of a radionuclide such as ^{99m}Tc, the results of the reconstruction will show a concentration which appears to be less in the center than at the edges (column of images shown on the left in Fig. 1.3). However by knowing the attenuation distribution, the effects of attenuation can be corrected, giving a true quantitative measure of the radionuclide concentration as can be seen from the column of images on the right in Fig. 1.3. The definition of the attenuated Radon transform for this study depends upon a knowledge of the distribution of attenuation coefficients. It is therefore the inversion of this transform which properly quantitates the radiopharmaceutical concentration.

The attenuated Radon transform mathematically describes the relationship between the number of photons emitted from radionuclide distributed in a transverse section of the body and the number of photons projected onto a scintillation detector. If we let $\rho(x,y)$ denote the concentration of the radiopharmaceutical in counts/area at the point $\hat{x} = (x,y)$, then the attenuated Radon transform is the mapping $A_\mu : \rho \to p_\gamma$ where the projection $p_\gamma(\xi,\theta)$ at the angle θ and lateral sampling ξ is given by

$$p_\gamma(\xi,\theta) = \int \rho(\hat{x}) \exp\left\{ - \int_{\langle \hat{x}', \underset{\sim}{\theta}^\perp \rangle \geq \langle \hat{x}, \underset{\sim}{\theta}^\perp \rangle} \mu(\hat{x}') \, \delta(\xi - \langle \hat{x}', \underset{\sim}{\theta} \rangle) \, d\hat{x}' \right\} \delta(\xi - \langle \hat{x}, \underset{\sim}{\theta} \rangle) d\hat{x}, \tag{1.1}$$

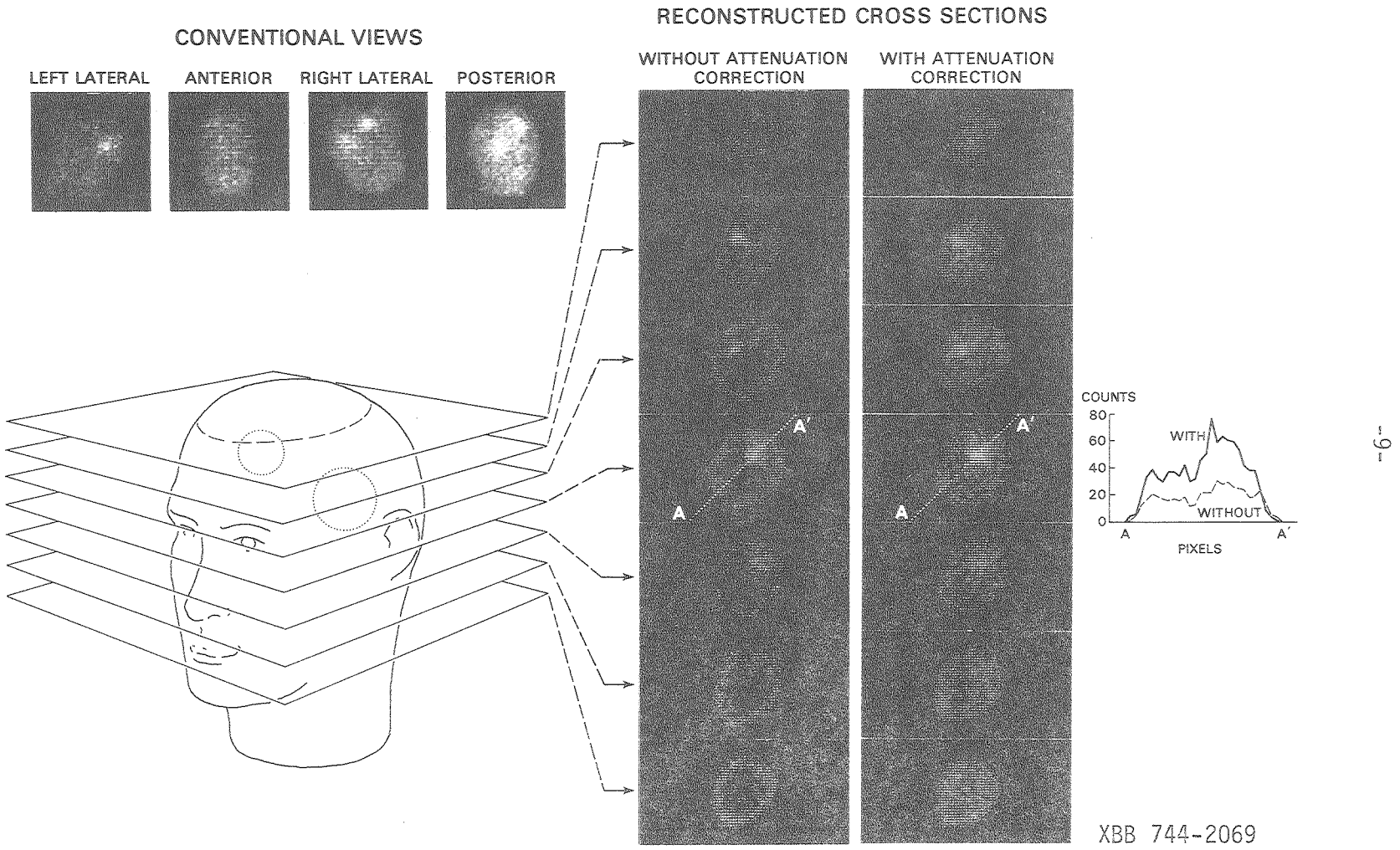

Figure 1.3. A comparison of reconstructing cross sections with and without attenuation compensation. The head phantom was filled with 1 mCi ^{99m}Tc. The two inner spheres had a source concentration of 2 times the surrounding head. The conventional views are the images which the scintillation camera records.

where $\underset{\sim}{\theta} = (-\sin\theta, \cos\theta)$ and $\underset{\sim}{\theta}^{\perp} = (\cos\theta, \sin\theta)$. In the case that $\mu=0$ everywhere the attenuated Radon transform reduces to the Radon transform defined by Radon (1917). Therefore the attenuated Radon transform is a generalization of the classical Radon transform. To define the attenuated Radon transform, the distribution of attenuation coefficients μ in units of $(\text{length})^{-1}$ for the cross section is required. In some situations this distribution can be assumed to be constant but for precise measurements requires the use of TCT.

To compensate for the attenuation effects the distribution of the attenuation coefficients must be determined by TCT using an external transmission source with the same energy as the emitted photon of the radiopharmaceutical (140 keV for ^{99m}Tc in the example above). The intensity of the transmitted beam is measured at different angles. These data are compared to the incident beam intensity and the result gives a measure of the attenuation of the photons for the tissue between the source and the detector. The distribution of attenuation coefficients is reconstructed for the same cross sections as those for the radiopharmaceutical cross-sectional images. With the a priori information about the distribution of the attenuating medium, ECT can describe the location and intensity of the source of emitted photons by inverting the attenuated Radon transform.

This thesis presents an analysis of the attenuated Radon transform and the implication of its properties relative to reconstruction algorithms used to invert the attenuated Radon transform. The work presented differs from previous work in the literature (Hsieh and Wee, 1976; Chang, 1978; Tretiak and Metz, 1979; Bellini et.al., 1979 a, b;

Natterer, 1978) in that the attenuated Radon transform is defined for arbitrary distributions of attenuation coefficients. Included is an iterative reconstruction algorithm which uses a transmission reconstruction to correct for attenuation and is able to reliabily reconstruct projection data of an internal radiopharmaceutical source which has been attenuated by any arbitrary attenuation distribution. For this algorithm, the propagation of errors is simulated for various transmission and emission statistics and is evaluated based on the spectral properties of the attenuated Radon transform. In the case of constant attenuation methods are given for obtaining convolvers and frequency space filters which accurately reconstruct projection data attenuated by a constant attenuation coefficient. The accuracy and efficiency of the reconstruction algorithms are shown to be a function of the attenuation coefficient. In most cases this functional relationship is such that as the attenuation coefficient increases then the reconstruction errors increase.

Following this introduction chapter 2 presents the concepts of emission computed tomography which includes a discussion about the theory of computed tomography, the aspects of transmission computed tomography, and the principles of emission computed tomography - in particular an explanation describing the differences between single-photon and positron emission computed tomography. Included is a discussion about the theory of exponential absorption of radiation which assumes a linear attenuation coefficient that depends on the atomic number of the absorbing material and the energy of the emitted photon. This is the premise upon which all

the mathematical theory is built for both ECT and TCT. The chapter concludes with a discussion of the history of the advances in single-photon ECT both in instrumentation and mathematical algorithm development.

Chapter 3 develops the properties of the attenuated Radon transform and of a modified transform which is independent of detector geometry. The theory of linear operators operating on Hilbert spaces, the definition of a generalized inverse, and the singular value decomposition of compact operators are described in order to develop a mathematical structure for the analysis of the mathematical properties of the attenuated Radon transform. Throughout it is assumed that the attenuation distribution is known a priori which enables one to define linear operators for both constant and variable attenuation coefficients. The chapter concludes with a discussion of the special properties that the modified attenuated Radon has in the case of constant attenuation coefficient. In particular these properties include inversion relationships.

Chapter 4 describes iterative methods for inversion of the attenuated Radon transform for arbitrary attenuation distributions. The discussion begins with a description of the basis functions which are characteristic functions with support over rectangular regions that approximate the picture function for the cross-sectional image. The attenuated Radon transform of these basis functions leads to a discrete matrix representation of the attenuated Radon transform for discrete angular and lateral sampling. At the present the size of the matrix is too large for a practical

evaluation of its inverse by a digital computer and thus iterative methods must be utilized. The spectral properties of these operators are considered. Then the statistical aspects of emission computed tomography are analyzed by reconstructing simulated projection data for various transmission and emission statistics. The reconstruction of attenuated data is complicated by not only statistical fluctuations in the emission data but also statistical fluctuations in the transmission data which amplify the errors in the emission reconstruction.

Chapter 5 investigates convolution algorithms which are applicable for inverting the attenuated Radon transform in the case of constant attenuation coefficient. The investigation into convolution methods is motivated by the computational speed of the algorithm. A method is described whereby optimum convolvers can be evaluated by fitting the attenuated back-projection of the convolver to a desired point spread function by either least-squares or series expansion methods. The reconstructed cross-sectional image is expected to closely represent the convolution of the true image with this point spread function. Filters used in TCT are shown to be applicable for ECT in the case of constant attenuation by modifying a window function. The chapter concludes with an investigation of the statistical aspects of the convolution algorithm for various attenuation coefficients representative of actual coefficients of radionuclides used in single-photon ECT.

2. EMISSION COMPUTED TOMOGRAPHY IN NUCLEAR MEDICINE

2.1 Introduction

Nuclear medicine is a discipline involved in measuring biological change as well as the anatomical distribution of these physiological and biochemical changes using injected radiopharmaceuticals (Wagner, 1968, 1978). Over 50 years ago Hevesy used radionuclides to trace biological function in animals and man (Hevesy, 1962). With the development of the Anger camera (Anger, 1966a, 1966b) brain scanning, kidney scans, liver scans, etc. have become routine clinical diagnostic procedures. The development of positron emitters by Tobias, Lawrence and colleagues (1945) for physiological studies and the development of the Anger positron camera in 1963 (Anger, 1973, 1974) gave a method for depth discrimination of biological changes in organs and body tissue. The recent development of positron and single-photon emission computed tomographic systems give even better spatial and contrast resolution for depth discrimination which is able to quantitate any where in the body the biological changes in healthy and diseased tissue (Phelphs, 1977).

The attenuated Radon transform embodies the concepts of single-photon emission computed tomography (ECT) of which transmission computed tomography (TCT) is an important enity. The attenuated Radon transform is the mapping $A_\mu : \rho \to p_\gamma$ of the cross-sectional radioactivity concentration ρ into the projections p given by

$$p_\gamma(\xi,\theta) = \int \rho(\hat{x}) \exp\left[- \int_{\langle \hat{x}', \underset{\sim}{\theta}^\perp \rangle \geq \langle \hat{x}, \underset{\sim}{\theta}^\perp \rangle} \mu(\hat{x}')\ \delta(\xi - \langle \hat{x}', \underset{\sim}{\theta} \rangle)\, d\hat{x}' \right] \delta(\xi - \langle \hat{x}, \underset{\sim}{\theta} \rangle) d\hat{x} \tag{1.1}$$

where $\underset{\sim}{\theta}^{\perp} = (-\sin\theta, \cos\theta)$ and $\underset{\sim}{\theta}^{\perp} = (\cos\theta, \sin\theta)$. This transform is a mathematical description which quantitates the physical process of measuring photons projected onto a detector perpendicular to the cross section and parallel to the axis of rotation. The measured photons are those photons which have been emitted from a radionuclide source located within the body and which have not been attenuated by body tissue between the source and detector.

In order to define the attenuated Radon transform given by Eq. (1.1) for a particular medium, the distribution of attenuation coefficients μ in the exponential factor must be known. The exponential factor assumes that the diminution in counts is based on an exponential law of radiation absorption. In both ECT and TCT the measured quantities are number of photons. The total number of photons measured are not equal to the total number of photons emitted by the source due to the attenuation of photons by body material. In TCT this absorption of radiation is used to measure the differences in attenuation density of body tissues; whereas in ECT the absorption eliminates from the projections the useful information about the internal source intensity. Thus the attenuated Radon transform includes an exponential factor which represents a measure of the probability that each source photon will reach the detector unattenuated.

The evaluation of the attenuation coefficient distribution μ requires the use of TCT and a thorough understanding of its concepts. The mathematical equations and algorithms used in single-photon computed tomography are an extension of the basic concepts of computed tomography used in TCT. Therefore in the following sections we review

the mathematical concepts of computed tomography, the principles of TCT and then describe emission computed tomography including the difference between single photon and positron emission computed tomography.

2.2 The Theory of Computed Tomography

Computed tomography is the process of reconstructing transverse sections of photon attenuation coefficients in transmission computed tomography or concentration of radioactivity in emission computed tomography from projections measured from external detectors. The application of computed tomography to nuclear medicine is not unique but is applied to many other fields such as radiology, radioastronomy, electron microscopy, zeumatography and others. For a review of the principles of computed tomography and its applications see (Gordon and Herman, 1974; and Brooks and DiChiro, 1976).

2.2.1 Projections

For the purpose of this introductory discussion $f(x,y)$ will denote the distribution of either emitter concentration or attenuation coefficients for the transverse section. The function $f(x,y)$ cannot be measured directly but is measured by external detectors. These external measurements are called projections and they are parameterized with an angle θ and a lateral sampling ξ. As shown in Fig. 2.1 the projections $p(\xi,\theta)$ in conventional TCT or positron ECT are line integrals of $f(x,y)$ given by

$$p(\xi,\theta) = \iint f(x,y)\ \delta(\xi + x\sin\theta - y\cos\theta)\ dxdy \qquad (2.1)$$

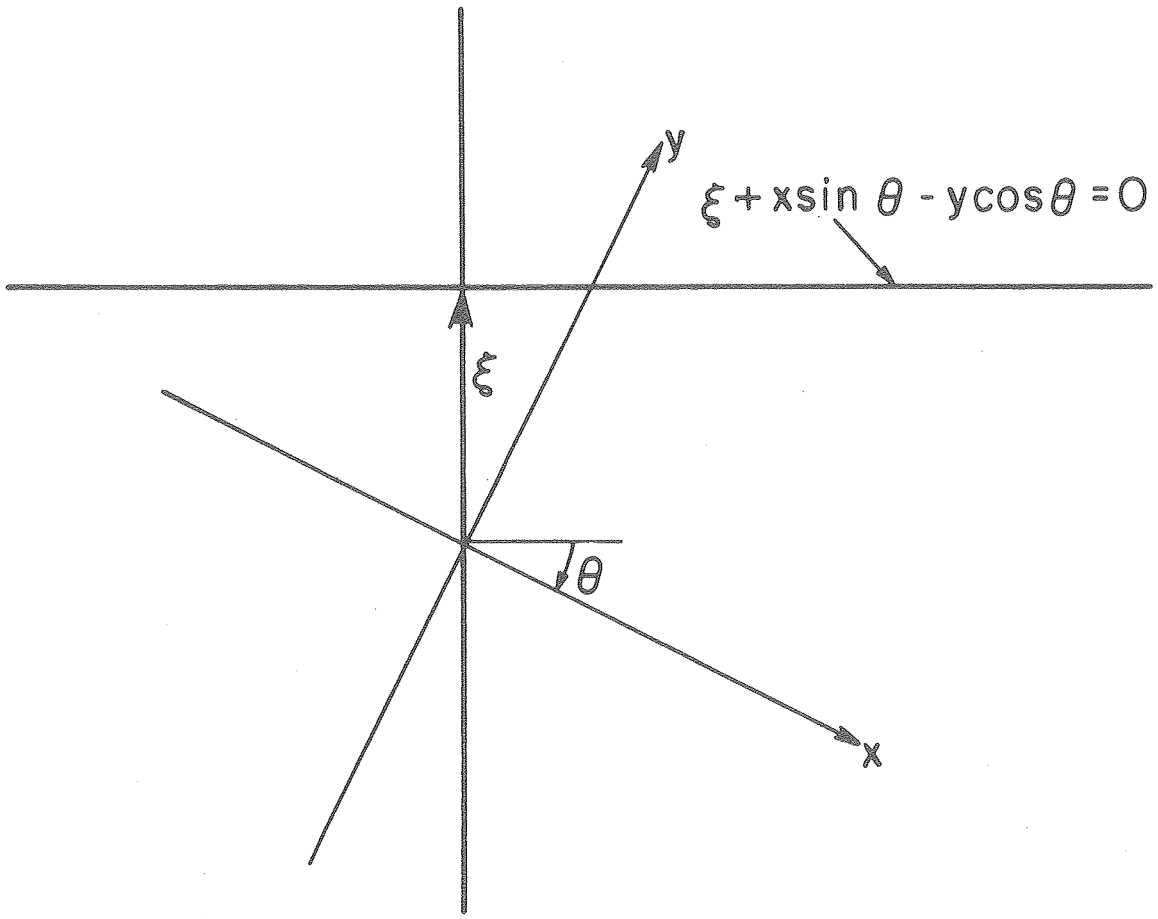

XBL787-3371

Figure 2.1. Parallel-beam geometry for data collected at the projection angle θ. The projection data $p(\xi,\theta)$ represent line integrals for the lines $\xi+x\sin\theta-y\cos\theta = 0$, where ξ is the projected distance measured from the center of rotation along a flat detector.

where δ denotes the Dirac delta function. These projections satisfy the relationship $p(\xi,\theta) = p(-\xi, \theta + \pi)$.

The concept of projections are not restricted to two or three dimensions but can be extended to n-dimensional Euclidean spaces where projections are integrals over (n-1)-dimensional hyperplanes (Gel'fand, Graev, and Vilenkin, 1966). For our purpose we will only be concerned with the two-dimensional case.

2.2.2 Radons's Inversion Formula

The Radon transform is the mapping $\mathcal{R}$ which takes the function f into the function p defined by Eq. (2.1). The inverse of this integral operator is due to Radon (1917) who gave an inversion formula which we will write as

$$f(r,\phi) = \frac{1}{2\pi^2} \int_0^{\pi} \int_{-\infty}^{\infty} \frac{\partial p(\xi,\theta)}{\partial \xi} \frac{d\xi}{r\sin(\phi-\theta)-\xi} \, d\theta \, . \qquad (2.2)$$

A derivation of Eq. (2.2) is given by Deans (1977). One sees from Eq. (2.2) that the reconstruction of f(x,y) at the point (x,y) depends on all possible line integrals of f(x,y) and not just the line integrals which pass through the point (x,y). In the three-dimensional case and in general the n-dimensional case of odd dimension the inversion formula is more local and depends only on the integrals of f over hyperplanes which pass through $\hat{x}$ and over hyperplanes infinitesimally close to these (Gel'fand, Graev, and Vilenkin, 1966). A discussion of the Radon transform and its inverse is also given by Ludwig (1966) and Deans (1978).

Note that the integral over ξ in Eq. (2.2) is a convolution of the partial derivative of the projections $p(\xi,\theta)$ with respect to ξ and the

function $1/\xi$, evaluated at the point $r\sin(\phi-\theta)$. If we let $q(\xi,\theta)$ denote this convolution, i.e.

$$q(\xi,\theta) = \frac{1}{2\pi^2} \left[\partial p(\xi,\theta)/\partial\xi\right] * (1/\xi) \qquad (2.3)$$

then we can rewrite Eq. (2.2) as

$$f(x,y) = \int_0^{\pi} q(r\sin(\phi-\theta),\ \theta)\ d\theta. \qquad (2.4)$$

Some practical considerations such as singularities, numerical stability, and computional speed do not make Eq. (2.4) a good method for reconstructing $f(x,y)$. However there are other algorithms which overcome the difficulties presented by Eq. (2.4).

2.2.3 Back-Projection

The operation in Eq. (2.4) maps the function q into the function f. This is called the back-projection operation which is symbolized as $f(x,y) = \mathcal{B}\{q(\xi,\theta)\}$. The early reconstruction methods of Kuhl (1963 and 1968) and others used this operation to obtain an estimate of the internal structure by back-projecting the measured projections $p(\xi,\theta)$ instead of the modified projections q given above. This process gives an estimate of the density at a point equal to the summation of the projection values of all line integrals that pass through the point. The result gives a blurred image which one can show is equal to the true density convolved with $(x^2+y^2)^{-1/2}$:

$$b(x,y) = \mathcal{B}\{p(\xi,\theta)\} = f(x,y) * \frac{1}{(x^2+y^2)^{1/2}} \ . \qquad (2.5)$$

2.2.4 Back-Projection of Filtered Projection Algorithm

Taking the Fourier transform of the convolution in Eq. (2.3) allows us to rewrite Eq. (2.2) as

$$f(x,y) = \int_0^{\pi} \int_{-\infty}^{\infty} |R|\, \tilde{p}(R,\theta)\, e^{-2\pi i R r \sin(\phi-\theta)}\, dR d\theta \qquad (2.6)$$

where $\mathcal{F}_1[\partial p(\xi,\theta)/\partial\xi] = i\, 2\pi\, R\, \tilde{p}(R,\theta)$ and $\mathcal{F}_1[1/\xi] = -i\pi\, \mathrm{sgn}\, R$ (see p. 130 and p. 183 Bracewell, 1965). The application of this equation to real data can only operate on data samples of finite length. With this motivation, we can replace $|R|$ with

$$\tilde{c}(R) = |R|\, w(R) \qquad (2.7)$$

and obtain an estimate of f:

$$\hat{f}(x,y) = \int_0^{\pi} \int_{-\infty}^{\infty} \tilde{c}(R)\, \tilde{p}(R,\theta)\, e^{-2\pi i\, Rr \sin(\phi-\theta)}\, dR d\theta\ . \qquad (2.8)$$

The window function w can be selected based on spatial and contrast resolution requirements.

The back-projection of the filtered projection algorithm digitally implements Eq. (2.8) by performing the following sequence of operations: Fourier transform the projection data; multiply the complex values of the Fourier transform by a filter function; inverse Fourier transform these modified frequencies; and back-project the modified projection data (Huesman et al., 1977). These algorithm operations are symbolized as:

$$\hat{f} = \mathcal{B}\{\mathcal{F}_1^{-1}\, [\tilde{c}\mathcal{F}_1(p)]\}\ . \qquad (2.9)$$

This method of reconstructing f is appealing since it lends itself to easily changing the noise propagation vs. resolution properties of the window function. One can improve resolution by changing the shape of the window function, but the noise amplification will increase. Alternatively, one can suppress noise; however this noise suppression will come at the cost of resolution.

2.2.5 Convolution Algorithm

Due to the convolution theorem Eq. (2.8) is equivalent to convolving the projections p with a convolution function in real space:

$$\hat{f}(x,y) = \int_0^{\pi} \int_{-\infty}^{\infty} c(r\sin(\phi-\theta)-\xi)\ p(\xi,\theta)\ d\xi d\theta\ . \tag{2.10}$$

The convolution algorithm first convolves the projection data with a convolver and then back-projects the modified projection data. These algorithm operations are symbolized by the equation

$$\hat{f} = \mathcal{B}\{c * p\}\ . \tag{2.11}$$

The convolution functions which are commonly used in reconstruction tomography were developed by Bracewell and Riddle (1967), Ramachandran and Lakshminarayanan (1971), and Shepp and Logan (1974). The convolution algorithm is now used in most commercial x-ray scanners and positron emission tomographic systems because of its computational efficiency and because it requires very little computer memory.

2.2.6 Filter of the Back-Projection Algorithm

The filter of the back-projection algorithm reconstructs f by

deconvolving the true image f from the back-projected image b given by Eq. (2.5) (Bates and Peters, 1971). The algorithm performs the following sequence of operations: back-project the projection data; Fourier transform the two-dimensional back-projection image; multiply the two-dimensionally distributed Fourier coefficients by a filter function; and perform the two-dimensional inverse Fourier transform (Huesman et al., 1977). These algorithm operations are symbolized by the equation

$$\hat{f} = \mathcal{F}_2^{-1} \{\tilde{c}\mathcal{F}_2[\mathcal{B}(p)]\} \tag{2.12}$$

where $\tilde{c}$ is the filter function given in Eq. (2.7). The derivation of the algorithm is based on the convolution theorem and the fact that $r^{-1} = \mathcal{F}_2^{-1}(R^{-1})$ (see definition of Hankel transform and tables, pp 244-250, Bracewell, 1965).

2.2.7 Iterative Algorithms

The algorithms previously discussed gave analytical expressions for the density function in terms of integral equations which assumed a continuous angular and lateral sampling of projections. The digital implemantation of these algorithms use either the fast Fourier transform or a finite convolution algorithm and numerically calculate the integrals over angle using the trapezoidal method. For finite projection samples another approach is to represent Eq. (2.1) as a system of linear equations

$$Ff = P \tag{2.13}$$

where F is the matrix projection operator, f is a vector of unknown densities, and P is a vector of projection samples. The solution to Eq. (2.13) is

$$f = F^{G} P \tag{2.14}$$

where F^{G} is the generalized inverse of F (Ben-Israel and Greville, 1974). For most reconstruction problems F has dimensions greater than 4096×4096 for which it is impractical to solve the generalized inverse by a digital computer. Therefore iterative methods such as ART (Gordon, Bender, and Herman, 1970) and gradient or conjugate gradient techniques (Huesman et al., 1977) are used to solve Eq. (2.13).

2.3 Transmission Computed Tomography

Transmission computed tomography (TCT) computes the spatial distribution of the linear attenuation coefficients from data obtained by passing an externally generated source of photons through the subject. X-ray TCT instruments such as the EMI scanner use an external x-ray tube which rotates around the patient (Fig. 2.2). The transmission data in single-photon ECT is obtained with an external gamma-ray emitting point source with the same energy as the internal emitting radionuclide. The newer single-photon ECT machines such as the Humongotron (Keyes et al., 1977) have the gamma-ray point source mounted to the rotating gantry. The Donner Ring positron ECT device (Derenzo et al., 1977) uses a ring of positron emitters distributed around the patient as the transmission source.

The photons that pass through the body are measured by an opposing detector. The intensity $I(\xi,\theta)$ of the transmitted beam is equal to

$$I(\xi,\theta) = I_0(\xi,\theta) \exp\left[-\iint \mu(x,y)\ \delta(\xi + x\sin\theta - y\cos\theta)\ dxdy\right] \tag{2.15}$$

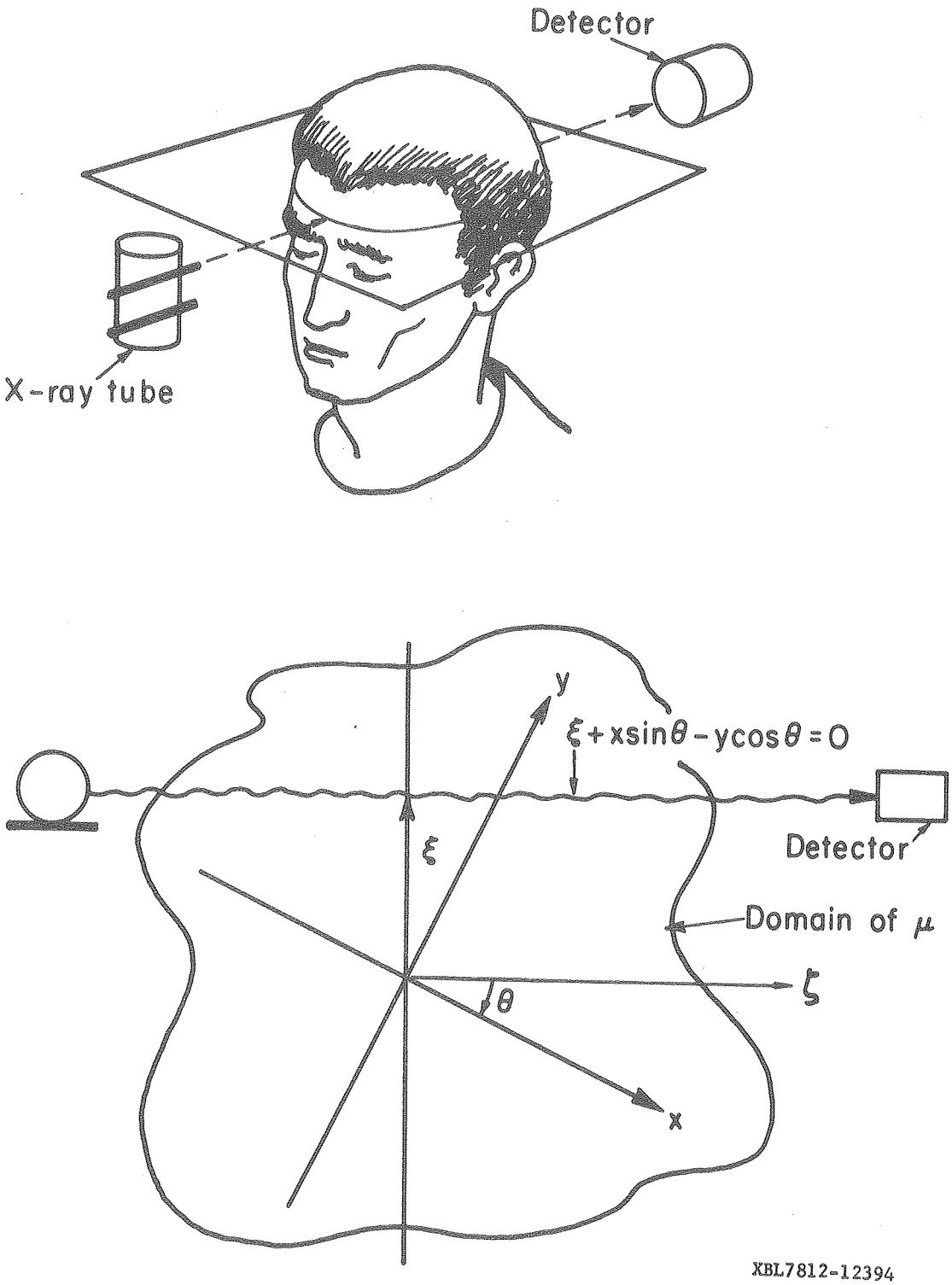

Figure 2.2. Transmission computed tomography. The source radiation such as x-rays pass through the subject along rays satisfying $\xi+x\sin\theta-y\cos\theta = 0$.

where $\mu(x,y)$ is the distribution of attenuation coefficients and I_o is the incident beam intensity. The function $\mu(x,y)\ \delta(\xi+x\sin\theta-y\cos\theta)$ is interpreted as a line of density $\mu(x,y)$ on the ray defined by the equation $\xi+x\sin\theta-y\cos\theta = 0$ (Fig. 2.2). The projection $p(\xi,\theta)$ of attenuation coefficients is related to the incident beam intensity I_o and the transmitted beam intensity I by the relation

$$p(\xi,\theta) = -\log[I(\xi,\theta)/I_o(\xi,\theta)] = \int\int \mu(x,y)\delta(\xi+x\sin\theta-y\cos\theta)dxdy. \quad (2.16)$$

The transverse section representing the distribution of photon linear attenuation coefficients is reconstructed from the projections $p(\xi,\theta)$ using one of the algorithms described in the previous sections.

2.3.1 The Exponential Absorption of Radiation

When x-rays or gamma rays pass through an absorbing medium such as body tissue, interactions occur between the photon and an electron by four distinct mechanisms known as the photoelectric process, the Compton process, coherent scattering, and pair production (Johns and Cunningham, 1974). The rate of change per distance of the total number of unscattered photons as a consequence of these four mechanisms is represented mathematically as

$$\frac{dI}{d\zeta} = -\mu I \quad (2.17)$$

where ζ is the linear dimension of the path being traversed by the photons, I is the total number of unscattered photons at ζ, and μ is the linear attenuation coefficient. In essence Eq. (2.17) states that the infintesimal change in the number of unscattered photons as it passes through the absorption medium is negatively proportional to the number of unscattered photons reaching that point (or distance or depth). The negative sign implies that the number of photons $I(\zeta)$ decreases as the linear path length increases.

The solution of the differential equation given by Eq. (2.17) is

$$I(\zeta) = I_0 e^{-\mu(\zeta-\zeta_0)} \tag{2.18}$$

where I_0 is the number of photons at $\zeta = \zeta_0$. The dimension of the attenuation coefficient μ is inverse distance. As photons pass through body tissue the linear attenuation coefficient will vary due to the variation in the composition of the biological material, i.e. lungs, bone, blood, etc. This changes Eq. (2.18) to

$$I(\zeta) = I_0 \exp\left\{-\int_{\zeta_0}^{\zeta} \mu(\zeta')\, d\zeta'\right\}. \tag{2.19}$$

It is this variation which is measured by TCT.

2.3.2 The Linear Attenuation Coefficient

The linear attenuation coefficient μ can be converted to either the mass, electronic or atomic attenuation coefficients by dividing μ by the mass density $\rho(\text{gm/cm}^3)$, electron density ρ_e (electrons/cm^3), or atomic density ρ_a(atoms/cm^3) of the material to give units of cm^2/gm,

cm^2/electron, or cm^2/atom, respectively. The values for these coefficients often expressed in barns (1 barn = $10^{-24} cm^2$) can be found in tables (see Hubbell and Berger, 1966; Johns and Cunningham, 1974). Since these coefficients are in units of cm^2/gm or cm^2/electron or cm^2/atom, they are often called cross sections.

From a geometric point of view the terms cross section can be thought of as the cross-sectional area of atoms or electrons seen by a photon as it passes through the tissue. This is truly an over simplification because for different types of interactions the cross-sectional area varies. One might say that for different interactions the atoms or electrons have differing cross-sectional force fields. It is more accurate to think of the cross section as a measure of the probability the photon will interact with the material. For example it can be shown from Eq. (2.17) that if a flux of N photons/cm^2/sec interacts with a target of tissue containing ρ_e electrons/cm^3 then the number of interactions per target (i.e. number of interactions per cm^3) in time t is $N\rho_e t$ x (electronic cross section).

The linear attenuation coefficient is obtained from the mass, electronic, or atomic cross section by multiplying by the density in gm/cm^3, electrons/cm^3, or atoms/cm^3 as appropriate. Thus the linear attenuation coefficient has units of inverse distance and is a measure of the fraction of photons removed from the beam per length of absorber. However it does not tell how photon energy is absorbed. Instead the linear attenuation coefficient is the sum of the photoelectric (τ), coherent (σ_{coh}), Compton (σ), and pair production (π) attenuation

coefficients all in units of inverse length. Each one of these coefficients is a measure of a physical process by which photons can set electrons in motion.

2.3.2.1 The Photoelectric Absorption Process

The photoelectric process involves a photon colliding with an atom and ejecting an electron either from the K, L, M, or N shells of the atom and absorbing the total photon energy. The probability of ejecting an electron is maximum if the photon has just enough energy to overcome the binding energy of the electron and knock it from its shell. The photoelectric absorption in tissue is most important at low energy representing the most probable mechanism for photon loss for energies less than 50 keV.

2.3.2.2 Coherent Scattering

Coherent scattering involves unbound electrons or virtually unbound electrons such as those in the outer shell of the atom which have binding energies of only a few electron volts. If we consider a photon as an electromagnetic wave, then as this wave comes near an electron it sets the electron vibrating which causes it to radiate energy at the same frequency as the incident wave. This process is called coherent scattering. The scattered photon has the same energy and same wave length as the incident photon.

2.3.2.3 Compton Scattering

In contrast to coherent scattering, Compton scattering is a process where the incoming photon gives up some of its energy to the electron in accordance with the conservation of energy and momentum. Even though Compton and coherent scattering do not absorb the photon totally, these processes are considered in the total linear attenuation coefficient. Any well collimated detector will not see many of these scattered photons and if detected the detector electronics will usually reject the photon because it has lost enough energy to no longer be within the selected energy window.

The Compton process depends on the number of electrons per gram and thus with the exception of hydrogen (which has twice the electrons per gram then any other material) the absorption per gram by the Compton process is nearly the same for all materials. The Compton cross section decreases with an increase in energy. The overall fraction of the energy scattered is large for low energy photons and is small for high energy photons. For photon energies from 100 keV to 10 MeV, Compton scattering is much more important in soft tissue than either coherent, photoelectric or pair production.

2.3.2.4 Pair Production

The process of pair production involves photons with energies greater than 1.02 Mev. When a photon with this energy comes near the nucleus of the atom it may become a positron and an electron pair. The positron and electron have the same mass of 511 keV. Thus by the conservation of energy and momentum, photon energies of less than

1.02 Mev cannot experience pair production.

2.3.2.5 The Total Linear Attenuation Coefficient in Bone and Tissue

The total linear attenuation coefficient μ is the sum of the photoelectric (τ), coherent (σ_{coh}), Compton (σ), and pair production (π) attenuation coefficients:

$$\mu = \tau + \sigma_{coh} + \sigma + \pi \ . \qquad (2.20)$$

At low Z materials found in biological tissues and at energies emitted by radioactive tracers, coherent scattering is negligible and is not considered. Also most radiopharmaceuticals used in single-photon ECT have radioactive nuclei which release photons of energies less than 1.02 MeV therefore for these energies the pair production cross section is zero. Thus the primary processes experienced by ECT are Compton scattering and photoelectric absorption which reduces Eq. (2.20) to

$$\mu = \tau + \sigma \ . \qquad (2.21)$$

Fig. 2.3 gives a plot of the photoelectric and Compton attenuation coefficients for water as a function of energy. For energies less than 27 keV, photoelectric is the primary absorption process and Compton is for energies greater than 27 keV.

Figure 2.4 compares the plot of the cross section (cm^2/gm) and linear attenuation coefficient for bone with that of water ($\approx$ soft tissue). For energies where photoelectric is the primary process (<27 keV), bone will absorb almost 5 times as much energy gram for gram as soft tissue. This means that at these energies the atomic number of the material is the determining factor for photon attenuation. At

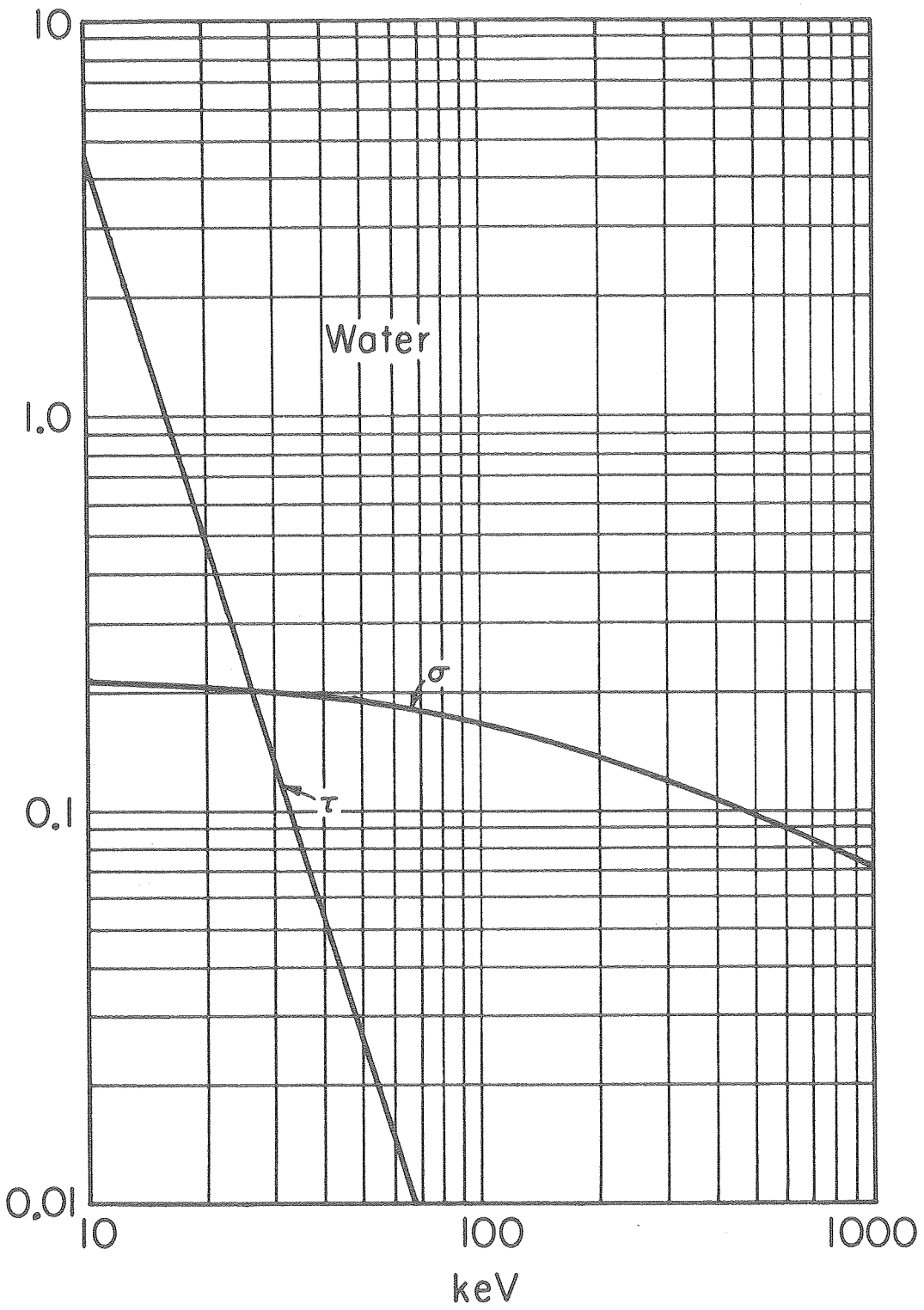

XBL789-3565

Figure 2.3. Photoelectric (τ) and Compton (σ) linear attenuation coefficients (cm^{-1}) for water as a function of energy.

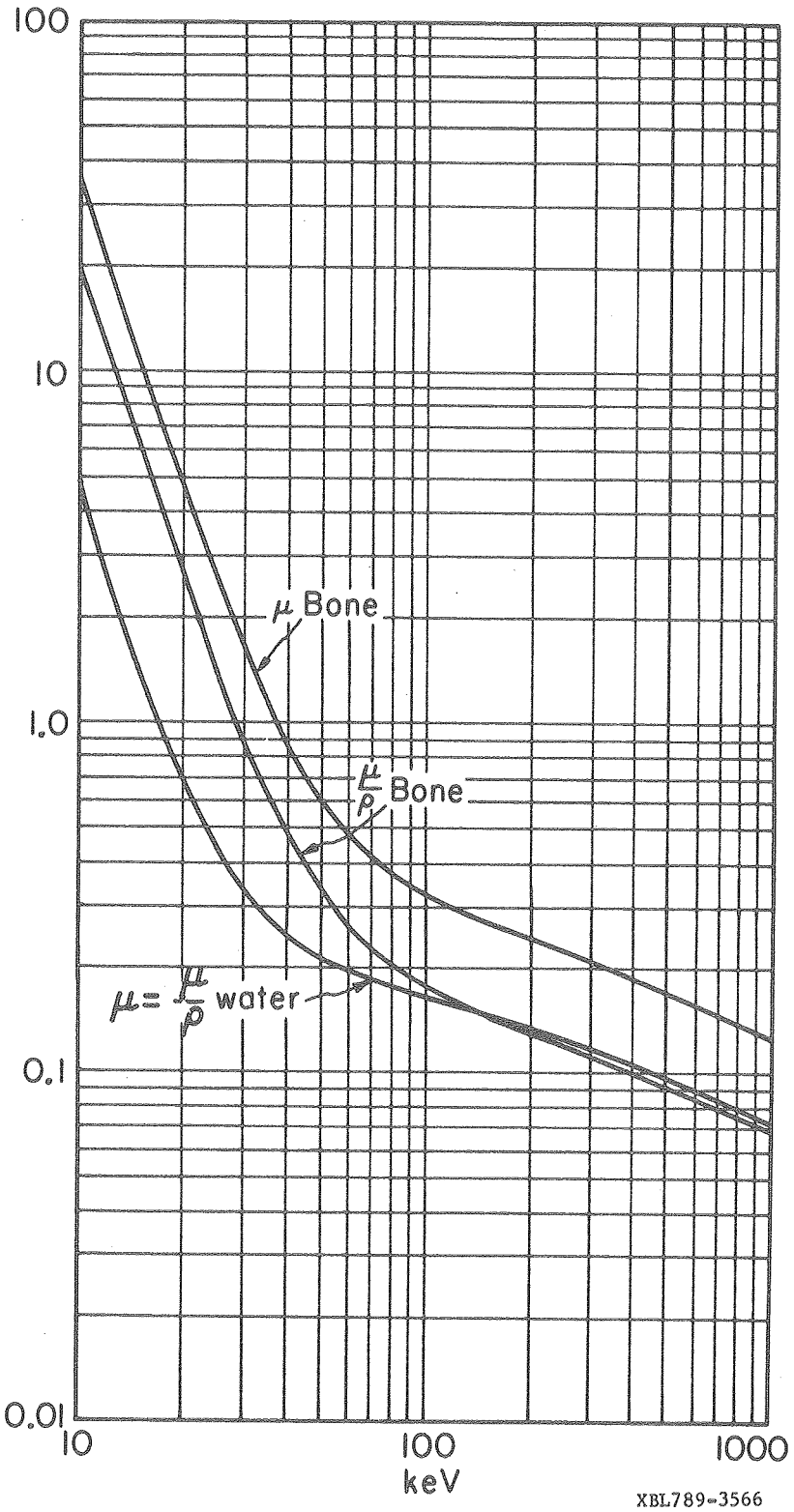

Figure 2.4. Mass attenuation coefficient μ/ρ (cm^2/gm) and linear attenuation coefficient μ (cm^{-1}) for bone and water. The density of water = 1.00 gm/cm^3 and the density of bone = 1.83 gm/cm^3.

energies from 200 keV to 2 Mev Compton absorption is the primary process suggesting that electron density is the determining factor. Since most materials except for H_2 have nearly the same number of electrons per gram, bone and soft tissue will absorb the same amount of energy gram for gram for these higher energy photons.

2.4 Emission Computed Tomography

Emission computed tomography uses two basic types of radionuclides; those which are positron emitters such as ^{11}C, ^{13}N, ^{15}O, ^{82}Rb and those which are gamma emitters such as ^{99m}Tc and ^{131}I. Some radionuclides can be both positron and gamma emitters whereby each radionuclide has a certain probability of either distintegrating by emitting a positron or a gamma ray. A comparison of positron and single-photon ECT is given in (Budinger, Derenzo, et al., 1977).

The decay process for a positron emitter involves radionuclides which are neutron deficient relative to the number of protrons. In such cases a protron is converted to a neutron with the loss of a positive charge with the same mass as an electron. This positive charge called a positron and also referred to as an antielectron is ejected from the nucleus and within millimeters annihilates with an electron producing two photons each having an energy of 511 keV and traveling away from each other at an angle of 180°.

The decay processes which lead to the release of single photons are isomeric transition, electron capture, and beta emission. Isomeric transition occurs when the atomic nucleus falls to a state of lower energy. For some nuclei this occurs rapidly with a very short half-life, whereas others such as ^{99m}Tc remain in a metastable state with a half-life

of 6 hours before falling to a state of lower energy with the release of a photon. In the electron capture process the nucleus makes use of the deeply penetrating orbital s electrons of the K shell of the atom and converts the electron and protron into a neutron. Energy in the form of characteristic x-rays are released when electrons cascade down from outer atomic shells to fill the gap left by the converted electron from the K shell. In most cases, after electron capture the nuclides are in an excited state and decay to a more stable state with the release of a photon. The third decay process occurs when a neutron in the nucleus is converted to a protron and this conversion process releases an electron. The emitted electron is known as a β^- particle. As in the case of electron capture the nucleus is usually in an excited state and decays to a stable state with the release of a photon.

2.4.1 Positron Emission Computed Tomography

Detection schemes as shown in Fig. 2.5 use the two photons obtained from the annihilation of an electron and a positron so that events are recorded if two opposing detectors detect both photons in coincidence, i.e. within a certain time interval ($\approx 10^{-8}$ sec). The probability that both photons will not be attenuated by the tissue interposed between the annihilation and the detector is

$$\text{Probability of both photons escaping} = \exp\{-\int_{D_1}^{\zeta_o} \mu(\zeta,\xi,\theta)d\zeta\} \times \exp\{-\int_{\zeta_o}^{D_2} \mu(\zeta,\xi,\theta)d\zeta\}$$

$$= \exp\{-\int_{D_1}^{D_2} \mu(\zeta,\xi,\theta)d\zeta\} \qquad (2.22)$$

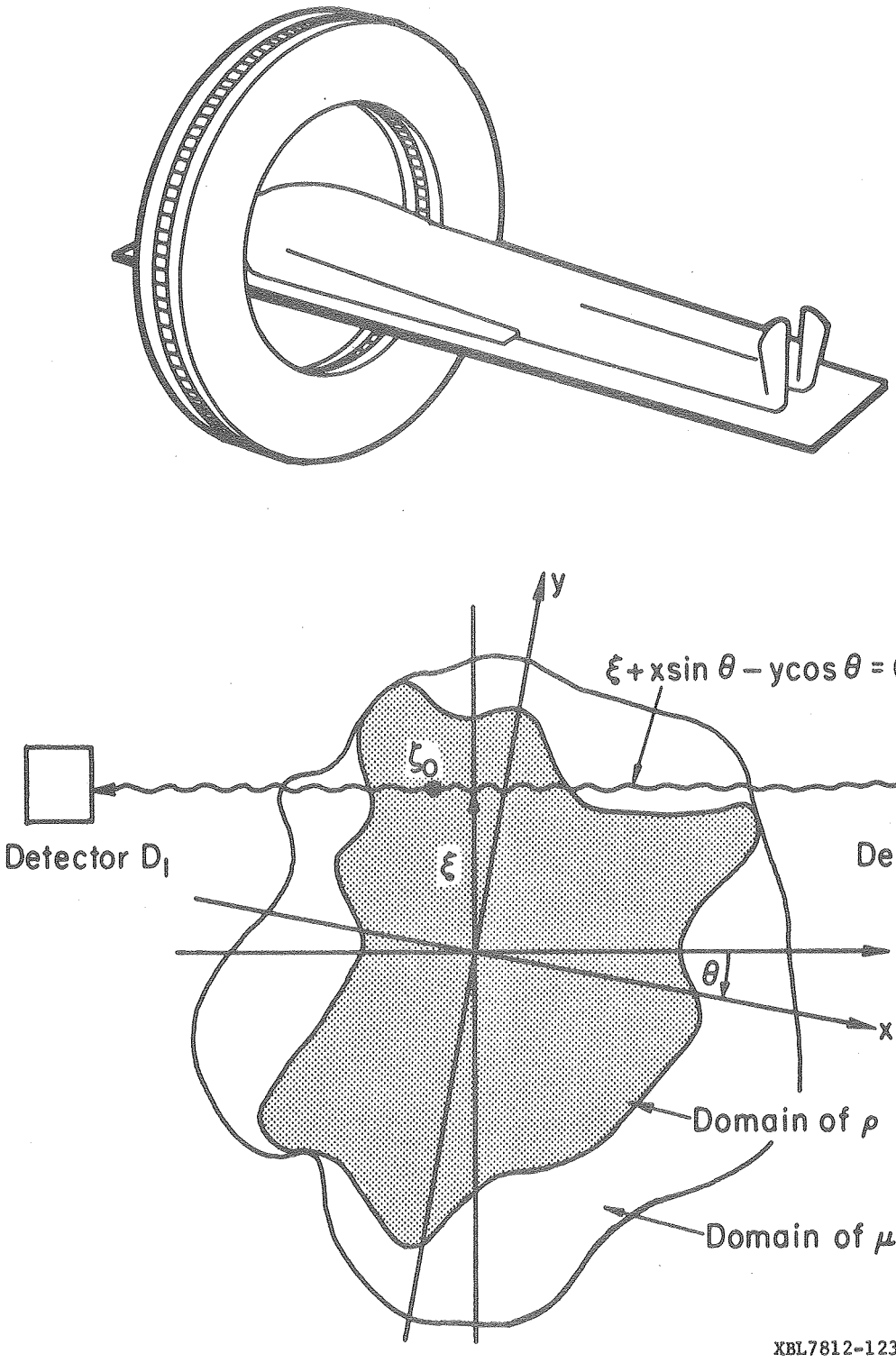

Figure 2.5. Positron emission computed tomography. At the rotation angle θ and lateral sampling ξ, the detectors D_1 and D_2 will detect those annihilations whose photons travel apart along the line $\xi+x\sin\theta-y\cos\theta=0$.

where μ is the distribution of attenuation coefficients. This is the same probability for every possible positron annihilation that may occur along the ray path imaged by the two detectors D_1 and D_2 at the same rotation angle θ and lateral sampling distance ξ. The projection $p_{\gamma\gamma}(\xi,\theta)$ of these annihilations along this ray path is

$$p_{\gamma\gamma}(\xi,\theta) = \exp\left[-\int\int \mu(x,y)\ \delta(\xi + x\sin\theta - y\cos\theta)\ dxdy\right]$$

$$\times \int\int \rho(x,y)\ \delta(\xi + x\sin\theta - y\cos\theta)dxdy \qquad (2.23)$$

where $\rho(x,y)$ is the concentration of positron emitter. Therefore, each projection value is the line integral of the positron concentration distribution multiplied by an exponential attenuation factor determined from the line integral of attenuation coefficients over the total ray path. These data are easily modified for attenuation effects giving the corrected projection data

$$p(\xi,\theta) = \exp\left[\int\int \mu(x,y)\ \delta(\xi + x\sin\theta - y\cos\theta)\ dxdy\right] p_{\gamma\gamma}(\xi,\theta)$$

$$= \int\int \rho(x,y)\ \delta(\xi + x\sin\theta - y\cos\theta)dxdy\ . \qquad (2.24)$$

2.4.2 Single-Photon Emission Computed Tomography

The attenuation compensation needed for single-photon emission computed tomography is not a simple multiplicative correction of the observed projection data as in the case of positron emission tomography (Eq. 2.24). The atomic decay processes which produce gamma radiation do not allow the advantage of coincidence detection to easily compensate for attenuation. Instead the physics requires one to model the detection

of single photons with a more difficult mathematical equation.

A scintillation detector illustrated in Fig. 2.6 is used to measure the photons released by radioactive nuclei. The projections for a particular transverse section represent photons which have been released by radioactive nuclei that lie in the transverse section perpendicular to the detector. The photons measured are only those photons which are released within a solid angle subtended by the detector and which are not attenuated by one of the processes discussed previously. Each nucleus which lies along the line $\xi+x\sin\theta-y\cos\theta = 0$ has a different probability of being detected dependent on the body material interposed between the nucleus and the detector.

For single photon emitters, the probability of detecting an event is not independent of position of the emitting radionuclide along the ray path as it is for positron emitters. Instead the probability that the photon will reach the detector is

$$\text{Probability of photon escaping} = \exp\left\{-\int_{\zeta_0}^{D} \mu(\zeta,\theta)d\zeta\right\} \qquad (2.25)$$

where ζ_0 is the position where the radionuclide decays, D is the detector coordinate, and μ is the distribution of attenuation coefficients which is a function of tissue density and photon energy. The probability therefore depends on the tissue distributed between the radionuclide and the detector, and on the energy of the emitted photon.

The projection $p_\gamma(\xi,\theta)$ (Fig. 2.6) for single-photon emission tomography is given by Eq. (1.1). Expanding the dot products

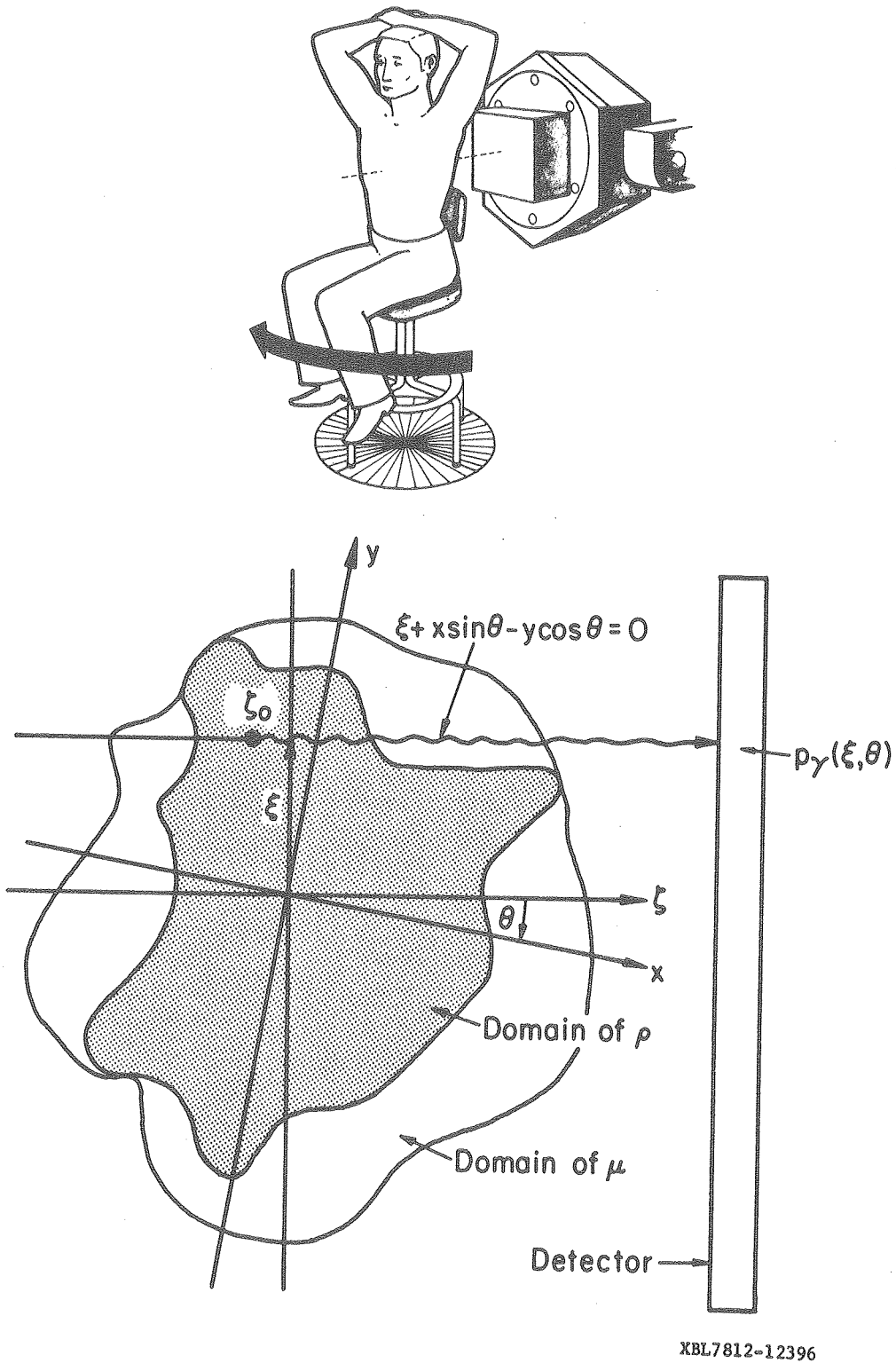

Figure 2.6. Single-photon emission computed tomography. At the rotation angle θ and lateral sampling ξ, the detector will see those photons which travel along the line $\xi+x\sin\theta-y\cos\theta = 0$ and are not attenuated by body tissue.

in the delta function gives an equivalent expression

$$p_\gamma(\xi,\theta) = \int\int \rho(x,y)a(x,y,\xi,\theta)\ \delta(\xi + x\sin\theta - y\cos\theta)dxdy \qquad (2.26)$$

where

$$a(x,y,\xi,\theta) = \exp\left[-\int_x^{\text{detector}}\int_y \mu(x',y')\delta(\xi + x'\sin\theta - y'\cos\theta)dx'dy'\right] .$$

A single-photon projection is the summation of isotope concentration at the points (x,y) modified by an exponential e^{-z} where z is the line integral of attenuation coefficients from the point (x,y) to the detector. The single-photon emission reconstruction problem is more difficult than either transmission or positron emission tomography. The influence of the term $a(x,y,\xi,\theta)$ depends on the distribution of attenuation coefficients, which unfortunately has such large values for all energies used in nuclear medicine that the reconstructed images are seriously affected using the computed tomography algorithms discussed in Section 2.2 without compensating for attenuation.

2.4.2.1 Examples of Reconstructing Single-Photon Data Without Compensating for Attenuation

Straightforward mathematical methods used to reconstruct x-ray transmission and positron emission modified projection data yield poor quality images in single-photon ECT because of the attenuation of the gamma radiation in the tissue. This can be seen from Fig. 2.7, where a phantom disc of 23 cm diameter and constant attenuation is used to illustrate the effect of reconstructing transverse sections without compensating for attenuation. The data were generated from computer

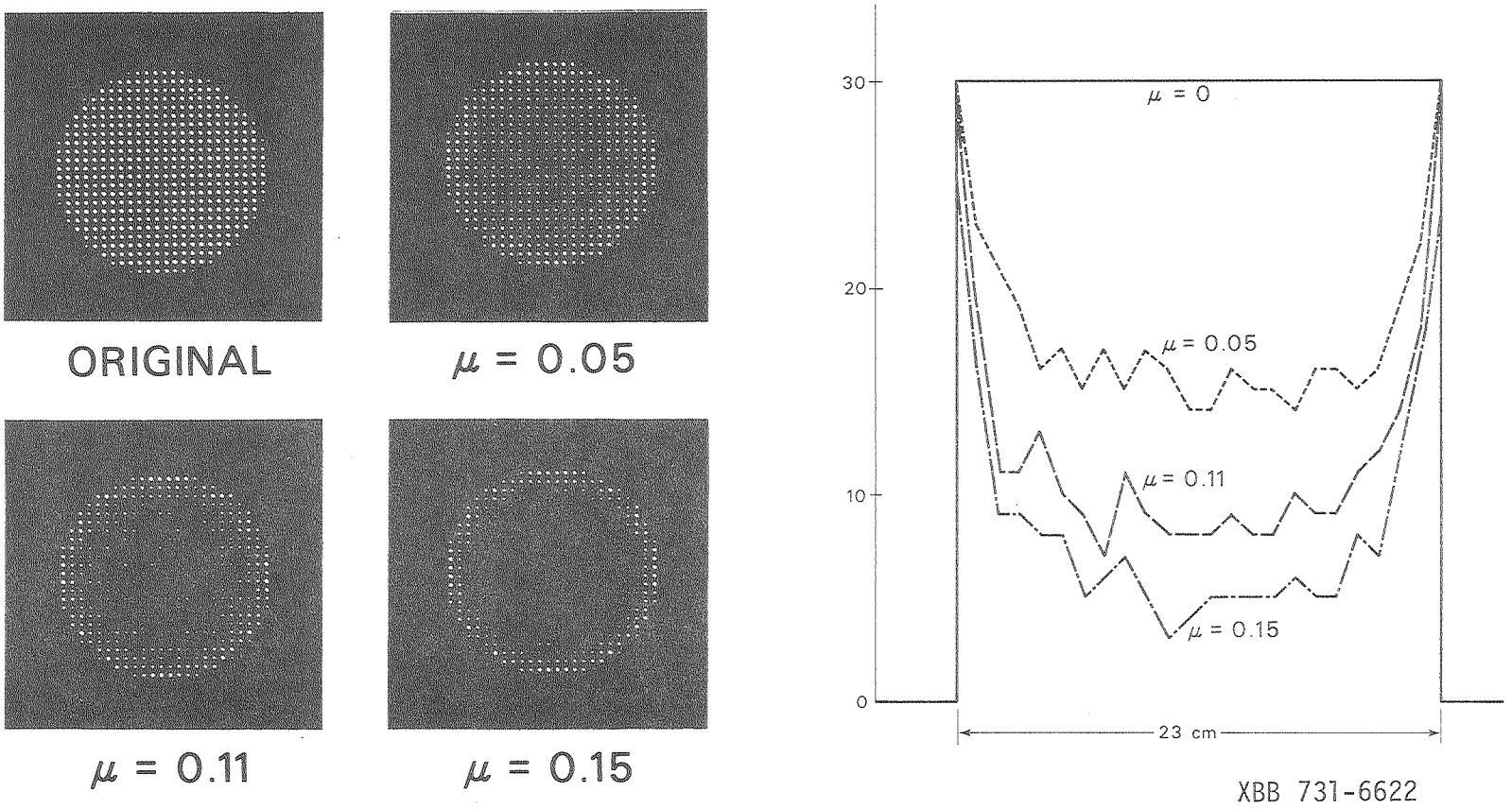

Figure 2.7. Computer simulations of transverse sections reconstructed without attenuation compensation for various attenuation coefficients. Statistical fluctuations were added to the projections. Profiles through the sections are shown at the right.

simulations for gamma rays of a few MeV ($\mu \cong 0.05$) and compared to those for gamma rays of 511 keV ($\mu \approx 0.10$) and 140 keV ($\mu \approx 0.15$). The images in the lower row show the serious artifact that results for the usual isotopes used in nuclear medicine if attenuation is not taken into account. For example, with an attenuation coefficient of 0.15 cm^{-1} for a ^{99m}Tc source in the center of a brain, only 18 out of 100 photons are detected compared to 86 out of 100 photons detected from 1 cm beneath the scalp. Thus for a truly quantitative reconstruction of gamma emitter concentration, compensation for attenuation must be employed.

As a numerical example, we can calculate the projections $p_\gamma(\xi,\theta)$ for a disc (transverse section through a sphere) containing a homogeneous emitter concentration ρ and a constant attenuation coefficient μ. The functions $\rho(x,y)$, and $\mu(x,y)$ of Eq. (2.26) are defined by the equations

$$\rho(x,y) = \begin{cases} C, & x^2 + y^2 \leq r_o^2 \\ 0, & \text{otherwise} \end{cases} \tag{2.27}$$

$$\mu(x,y) = \begin{cases} \mu, & x^2 + y^2 \leq r_o^2 \\ 0, & \text{otherwise} \end{cases} . \tag{2.28}$$

Substituting these expressions into Eq. (2.26) we see that the problem is reduced to determining the attenuation factor $e^{-\mu\ell}$ where ℓ is the distance between the point (x,y) and the boundary of the disc (Fig. 2.8). Thus, for $\theta=0$, the weight function $a(x,y,\xi,\theta = 0)$ becomes $\exp[-\mu\ell(x,y,\xi,0)]$ where $\ell(x,y,\xi,0)$ is just $-x + \sqrt{r_o^2-\xi^2}$ as can be seen from Fig. 2.8. Also, for a disc, the attenuated Radon transform

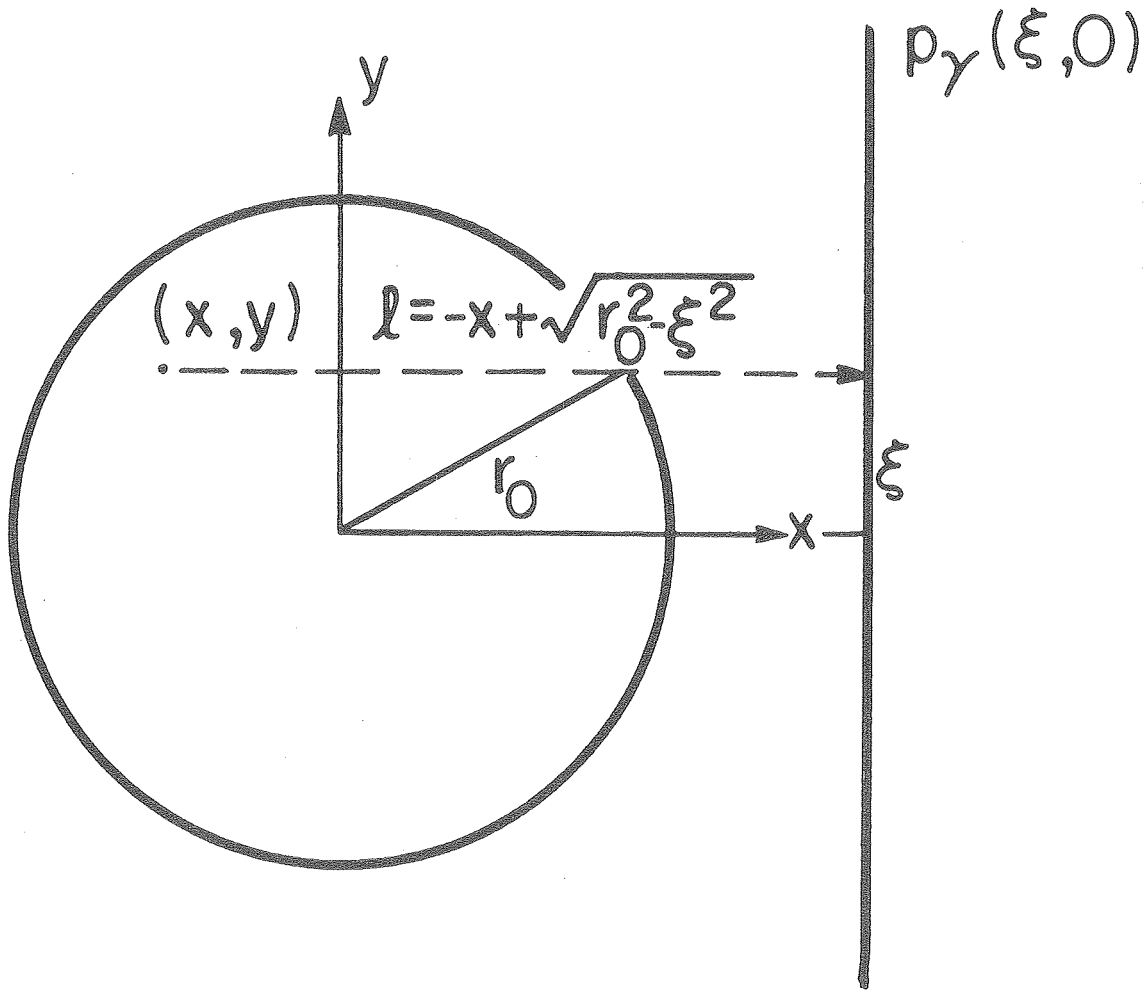

XBL786-3308

Figure 2.8. For a circular disc with constant attenuation and constant emitter concentration, the attenuation factor $a(x,y,\xi,\theta)$ reduces to $e^{-\mu\ell}$ where ℓ is the length of the line segment between the point (x,y) and the edge of the circular disc.

is independent of θ because of circular symmetry. Thus Eq. (2.26) reduces to

$$p_\gamma(\xi) = \int_{-\sqrt{r_o^2-\xi^2}}^{\sqrt{r_o^2-\xi^2}} C \exp[-\mu(-x + \sqrt{r_o^2-\xi^2})]dx \ . \qquad (2.29)$$

Integration of Eq. (2.29) gives

$$p_\gamma(\xi) = \frac{C}{\mu} - \frac{C}{\mu} \exp[-2\mu \sqrt{r_o^2-\xi^2}\ ] \ . \qquad (2.30)$$

This is the case for constant attenuation coefficient μ. To compare this to the case where there is no significant attenuation ($\mu \to 0$) the projections are simply

$$p_\gamma(\xi) = 2C\sqrt{r_o^2-\xi^2} \ . \qquad (2.31)$$

These two functions, Eqs. (2.30) and (2.31), are shown for $\mu = 0.15$ cm^{-1} and $r_o = 20$ cm. in Fig. 2.9.

For no attenuation the reconstruction is given by Radon's inversion formula:

$$\rho(r,\phi) = \frac{1}{2\pi^2} \int_0^\pi \int_{-\infty}^{\infty} \frac{\partial p(\xi,\theta)}{\partial \xi} \frac{d\xi d\theta}{r \sin(\phi - \theta) - \xi} \qquad (2.32)$$

where $\rho(r,\phi)$ is the true distribution in polar coordinates and $p(\xi,\theta)$ is the projection function. For circular symmetry, this reduces to the inverse of the Abel transform:

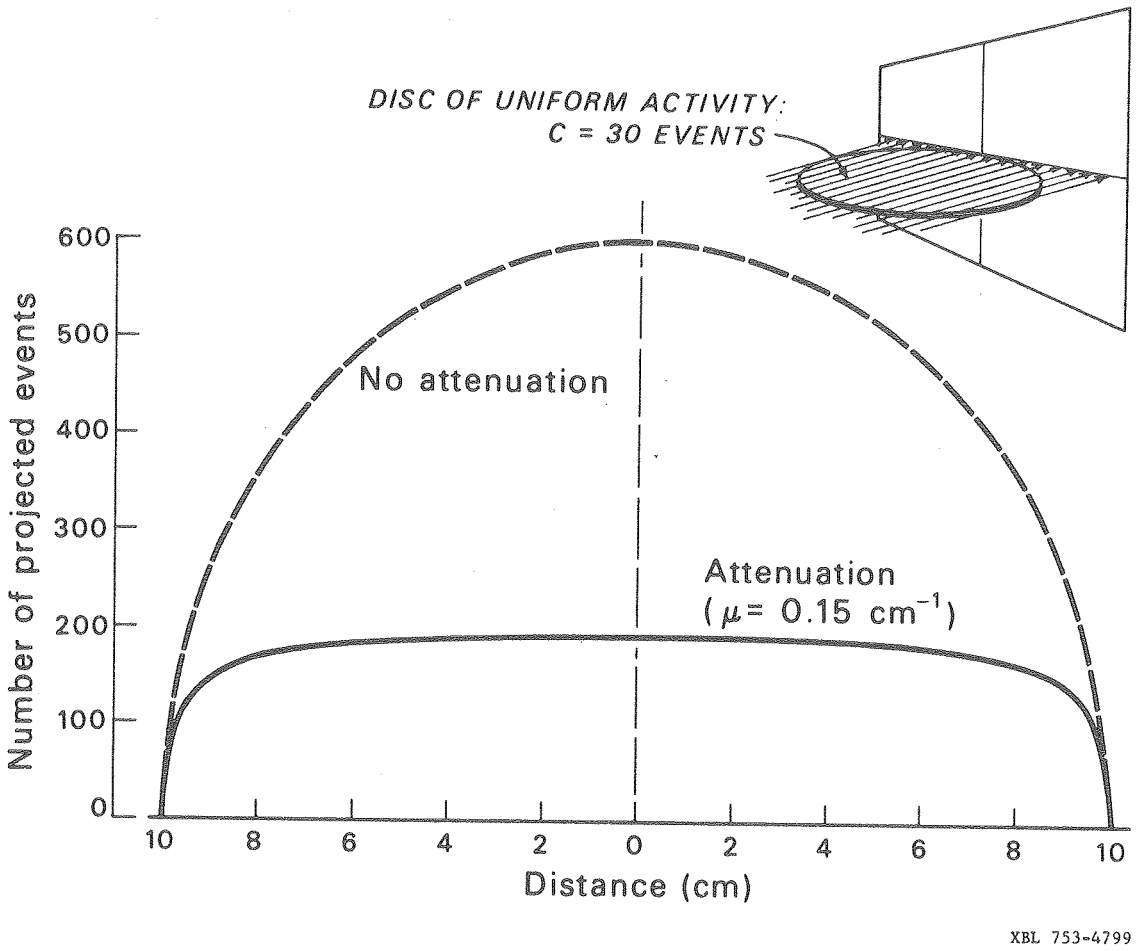

Figure 2.9. The projection value for a disc with attenuation $\mu = 0.15$ and emitter concentration C = 30 results in a diminution at the center by a factor of 3.16.

$$\rho(r) = \frac{1}{\pi} \int_r^\infty \frac{\partial p(\xi)}{\partial \xi} \frac{d\xi}{(\xi^2 - r^2)^{1/2}} \quad . \tag{2.33}$$

The operation of Eq. (2.33) on the projection function in Eq. (2.31) gives C for points in the domain of ρ, as expected. However, for attenuated projection data, Eq. (2.30), Abel's inversion formula gives

$$\rho(r) = \begin{cases} C \sum_{n=0}^{\infty} \left\{ \frac{\mu^{2n}}{(n!)^2} (r_o^2 - r^2)^n - \frac{1}{\pi} \frac{(n!)^2 2^{4n+2}}{[(2n+1)!]^2} \mu^{2n+1} (r_o^2 - r^2)^{\frac{2n+1}{2}} \right\}, & r \leq r_o \\ 0, & \text{otherwise} \quad . \end{cases} \tag{2.34}$$

Equation (2.34) is plotted in Fig. 2.10 for various attenuation coefficients showing the reconstructed profiles of a 23 cm disc when attenuation is ignored.

2.4.2.2 Development of Instrumentation for Single-Photon ECT

Single-photon ECT was pioneered by Kuhl and Edwards who began to develop the principles of emission computed tomography as early as the late 1950's, with the eventual development of the MARK I scanner (Kuhl and Edwards, 1963). The MARK I uses a single detector which moves back and forth in a linear fashion at each projection angle. The concept of this type of rectilinear scanner is shown schematically in Fig. 2.11A. Kuhl first used analog reconstruction methods which gave a back projection showing a blurred tomogram. Subsequently the system was modified with the introduction of a computer applied correction which enabled it to yield quantitative data.

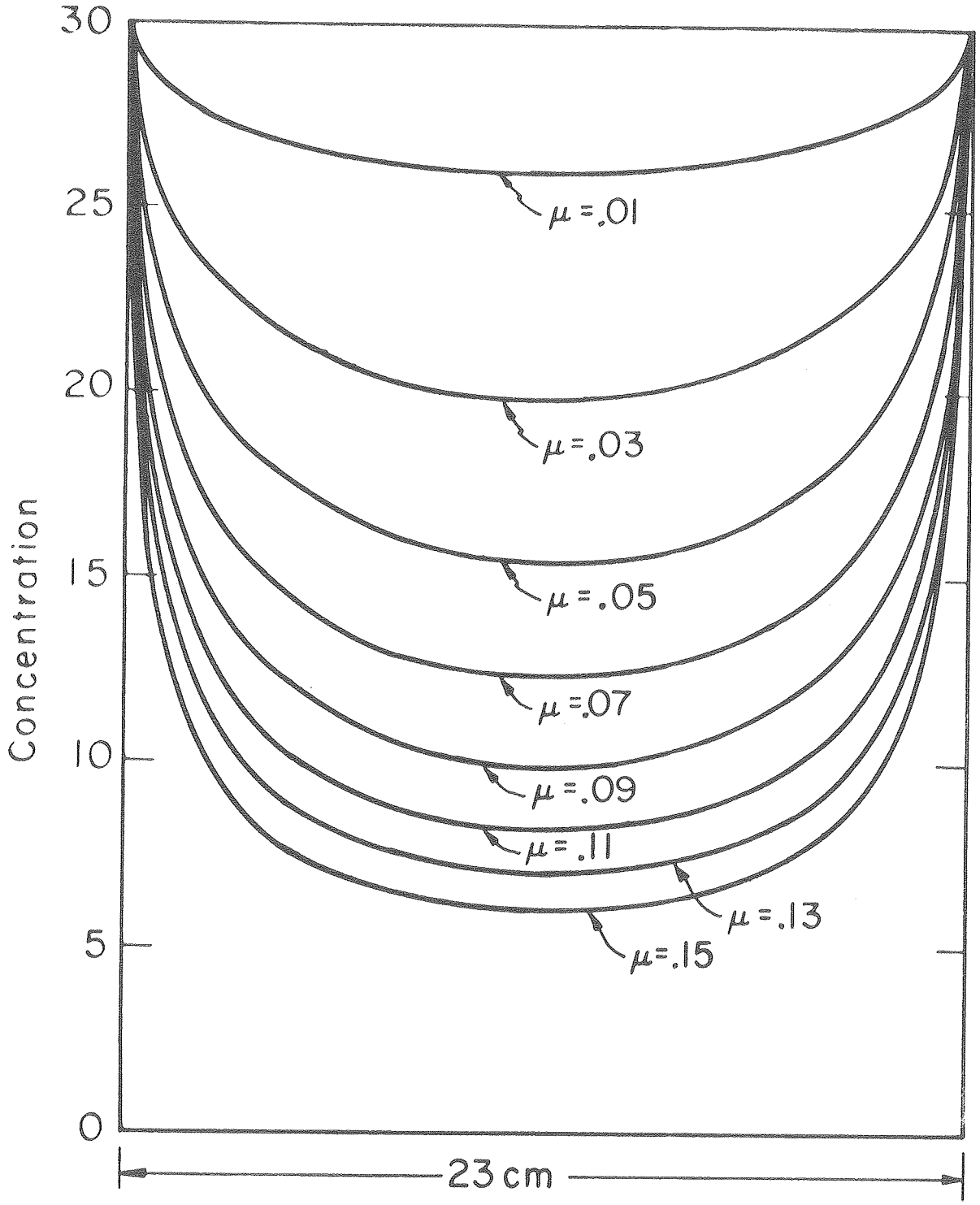

XBL785-3190

Figure 2.10. The profiles of a 23 cm disc reconstructed using Radon's inversion formula from data attenuated for various attenuation coefficients.

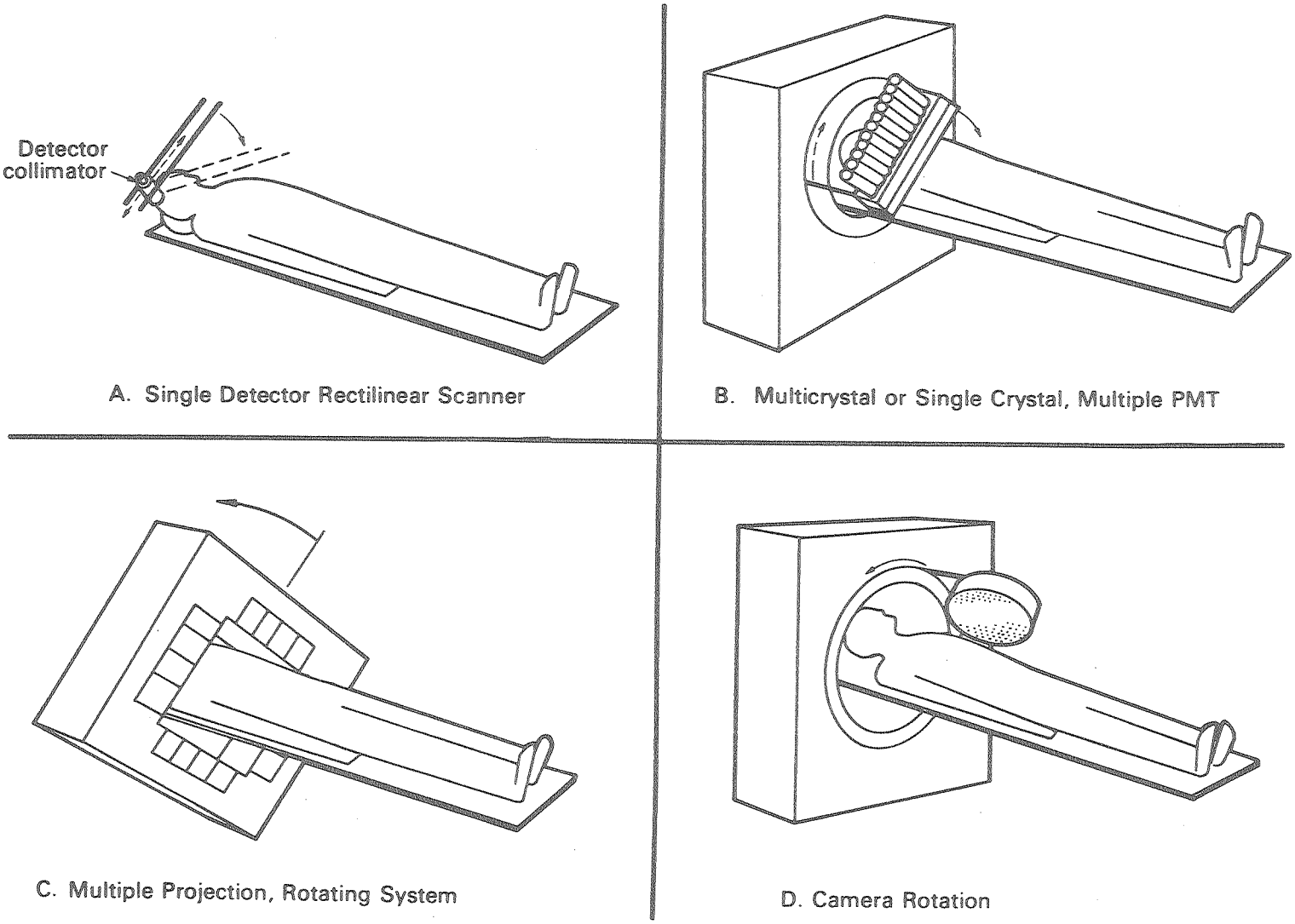

Figure 2.11. Detector concepts for single-photon emission computed tomography.

In 1964 the MARK II was developed which used two opposing detectors to scan simultaneously and thus increase sensitivity (Kuhl and Edwards, 1964). Kuhl's early work primarily emphasized the sectional scanning of the brain (Kuhl et al., 1966 a,b). With the development of the MARK III scanner he was able to further improve sensitivity by using four detectors which rectilinearly and simultaneously scanned the brain (Kuhl and Edwards, 1970).

Besides Kuhl other researchers have developed rectilinear scanners for single-photon ECT. These include Todd-Pokropek and Keeling (see Todd-Pokropek, 1971; Keeling, 1971), Myers and co-workers (1972), Bowley and co-workers (1973), and Tanaka and co-workers (1974).

The sensitivity was improved in the rectilinear scanners with the addition of multiple detectors as in the design of Genna and co-workers (1976) who used multiple detectors in a curved array. An illustration of a rectilinear scanner with multiple detectors is shown in Fig. 2.11B. The MARK III system was also improved upon by Kuhl and co-workers (1976) with the development of the MARK IV system which is a four sided arrangement of 32 independent detectors which rotates continuously as a unit (Fig. 2.11C). A similar multiple detector arrangement is being developed by Union Carbide.

Studies done at Donner Lab with single-photon ECT began by rotating patients in front of an Anger camera as shown in Fig. 2.12 (Budinger and Gullberg, 1974). The cross-sectional images of radiopharmaceutical distributions were reconstructed using an iterative method due to Goitein (1971). Compensation for photon attenuation was accomplished

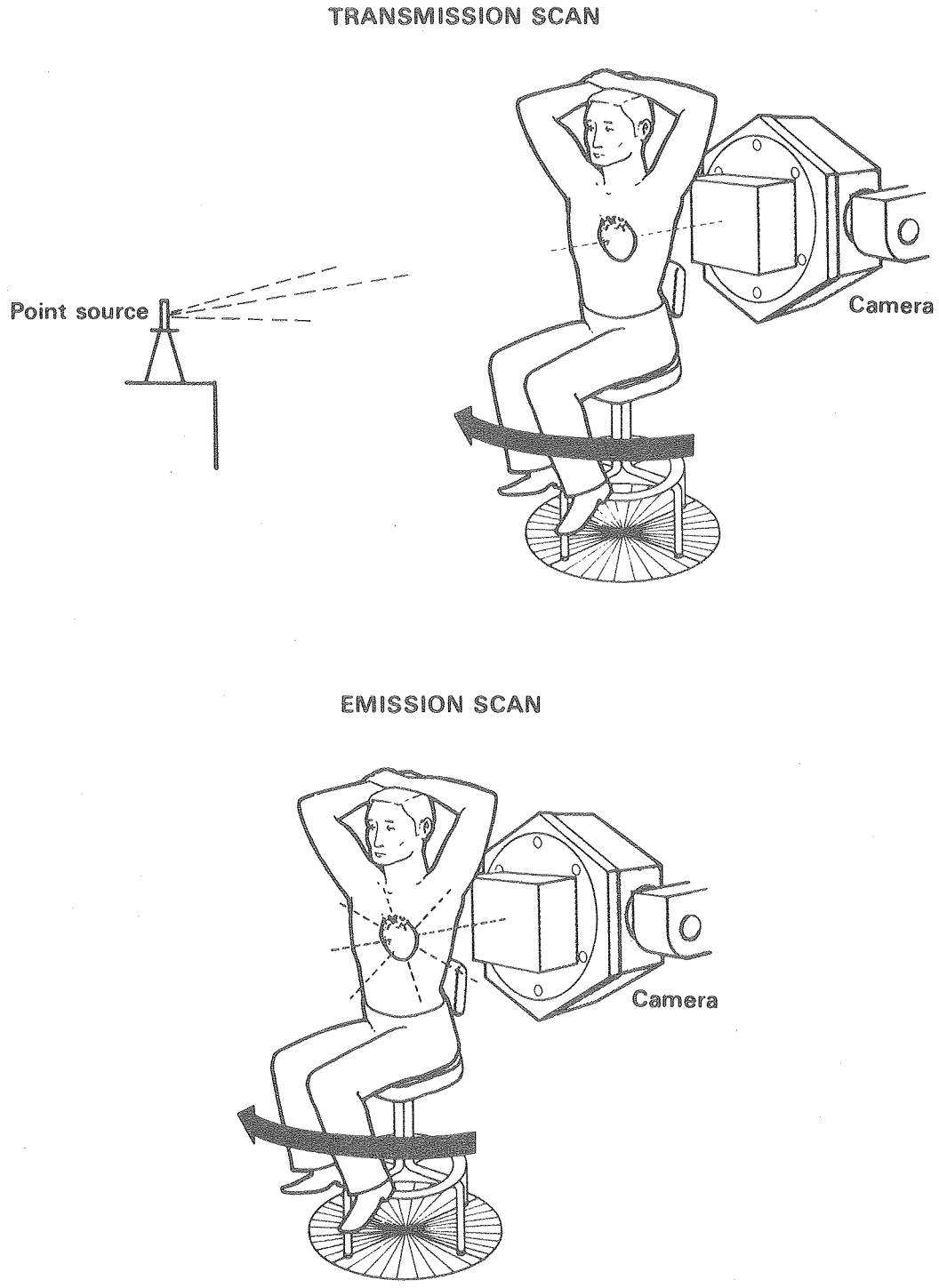

Figure 2.12. Single-photon ECT was done at Donner by rotating the patient in front of an Anger camera. The transmission scan used a 10-20 mCi point source of gamma emitter placed approximately 3.5 m from the camera. For the emission scan the radiopharmaceutical was injected into the patient.

by using the attenuation factors that were evaluated from the distribution of attenuation coefficients reconstructed from a transmission study. The advantage of the Anger camera over the rectilinear scanners of Kuhl and other researchers is that projection data for multiple sections can be collected at one time.

A system more appropriate for patient studies is shown in Fig. 2.11D where an area detector such as the Anger camera is rotated around the patient using a cantilever structure. Such a system called the Humongotron, was developed by Keyes and co-workers (1977) for imaging the whole body. Similar but smaller systems for imaging the brain were developed by Searle (Jaszczak et al., 1977) and by Selo (Societa Electronica Lobarda) in Milan, Italy. These systems have the advantage of collecting projection data for multiple transverse sections simultaneously without patient movement. However the devices must rotate to obtain angular sampling. This requires more time for total data collection than multiple detector systems positioned around the patient. Therefore these rotating Anger camera systems are not suited for dynamic biological studies such as measuring coronary blood flow. Searle is improving the angular sampling by producing a new system which will consist of two directly opposing large field of view scintillation cameras and will be designed for whole body studies (Phelps, 1977).

2.4.2.3 Development of Algorithms for Single-Photon ECT

The early scanners of Kuhl used basically the back-projection or simple superposition to reconstruct the cross-sectional image (Kuhl

and Edwards, 1968). This method of reconstruction was later improved upon by using an orthogonal tangent correction method (Kuhl et al., 1973). The MARK IV system (Kuhl et al., 1976) reconstructs the transverse section image as it rotates using an iterative technique similar to ART (Gordon et al., 1970). At the end of the study a single correction for attenuation and detector response is applied based on the assumption that the results of scanning the head can be related directly to the results of scanning a cylinder of radioactive water.

The attenuated Radon transform for variable attenuation coefficients was first described in (Budinger and Gullberg, 1977). Various methods for inverting the attenuated Radon transform have been researched and discussed in the literature; these include iterative least-squares methods, which use TCT to determine the attenuation coefficients (Budinger and Gullberg, 1974), iterative convolution methods (Walters, Simon, et al., 1976), attenuation compensation methods which preprocess the projection data (Kay and Keys, 1975; and Budinger and Gullberg, 1977), correction of each reconstructed pixel value by a mean attenuation factor determined by using the sum of attenuation along all rays through the pixel divided by the number of rays (Chang, 1978), and a special iterative method applied in Fourier space to compensate for both attenuation and the spacially variant point spread function of the imaging system (Hsieh and Wee, 1976).

Direct inversion relationships have been developed for the case when the attenuation distribution is constant. Bellini and co-workers

(1979 a,b) have developed an inversion formula which involves modifying the Fourier transform of the projection data in such a way that the modification represents the Fourier transform of unattenuated data. Tretiak and co-workers (1978, 1979) have developed a back-projection of filtered projection method which gives a reconstructed image that is equal to the true image convolved with a desired point spread function. This point spread function determines the spatial resolution and noise amplification of the filter applied to the projection data. Natterer (1978) has developed an inversion formula which is accurate up to $O(\mu^4)$. This formula is derived by applying Cauchy's theorem to a Fourier projection theorem derived for a constant attenuation coefficient.

The remainer of this thesis will investigate the properties of the attenuated Radon transform and its relationship to efficient and reliable reconstruction algorithms. We will concentrate on iterative methods and an extension of the back-projection of filtered projection algorithm as is appropriate for an attenuating medium with a constant attenuation coefficient.

3. PROPERTIES FOR ATTENUATED RADON TRANSFORMS

3.1 Introduction

In this chapter we will develop the properties of two basic types of attenuated transforms. The attenuated Radon transform ($A_\mu: \rho \to p_\gamma$) is that given by Eq. (1.1) -

$$p_\gamma(\xi,\theta) = \int \rho(\hat{x}) \exp\left\{ - \int_{\langle \hat{x}', \underset{\sim}{\theta}^\perp \rangle \geqslant \langle \hat{x}, \underset{\sim}{\theta}^\perp \rangle} \mu(\hat{x}')\, \delta(\xi - \langle \hat{x}', \underset{\sim}{\theta} \rangle) d\hat{x}' \right\} \delta(\xi - \langle \hat{x}, \underset{\sim}{\theta} \rangle) d\hat{x} \ , \quad (1.1)$$

where ρ is the concentration of the emitter and $p_\gamma(\xi,\theta)$ are the projections. The projections $p_\gamma(\xi,\theta)$ can be modified in such a way that we can define a new transform ($A_\mu: \rho \to p$) which is independent of detector geometry -

$$p_\gamma(\xi,\theta) = \int \rho(\hat{x}) \exp\left\{ - \int_{0 \leqslant \langle \hat{x}', \underset{\sim}{\theta}^\perp \rangle \leqslant \langle \hat{x}, \underset{\sim}{\theta}^\perp \rangle} \mu(\hat{x}')\, \delta(\xi - \langle \hat{x}', \underset{\sim}{\theta} \rangle) d\hat{x}' \right\} \delta(\xi - \langle \hat{x}, \underset{\sim}{\theta} \rangle) d\hat{x}.$$

When the attenuation coefficient is constant, explicit inverse equations can be developed for this modified transform.

These two transforms -- the attenuated Radon transform and the modified attenuated Radon transform -- assume that the attenuation distribution μ is known a priori. A transform which does not assume a priori knowledge about the attenuation distribution is given by $A: (\rho,\mu) \to p_\gamma$ which maps the ordered pair of functions (ρ,μ) - ρ and μ are allowed to vary - into the projection function p_γ defined by Eq. (1.1). This transform is not linear due to the exponential

attenuation factor in the integral equation. Methods for inverting this nonlinear transform have been investigated by us but with very little success. Presently Censor and co-workers (1979) are pursuing this using algebraic reconstruction techniques. This thesis will concern itself only with the case where the attenuation distribution μ is assumed to be known or has been determined by an experiment. For this case we have denoted the attenuated Radon transform as A_μ and the modified attenuated Radon transform as A_μ.

The work presented in this chapter differs from previous work in the literature (Tretiak and Metz, 1979; Bellini et al., 1979 a,b; Natterer, 1978) in that the attenuated Radon transform is defined for arbitrary distributions of attenuation coefficients. This chapter deals first with the attenuated Radon transform for arbitrary attenuation distribution, then shows how one can obtain from this operator the modified attenuated Radon transform. After the properties of the modified transform are discussed it is then shown how the modified attenuated Radon transform in the case of constant attenuation coefficient reduces to the attenuation transform discussed by Tretiak and Delaney (1978), Natterer (1978), Tretiak and Metz (1979), Bellini and co-workers (1979a and b). The results presented for the case of constant attenuation represent contributions from these authors along with some new results derived from the general theory of the modified attenuated Radon transform as it applies to the case of constant attenuation.

3. PROPERTIES FOR ATTENUATED RADON TRANSFORMS

3.1 Introduction

In this chapter we will develop the properties of two basic types of attenuated transforms. The attenuated Radon transform ($A_\mu:\rho \to p_\gamma$) is that given by Eq. (1.1) -

$$p_\gamma(\xi,\theta) = \int \rho(\hat{x}) \exp\left\{ - \int_{\langle \hat{x}', \underset{\sim}{\theta}^\perp \rangle \geq \langle \hat{x}, \underset{\sim}{\theta}^\perp \rangle} \mu(\hat{x}')\, \delta(\xi - \langle \hat{x}', \underset{\sim}{\theta} \rangle) d\hat{x}' \right\} \delta(\xi - \langle \hat{x}, \underset{\sim}{\theta} \rangle) d\hat{x} \ , \quad (1.1)$$

where ρ is the concentration of the emitter and $p_\gamma(\xi,\theta)$ are the projections. The projections $p_\gamma(\xi,\theta)$ can be modified in such a way that we can define a new transform ($A_\mu:\rho \to p$) which is independent of detector geometry -

$$p_\gamma(\xi,\theta) = \int \rho(\hat{x}) \exp\left\{ - \int_{0 \leq \langle \hat{x}', \underset{\sim}{\theta}^\perp \rangle \leq \langle \hat{x}, \underset{\sim}{\theta}^\perp \rangle} \mu(\hat{x}')\, \delta(\xi - \langle \hat{x}', \underset{\sim}{\theta} \rangle) d\hat{x}' \right\} \delta(\xi - \langle \hat{x}, \underset{\sim}{\theta} \rangle) d\hat{x}.$$

When the attenuation coefficient is constant, explicit inverse equations can be developed for this modified transform.

These two transforms -- the attenuated Radon transform and the modified attenuated Radon transform -- assume that the attenuation distribution μ is known a priori. A transform which does not assume a priori knowledge about the attenuation distribution is given by $A:(\rho,\mu) \to p_\gamma$ which maps the ordered pair of functions (ρ,μ) - ρ and μ are allowed to vary - into the projection function p_γ defined by Eq. (1.1). This transform is not linear due to the exponential

attenuation factor in the integral equation. Methods for inverting this nonlinear transform have been investigated by us but with very little success. Presently Censor and co-workers (1979) are pursuing this using algebraic reconstruction techniques. This thesis will concern itself only with the case where the attenuation distribution μ is assumed to be known or has been determined by an experiment. For this case we have denoted the attenuated Radon transform as A_μ and the modified attenuated Radon transform as A_μ.

The work presented in this chapter differs from previous work in the literature (Tretiak and Metz, 1979; Bellini et al., 1979 a,b; Natterer, 1978) in that the attenuated Radon transform is defined for arbitrary distributions of attenuation coefficients. This chapter deals first with the attenuated Radon transform for arbitrary attenuation distribution, then shows how one can obtain from this operator the modified attenuated Radon transform. After the properties of the modified transform are discussed it is then shown how the modified attenuated Radon transform in the case of constant attenuation coefficient reduces to the attenuation transform discussed by Tretiak and Delaney (1978), Natterer (1978), Tretiak and Metz (1979), Bellini and co-workers (1979a and b). The results presented for the case of constant attenuation represent contributions from these authors along with some new results derived from the general theory of the modified attenuated Radon transform as it applies to the case of constant attenuation.

3.2 The Attenuated Radon Transform Operating on a Hilbert Space

Hilbert space theory (Halmos, 1951) contains the mathematical structure which enables us to describe geometrical concepts such as orthogonality. The objects of greatest interest in connection with Hilbert spaces are the linear transformations of which the attenuated Radon transform is one example. Hilbert spaces have a natural correspondence with their dual space (the space of all linear functionals defined on the Hilbert space) so that the Hilbert space and its dual can be considered as equivalent (Simmons, 1963, Chapter 10). This structure leads to the concept of the adjoint of the operator from which the generalized inverse of the attenuated Radon transform can be described and formulated as the generalized inverse of the self-adjoint operator equal to the composition of the attenuated Radon transform and its adjoint (Kammerer and Nashed, 1972).

For a Hilbert space X and a submanifold S, $S^{\perp}$ denotes the orthogonal complement of S and $\bar{S}$ is the closure of S. As illustrated in Fig. 3.1, the linear operator A_μ maps the Hilbert space X of concentration functions ρ into the Hilbert space Y of projection functions p_γ, where the range and the null space of the linear operator A_μ is denoted as $\mathcal{R}(A_\mu)$ and $\mathcal{N}(A_\mu)$, respectively. In reconstruction tomography, the null space of A_μ has been given the term "the space of invisible functions" (Hamaker and Solmon, 1978).

The adjoint operator of A_μ, denoted by A_μ^*, maps the Hilbert space Y into X and is defined such that $\langle \rho, A_\mu^* p \rangle = [A_\mu \rho, p]$ where $\langle \cdot, \cdot \rangle$ and $[\cdot, \cdot]$ are the inner products in the Hilbert space X and Y,

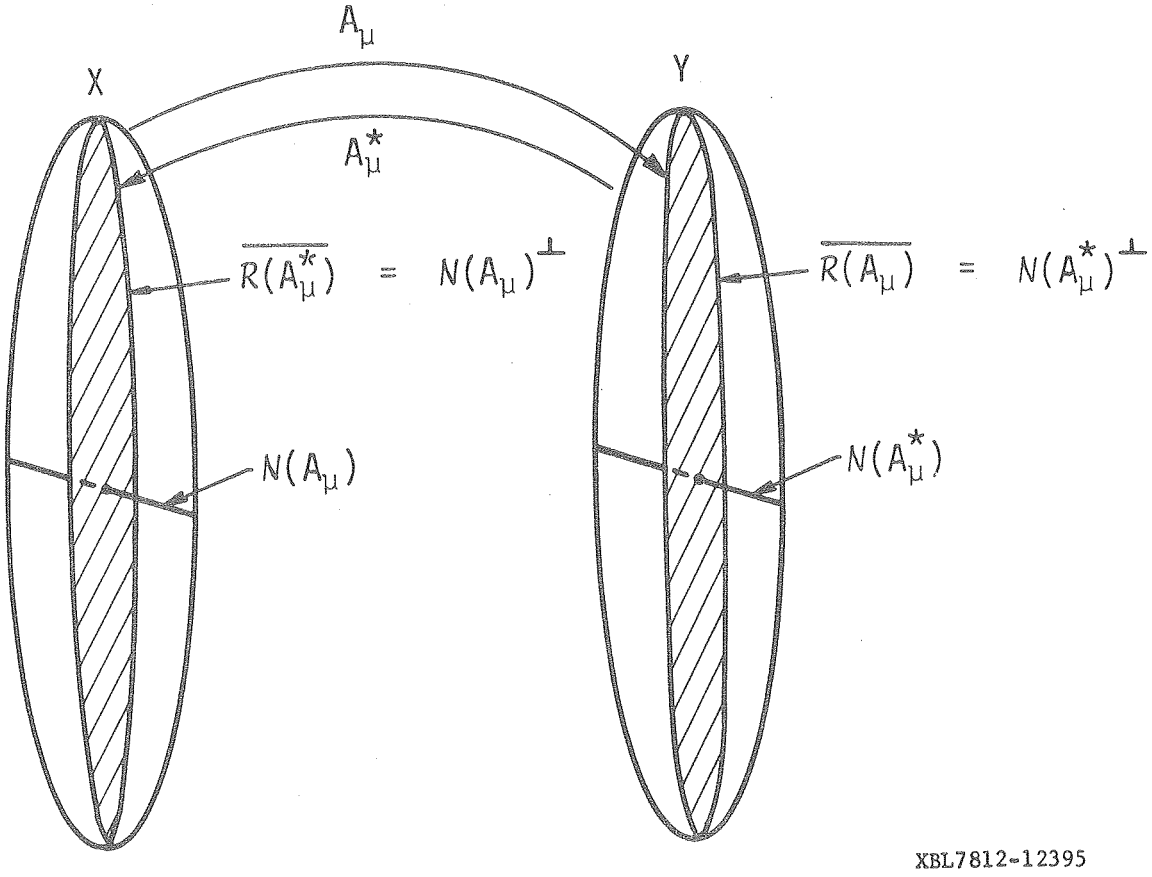

Figure 3.1. The attenuated Radon transform maps the Hilbert space X into the Hilbert space Y with range and null space denoted as $R(A_\mu)$ and $N(A_\mu)$, respectively. The adjoint transform A_μ^* maps the Hilbert space Y into the Hilbert space X with range and null space denoted as $R(A_\mu^*)$ and $N(A_\mu^*)$, respectively.

respectively. One particular Hilbert space which we will consider is the Hilbert space $L^2(\Omega,W)$ which represents the space of real valued functions ρ defined on the set $\Omega \subseteq \mathbb{R}^2$ ($\rho:\Omega \to \mathbb{R}$) which are square integrable with respect to the weight function W(i.e. $\iint |\rho(x,y)|^2 \times W(x,y)\, dxdy < \infty$). The attenuated Radon transform maps this Hilbert space into the Hilbert space $L^2(\mathbb{C},w)$ of functions p defined on the set $\mathbb{C} \subseteq \mathbb{R} \times [0,2\pi)$ ($p:\mathbb{C} \to \mathbb{R}$) which are square integrable with respect to the weight function w(i.e. $\iint_{\mathbb{C}} |p(\xi,\theta)|^2\, w(\xi,\theta)\, d\xi d\theta < \infty$). If $\Omega = \mathbb{R}^2$ then we will denote X as $L^2(\mathbb{R}^2,W)$. The inner product for $L^2(\Omega,W)$ is defined to be $\langle \rho,\rho' \rangle_{\Omega,W} = \iint_{\Omega} \rho(x,y)\, \rho'(x,y)\, W(x,y)dxdy$ and the inner product for $L^2(\mathbb{C},w)$ is defined to be $[p,g]_{\mathbb{C},w} = \iint_{\mathbb{C}} p(\xi,\theta) \times g(\xi,\theta)\, w(\xi,\theta)d\xi d\theta$.

In our discussion, we will only consider Hilbert spaces for which the attenuated Radon transform is a bounded linear operator. If $A_\mu:X \to Y$ is a bounded linear operator, then $N(A_\mu)$ and $N(A_\mu^*)$ (Fig. 3.1) are closed subspaces of X and Y, respectively. Therefore, we can write $X = N(A_\mu) + N(A_\mu)^\perp$ and $Y = N(A_\mu^*) + N(A_\mu^*)^\perp$ (Theorem D, p. 251, Simmons, 1963). The following relations are also valid (see Yosida, 1974; Kammerer and Nashed, 1972):

$$\begin{aligned}
\overline{R(A_\mu)} &= N(A_\mu^*)^\perp \\
\overline{R(A_\mu^*)} &= N(A_\mu)^\perp \\
R(A_\mu)^\perp &= N(A_\mu^*) \\
R(A_\mu^*)^\perp &= N(A_\mu) \\
\overline{R(A_\mu)} &= \overline{R(A_\mu A_\mu^*)} \\
\overline{R(A_\mu^*)} &= \overline{R(A_\mu^* A_\mu)} \, .
\end{aligned}$$

For finite-dimensional Hilbert spaces the range of a bounded operator and its adjoint are closed and are related to each other by a function which is one-to-one and onto. The attenuated Radon transform operating on a finite-dimensional Hilbert space will be discussed in Chapter 4. In this chapter properties will be developed for the attenuated Radon transform and the modified attenuated Radon transform for function spaces which are infinite-dimensional Hilbert spaces.

3.3 The Reconstruction Problem

An approach for solving the reconstruction problem in single-photon ECT involves evaluating the generalized inverse of the attenuated Radon transform. We will develope the generalized inverse in a manner similar to that given by Kammerer and Nashed (1972). Then we will show that in certain cases the attenuated Radon transform and its generalized inverse can be decomposed and represented as a sum of eigenfunctions.

3.3.1 The Generalized Inverse

Reconstructing attenuated data for a known attenuation distribution μ requires solving the linear operator equation

$$A_\mu(\rho) = p_\gamma \tag{3.1}$$

where $A_\mu: X \to Y$ is the attenuated Radon transform given by Eq. (1.1), ρ is the distribution of isotope concentration, and p_γ is the projection. The concentration $\hat{\rho} \in X$ is called the best approximate solution of Eq. (3.1), if $\inf \{\|A_\mu(\rho) - p_\gamma\| \mid \rho \in X\} = \|A_\mu(\hat{\rho}) - p_\gamma\|$. This is equivalent to minimizing $\|p - p_\gamma\|$ over all $p \in R(A_\mu)$. The minimum $\hat{p}$ is characterized as illustrated in Fig. 3.2 by the condition $p_\gamma - \hat{p}$,

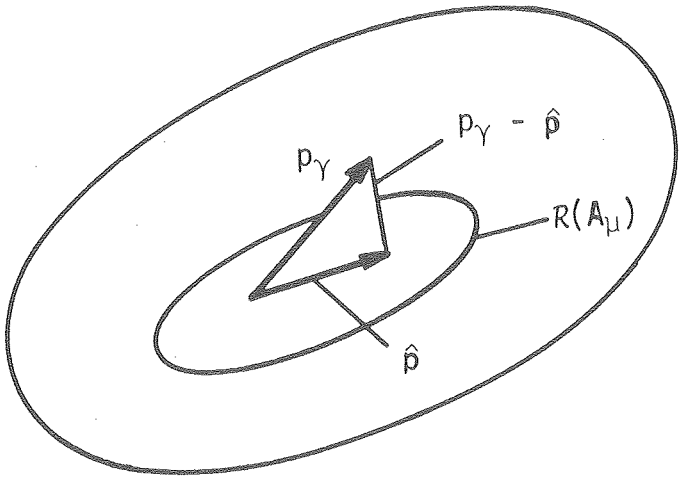

XBL791-3067

Figure 3.2. The minimum of $\|p - p_\gamma\|$ over all $p \in R(A_\mu)$ is the projection of p_γ onto $R(A_\mu)$ denoted as $\hat{p}$.

is orthogonal to the space $R(A_\mu)$ (i.e. $p_\gamma - \hat{p} \in R(A_\mu)^\perp$) which we know from the properties listed in Section 3.2 is equivalent to $p_\gamma - \hat{p} \in N(A_\mu^*)$. This implies that $A_\mu^* A_\mu(\hat{\rho}) = A_\mu^*(p_\gamma)$. Therefore $\hat{\rho} \in X$ is a best approximate solution of Eq. (3.1) if and only if it is a solution of the equation

$$A_\mu^* A_\mu(\rho) = A_\mu^*(p_\gamma) \ . \tag{3.2}$$

The linear manifold $R(A_\mu)$ may not be closed in Y. Therefore the orthogonal projection of p_γ onto $\overline{R(A_\mu)}$ may not be in $R(A_\mu)$ and Eq. (3.1) and (3.2) do not have a solution. However if we only consider those projection functions which are in $R(A_\mu) + R(A_\mu)^\perp$ (If $R(A_\mu)$ is closed then $R(A_\mu) + R(A_\mu)^\perp = Y$.), the solution to Eq. (3.1) is determined by evaluating the generalized inverse A_μ^G of the attenuated Radon transform A_μ. A_μ^G is the mapping whose domain is given by $\mathcal{D}(A_\mu^G) = R(A_\mu) + R(A_\mu)^\perp$ such that for $p \in \mathcal{D}(A_\mu^G)$,

$$A_\mu^G p = \rho_0 \in S = \left\{ \hat{\rho} \in X \,|\, \inf \| A_\mu(\rho) - p \| = \| A_\mu(\hat{\rho}) - p \| \ , \ \rho \in X \right\}$$

and $\|\rho_0\| < \|\hat{\rho}\|$ for all $\hat{\rho} \in S$, $\hat{\rho} \neq \rho_0$. Therefore for each $p \in R(A_\mu) + R(A_\mu)^\perp = \mathcal{D}(A_\mu^G)$, $A_\mu^G(p)$ is a unique solution. The set S of all best approximate solutions of Eq. (3.1) for a fixed $p_\gamma \in \mathcal{D}(A_\mu^G)$ is given by

$$A_\mu^G(p_\gamma) + N(A_\mu^* A_\mu) = A_\mu^G \, p_\gamma + N(A_\mu) \ . \tag{3.3}$$

Equation (3.3) shows that the null space of the operator A_μ is a measure of nonuniqueness.

The generalized inverse is an operator which is applicable to both finite and infinite dimensional Hilbert spaces. Before the wide spread usage of the generalized inverse in matrix theory (see Ben-Israel and Greville, 1974; and Boullion and Odell, 1971) it was developed to determine the solution to integral and differential equations (Reid, 1968).

3.3.2 Singular Value Decomposition of Compact Operators

From Eq. (3.2) we see that the generalized inverse of A_μ is closely related to the generalized inverse of the self adjoint operator $A_\mu^* A_\mu$. In fact

$$\rho_o = A^G p_\gamma = (A_\mu^* A_\mu)^G A_\mu^* (p_\gamma) .$$

In the discussion to follow we will show that the knowledge of the eigenfunctions of $A_\mu^* A_\mu$ and $A_\mu A_\mu^*$ lead to a singular value decomposition of A_μ and A_μ^G.

If $\mathcal{R}(A_\mu)$ is closed then by the closed range theorem (p.205, Yosida, 1974), $\mathcal{R}(A_\mu^*)$ is also closed and $\mathcal{R}(A_\mu^*) = \mathcal{N}(A_\mu)^\perp = \mathcal{R}(A_\mu^* A_\mu)$. In this case the operator $A_\mu^* A_\mu$ restricted to the space $\mathcal{R}(A_\mu^*) = \mathcal{N}(A_\mu)^\perp$ is a one-to-one and onto mapping of $\mathcal{N}(A_\mu)^\perp$ onto itself. For the attenuated Radon transform A_μ, the operator $A_\mu^* A_\mu : \rho \to \beta$ is given by the Fredholm integral equation of the first kind:

$$\beta(x',y') = \int\int \rho(x,y)\ K(x',y'|x,y)\ dxdy , \qquad (3.4)$$

where K is the kernel of the transformation. For the Radon transform (i.e. $\mu=0$) and weight functions $W(x,y) = w(\xi,\theta) = 1$ this kernel is the well known function

$$K(x',y'|x,y) = \frac{1}{\| \hat{x} - \hat{x}' \|} \tag{3.5}$$

where $\hat{x} = (x,y)$ and $\hat{x}' = (x',y')$ and for which the result in Eq. (3.4) is a convolution.

If $R(A_\mu)$ is closed we also know by the closed range theorem that $R(A_\mu) = N(A_\mu^*)^\perp = R(A_\mu A_\mu^*)$. Since the solution to Eq. (3.1) is equivalent to minimizing $\|p-p_\gamma\|$ over all $p \in R(A_\mu)$, then when $R(A_\mu)$ is closed the solution to Eq. (3.1) is equivalent to minimizing $\|A_\mu A_\mu^* p - p_\gamma\|$ over all $p \in R(A_\mu A_\mu^*)$. This gives a different formulation of the reconstruction problem, namely the solution to the linear operator equation

$$A_\mu A_\mu^* p = p_\gamma \tag{3.6}$$

where the reconstructed isotope concentration function $\hat{\rho}$ is given by $\hat{\rho} = A^*\hat{p}$ such that $\hat{p}$ is the best approximate solution to Eq. (3.6). The operator $A_\mu A_\mu^*$ restricted to the space $R(A_\mu)$ is a one-to-one and onto mapping of $N(A_\mu^*)^\perp$ onto itself. For the attenuated Radon transform A_μ, the operator $A_\mu A_\mu^*: p \to g$ is given by

$$g(\xi,\theta) = \int\int p(\xi',\theta')\ I(\xi,\theta|\xi',\theta')\ d\xi' d\theta' \tag{3.7}$$

where I is the kernel of the transformation. For the Radon transform, $\mathcal{R}: L^2(\mathbb{R}^2) \to L^2(\mathbb{R} \times [0,2\pi))$ this kernel is

$$I(\xi,\theta|\xi',\theta') = \frac{1}{|\sin(\theta-\theta')|} \quad . \tag{3.8}$$

From the discussion above we see that the operators $A_\mu^* A_\mu$ and $A_\mu A_\mu^*$ can be represented as integral equations with kernels K and I respectively. Operators such as these for which $\iint |K(\hat{x}',\hat{x})|^2 \, d\hat{x}' d\hat{x} < \infty$ are called Hilbert-Schmidt operators (p.1009, Dunford and Schwartz, 1963) and K is called an L^2 kernel. These are compact operators (p.277, Yosida, 1974) which share special properties which are not true in general for linear operators. From the Hilbert-Schmidt theorem (p. 68, Petrovskii, 1957) we know that if K and I are symmetric kernels then β in Eq. (3.4) and g in Eq. (3.7) can be expanded in an absolutely and uniformly convergent series of eigenfunctions of the operators $A_\mu^* A_\mu$ and $A_\mu A_\mu^*$, respectively. (See also Tricomi, 1965 and Lovitt, 1950.) For real functions K and I these eigenfunctions are necessarily real.

If we examine the kernel given for the Radon transform in Eq. (3.5), we see that this is not square integrable (i.e. $\iint 1/\|\hat{x}-\hat{x}'\|^2 \, d\hat{x}d\hat{x}' \not< \infty$) and thus not an L^2 kernel. In order to use the Hilbert-Schmidt theory of singular value decomposition applicable to symmetric L^2 kernels, we need to introduce weight functions $W(x,y)$ and $w(\xi,\theta) \neq 1$ for the Hilbert spaces $L^2(\Omega,W)$ and $L^2(\mathbb{C},w)$. Then we can consider kernels for the operator $A_\mu^* A_\mu$ which are square integrable in the sense $\iint_{\Omega\Omega} |K(\hat{x}|\hat{x}')|^2 \, W(\hat{x}) \, W(\hat{x}') \, d\hat{x}d\hat{x}' < \infty$. The notion of a symmetric kernel is replaced with that of a Hermitian kernel. Using the notation of $K\rho$ to mean the same as $A_\mu^* A_\mu$ operating on ρ, the kernel K is called Hermitian if $K^*(\hat{x}|\hat{x}') = K(\hat{x}'|\hat{x})$ where the adjoint kernel is defined such that $\langle K\rho,\rho' \rangle_{\Omega,W} = \langle \rho,K^*\rho' \rangle_{\Omega,W}$. In the case of the Radon transform if we take $L^2(\mathbb{R}^2,W)$ and $L^2(\mathbb{C},w)$ with weight functions $W(x,y) = e^{x^2+y^2}$

and $w(\xi,\theta) = e^{\xi^2}$ (Eggermont, 1975; Miller, 1978), this will give a Hermitian L^2 kernel for $A_\mu^* A_\mu$:

$$K(x',y'|x,y) = \frac{1}{\|\hat{x}-\hat{x}'\|} \exp\left\{ \frac{-\langle \hat{x}', \hat{x}'-\hat{x} \rangle^2}{\|\hat{x}'-\hat{x}\|^2} \right\} \tag{3.9}$$

(i.e. $\iint |K(\hat{x}'|\hat{x})|^2 W(\hat{x}) W(\hat{x}') d\hat{x} d\hat{x}' < \infty$). For the Radon transform other weight functions have been used by Marr (1974) and Davison and Grunbaum (1979).

With the modification that incorporates weight functions in the definition of inner products, we can apply the Hilbert-Schmidt theory presented by Smithies (Chapter 7 and 8, 1958) to determine a singular value decomposition of the attenuated Radon transform. This means that if the Hermitian operators $A_\mu^* A_\mu$ and $A_\mu A_\mu^*$ have L^2 kernels then both have the same set of eigenvalues denoted by λ_i. We will denote $\phi_i(x,y)$ to be the eigenfunctions of the operator $A_\mu^* A_\mu$ corresponding to the eigenvalue λ_i and denote $\psi_i(\xi,\theta)$ to be the eigenfunction of the operator $A_\mu A_\mu^*$ corresponding to the same eigenvalue λ_i. The system $(\phi_i, \phi_i; \lambda_i)$ is called a singular system for the kernel K corresponding to $A_\mu^* A_\mu$ and $(\psi_i, \psi_i; \lambda_i)$ is a singular system for the kernel I corresponding to $A_\mu A_\mu^*$ (Smithies, 1958). The eigenfunctions ϕ_i are orthogonal relative to the weight function $W(x,y)$ (i.e. $\iint \phi_i(x,y) \phi_j(x,y) W(x,y)\, dxdy = \delta_{ij}$) and the eigenfunctions ψ_i are orthogonal relative to the weight function $w(\xi,\theta)$. The kernel given in Eq. (3.4) can be represented as

$$K(x',y'|x,y) = \sum_{i=1}^{\infty} \lambda_i \, \phi_i(x',y') \, \phi_i(x,y) \, W(x,y) \qquad (3.10)$$

(see Theorem 8.6.5, p.158, Smithies, 1958), and the operator $A_\mu^* A_\mu$ operating on the function $\rho(x,y)$ is given by

$$(A_\mu^* A_\mu \, \rho)(x',y') = \sum_{i=1}^{\infty} \lambda_i \int\int \rho(x,y) \, \phi_i(x,y) \, W(x,y) dx dy \, \phi_i(x',y') .$$

Likewise the kernel given in Eq. (3.7) is given by

$$I(\xi,\theta|\xi',\theta') = \sum_{i=1}^{\infty} \lambda_i \psi_i(\xi,\theta) \, \psi_i(\xi',\theta') \, w(\xi',\theta') \ , \qquad (3.11)$$

and the operator $A_\mu A_\mu^*$ operating on the function $p(\xi,\theta)$ is given by

$$(A_\mu A_\mu^* \, p)(\xi,\theta) = \sum_{i=1}^{\infty} \lambda_i \int\int p(\xi',\theta') \, \psi_i(\xi',\theta') \, w(\xi',\theta') d\xi' d\theta' \, \psi_i(\xi,\theta) . \qquad (3.12)$$

In the case of the Radon transform the kernel given in Eq. (3.9) can be represented as in Eq. (3.10) with

$$\phi_i(x,y) = (-1)^K \left[\frac{K!}{\pi(|n|+K)!} \right]^{1/2} (x \pm iy)^{|n|} \, L_K^{|n|}(x^2+y^2) e^{-x^2-y^2}$$

where $L_K^{|n|}$ are the Laguerre polynomials and the indices K and n are determined from the single index i. The eigenfunctions ψ_i corresponding to the kernel I given in Eq. (3.11) are given by

$$\psi_i(\xi,\theta) = [2^{2|n|+4K} \, K!(|n|+K)!]^{-1/2} \, e^{in\theta} \, H_{|n|+2K}(\xi) \, e^{-\xi^2}$$

where $H_m(\xi)$ is the Hermite polynomial of degree m and the indices K and n are determined from the single index i. (See Magnus, Oberhettinger, and Soni, 1966).

If the eigenvalues λ_i and eigenfunctions ϕ_i and ψ_i are known then the attenuated Radon transform can be decomposed as

$$(A_\mu \rho)(\xi,\theta) = \sum_{i=1}^{\infty} \lambda_i^{1/2} \iint \rho(x,y)\, \phi_i(x,y)\, W(x,y)dxdy\ \psi_i(\xi,\theta) \qquad (3.13)$$

where $(\phi_i, \psi_i; \lambda_i^{1/2})$ is a singular system for the attenuated Radon transform (see Theorem 8.3.2, p. 145, Smithies, 1958). From this singular value decomposition of A_μ, we can write the generalized inverse as

$$(A_\mu^G\ p_\gamma)(x,y) = \sum_{i=1}^{\infty} \lambda_i^{-1/2} \iint p_\gamma(\xi,\theta)\, \psi_i(\xi,\theta)\, w(\xi,\theta)d\xi d\theta\ \phi_i(x,y). \qquad (3.14)$$

In the sections that follow, we will give expressions for the kernel functions K and I. However, explicit expressions for the eigenfunctions ϕ_i and ψ_i are not developed.

3.4 The Attenuated Radon Transform

The definition of the attenuated Radon transform given by Eq. (1.1) can be rewritten using the rotated coordinates (see Fig. 2.6):

$$\begin{aligned} x &= -\xi \sin\theta + \zeta \cos\theta \\ y &= \xi \cos\theta + \zeta \sin\theta\ . \end{aligned} \qquad (3.15)$$

This gives

$$p_\gamma(\xi,\theta) = \int_{-\infty}^{\infty} \rho(-\xi\sin\theta + \zeta\cos\theta,\ \xi\cos\theta + \zeta\sin\theta)\ a(\zeta,\xi,\theta)d\zeta \qquad (3.16)$$

where

$$a(\zeta,\xi,\theta) = \exp\left[-\int_{\zeta}^{\infty} \mu(-\xi\sin\theta + \zeta'\cos\theta,\ \xi\cos\theta + \zeta'\sin\theta)d\zeta'\right] . \quad (3.17)$$

The upper limit is chosen to be at infinity for mathematical convenience. This allows for general distributions of both concentration and attenuation coefficients; and in practical situations, it does not matter if the detector is placed at infinity since the distribution of isotope concentration and attenuation coefficients is zero outside a compact subset of $\mathbb{R}^2$.

The attenuated Radon transform A_μ defined by Eq. (3.16) maps real valued functions ρ with domain $\Omega \subseteq \mathbb{R}^2$ ($\rho:\Omega \to \mathbb{R}$) into real valued functions p_γ with domain $\mathbb{C} \subseteq \mathbb{R} \times [0,2\pi)$ ($p_\gamma:\mathbb{C} \to \mathbb{R}$).

The following are equivalent definitions for the attenuated Radon transform $A_\mu:\rho \to p_\gamma$ -

1. $$p_\gamma(\xi,\theta) = \iint \rho(x,y)\ a(x,y,\xi,\theta)\ \delta(\xi + x\sin\theta - y\cos\theta)dxdy$$

where

$$a(x,y,\xi,\theta) = \exp\left[-\int_{x\cos\theta+y\sin\theta}^{\infty} \mu(-\xi\sin\theta + \zeta'\cos\theta,\ \xi\cos\theta + \zeta'\sin\theta)d\zeta'\right] \quad (3.16a)$$

2. $$p_\gamma(\xi,\theta) = \int_{r=|\xi|}^{\infty} \left\{\rho\{r,\theta + \pi/2 + \cos^{-1}(\xi/r)\} \exp\left[-\int_{r}^{\infty} \mu\{s,\theta + \pi/2 + \cos^{-1}(\xi/s)\}\right.\right.$$

$$\left.\left. \times \frac{sds}{\sqrt{s^2-\xi^2}}\right] + \rho\{r,\theta + \pi/2 - \cos^{-1}(\xi/r)\}\right.$$

$$\times \exp\left[-\int_{r}^{\infty} \mu\{t,\theta+\pi/2-\cos^{-1}(\xi/t)\}\,\frac{t\,dt}{\sqrt{t^2-\xi^2}}\right]\Bigg\}\,\frac{r\,dr}{\sqrt{r^2-\xi^2}} \qquad (3.16b)$$

$$3.\quad p_\gamma(\xi,\theta) = \int_{-\infty}^{\infty} \rho(\xi\underset{\sim}{\theta}+\zeta\underset{\sim}{\theta}^{\perp})\,\exp\left\{-\int_{\zeta}^{\infty} \mu(\xi\underset{\sim}{\theta}+\zeta'\underset{\sim}{\theta}^{\perp})\,d\zeta'\right\}\,d\zeta \qquad (3.16c)$$

where $\underset{\sim}{\theta} = (-\sin\theta, \cos\theta)$ and $\underset{\sim}{\theta}^{\perp} = (\cos\theta, \sin\theta)$. As illustrated in Fig. 3.3, the integration of ρ in Eq. (3.16b) along the line $\xi+x\sin\theta-y\cos\theta = 0$ in polar coordinates from $r=\xi$ to ∞ must include two portions of ρ for the projection, namely the concentration at $(r,\theta+\pi/2+\cos^{-1}(\xi/r))$ and at $(r,\theta+\pi/2-\cos^{-1}(\xi/r))$. The infinitesimal line length $d\zeta$ used in the definition in Eq. (3.16) is related to dr by $d\zeta = r(r^2-\xi^2)^{-1/2}\,dr$. The vectors $\underset{\sim}{\theta}$ and $\underset{\sim}{\theta}^{\perp}$ are both unit directional vectors.

Using the definition in Eq. (3.16) we prove the following result for attenuated projections when both the concentration distribution and attenuation distribution are shifted relative to a fixed coordinate system.

THEOREM 3.1. The attenuated Radon transform of $\rho(x+a, y+b)$ with respect to the attenuation coefficient distribution $\mu(x+a, y+b)$ is

$$A\{\rho(x+a, y+b), \mu(x+a, y+b); \xi,\theta\} = A\{\rho(x,y), \mu(x,y); \xi',\theta\} \qquad (3.18)$$

where $\xi' = \xi - a\sin\theta + b\cos\theta$.

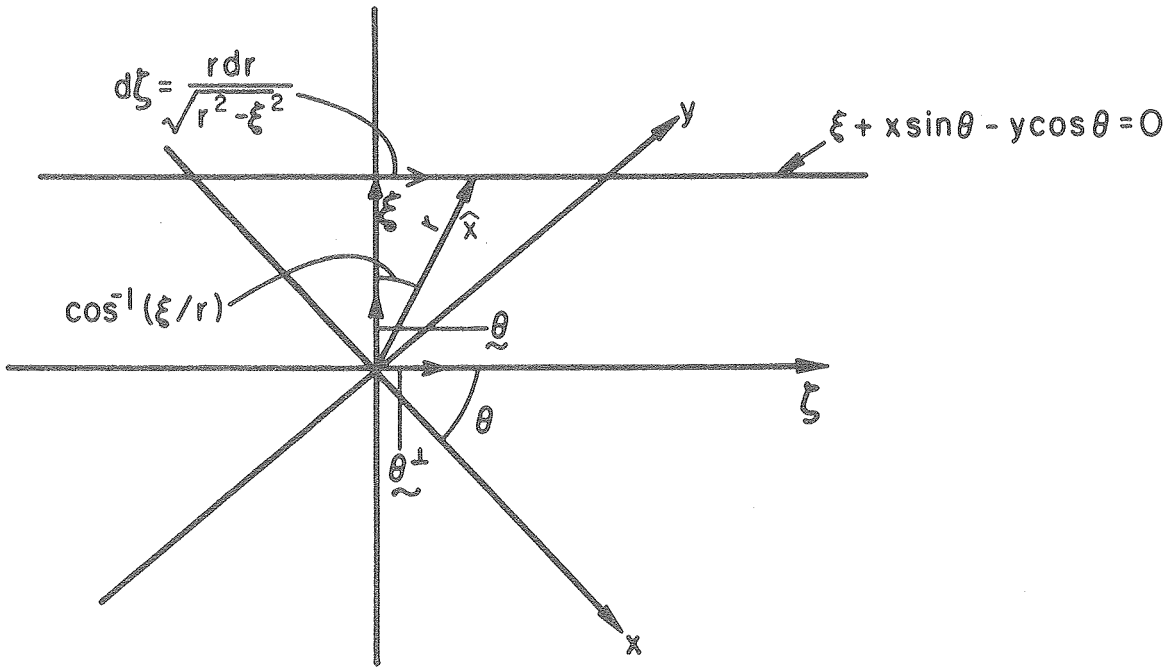

XBL791-3071

Figure 3.3. The unit directional vector $\underset{\sim}{\theta}$ lies along the ξ axis and $\underset{\sim}{\theta}^{\perp}$ lies along the ζ axis. The polar coordinate r of a vector $\hat{x}$ in the xy-plane and the coordinate ζ in the $\xi\zeta$-plane satisfy $d\zeta = r(r^2-\xi^2)^{-1/2}\,dr$. The angle between the vector $\hat{x}$ and the ξ axis is equal to $\cos^{-1}(\xi/r)$.

COMMENT: The notation $A\{\rho,\mu;\ \xi,\theta\}$ denotes the transformed function which is the attenuated Radon transform of ρ with respect to the attenuation distribution μ. This function is evaluated at ξ and θ.

PROOF. The attenuated Radon transform of $\rho(x+a,\ y+b)$ for the attenuation distribution $\mu(x+a,\ y+b)$ is

$$A\{\rho(x+a,\ y+b),\ \mu(x+a,\ y+b);\ \xi,\theta\} = \int_{-\infty}^{\infty} \rho(-\xi\sin\theta+\zeta\cos\theta+a,\ \xi\cos\theta+\zeta\sin\theta+b)$$

$$\times \exp\left[-\int_{\zeta}^{\infty} \mu(-\xi\sin\theta+\zeta'\cos\theta+a,\ \xi\cos\theta+\zeta'\sin\theta+b)d\zeta'\right] d\zeta\ . \qquad (3.19)$$

Let $\xi' = \xi - a\sin\theta + b\cos\theta$, then we can rewrite Eq. (3.19) as

$$A\{\rho(x+a,\ y+b),\ \mu(x+a,\ y+b);\ \xi,\theta\} =$$

$$\int_{-\infty}^{\infty} \rho\{-\xi'\sin\theta+(\zeta+a\cos\theta+b\sin\theta)\cos\theta,\xi'\cos\theta+(\zeta+a\cos\theta+b\sin\theta)\sin\theta\}$$

$$\times \exp\left[-\int_{\zeta}^{\infty} \mu(-\xi'\sin\theta+(\zeta'+a\cos\theta+b\sin\theta)\cos\theta,\xi'\cos\theta+(\zeta'+a\cos\theta+b\sin\theta)\sin\theta\}d\zeta'\right]d\zeta.$$

Making the further change of variables

$$u = \zeta + a\cos\theta + b\sin\theta$$

$$u' = \zeta' + a\cos\theta + b\sin\theta$$

gives

$$A\{\rho(x+a,\ y+b),\ \mu(x+a,\ y+b);\ \xi,\theta\} = \int_{-\infty}^{\infty} \rho(-\xi'\sin\theta+u\cos\theta,\ \xi'\cos\theta+u\sin\theta)$$

$$\times \exp\left[-\int_{u}^{\infty} \mu(-\xi'\sin\theta+u'\cos\theta,\xi'\cos\theta+u'\sin\theta)du'\right] du. \quad \|$$

This result will become useful in Chapter 4 when we digitize the reconstruction domain and consider transforms of characteristic functions over square pixels. If we know the transform at the origin we can invoke the shift property given in Theorem 3.1 and evaluate the attenuated Radon transform of characteristic functions over any region in $\mathbb{R}^2$.

The result in Theorem 3.1 requires that the distribution of attenuation coefficients μ translate in the same manner as the emitter concentration ρ. If we consider the situation where μ is held fixed then we get a different result.

THEOREM 3.2. The attenuated Radon transform A_μ of $\rho(x+a,\ y+b)$ is given by

$$A\{\rho(x+a,\ y+b),\ \mu(x,y);\ \xi,\theta\} = A\{\rho(x,y),\ \mu(x-a,\ y-b);\ \xi',\theta\} \qquad (3.20)$$

where $\xi' = \xi - a\sin\theta + b\cos\theta$.

PROOF. The attenuated Radon transform A_μ of $\rho(x+a,\ y+b)$ is given by

$$A\{\rho(x+a,\ y+b),\ \mu(x,y);\ \xi,\theta\} = \int_{-\infty}^{\infty} \rho(-\xi\sin\theta+\zeta\cos\theta+a,\ \xi\cos\theta+\zeta\sin\theta+b)$$

$$\times \exp\left[-\int_{\zeta}^{\infty} \mu(-\xi\sin\theta+\zeta'\cos\theta,\ \xi\cos\theta+\zeta'\sin\theta)d\zeta'\right] d\zeta \ . \qquad (3.21)$$

Let $\xi' = \xi - a\sin\theta + b\cos\theta$, then we can rewrite Eq. (3.21) as

$$A\{\rho(x+a, y+b), \mu(x,y); \xi,\theta\} =$$

$$\int_{-\infty}^{\infty} \rho\{-\xi'\sin\theta+(\zeta+a\cos\theta+b\sin\theta)\cos\theta,\ \xi'\cos\theta+(\zeta+a\cos\theta+b\sin\theta)\sin\theta\}$$

$$\times \exp\left[-\int_{\zeta}^{\infty} \mu\{-\xi'\sin\theta+(\zeta'+a\cos\theta+b\sin\theta)\cos\theta-a,\right.$$

$$\left.\xi'\cos\theta+(\zeta'+a\cos\theta+b\sin\theta)\sin\theta-b\}d\zeta'\right] d\zeta \quad .$$

Making the further change of variables

$$u = \zeta + a\cos\theta + b\sin\theta$$

$$u' = \zeta' + a\cos\theta + b\sin\theta$$

gives

$$A\{\rho(x+a, y+b), \mu(x,y); \xi,\theta\} = \int_{-\infty}^{\infty} \rho(-\xi'\sin\theta+u\cos\theta,\ \xi'\cos\theta+u\sin\theta)$$

$$\times \exp\left[-\int_{u}^{\infty} \mu(-\xi'\sin\theta+u'\cos\theta-a,\ \xi'\cos\theta+u'\sin\theta-b)du'\right] du. \quad \|$$

From Theorem 3.2 one can see how the projection data will change when the concentration is shifted within a fixed attenuator. This has practical application for in vivo dynamic studies.

3.4.1 Adjoint and Back-Projection Operators

The reconstruction problem involves determining the generalized inverse of the attenuated Radon transform $A_{\mu}^{G}: Y \to X$. As discussed in

Section 3.3, one can describe this inverse transform in terms of the adjoint transform A_μ^* which maps the Hilbert space Y into the Hilbert space X. To develop the adjoint transform let us consider the mapping $A_\mu : L^2(\mathbb{R}^2,W) \to L^2(\mathbb{C},w)$. Using $[A_\mu \rho,g]_{\mathbb{C},w} = \langle \rho, A_\mu^* g \rangle_{\mathbb{R}^2,W}$

$$\left(\langle \rho,\rho' \rangle_{\mathbb{R}^2,W} = \int_{\mathbb{R}^2}\int \rho(x,y)\ \rho'(x,y)\ W(x,y)dxdy \right.$$

and

$$\left. [p,g]_{\mathbb{C},w} = \int_0^{2\pi}\int_{-\infty}^{\infty} p(\xi,\theta)\ g(\xi,\theta)\ w(\xi,\theta)d\xi d\theta \right)$$

as the definition of the adjoint, the following sequence of equations

$$[A_\mu \rho,g]_{\mathbb{C},w} = \int_0^{2\pi}\int_{-\infty}^{\infty} (A_\mu \rho)(\xi,\theta)\ g(\xi,\theta)\ w(\xi,\theta)d\xi d\theta$$

$$= \int_0^{2\pi}\int_{-\infty}^{\infty}\int_{\mathbb{R}^2}\int \rho(x,y)\ a(x,y,\xi,\theta)\ \delta(\xi+x\sin\theta-y\cos\theta)dxdy\ g(\xi,\theta)w(\xi,\theta)d\xi d\theta$$

$$= \iint_{\mathbb{R}^2} \rho(x,y)\left\{ \int_0^{2\pi} g(-x\sin\theta+y\cos\theta,\theta)\ a(x,y,-x\sin\theta+y\cos\theta,\theta) \right.$$

$$\left. \times\ w(-x\sin\theta+y\cos\theta,\theta)d\theta \right\} dxdy$$

shows that the adjoint A_μ^* of the attenuated Radon transform is given by

$$(A_\mu^* g)(x,y) = \frac{1}{W(x,y)} \int_0^{2\pi} g(-x\sin\theta+y\cos\theta,\theta)\ a(x,y,-x\sin\theta+y\cos\theta,\theta) \tag{3.22}$$

$$\times\ w(-x\sin\theta+y\cos\theta,\theta)d\theta$$

where

$$a(x,y,-x\sin\theta+y\cos\theta,\theta) =$$

$$\exp\left[-\int_{x\cos\theta+y\sin\theta}^{\infty} \mu(x\sin^2\theta-y\cos\theta\sin\theta+\zeta'\cos\theta,-x\sin\theta\cos\theta+y\cos^2\theta+\zeta'\sin\theta)d\zeta'\right] . \tag{3.23}$$

By the property of functionals on Hilbert spaces (Taylor, 1966), we know that $A_\mu^* g$ is unique. Another way of writing Eq. (3.22) is

$$(A_\mu^* g)(x,y) = \frac{1}{W(x,y)}\int_0^{2\pi}\int_{-\infty}^{\infty} g(\xi,\theta)\, a(x,y,\xi,\theta)\, w(\xi,\theta)\delta(\xi+x\sin\theta-y\cos\theta)d\xi d\theta. \tag{3.24}$$

The adjoint transform A_μ^* is an inverse mapping in the sense that it maps the Hilbert space of projection functions $L^2(\mathbb{C},w)$ into the Hilbert space of concentration functions $L^2(\mathbb{R}^2,W)$.

Another operator which operates on $L^2(\mathbb{C},w)$ is the back-projection operator B_μ defined by

$$(B_\mu g)(x,y) = \int_0^{2\pi} g(-x\sin\theta+y\cos\theta,\theta)/a(x,y,-x\sin\theta+y\cos\theta,\theta)d\theta. \tag{3.25}$$

This operator differs from the adjoint transform (Eqs. (3.22) and (3.23)) in that the weighting functions W and w do not appear and the attenuation factor is equal to the reciprocal of the attenuation factor given in Eq. (3.23). Both the adjoint transform A_μ^* and the back-projection operator B_μ can be considered as "back-projection" operators since they both correspond to back-projecting the projection values

for all projection rays passing through the same point (x,y) weighted by the appropriate weighting functions and attenuation factors.

3.4.2 The Composite of the Projection and Back-Projection Operators

As discussed in Section 3.3, the operator $A_\mu^* A_\mu$ restricted to the space $R(A_\mu^*) = N(A_\mu)^\perp$ is a one-to-one and onto mapping of $N(A_\mu)^\perp$ onto itself if $R(A_\mu)$ is closed. For the attenuated Radon transform A_μ, the operator $A_\mu^* A_\mu : \rho \to \beta$ can be written as

$$\beta(x',y') = \int\int \rho(x,y)\ K(x',y'|x,y)\,dxdy \tag{3.4}$$

where the kernel K is given by the following theorem.

THEOREM 3.3. For the attenuated Radon transform $A_\mu : L^2(\mathbb{R}^2,W) \to L^2(\mathbb{C},w)$ defined by Eq. (3.16) and the adjoint operator A_μ^* defined by Eq. (3.22) and $w(\xi,\theta)$ independent of θ and satisfying $w(\xi) = w(-\xi)$, the operator $A_\mu^* A_\mu : \rho \to \beta$ maps ρ into β where β is given by Eq. (3.4) with the kernel K given by

$$K(x',y'|x,y) = \frac{\widetilde{K}(x',y'|x,y)}{W(x',y')}\ w\left(\frac{xy'-yx'}{\|\hat{x}-\hat{x}'\|}\right) \tag{3.26}$$

where

$$\widetilde{K}(x',y'|x,y) = \frac{1}{\|\hat{x}-\hat{x}'\|}\left[\exp\left\{-\int_d^\infty \mu(b+\zeta'e,c+\zeta'f)d\zeta' - \int_{d'}^\infty \mu(b+\zeta'e,c+\zeta'f)d\zeta'\right\}\right.$$
$$\left. + \exp\left\{-\int_{-d}^\infty \mu(b-\zeta'e,c-\zeta'f)d\zeta' - \int_{-d'}^\infty \mu(b-\zeta'e,c-\zeta'f)d\zeta'\right\}\right], \tag{3.27}$$

and

$$d = \frac{x(x-x') + y(y-y')}{\|\hat{x}-\hat{x}'\|} = \frac{\langle \hat{x},(\hat{x}-\hat{x}')\rangle}{\|\hat{x}-\hat{x}'\|} \tag{3.28}$$

$$d' = \frac{x'(x-x')+y'(y-y')}{\|\hat{x}-\hat{x}'\|} = \frac{\langle \hat{x}',(\hat{x}-\hat{x}')\rangle}{\|\hat{x}-\hat{x}'\|} \tag{3.29}$$

$$b = \frac{(y-y')(yx'-xy')}{\|\hat{x}-\hat{x}'\|^2} \tag{3.30}$$

$$c = \frac{(x-x')(xy'-yx')}{\|\hat{x}-\hat{x}'\|^2} \tag{3.31}$$

$$e = \frac{(x-x')}{\|\hat{x}-\hat{x}'\|} \tag{3.32}$$

$$f = \frac{(y-y')}{\|\hat{x}-\hat{x}'\|} \quad . \tag{3.33}$$

PROOF. Using Eqs. (3.16a) and (3.24) we see that $A_\mu^* A_\mu\ (\rho)$ can be written as

$$\beta(x',y') = \int_{-\infty}^{\infty}\int_{-\infty}^{\infty} \rho(x,y)\ K(x',y'|x,y)dxdy$$

where

$$K(x',y'|x,y) = \frac{1}{W(x,y)} \int_0^{2\pi}\int_{-\infty}^{\infty} a(x,y,\xi,\theta)\ a(x',y',\xi,\theta)$$

$$\times\ w(\xi)\ \delta(\xi+x\sin\theta-y\cos\theta)\ \delta(\xi+x'\sin\theta-y'\cos\theta)d\xi d\theta \tag{3.34}$$

$$K(x',y'|x,y) =$$

$$= \frac{1}{W(x,y)} \int_0^{2\pi} a(x,y,-x\sin\theta+y\cos\theta,\theta)\; a(x',y',-x\sin\theta+y\cos\theta,\theta)$$

$$\times\, w(-x\sin\theta+y\cos\theta)\; \delta(-(x-x')\sin\theta+(y-y')\cos\theta)d\theta\ . \qquad (3.35)$$

To evaluate Eq. (3.35) we use the relationship (Papoulis, 1968, p.38)

$$\int_0^{2\pi} \delta\{g(\theta)\}d\theta = \int_0^{2\pi} \sum_i \frac{\delta(\theta-\theta_i)}{\left|\frac{dg(\theta)}{d\theta}\right|_{\theta=\theta_i}}\, d\theta$$

where θ_i are the zeros of $g(\theta)$,

$$g(\theta) = -(x-x')\sin\theta + (y-y')\cos\theta.$$

The function $g(\theta)$ has two zeros θ_1 and θ_2 which satisfy the following relationships

$$\sin\theta_1 = \frac{y-y'}{\|\hat{x}-\hat{x}'\|} \qquad \cos\theta_1 = \frac{x-x'}{\|\hat{x}-\hat{x}'\|} \qquad (3.36)$$

$$\sin\theta_2 = \frac{-(y-y')}{\|\hat{x}-\hat{x}'\|} \qquad \cos\theta_2 = \frac{-(x-x')}{\|\hat{x}-\hat{x}'\|}\ . \qquad (3.37)$$

The derivative of g with respect to θ is given by

$$\frac{dg(\theta)}{d\theta} = -(x-x')\cos\theta - (y-y')\sin\theta \quad .$$

Evaluating this at θ_1 and θ_2 gives

$$\left| \frac{dg(\theta)}{d\theta} \right|_{\theta=\theta_1,\theta_2} = \|\hat{x} - \hat{x}'\| \quad .$$

Therefore Eq. (3.35) can be rewritten as

$$K(x',y'|x,y) = \frac{1}{W(x,y)} \int_0^{2\pi} a(x,y,-x\sin\theta+y\cos\theta,\theta)\, a(x',y',-x\sin\theta+y\cos\theta,\theta)$$

$$\times w(-x\sin\theta+y\cos\theta)\, \frac{[\delta(\theta-\theta_1) + \delta(\theta-\theta_2)]}{\|\hat{x} - \hat{x}'\|}\, d\theta \quad . \qquad (3.38)$$

Integrating Eq. (3.38) with respect to θ gives

$$K(x',y'|x,y) = [a(x,y,-x\sin\theta_1+y\cos\theta_1,\theta_1)a(x',y',-x\sin\theta_1+y\cos\theta_1,\theta_1)$$

$$\times w(-x\sin\theta_1+y\cos\theta_1) + a(x,y,-x\sin\theta_2+y\cos\theta_2,\theta_2)$$

$$\times a(x',y',-x\sin\theta_2+y\cos\theta_2,\theta_2)\, w(-x\sin\theta_2+y\cos\theta_2)]\, \frac{\|\hat{x}-\hat{x}'\|^{-1}}{W(x,y)} \quad .$$

Substituting the expressions for $\sin\theta_1$, $\cos\theta_1$, $\sin\theta_2$, $\cos\theta_2$ into the definition of the attenuation function given in Eq. (3.23) and using the assumption $w(\xi) = w(-\xi)$ gives the expression for $K(x',y'|x,y)$ in Eq. (3.26) and $\tilde{K}(x',y'|x,y)$ in Eq. (3.27). ‖

We see from Fig. 3.4 that the function $\tilde{K}$ is twice the inverse of the distance between the two points $\hat{x}$ and $\hat{x}'$ times the sum of attenuation factors which represent the attenuation between the respective

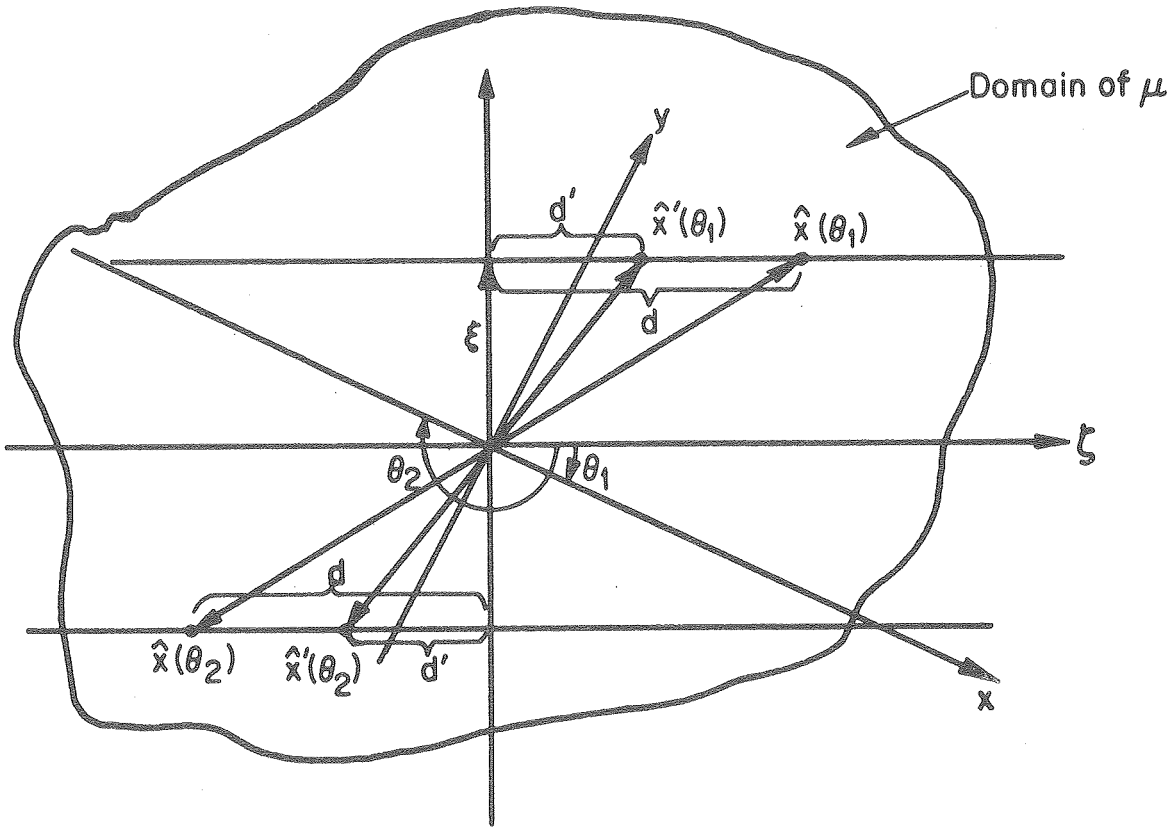

XBL791-3070

Figure 3.4. The integrals in the first exponential of Eq. (3.27) are the line integrals of the attenuation distribution μ along the top line from the points $\hat{x}(\theta_1)$ and $\hat{x}'(\theta_1)$, respectively. The integrals in the second exponential of Eq. (3.27) are the line integrals of μ along the bottom line from the points $\hat{x}(\theta_2)$ and $\hat{x}'(\theta_2)$, respectively.

points $\hat{x}$ and $\hat{x}'$ and the detectors as viewed from angles 180° apart. The function $\tilde{K}$ is also symmetric in the sense that $\tilde{K}(\hat{x}'|\hat{x}) = \tilde{K}(\hat{x}|\hat{x}')$.

We know from the discussion about Hilbert-Schmidt operators in Section 3.3 that if the weight functions W and w are choosen so that K is square integrable (i.e. $\iint K(\hat{x}'|\hat{x})\, W(\hat{x}')\, W(\hat{x})\, d\hat{x}d\hat{x}' < \infty$) then eigenfunctions exist for the attenuated Radon transform.

For the composite of the Radon transform and the back-projection operator [Eq. (2.4)], the kernel K is given in Eq. (3.5) for which the result in Eq. (3.4) is a convolution. It follows from the next theorem that the kernel function for the composite of the attenuated Radon transform and the back-projection operator given in Eq. (3.25) allows us to write Eq. (3.4) as a convolution only if the attenuation distribution is constant.

THEOREM 3.4. For the back-projection operator B_μ defined by Eq. (3.25), the operator $B_\mu A_\mu : \rho \to \beta$ maps ρ into β where β is given by Eq. (3.4) with the kernel given by

$$K(x',y'|x,y) = \frac{2}{\|\hat{x}-\hat{x}'\|} \cosh\left\{\int_{d'}^{d} \mu(b+\zeta' e,\ c+\zeta' f)\, d\zeta'\right\} \tag{3.39}$$

where d, d', b, c, e, f are given by Eqs. (3.28)-(3.33).

PROOF. Proceeding as in Theorem 3.3, the kernel can be evaluated giving

$$K(x',y'|x,y) = [a(x,y,-x\sin\theta_1+y\cos\theta_1,\theta_1)/a(x',y',-x\sin\theta_1+y\cos\theta_1,\theta_1)$$

$$+ a(x,y,-x\sin\theta_2+y\cos\theta_2,\theta_2)/a(x',y',-x\sin\theta_2+y\cos\theta_2,\theta_2)]\, \|\hat{x}-\hat{x}'\|^{-1}. \tag{3.40}$$

Substituting the expressions for $\sin\theta_1$, $\cos\theta_1$, $\sin\theta_2$, $\cos\theta_2$ into the definition of the attenuation functions given in Eq. (3.23) gives

$$K(x',y'|x,y) =$$

$$\exp\left\{-\int_{d}^{\infty}\mu(b+\zeta'e,c+\zeta'f)d\zeta' + \int_{d'}^{d}\mu(b+\zeta'e,c+\zeta'f)d\zeta' + \int_{d}^{\infty}\mu(b+\zeta'e,c+\zeta'f)d\zeta'\right\}$$

$$+ \exp\left\{-\int_{-d}^{-d'}\mu(b-\zeta'e,c-\zeta'f)d\zeta' - \int_{-d'}^{\infty}\mu(b-\zeta'e,c-\zeta'f)d\zeta' + \int_{-d'}^{\infty}\mu(b-\zeta'e,c-\zeta'f)d\zeta'\right\}. \tag{3.41}$$

The integral in the argument of the first exponential function representing the function 1/a has been written as the sum of two integrals as has the integral in the argument of the second exponential function representing the function a. We see then that the expression for the kernel function can be simplified giving the result in Eq. (3.39). ‖

3.4.3 The Composite of the Back-Projection and Projection Operators

As described in Section 3.3 the operator $A_\mu A_\mu^*$ restricted to the space $R(A_\mu) = N(A_\mu^*)^\perp$ is a one-to-one and onto mapping of $N(A_\mu^*)^\perp$ onto itself if the $R(A_\mu)$ is closed. For the attenuated Radon transform A_μ, the operator $A_\mu A_\mu^*: p \to g$ is given by the integral equation

$$g(\xi,\theta) = \iint p(\xi',\theta')\ I(\xi,\theta|\xi',\theta')d\xi'd\theta' \tag{3.7}$$

where the kernel I is given by the following theorem.

THEOREM 3.5. For the attenuated Radon transform $A_\mu: L^2(\mathbb{R}^2,W) \to L^2(\mathbb{C},w)$ defined by Eq. (3.16) and the adjoint operator A_μ^* defined by

Eq. (3.22), the operator $A_\mu A_\mu^*: p \to g$ maps p into g where g is given by Eq. (3.7) with the kernel I given by

$$I(\xi,\theta|\xi',\theta') = \frac{\tilde{I}(\xi,\theta|\xi',\theta')\ w(\xi',\theta')}{W\left(\frac{\xi'\cos\theta - \xi\cos\theta'}{\sin(\theta-\theta')},\ \frac{\xi'\sin\theta - \xi\sin\theta'}{\sin(\theta-\theta')}\right)}$$

where

$$\tilde{I}(\xi,\theta|\xi',\theta') = \frac{1}{|\sin(\theta-\theta')|}\ \exp\left[-\int_{\zeta_0}^{\infty} \mu(-\xi\sin\theta+\zeta\cos\theta, \xi\cos\theta+\zeta\sin\theta)d\zeta\right.$$

$$\left. - \int_{\zeta_0'}^{\infty} \mu(-\xi'\sin\theta'+\zeta'\cos\theta',\ \xi'\cos\theta'+\zeta'\sin\theta')d\zeta'\right] \qquad (3.42)$$

and

$$\zeta_0 = \xi\cot(\theta'-\theta) - \xi'\csc(\theta'-\theta) \qquad (3.43)$$

$$\zeta_0' = \xi\csc(\theta'-\theta) - \xi'\cot(\theta'-\theta)\ . \qquad (3.44)$$

PROOF. Using Eqs. (3.16a) and (3.24) we see that $A_\mu A_\mu^*(p)$ can be written as

$$g(\xi,\theta) = \int_0^{2\pi}\int_{-\infty}^{\infty} p(\xi',\theta')\ I(\xi,\theta|\xi',\theta')d\xi'd\theta'$$

where

$$I(\xi,\theta|\xi',\theta') = \int_{-\infty}^{\infty}\int_{-\infty}^{\infty} a(x,y,\xi,\theta)\ a(x,y,\xi,\theta)\ \delta(\xi+x\sin\theta-y\cos\theta)$$

$$\times\ \delta(\xi'+x\sin\theta'-y\cos\theta')\ \frac{dxdy}{W(x,y)}\ w(\xi',\theta').$$

Integrating with respect to x gives

$$I(\xi,\theta|\xi',\theta') = \int_{-\infty}^{\infty} \frac{a(x^*(y),y,\xi,\theta)\, a(x^*(y),y,\xi',\theta')\, \delta(\xi+x^*(y)\sin\theta-y\cos\theta)}{|\sin\theta'|\, W(x^*(y),y)}\, dy$$

$$\times\ w(\xi',\theta')$$

where $x^*(y) = \dfrac{y\cos\theta'-\xi'}{\sin\theta'}$. Integrating with respect to y gives

$$I(\xi,\theta|\xi',\theta') = \frac{a(x^*(y^*),y^*,\xi,\theta)\ a(x^*(y^*),y^*,\xi',\theta')}{|\sin(\theta-\theta')|\, W(x^*(y^*),y^*)}\ w(\xi',\theta')$$

where

$$x^*(y^*) = \frac{\xi'\cos\theta - \xi\cos\theta'}{\sin(\theta-\theta')}$$

and

$$y^* = \frac{\xi'\sin\theta - \xi\sin\theta'}{\sin(\theta-\theta')} \quad .$$

This gives

$$a(x^*(y^*),y^*,\xi,\theta) = \exp\left[-\int_{\zeta_0}^{\infty} \mu(-\xi\sin\theta+\zeta\cos\theta,\ \xi\cos\theta+\zeta\sin\theta)\,d\zeta\right]$$

with

$$\zeta_0 = \xi\ \cot(\theta'-\theta) - \xi'\ \csc(\theta'-\theta)\ ,$$

and

$$a(x^*(y^*),y^*,\xi',\theta') = \exp\left[-\int_{\zeta_0'}^{\infty} \mu(-\xi'\sin\theta'+\zeta'\cos\theta',\xi'\cos\theta'+\zeta'\sin\theta')\,d\zeta'\right]$$

with

$$\zeta_0' = \xi \csc(\theta'-\theta) - \xi' \cot(\theta'-\theta). \quad \|$$

Figure 3.5 shows that the coordinates $(\zeta_0 = -d, \xi)$ and $(\zeta_0' = d', \xi')$ are the coordinates of the intersection of the lines $\xi+x\sin\theta-y\cos\theta=0$ and $\xi'x\sin\theta'-y\cos\theta'=0$ in the $\zeta\xi$- and $\zeta'\xi'$-coordinate system, respectively. The line integrals in Eq. (3.42) represent integrals of the attenuation distribution μ along the two lines from the point of intersection.

3.4.4 The Single Angle Projection Operator

In Eq. (3.16), we see that the attenuated Radon transform maps a function $\rho:\mathbb{R}^2 \to \mathbb{R}$ with domain $\mathbb{R}^2$ and range $\mathbb{R}$ into the function $A_\mu\rho:\mathbb{R}\times[0,2\pi) \to \mathbb{R}$ whose domain is the direct product of the real numbers with $[0,2\pi)$. By fixing the angle θ, we can define a single angle projection operator denoted by $A_{\mu,\theta}$ such that $(A_{\mu,\theta}\rho)(\xi) = (A_\mu\rho)(\xi,\theta)$ is a single projection at the angle θ.

In emission computed tomography, one tries to find the function ρ from a finite number of these single projections, $A_{\mu,\theta_1}\rho$, $A_{\mu,\theta_2}\rho$, ..., $A_{\mu,\theta_N}\rho$, which are called scintigrams. Even though in practice each $A_{\mu,\theta_i}\rho$ is known only at a finite number of discrete points, we will assume that each projection $(A_{\mu,\theta}\rho)(\xi)$ is known for all ξ. The single angle projection operator $A_{\mu,\theta}$ can be generalized to N angles by defining the N-fold operator $A_{\mu,N}:\rho \to A_{\mu,N}\rho = (A_{\mu,\theta_1}\rho, A_{\mu,\theta_2}\rho,$ ..., $A_{\mu,\theta_N}\rho)$ which maps the function ρ into the N-tuple of single angle projections. The N-fold projection operator will be discussed in the next section.

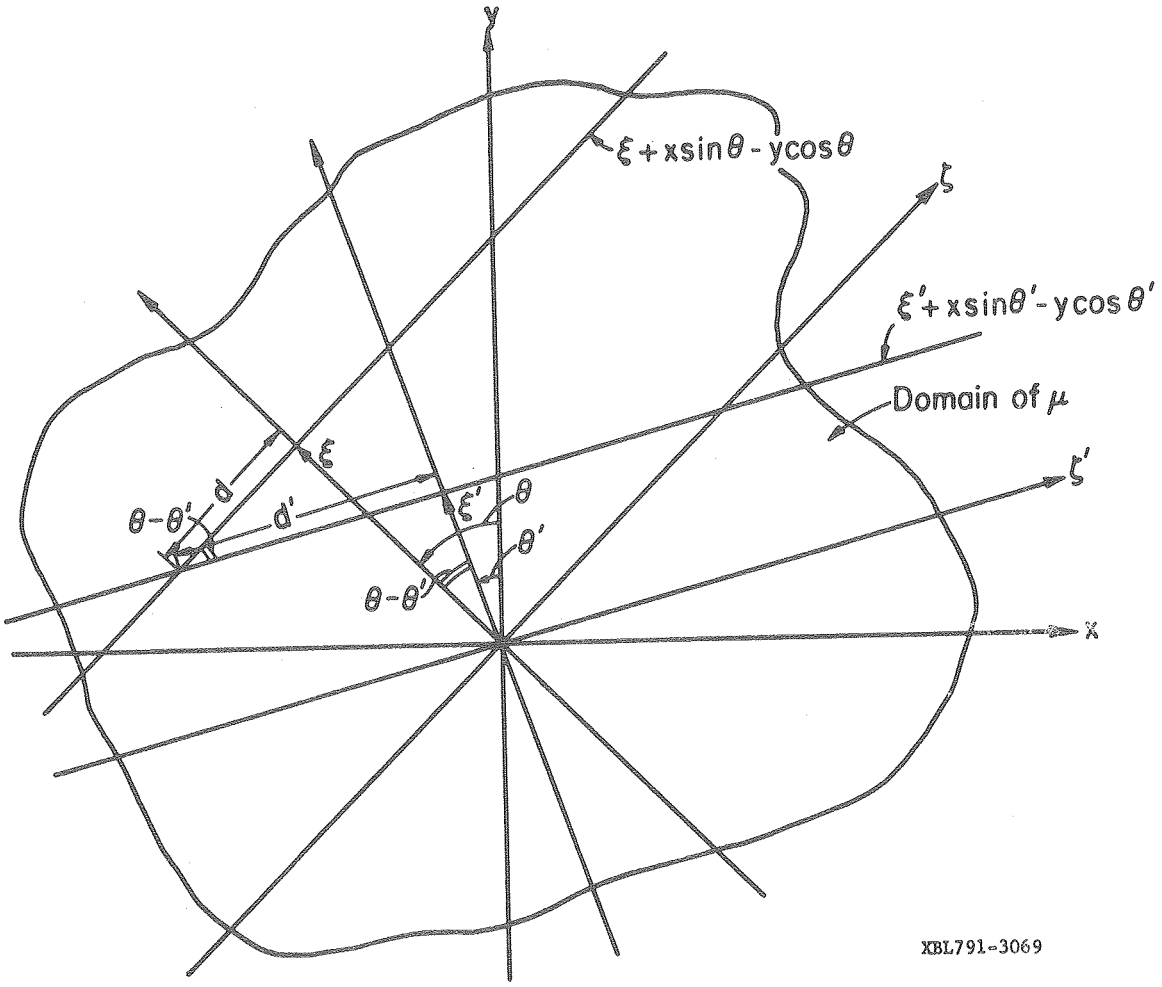

Figure 3.5. The first integral in the exponential argument of Eq. (3.42) is the line integral of the attenuation distribution μ along the line $\xi+x\sin\theta-y\cos\theta = 0$ from the point of intersection with the line $\xi'+x\sin\theta'-y\cos\theta' = 0$. The second integral is the integral of μ along the line $\xi'+x\cos\theta'-y\cos\theta' = 0$ from the same point of intersection. The distances d and d' satisfy $d = \xi\cot(\theta-\theta')-\xi'\csc(\theta-\theta')$ and $d' = \xi\csc(\theta-\theta')-\xi'\cot(\theta-\theta')$, and the coordinates ζ_o and ζ_o' satisfy $\zeta_o = -d$ and $\zeta_o' = -d'$, respectively.

First we investigate some of the properties of the single angle projection operator $A_{\mu,\theta}$. These results parallel similar results developed by Marr (1979) for the Radon transform. In the following theorems we will use the attenuation function

$$a(x,y,-x\sin\theta+y\cos\theta,\theta) =$$

$$\exp \int_{x\cos\theta+y\sin\theta}^{\infty} \mu(x\sin^2\theta-y\cos\theta\sin\theta+\zeta'\cos\theta, -x\sin\theta\cos\theta+y\cos^2\theta+\zeta'\sin\theta)d\zeta' \tag{3.23}$$

as a weight function for the Hilbert space $L^1(\mathbb{R}^2,a)$. Functions $\rho \in L^1(\mathbb{R}^2,a)$ satisfy

$$\iint_{\mathbb{R}^2} |\rho(x,y)|\, a(x,y,-x\sin\theta+y\cos\theta,\theta)dxdy < \infty .$$

The weight function $a(x,y,-x\sin\theta+y\cos\theta,\theta)$ represents the integral of the attenuation coefficients from the point (x,y) to ∞ for the projection angle θ. The inner product for the Hilbert space $L^1(\mathbb{R}^2,a)$ is given by $\langle f,g\rangle_{\mathbb{R}^2,a} = \iint_{\mathbb{R}^2} f(x,y)\, g(x,y)\, a(x,y,-x\sin\theta+y\cos\theta,\theta)dxdy$.

THEOREM 3.6. For any θ, $A_{\mu,\theta}$ is a bounded linear map from $L^1(\mathbb{R}^2,a)$ into $L^1(\mathbb{R})$ with $\|A_{\mu,\theta}\| = 1$.

PROOF. Using the definition of $(A_{\mu,\theta}\,\rho)(\xi)$ given by Eq. (3.16), we have

$$\int |(A_{\mu,\theta}\rho)(\xi)|d\xi = \int \left|\int \rho(-\xi\sin\theta+\zeta\cos\theta,\ \xi\cos\theta+\zeta\sin\theta)\ a(\zeta,\xi,\theta)d\zeta\right| d\xi$$

$$\leq \iint |\ \rho(-\xi\sin\theta+\zeta\cos\theta,\ \xi\cos\theta+\zeta\sin\theta)\ a(\zeta,\xi,\theta)|d\zeta d\xi .$$

Using Fubini's theorem, we have for $\rho \in L'(\mathbb{R}^2,a)$

$$\int |(A_{\mu,\theta}\rho)(\xi)|d\xi \leq \int\int |\rho(x,y)\ a(x,y,-x\sin\theta+y\cos\theta,\theta)|dxdy < \infty .$$

Therefore $A_{\mu,\theta}\rho \in L^1(\mathbb{R})$. Rewriting we can express this as

$$\|A_{\mu,\theta}\rho\| \leq \|\rho\| .$$

This implies that

$$\|A_{\mu,\theta}\| = \sup_{\|\rho\| \leq 1} \frac{\|A_{\mu,\theta}\rho\|}{\|\rho\|} \leq 1 .$$

If we let $\rho(x,y) = \delta(x)\ \delta(y)\ [a(x,y,-x\sin\theta+y\cos\theta,\theta)]^{-1}$ we see that $\|A_{\mu,\theta}\| = 1$. ||

In the next theorem we consider $A_{\mu,\theta}$ operating on the Hilbert space $L^2(\mathbb{R}^2)$. If the attenuation function $a(x,y,-x\sin\theta+y\cos\theta,\theta) \in L^2(\mathbb{R}^2)$ for any θ then $A_{\mu,\theta}$ will map functions in $L^2(\mathbb{R}^2)$ into functions in the Hilbert space $L^2(\mathbb{R})$.

THEOREM 3.7. For any θ, $A_{\mu,\theta}$ is a bounded linear map from $L^2(\mathbb{R}^2)$ into $L^2(\mathbb{R})$ if $\|A_{\mu,\theta}\| = [\iint |a(x,y,-x\sin\theta+y\cos\theta,\theta)|^2\ dxdy]^{1/2} < \infty$.

PROOF. Using the definition of $(A_{\mu,\theta}\ \rho)(\xi)$ given by Eq. (3.16) and Schwartz's inequality, we have

$$|(A_{\mu,\theta}\rho)(\xi)| = |\int \rho(-\xi\sin\theta+\zeta\cos\theta,\ \xi\cos\theta+\zeta\sin\theta)\ a(\zeta,\xi,\theta)d\zeta|$$

$$\leq \left(\int |\rho(-\xi\sin\theta+\zeta\cos\theta,\ \xi\cos\theta+\zeta\sin\theta)|^2 d\zeta\right)^{1/2} \left(\int |a(\zeta,\xi,\theta)|^2 d\zeta\right)^{1/2}.$$

Using Fubini's theorem, we have for $\rho \in L^2(\mathbb{R}^2)$

$$\left(\int |(A_{\mu,\theta}\rho)(\xi)|^2 \, d\xi\right)^{1/2} \leq \left(\int\int |\rho(x,y)|^2 \, dxdy\right)^{1/2}$$

$$\times \left(\int\int |a(x,y,-x\sin\theta+y\cos\theta,\theta)|^2 dxdy\right)^{1/2} < \infty ,$$

if $\|A_{\mu,\theta}\| = (\iint |a(x,y,-x\sin\theta+y\cos\theta,\theta)|^2 \, dxdy)^{1/2} < \infty$. Therefore $A_{\mu,\theta} \rho \in L^2(\mathbb{R})$. ‖

In Theorem 3.7 the norm of the projection operator $A_{\mu,\theta}$ is a measure of the detectability of photons - detectability meaning that they are not attenuated by Compton scatter or photoelectric absorption. The density of the attenuating material and the energy of the emitted photon from the radionuclide are two physical factors which directly influence the norm of $A_{\mu,\theta}$. The higher the energy then the greater is $\|A_{\mu,\theta}\|$, whereas the denser the body tissue then the smaller is $\|A_{\mu,\theta}\|$. This has important application when considering, for a particular attenuating material, the required number of photons that must be collected in order to insure a desired contrast resolution. In ECT imaging, this means that the larger the norm of $A_{\mu,\theta}$ the shorter is the time required for collecting data and/or the lower is the required injected dose. This is desirable for patient studies.

Next we want to investigate the adjoint transforms of $A_{\mu,\theta}$ for the functional spaces $L^2(\mathbb{R}^2)$ and $L^1(\mathbb{R}^2,a)$. The operator $A^*_{\mu,\theta}$ maps the function h defined on $\mathbb{R}$ into the function $A^*_{\mu,\theta}$ h given by

$$(A^*_{\mu,\theta} h)(x,y) = h(-x\sin\theta+y\cos\theta) \; a(x,y,-x\sin\theta+y\cos\theta,\theta) \qquad (3.45)$$

where $a(x,y,-x\sin\theta+y\cos\theta,\theta)$ is given by Eq. (3.23). The operator B_θ maps the function h defined on $\mathbb{R}$ into the function $B_\theta\, h$ given by

$$(B_\theta\, h)(x,y) = h(-x\sin\theta+y\cos\theta) \ . \tag{3.46}$$

The function $B_\theta\, h$ is a ridge function (Logan and Shepp, 1975) which is constant along lines that are parallel to $\underset{\sim}{\theta}^\perp$ (Fig. 3.3). The function $A^*_{\mu,\theta}\, h$ is an exponential ridge function which varies exponentially along lines that are parallel to $\underset{\sim}{\theta}^\perp$.

The inner product for the Hilbert spaces $L^1(\mathbb{R})$ and $L^2(\mathbb{R})$ is given by $[p,q]_{\mathbb{R}} = \int_{\mathbb{R}} p(\xi)\, q(\xi)d\xi$. Using the definitions of the corresponding inner products for the Hilbert spaces $L^1(\mathbb{R}^2,a)$ and $L^2(\mathbb{R}^2)$, the following two theorems show that the operator $A^*_{\mu,\theta}$ given by Eq. (3.45) is the adjoint of $A_{\mu,\theta}: L^2(\mathbb{R}^2) \to L^2(\mathbb{R})$ and the operator B_θ given by Eq. (3.46) is the adjoint of $A_{\mu,\theta}: L^1(\mathbb{R}^2,a) \to L^1(\mathbb{R})$.

THEOREM 3.8. For any function $\rho \in L^2(\mathbb{R}^2)$ and any function $h \in L^2(\mathbb{R})$, $\langle \rho, A^*_{\mu,\theta}\, h\rangle_{\mathbb{R}^2} = [A_{\mu,\theta}\rho, h]_{\mathbb{R}}$.

PROOF. Using the definition of the inner product for $L^2(\mathbb{R}^2)$ we can write

$$\langle \rho, A^*_{\mu,\theta}\, h\rangle_{\mathbb{R}^2} = \iint \rho(x,y)\ (A^*_{\mu,\theta}\, h)(x,y)dxdy$$

$$= \iint \rho(x,y)\, h(-x\sin\theta+y\cos\theta)\, a(x,y,-x\sin\theta+y\cos\theta,\theta)dxdy$$

for the function $h \in L^2(\mathbb{R})$. This can be rewritten as

$$\langle \rho, A^*_{\mu,\theta} h \rangle_{\mathbb{R}^2} = \iiint \rho(x,y)\, h(\xi)\, a(x,y,\xi,\theta)\, \delta(\xi+\sin\theta-y\cos\theta)\, d\xi dx dy$$

$$= \int (A_{\mu,\theta}\ \rho)(\xi) h(\xi) d\xi$$

$$= [A_{\mu,\theta}\ \rho, h]_{\mathbb{R}} \cdot \|$$

THEOREM 3.9. For any function $\rho \in L(\mathbb{R}^2, a)$ and any function $h \in L^1(\mathbb{R})$, $\langle \rho, B_\theta h \rangle_{\mathbb{R}^2, a} = [A_{\mu,\theta}\ \rho, h]_{\mathbb{R}}$.

PROOF. The proof follows similar steps as given in Theorem 3.8. ‖

In the next results we need to define the following functions:

DEFINITION. The function $\chi \in L^1(\mathbb{R}^2, a)$ will denote the characteristic function for some subset Ω of $\mathbb{R}^2$ (i.e. $\chi = 1$ for points in the subset Ω and 0 otherwise.) and $\hat{\chi}_{\mu,\theta} = A_{\mu,\theta}\ \chi$. The operator M_f will denote the multiplication operator such that $(M_f\ g)(x,y) = f(x,y)\ g(x,y)$.

THEOREM 3.10. If $\chi \in L^2(\mathbb{R}^2, a)$ and $h \in L^2(\mathbb{R})$ then

$$(A_{\mu,\theta}\ M_\chi\ B_\theta) h = M_{\hat{\chi}_{\mu,\theta}}\ h\ . \tag{3.47}$$

PROOF. By the definition of B_θ in Eq. (3.46), we have $(B_\theta\ h)(x,y) = h(-x\sin\theta+y\cos\theta)$. Applying the operator M_χ to this gives $\chi(x,y) \times h(-x\sin\theta+y\cos\theta)$. Therefore the expression on the left of Eq. (3.47) is given by

$$(A_{\mu,\theta}\ M_\chi\ B_\theta h)(\xi) = \iint_{\mathbb{R}^2} \chi(x,y) h(-x\sin\theta+y\cos\theta) a(x,y,\xi,\theta) \delta(\xi+x\sin\theta-y\cos\theta) dx dy$$

$$= \iiint_{\mathbb{R}^2} \int_{-\infty}^{\infty} \chi(x,y) h(\xi') a(x,y,\xi,\theta) \delta(\xi'+x\sin\theta-y\cos\theta) \delta(\xi+x\sin\theta-y\cos\theta) d\xi' dx dy.$$

Since $\chi \in L^2(\mathbb{R}^2,a)$ and $h \in L^2(\mathbb{R})$ we can change the order of integration. Doing this plus using the transformation of coordinates (Eq. 3.15) we have

$$(A_{\mu,\theta} M_\chi B_\theta\, h)(\xi) = \int h(\xi') \int \chi(\zeta,\xi)\, a(\zeta,\xi,\theta)\, d\zeta\, \delta(\xi'-\xi)\, d\xi'$$

$$= \int h(\xi')\, \hat{\chi}_{\mu,\theta}(\xi)\, \delta(\xi'-\xi)\, d\xi' = h(\xi)\, \hat{\chi}_{\mu,\theta}(\xi)$$

$$= M_{\hat{\chi}_{\mu,\theta}}\, h .\|$$

DEFINITION. The θ-silhouette of Ω is the set $\hat{\Omega}_\theta = \{\langle \hat{x}, \underset{\sim}{\theta} \rangle \mid \hat{x} \in \Omega\}$. The intersection of the line $\xi + x\sin\theta - y\cos\theta = 0$ and the set Ω is $\Omega_{\xi,\theta}$.

We next show that the operator $A_{\mu,\theta}$ maps $L^1(\Omega,a)$ onto $L^1(\hat{\Omega}_\theta)$.

THEOREM 3.11. The operator $A_{\mu,\theta}$ maps $L^1(\Omega,a)$ onto $L^1(\hat{\Omega}_\theta)$ with $\|A_{\mu,\theta}\| = 1$.

PROOF. To show that $A_{\mu,\theta}$ is an into mapping follows similar stops given in Theorem 3.6. To show that it is an onto mapping, take a function $h \in L^1(\hat{\Omega}_\theta)$ and let

$$\rho(x,y) = \chi(x,y)\, \frac{h(-x\sin\theta+y\cos\theta)}{\hat{\chi}_{\mu,\theta}(-x\sin\theta+y\cos\theta)} \quad . \tag{3.48}$$

Using Eqs. (3.16) and (3.17) -

$$(A_{\mu,\theta}\, \rho)(\xi) = \int_{\Omega_{\xi,\theta}} \chi(\zeta,\xi,\theta)\, \frac{h(\xi)}{\hat{\chi}_{\mu,\theta}(\xi)}\, a(\zeta,\xi,\theta)\, d\zeta$$

$$= \hat{\chi}_{\mu,\theta}(\xi)\, \frac{h(\xi)}{\hat{\chi}_{\mu,\theta}(\xi)} = h(\xi) \quad .$$

To show that ρ in Eq. (3.48) is in $L^1(\Omega,a)$ we have, using Schwartz's inequality and applying Fubini's theorem,

$$\iint_{\Omega} |\rho(x,y)|\, a(x,y,-x\sin\theta+y\cos\theta,\theta)\,dxdy$$

$$= \iint_{\Omega} \left| \chi(x,y)\, \frac{h(-x\sin\theta+y\cos\theta)}{\hat{\chi}_{\mu,\theta}(-x\sin\theta+y\cos\theta)} \right| a(x,y,-x\sin\theta+y\cos\theta,\theta)\,dxdy$$

$$= \iint_{\Omega} \left| \chi(\zeta,\xi)\, \frac{h(\xi)}{\hat{\chi}_{\mu,\theta}(\xi)} \right| a(\zeta,\xi,\theta)\,d\zeta d\xi$$

$$= \int_{\hat{\Omega}_\theta} |h(\xi)|\,d\xi\ .$$

Since $h \in L^1(\hat{\Omega}_\theta)$ then $\rho \in L^1(\Omega,a)$. To show that the norm of $A_{\mu,\theta}$ is equal to 1 follows immediately from similar steps to those given in Theorem 3.6. ||

Next we want to define a new single angle projection operator for the attenuated Radon transform. It will be shown that this operator has an important application in defining an ART algorithm for reconstructing attenuated projection data.

DEFINITION. For a set $\Omega \subseteq \mathbb{R}^2$ with characteristic function χ, the operators $R_{\mu,\theta}$ and $R^*_{\mu,\theta}$ are defined as follows

$$\text{i)}\quad R_{\mu,\theta} = M_{(\hat{\chi}_{\mu,\theta})^{-1}}\, A_{\mu,\theta} \tag{3.49}$$

$$\text{ii)}\quad R^*_{\mu,\theta} = M_{\chi}\, B_{\theta} \tag{3.50}$$

where B_θ is defined by Eq. (3.46).

THEOREM 3.12. For any θ and any bounded open set $\Omega \subseteq \mathbb{R}^2$ the following are true

(i) $R_{\mu,\theta}$ maps $L^2(\Omega,a)$ onto $L^2(\hat{\Omega}_\theta, \hat{\chi}_{\mu,\theta})$.

(ii) The composite operator $R_{\mu,\theta}\, R^*_{\mu,\theta} = 1$ is an identity on $L^2(\hat{\Omega}_\theta, \hat{\chi}_{\mu,\theta})$.

(iii) The composite operator $R^*_{\mu,\theta}\, R_{\mu,\theta}$ is an idempotent operator (i.e. $(R^*_{\mu,\theta}\, R_{\mu,\theta})^2 = R^*_{\mu,\theta}\, R_{\mu,\theta}$).

PROOF. (i) Using Schwartz's inequality and the definitions of $A_{\mu,\theta}$ (Eq. 3.16) and $R_{\mu,\theta}$ (Eq. 3.49), we see from the following sequence of inequalities that $R_{\mu,\theta}$ maps $L^2(\Omega,a)$ into $L^2(\hat{\Omega}_\theta, \hat{\chi}_{\mu,\theta})$:

$$
\begin{aligned}
|(A_{\mu,\theta}\,\rho)(\xi)| &= \Big| \int_{\Omega_{\xi,\theta}} \rho(\zeta,\xi)\, \chi(\zeta,\xi)\, a(\zeta,\xi,\theta)\, d\zeta \Big| \\
&\leq \Big(\int |\rho(\zeta,\xi)|^2\, a(\zeta,\xi,\theta)\, d\zeta \Big)^{1/2} \Big(\int \chi(\zeta,\xi)\, a(\zeta,\xi,\theta)\, d\zeta \Big)^{1/2} \\
&\leq \Big(\int |\rho(\zeta,\xi)|^2\, a(\zeta,\xi,\theta)\, d\zeta \Big)^{1/2} \big[\hat{\chi}_{\mu,\theta}(\xi)\big]^{1/2} .
\end{aligned}
$$

For $\rho \in L^2(\Omega,a)$

$$
\int_{\hat{\Omega}_\theta} \left| \frac{(A_{\mu,\theta}\rho)(\xi)}{\hat{\chi}_{\mu,\theta}(\xi)} \right|^2 \hat{\chi}_{\mu,\theta}(\xi)\, d\xi \leq \Big(\iint_{\Omega} |\rho(\zeta,\xi)|^2\, a(\zeta,\xi,\theta)\, d\zeta d\xi \Big) < \infty .
$$

Therefore $R_{\mu,\theta}\,\rho = A_{\mu,\theta}\,\rho/\hat{\chi}_{\mu,\theta} \in L^2(\hat{\Omega}_\theta, \hat{\chi}_{\mu,\theta})$.

To show that $R_{\mu,\theta}$ is an onto mapping, take a function $h \in L^2(\hat{\Omega}_\theta, \hat{\chi}_{\mu,\theta})$

and let

$$\rho(x,y) = \chi(x,y)\ h(-x\sin\theta+y\cos\theta)\ .$$

Then using Eqs. (3.16), (3.17), and (3.49)

$$(R_{\mu,\theta}\ \rho)(\xi) = \frac{1}{\hat{\chi}_{\mu,\theta}} \int_{\Omega_{\xi,\theta}} \chi(\zeta,\xi)\ h(\xi)\ a(\zeta,\xi,\theta)d\zeta$$

$$= h(\xi).$$

To show that $\rho \in L^2(\Omega,a)$ we have, using Schwartz's inequality and Fubini's theorem,

$$\left(\iint_{\Omega} |\rho(x,y)|^2\ a(x,y,-x\sin\theta+y\cos\theta,\theta)dxdy\right)^{1/2}$$

$$= \left(\iint_{\Omega} |\chi(x,y)\ h(-x\sin\theta+y\cos\theta)|^2\ a(x,y,-x\sin\theta+y\cos\theta,\theta)dxdy\right)^{1/2}$$

$$= \left(\iint_{\Omega} \chi(\zeta,\xi)|h(\xi)|^2\ a(\zeta,\xi,\theta)d\zeta d\xi\right)^{1/2}$$

$$= \left(\int_{\hat{\Omega}_\theta} |h(\xi)|^2\ \hat{\chi}_{\mu,\theta}(\xi)\ d\xi\right)^{1/2} < \infty\ .$$

(ii) The proof that $R_{\mu,\theta}\ R^*_{\mu,\theta}$ is an identity on $L^2(\hat{\Omega}_\theta,\ \hat{\chi}_{\mu,\theta})$ follows immediately from Theorem 3.10.

(iii) Using the result in (ii) we have

$$(R^*_{\mu,\theta}\ R_{\mu,\theta})^2 = R^*_{\mu,\theta}\ R_{\mu,\theta}\ R^*_{\mu,\theta}\ R_{\mu,\theta}$$

$$= R^*_{\mu,\theta}\ 1\ R_{\mu,\theta}$$

$$= R^*_{\mu,\theta}\ R_{\mu,\theta}\ .\ \|$$

COROLLARY 3.12.1. For any function $\rho \in L^2(\Omega,a)$ the operator $P_{\mu,\theta}$ operating on ρ' defined as

$$P_{\mu,\theta}\, \rho' = \rho' + R^*_{\mu,\theta}\, R_{\mu,\theta}\, (\rho-\rho') \ , \tag{3.51}$$

is a projection operator mapping $L^2(\Omega,a)$ onto the subspace $\rho + N(R_{\mu,\theta})$.

PROOF. The operator $P_{\mu,\theta}$ is an idempotent operator, which can be shown as follows

$$P_{\mu,\theta}\, (P_{\mu,\theta}\, \rho') = P_{\mu,\theta}\, \rho' + R^*_{\mu,\theta}\, R_{\mu,\theta}\, (\rho - P_{\mu,\theta}\, \rho')$$

$$= \rho' + R^*_{\mu,\theta}\, R_{\mu,\theta}\, (\rho-\rho') + R^*_{\mu,\theta} R_{\mu,\theta} [\rho-\rho' - R^*_{\mu,\theta} R_{\mu,\theta} (\rho-\rho')].$$

By Theorem 3.12 (iii) we know that $(R^*_{\mu,\theta}\, R_{\mu,\theta})^2 = (R^*_{\mu,\theta}\, R_{\mu,\theta})$, therefore

$$P_{\mu,\theta}(P_{\mu,\theta}\, \rho') = \rho' + R^*_{\mu,\theta}R_{\mu,\theta}(\rho-\rho') + R^*_{\mu,\theta}R_{\mu,\theta}(\rho-\rho') - R^*_{\mu,\theta}R_{\mu,\theta}(\rho-\rho')$$

$$= \rho' + R^*_{\mu,\theta}R_{\mu,\theta}(\rho-\rho') \ .$$

Further one can show that $P_{\mu,\theta}$ is Hermitian and the subspace $\rho + N(R_{\mu,\theta})$ is equal to $\{\rho' | P_{\mu,\theta}\, \rho' = \rho'\}$. Using (Theorem 3, p. 44, Halmos 1957), we know that $P_{\mu,\theta}$ is a projection operator mapping $L^2(\Omega,a)$ onto the subspace $\rho + N(R_{\mu,\theta})$. ||

This result has important application in developing an algorithm for determining a solution to a finite set of projections $R_{\mu,\theta_1}\, \rho$, $R_{\mu,\theta_2}\, \rho$, ..., $R_{\mu,\theta_N}\, \rho$. The algorithm is due to Kaczmarz (Hamaker and Solmon, 1978) and in computed tomography is more commonly called ART

(Gordon, Bender, and Herman, 1970). The concentration functions which have the same projections as the solution ρ are those in the subspace $M = (\rho + \bigcap_{i=1}^{N} N(R_{\mu,\theta_i}))$. If $P_{\mu,N}$ is the projection operation given by $P_{\mu,N} = \prod_{i=1}^{N} P_{\mu,\theta_i}$, then for an initial guess ρ_0 the theorem due to Kaczmarz (Durand, 1960) shows that $P^K_{\mu,N}\,\rho_0$ converges to the projection of ρ_0 on M. If ρ_0 is choosen to be zero, then $P^K\,\rho_0$ converges to the unique function $\hat{\rho}$ of smallest norm that satisfies $R_{\mu,\theta_i}\,\rho = R_{\mu,\theta_i}\,\hat{\rho}$ for $i=1,\ldots,N$.

In keeping consistent with the results given for the composite of the projection and adjoint transforms for the attenuated Radon transform A_μ given in Theorem 3.3, we give the following result for the single angle projection operators $A_{\mu,\theta}$ and $R_{\mu,\theta}$.

THEOREM 3.13. For the operator $A_{\mu,\theta}:L^2(\mathbb{R}^2) \to L^2(\mathbb{R})$ defined by Eq. (3.16) and the adjoint operator $A^*_{\mu,\theta}$ defined by Eq. (3.45), the operator $A^*_{\mu,\theta}\,A_{\mu,\theta}:\rho \to \beta$ where β is given by Eq. (3.4) with the kernel K given by

$$K(x',y'|x,y) = a(x,y,-x'\sin\theta+y'\cos\theta,\theta)\; a(x',y',-x'\sin\theta+y'\cos\theta,\theta)$$
$$\times\, \delta(-(x'-x)\sin\theta+(y'-y)\cos\theta)\,. \qquad (3.52)$$

PROOF. This follows immediately by evaluating $A^*_{\mu,\theta}\,A_{\mu,\theta}$ using Eqs. (3.16) and (3.45). ||

THEOREM 3.14. For the operator $R_{\mu,\theta}:L^2(\Omega,a) \to L^2(\hat{\Omega},\hat{\chi}_{\mu,\theta})$ defined by Eq. (3.49) and the adjoint operator $R^*_{\mu,\theta}$ defined by Eq. (3.50), the

operator $R^*_{\mu,\theta}\ R_{\mu,\theta}: \rho \to \beta$ where β is given by Eq. (3.4) with the kernel K given by

$$K(x',y'|x,y) = \chi(x',y')\ \chi(x,y)\ a(x,y,-x'\sin\theta+y'\cos\theta,\theta) \times \delta(-(x'-x)\sin\theta+(y'-y)\cos\theta)/\hat{\chi}_\theta(-x'\sin\theta+y'\cos\theta). \tag{3.53}$$

PROOF. This follows immediately by evaluating $R^*_{\mu,\theta}\ R_{\mu,\theta}$ using Eqs. (3.49) and (3.50). ||

3.4.5. The N-fold Projection Operator

The N-fold projection operator, $A_{\mu,N}$, maps the function ρ into the N-tuple made up of the projections at the angles $\theta_1,\ldots,\theta_N$ (i.e. $A_{\mu,N}: \rho \to A_{\mu,N}\ \rho = (A_{\mu,\theta_1}\rho,\ A_{\mu,\theta_2}\ \rho,\ldots,\ A_{\mu,\theta_N}\ \rho)$). For $A_{\mu,N}$ we will consider only situations where $A_{\mu,N}$ is a bounded linear operator; then the space of invisible functions (i.e. $A_{\mu,N}\ \rho \equiv 0$) commonly referred to as the null space of the operator, $N(A_{\mu,N})$, is a closed subspace. The optimum reconstruction is to seek a function ρ whose projections $A_{\mu,N}\ \rho$ are close to the sampled projections in an L^2 sense. Unfortunately this is not a well posed problem in that the space of invisible functions, $N(A_{\mu,N})$, is nonempty.

From Theorem 3.7 we see that if $\iint_{\mathbb{R}^2} |a(x,y,-x\sin\theta_i+y\cos\theta_i,\theta_i)|^2\ dxdy < \infty$ for angles θ_i, $i=1,\ldots,N$, then $A_{\mu,N}$ maps $L^2(\mathbb{R}^2)$ into $L^2(\mathbb{R}) \oplus \ldots \oplus L^2(\mathbb{R})$. We define the operator $A^*_{\mu,N}$ to be the mapping of N-tuples of real valued functions defined on $\mathbb{R}$ denoted as $\underline{h} = (h_1, h_2,\ldots, h_N)$ into the functions $A^*_{\mu,N}\ \underline{h}$ given by

$$A^*_{\mu,N}\,\underline{h}(x,y) = \frac{1}{N}\sum_{j=1}^{N} h_j(-x\sin\theta_j+y\cos\theta_j)\; a(x,y,-x\sin\theta_j+y\cos\theta_j,\theta_j) \tag{3.54}$$

where

$$a(x,y,-x\sin\theta_j+y\cos\theta_j,\theta_j) =$$

$$\exp\left[-\int_{x\cos\theta_j+y\sin\theta_j}^{\infty}\mu(x\sin^2\theta_j-y\cos\theta_j\sin\theta_j+\zeta'\cos\theta_j,-x\sin\theta_j\cos\theta_j+y\cos^2\theta_j+\zeta'\sin\theta_j)\,d\zeta'\right]. \tag{3.55}$$

For the N-tuples $\underline{g}$ and $\underline{h}$ the inner product for $L^2_N(\mathbb{R}) = \bigoplus_{i=1}^{N} L^2(\mathbb{R})$ is

$$[\underline{g},\underline{h}]_{L^2_N(\mathbb{R})} = \frac{1}{N}\sum_{j=1}^{N}\int_{\mathbb{R}} g_j(\xi)\,h_j(\xi)\,d\xi\ . \tag{3.56}$$

Using this inner product it is easy to show that $A^*_{\mu,N}$ is an adjoint of the operator $A_{\mu,N}: L^2(\mathbb{R}^2) \to L^2_N(\mathbb{R})$.

The results given in Theorems 3.6, 3.10, 3.11, and 3.12 used the attenuation function $a(x,y,-x\sin\theta+y\cos\theta,\theta)$ as a weight function in the spaces $L'(\mathbb{R}^2,a)$ and $L^2(\Omega,a)$. Since $a(x,y,-x\sin\theta+y\cos\theta,\theta)$ is a function of θ, we define a new weight function $\tilde{a}(x,y)$ which is independent of θ in order to generalize the results for a single projection angle to N projection angles $\theta_1,\ldots,\theta_N$:

$$\tilde{a}(x,y) = \max_{i=1,N}\{a(x,y,-x\sin\theta_i+y\cos\theta_i,\theta_i)\}\ . \tag{3.57}$$

The function $\tilde{a}(x,y)$ represents the minimum attenuation that photons emitted at (x,y) will experience for the N projection angles.

Now we can investigate a generalization of the single angle projection operator $R_{\mu,\theta}$ given in Eq. (3.49).

DEFINITION. For a set $\Omega \subseteq \mathbb{R}^2$ with characteristic function χ, the operators $R_{\mu,N}$ and $R^*_{\mu,N}$ are defined as follows

$$\text{(i)} \quad R_{\mu,N}:\rho \to (R_{\mu,\theta_1}\rho,\ R_{\mu,\theta_2}\rho,\ldots,\ R_{\mu,\theta_N}\rho) \tag{3.58}$$

$$\text{(ii)} \quad R^*_{\mu,N}:\underline{h} = (h_1,\ h_2,\ldots,\ h_N) \to (A^*_{\mu,N}\ \underline{h})(x,y)/\tilde{a}(x,y) \tag{3.59}$$

where R_{μ,θ_i} is given by Eq. (3.49).

We will use the notation $L^2_N(\hat{\chi}_\mu)$ to be the direct sum of the spaces $L^2(\hat{\Omega}_{\theta_i},\ \hat{\chi}_{\mu,\theta_i})$; that is,

$$L^2_N(\hat{\chi}_\mu) = L^2(\hat{\Omega}_{\theta_1},\ \hat{\chi}_{\mu,\theta_1}) \oplus \ldots \oplus L^2(\hat{\Omega}_{\theta_N},\ \hat{\chi}_{\mu,\theta_N})\ . \tag{3.60}$$

THEOREM 3.15. For any bounded open set $\Omega \subseteq \mathbb{R}^2$ the following are true

(i) $R_{\mu,N}$ maps $L^2(\Omega,\tilde{a})$ into $L^2_N(\hat{\chi}_\mu)$.

(ii) $R^*_{\mu,N}$ maps $L^2_N(\hat{\chi}_\mu)$ into $L^2(\Omega,\tilde{a})$.

PROOF. (i) Using Schwartz's inequality and the definition of $A_{\mu,\theta}$ in Eq. (3.16), we see for θ_i, i=1, N that

$$|(A_{\mu,\theta_i}\ \rho)(\xi)| = \Big|\int_{\Omega_{\xi,\theta_i}} \rho(\zeta,\xi)\ \chi(\zeta,\xi)\ a(\zeta,\xi,\theta_i)d\zeta\Big|$$

$$\leq \Big(\int |\rho(\zeta,\xi)|^2\ a(\zeta,\xi,\theta_i)d\zeta\Big)^{1/2}\ \Big(\int \chi(\zeta,\xi)\ a(\zeta,\xi,\theta_i)d\zeta\Big)^{1/2}$$

$$\leq \left(\int |\rho(\zeta,\xi)|^2\, a(\zeta,\xi,\theta_i)\, d\zeta\right)^{1/2} \left[\hat{\chi}_{\mu,\theta_i}(\xi)\right]^{1/2}.$$

Since $a(\zeta,\xi,\theta_i) \leq \tilde{a}(\zeta,\xi)$ where $\tilde{a}$ is given in Eq. (3.57),

$$|(A_{\mu,\theta_i}\rho)(\xi)| \leq \left(\int |\rho(\zeta,\xi)|^2\, \tilde{a}(\zeta,\xi)d\zeta\right)^{1/2} \left[\hat{\chi}_{\mu,\theta_i}(\xi)\right]^{1/2}.$$

This implies that for $\rho \in L^2(\Omega,\tilde{a})$

$$\int_{\hat{\Omega}_{\theta_i}} \left|\frac{(A_{\mu,\theta_i}\rho)(\xi)}{\hat{\chi}_{\mu,\theta_i}(\xi)}\right|^2 \hat{\chi}_{\mu,\theta_i}(\xi)d\xi \leq \left(\int|\rho(\zeta,\xi)|^2\, \tilde{a}(\zeta,\xi)d\zeta\right)^{1/2} < \infty .$$

Therefore $R_{\mu,\theta_i}\rho = A_{\mu,\theta_i}\rho/\hat{\chi}_{\mu,\theta_i} \in L^2(\hat{\Omega}_{\theta_i}, \hat{\chi}_{\mu,\theta_i})$ for i=1,N and $R_{\mu,N}$ maps $L^2(\Omega,\tilde{a})$ into $L^2_N(\hat{\chi}_\mu)$.

(ii) Using Schwartz's inequality and the definition of $R^*_{\mu,N}$ in Eq. (3.59) we have the following sequence of inequalities:

$$(R^*_{\mu,N}\underline{h})(x,y) = \frac{1}{N\,\tilde{a}(x,y)} \sum_{i=1}^{N} h_i(-x\sin\theta_i+y\cos\theta_i)\, a(x,y,-x\sin\theta_i+y\cos\theta_i,\theta_i)$$

$$\leq \frac{1}{N\,\tilde{a}(x,y)} \left\{\left(\sum_{i=1}^{N} h_i^2(-x\sin\theta_i+y\cos\theta_i)\, a(x,y,-x\sin\theta_i+y\cos\theta_i,\theta_i)\right)^{1/2}\right.$$

$$\left. \times \left(\sum_{i=1}^{N} a(x,y,-x\sin\theta_i+y\cos\theta_i,\theta_i)\right)^{1/2}\right\}$$

$$|(R^*_{\mu,N}\underline{h})(x,y)|^2\,\tilde{a}(x,y) \leq \frac{1}{N^2}\left\{\sum_{i=1}^{N} h_i^2(-x\sin\theta_i+y\cos\theta_i)a(x,y,-x\sin\theta_i+y\cos\theta_i,\theta_i)\right.$$

$$\left. \times \sum_{i=1}^{N} \frac{a(x,y,-x\sin\theta_i+y\cos\theta_i,\theta_i)}{\tilde{a}(x,y)}\right\} .$$

Since $a(x,y,-x\sin\theta_i+y\cos\theta_i,\theta_i) \leq \tilde{a}(x,y)$ we know that the second sum is less than or equal to N. Therefore

$$|(R^*_{\mu,N}\underline{h})(x,y)|^2\,\tilde{a}(x,y) \leq \frac{1}{N}\sum_{i=1}^{N} h_i^2(-x\sin\theta_i+y\cos\theta_i)a(x,y,-x\sin\theta_i+y\cos\theta_i,\theta_i).$$

Integrating over Ω and using Fubini's theorem, we have for $\underline{h} \in L^2_N(\hat{\chi}_\mu)$

$$\iint_\Omega |(R^*_{\mu,N}\underline{h})(x,y)|^2\,\tilde{a}(x,y)\,dxdy \leq \frac{1}{N}\sum_{i=1}^{N}\iint_\Omega h_i^2(\xi)\; a(\zeta,\xi,\theta_i)\,d\zeta d\xi$$

$$\leq \frac{1}{N}\sum_{i=1}^{N}\int h_i^2(\xi)\;\hat{\chi}_{\mu,\theta_i}(\xi)\,d\xi < \infty\ .$$

Therefore $R^*_{\mu,N}\,\underline{h} \in L^2(\Omega,\tilde{a})$. ||

THEOREM 3.16. For the operator $R_{\mu,N}: L^2(\Omega,\tilde{a}) \to L^2_N(\hat{\chi}_\mu)$ defined by Eq. (3.58) and the adjoint operator $R^*_{\mu,N}$ defined by Eq. (3.59), the operator $R^*_{\mu,N}\,R_{\mu,N}: \rho \to \beta$ where β is given by Eq. (3.4) with the kernel K given by

$$K(x',y'|x,y) =$$

$$\frac{\chi(x',y')\chi(x,y)}{N}\sum_{j=1}^{N}\frac{a(x,y,-x'\sin\theta_j+y'\cos\theta_j,\theta_j)a(x',y',-x'\sin\theta_j+y'\cos\theta_j,\theta_j)}{\hat{\chi}_{\mu,\theta_j}(-x'\sin\theta_j+y'\cos\theta_j)\;\tilde{a}(x',y')} \tag{3.61}$$

$$\times\,\delta(-(x'-x)\sin\theta_j+(y'-y)\cos\theta_j)\ .$$

PROOF. This follows immediately by evaluating $R^*_{\mu,N}\, R_{\mu,N}$ using Eqs. (3.58) and (3.59). ||

The operator $I_{\mu,N} = R_{\mu,N} \circ R^*_{\mu,N}$ is the composite of the adjoint and projection operations such that $I_{\mu,N}\, \underline{h}$ is an N-tuple with components given by

$$(I_{\mu,N}\, \underline{h})_j(\xi) = \frac{1}{N} \sum_{k=1}^{N} (R_{\mu,\theta_j}\, R^*_{\mu,\theta_k}\, h_k)(\xi) \ . \tag{3.62}$$

The next theorem gives the integral expression for the operator $I_{\mu,N}$

THEOREM 3.17. The operator $I_{\mu,N}$ is given as follows

$$(I_{\mu,N}\, \underline{h})_j(\xi) = \frac{1}{N} \sum_{k=1}^{N} (I_{\mu,jk}\, h_k)(\xi). \tag{3.63}$$

The operator $I_{\mu,jk}$ is defined by the integral equation

$$(I_{\mu,jj}\, h)(\xi) = \iint_{\Omega} \frac{h(-x\sin\theta_j + y\cos\theta_j)[a(x,y,\xi,\theta_j)]^2\, \delta(\xi + x\sin\theta_j - y\cos\theta_j)\,dxdy}{\hat{\chi}_{\mu,\theta_j}(\xi)\, \tilde{a}(x,y)} \tag{3.64}$$

and for $j \neq k$

$$(I_{\mu,jk}\, h)(\xi) = \int_{-\infty}^{\infty} h(\xi')\, I_{\mu,jk}(\xi|\xi')\,d\xi' \tag{3.65}$$

where

$$I_{\mu,jk}(\xi|\xi') = \frac{\Phi_{jk}(\xi,\xi')}{\hat{\chi}_{\mu,\theta_j}(\xi)|\sin(\theta_j-\theta_k)|\tilde{a}\left(\frac{\xi'\cos\theta_j-\xi\cos\theta_k}{\sin(\theta_j-\theta_k)}, \frac{\xi'\sin\theta_j-\xi\sin\theta_k}{\sin(\theta_j-\theta_k)}\right)}$$

$$\times \exp\left[-\int_{\zeta_0}^{\infty} \mu(-\xi\sin\theta_j+\zeta\cos\theta_j,\ \xi\cos\theta_j+\zeta\sin\theta_j)d\zeta\right.$$

$$\left.-\int_{\zeta_0'}^{\infty} \mu(-\xi'\sin\theta_k+\zeta'\cos\theta_k,\ \xi'\cos\theta_k+\zeta\sin\theta_k)d\zeta'\right] \tag{3.66}$$

and

$$\zeta_0 = \xi\cot(\theta_k-\theta_j) - \xi'\csc(\theta_k-\theta_j) \tag{3.67}$$

$$\zeta_0' = \xi\csc(\theta_k-\theta_j) - \xi'\cot(\theta_k-\theta_j) \tag{3.68}$$

$$\Phi_{jk}(\xi,\xi') = \begin{cases} 1 & \text{if } \ell(\xi,\theta_j)\cap\ell(\xi',\theta_k)\in\Omega \\ 0 & \text{otherwise} \end{cases} \tag{3.69}$$

$$\ell(\xi,\theta_j) = \{(x,y)|\xi+\sin\theta_j-y\cos\theta_j = 0\} \tag{3.70}$$

$$\ell(\xi',\theta_k) = \{(x,y)|\xi'+x\sin\theta_k-y\cos\theta_k = 0\}\ . \tag{3.71}$$

PROOF. The proof follows similar steps as given in the proof of Theorem 3.5. ‖

Figure 3.5, shows the lines $\ell(\xi,\theta_j)$ and $\ell(\xi',\theta_k)$ where $\theta_j = \theta$ and $\theta_k = \theta'$, and the coordinates ζ_0 (Eq. (3.67)) and ζ_0' (Eq. (3.68)) which satisfy $\zeta_0 = -d$ and $\zeta_0' = -d'$, respectively.

3.5 The Modified Attenuated Radon Transform

The attenuation factor in Eq. (3.17) can be rewritten so that the argument in the exponential is the sum of two integrals; namely the integral of the attenuation distribution from ζ to 0 plus the integral from 0 to ∞. If we let $G_\mu(\xi,\theta)$ be the latter integral:

$$G_\mu(\xi,\theta) = \exp\left[-\int_0^\infty \mu(-\xi\sin\theta+\zeta'\cos\theta,\ \xi\cos\theta+\zeta'\sin\theta)d\zeta'\right], \quad (3.72)$$

then we can rewrite Eq. (3.16) as

$$p_\gamma(\xi,\theta) = G_\mu(\xi,\theta)\int_{-\infty}^{\infty} \rho(-\xi\sin\theta+\zeta\cos\theta,\ \xi\cos\theta+\zeta\sin\theta)a(\zeta,\xi,\theta)d\zeta \quad (3.73)$$

where

$$a(\zeta,\xi,\theta) = \exp\left[\int_0^\zeta \mu(-\xi\sin\theta+\zeta'\cos\theta,\ \xi\cos\theta+\zeta'\sin\theta)d\zeta'\right]. \quad (3.74)$$

The factor $G_\mu(\xi,\theta)$ represents the integral of the attenuation distribution between the central axis and the detector. Note that the variable ζ in the limit for the integral may be positive or negative. Therefore for a positive function μ, the integral from 0 to ζ may be either positive or negative and the exponential in Eq. (3.74) multiplied by $G_\mu(\xi,\theta)$ is equivalent to the exponential factor given in Eq. (3.17).

Eliminating $G_\mu(\xi,\theta)$ from Eq. (3.73), we can define a modified attenuated Radon transform for a fixed attenuation distribution μ, to be the mapping $A_\mu:\rho \to p$ where

$$p(\xi,\theta) = \int_{-\infty}^{\infty} \rho(-\xi\sin\theta+\zeta\cos\theta,\ \xi\cos\theta+\zeta\sin\theta)\ a(\zeta,\xi,\theta)d\zeta \qquad (3.75)$$

and $a(\zeta,\xi,\theta)$ is given in Eq. (3.74). Thus the modified attenuated projections $(A_\mu\ \rho)(\xi,\theta)$ and the measured attenuated projections $(A_\mu\ \rho)(\xi,\theta)$ are related by

$$(A_\mu\ \rho)(\xi,\theta) = G_\mu(\xi,\theta)\ A_\mu\ \rho(\xi,\theta). \qquad (3.76)$$

A transform such as A_μ is appealing to work with since it is independent of any sort of detector geometry and gives for a particular θ and ξ an attenuation factor a which is only dependent on the coordinate ζ whose absolute value is the distance from the central rotation axis. One can think of the detector as being placed at the center of rotation in the coordinate system shown in Fig. 2.6. Photons emitted left of the detector will be attenuated as usual with a reduction in the measured number; whereas photons emitted right of the detector will be increased in number as if they were experiencing a negative attenuation coefficient.

The following are equivalent definitions for the attenuated Radon transform A:

1. $$p(\xi,\theta) = \iint \rho(x,y)\ a(x,y,\xi,\theta)\ \delta(\xi+x\sin\theta-y\cos\theta)dxdy \qquad (3.75a)$$

where

$$a(x,y,\xi,\theta) = \exp\left[\int_0^y \int_0^x \mu(x,y)\ \delta(\xi+x'\sin\theta-y'\cos\theta)dx'dy'\right] \qquad (3.74a)$$

or

$$a(x,y,\xi,\theta) = \exp\left[\int_0^{x\cos\theta+y\sin\theta} \mu(-\xi\sin\theta+\zeta'\cos\theta,\ \xi\cos\theta+\zeta'\sin\theta)d\zeta'\right] \tag{3.74b}$$

2. $$p(\xi,\theta) = \int_{r=|\xi|}^{\infty} \left\{\rho\{r,\theta+\pi/2+\cos^{-1}(\xi/r)\} \exp\left[-\int_0^r \mu\{s,\theta+\pi/2+\cos^{-1}(\xi/s)\}\right.\right.$$

$$\left.\times \frac{s\ ds}{\sqrt{s^2-\xi^2}}\right] + \rho\{r,\theta+\pi/2-\cos^{-1}(\xi/r)\}$$

$$\left.\times \exp\left[\int_0^r \mu\{t,\theta+\pi/2-\cos^{-1}(\xi/t)\}\frac{t\ dt}{\sqrt{t^2-\xi^2}}\right]\right\}\frac{r\ dr}{\sqrt{r^2-\xi^2}} \tag{3.75b}$$

3. $$p(\xi,\theta) = \int_{-\infty}^{\infty} \rho(\xi\underset{\sim}{\theta}+\zeta\underset{\sim}{\theta}^{\perp}) \exp\left[\int_0^{\zeta} \mu(\xi\underset{\sim}{\theta}+\zeta'\underset{\sim}{\theta}^{\perp})d\zeta'\right] d\zeta \tag{3.75c}$$

where $\underset{\sim}{\theta} = (-\sin\theta, \cos\theta)$ and $\underset{\sim}{\theta}^{\perp} = (\cos\theta, \sin\theta)$.

The results which were proven for the attenuated Radon transform for the single angle projection operator and the N-fold operator also apply for the modified attenuated Radon transform. All one needs to do is replace the attenuation function $a(x,y,\xi,\theta)$ with the attenuation function $a(x,y,\xi,\theta)$. The important case when the modified attenuated Radon transform has interesting properties is when the attenuation coefficient distribution is constant. These results will be investigated in Section 3.5.4.

The following two theorems give the shift properties for the modified attenuated Radon transform similar to those given for the attenuated Radon transform in Theorems 3.1 and 3.2.

THEOREM 3.18. The modified attenuated Radon transform of $\rho(x+a, y+b)$ with respect to the attenuation coefficient distribution $\mu(x+a, y+b)$ is

$$A\{\rho(x+a, y+b), \mu(x+a, y+b); \xi,\theta\} = A\{\rho(x,y), \mu(x,y); \xi',\theta\}$$

$$\times \exp\left[-\int_0^{a\cos\theta+b\sin\theta} \mu(-\xi'\sin\theta+\zeta'\cos\theta, \xi'\cos\theta+\zeta'\sin\theta)d\zeta'\right] \qquad (3.77)$$

where $\xi' = \xi - a\sin\theta + b\cos\theta$.

PROOF. The modified attenuated Radon transform of $\rho(x+a, y+b)$ for the attenuation distribution $\mu(x+a, y+b)$ is

$$A\{\rho(x+a, y+b, \mu(x+a, y+b); \xi,\theta\} = \int_{-\infty}^{\infty} \rho(-\xi\sin\theta+\zeta\cos\theta+a, \xi\cos\theta+\zeta\sin\theta+b)$$

$$\times \exp\left[\int_0^{\zeta} \mu(-\xi\sin\theta+\zeta'\cos\theta+a, \xi\cos\theta+\zeta'\sin\theta+b)d\zeta'\right] d\zeta. \qquad (3.78)$$

Let $\xi' = \xi - a\sin\theta + b\cos\theta$, then we can rewrite Eq. (3.78) as

$$A\{\rho(x+a,\ y+b),\ \mu(x+a,y+b);\ \xi,\theta\} =$$

$$\int_{-\infty}^{\infty} \rho\{-\xi'\sin\theta+(\zeta+a\cos\theta+b\sin\theta)\cos\theta,\ \xi'\cos\theta+(\zeta+a\cos\theta+b\sin\theta)\sin\theta\}$$

$$\times \exp\left[\int_{0}^{\zeta} \mu\{-\xi'\sin\theta+(\zeta'+a\cos\theta+b\sin\theta)\cos\theta,\xi'\cos\theta+(\zeta'+a\cos\theta+b\sin\theta)\sin\theta\}d\zeta'\right] d\zeta$$

Making the further change of variables

$$u = \zeta + a\cos\theta + b\sin\theta$$

$$u' = \zeta' + a\cos\theta + b\sin\theta$$

gives

$$A\{\rho(x+a,\ y+b),\ \mu(x+a,\ y+b);\ \xi,\theta\} = \int_{-\infty}^{\infty} \rho(-\xi'\sin\theta+u\cos\theta,\ \xi'\cos\theta+u\sin\theta)$$

$$\times \exp\left[\int_{a\cos\theta+b\sin\theta}^{u} \mu(-\xi'\sin\theta+u'\cos\theta,\ \xi'\cos\theta+u'\sin\theta)du'\right] du. \tag{3.79}$$

By integrating from 0 to u in the integral of the exponential term, we can rewrite Eq. (3.79) as

$$A\{\rho(x+a,\ y+b),\ \mu(x+a,\ y+b);\ \xi,\theta\}$$

$$= \int_{-\infty}^{\infty} \rho(-\xi'\sin\theta+u\cos\theta,\ \xi'\cos\theta+u\sin\theta)$$

$$\times \exp\left[\int_{0}^{u} \mu(-\xi'\sin\theta+u'\cos\theta,\ \xi'\cos\theta+u'\sin\theta)du'\right] du$$

$$\times \exp\left[-\int_{0}^{a\cos\theta+b\sin\theta} \mu(-\xi'\sin\theta+u'\cos\theta,\ \xi'\cos\theta+u'\sin\theta)du'\right]$$

$$= A\{\rho(x,y),\ \mu(x,y);\ \xi',\theta\}$$

$$\times \exp\left[-\int_{0}^{a\cos\theta+b\sin\theta} \mu(-\xi'\sin\theta+u'\cos\theta,\ \xi'\cos\theta+u'\sin\theta)du'\right]. \quad \|$$

THEOREM 3.19. The modified attenuated Radon transform A_μ of $\rho(x+a, y+b)$ is

$$A\{\rho(x+a,y+b), \mu(x,y); \xi,\theta\} = A\{\rho(x,y), \mu(x-a,y-b); \xi',\theta\}$$

$$\times \exp\left[-\int_0^{a\cos\theta+b\sin\theta} \mu(-\xi'\sin\theta+\zeta'\cos\theta-a,\ \xi'\cos\theta+\zeta'\sin\theta-b)d\zeta'\right] \qquad (3.80)$$

where $\xi' = \xi - a\sin\theta + b\cos\theta$.

PROOF. This proof follows similar steps as those given for the proof of Theorem 3.18, except the attenuation distribution $\mu(x+a, y+b)$ is replaced with $\mu(x,y)$. ||

When Theorems 3.18 and 3.19 are compared with the corresponding theorems for the attenuated Radon transform (Theorems 3.1 and 3.2), one can see that for the modified attenuated Radon transform there is an extra exponential factor which must multiply the transform of the unshifted isotope concentration distribution.

3.5.1 Adjoint and Back-Projection Operators

The adjoint transform for the modified attenuated Radon transform which maps $L^2(\mathbb{R}^2,W)$ into $L^2(\mathbb{C},w)$ is a mapping $A_\mu^*: L^2(\mathbb{C},w) \to L^2(\mathbb{R}^2,W)$ given by

$$(A_\mu^* \rho)(x,y) =$$

$$\frac{1}{W(x,y)} \int_0^{2\pi} p(-x\sin\theta+y\cos\theta,\theta)\tilde{a}(x,y,-x\sin\theta+y\cos\theta,\theta)w(-x\sin\theta+y\cos\theta,\theta)d\theta \qquad (3.81)$$

where

$$a(x,y,-x\sin\theta+y\cos\theta,\theta) = \exp\left[\int_0^{x\cos\theta+y\sin\theta} \mu(x\sin^2\theta-y\cos\theta\sin\theta+\zeta'\cos\theta,-x\sin\theta\cos\theta+y\cos^2\theta+\zeta'\sin\theta)d\zeta'\right] \tag{3.82}$$

The back-projection operator $\mathcal{B}_\mu$ which operates on $L^2(\mathbb{C},w)$ is defined by

$$(\mathcal{B}_\mu\, p)(x,y) = \int_0^{2\pi} p(-x\sin\theta+y\cos\theta,\theta)/a(x,y,-x\sin\theta+y\cos\theta,\theta)d\theta. \tag{3.83}$$

The adjoint operator and the back-projection operator for the modified attenuated Radon transform differ from the corresponding operators for the attenuated Radon transform only in the limits of integration for the integral in the exponential factor in Eq. (3.82). (Compare Eq. (3.82) and Eq. (3.23)).

3.5.2 The Composite of the Projection and Back-Projection Operators

The operator $A_\mu^* A_\mu$ restricted to the space $R(A_\mu^*) = N(A_\mu)^\perp$ is a one-to-one and onto mapping of $N(A_\mu)^\perp$ onto itself if the space $R(A_\mu)$ is closed. For the modified attenuated Radon transform A_μ, the operator $A_\mu^* A_\mu$: $\rho \to \beta$ is defined by

$$\beta(x',y') = \iint \rho(x,y)\, K(x',y'|x,y)dxdy \tag{3.84}$$

where the kernel K is given by the following theorem.

THEOREM 3.20. For the modified attenuated Radon transform $A_\mu: L^2(\mathbb{R}^2,W) \to L^2(\mathbb{C},w)$ defined by Eq. (3.75) and the adjoint operator A_μ^* defined by Eq. (3.81) and $w(\xi,\theta)$ independent of θ and satisfying $w(\xi) = w(-\xi)$, the operator $A_\mu^* A_\mu: \rho \to \beta$ maps ρ into β where β is given by Eq. (3.84) with the kernel K given by

$$K(x',y'|x,y) = \frac{\widetilde{K}(x',y'|x,y)}{W(x',y')} \; w\left(\frac{xy'-yx'}{\|\hat{x}-\hat{x}'\|}\right) \tag{3.85}$$

where

$$\widetilde{K}(x',y'|x,y) = \frac{2}{\|\hat{x}-\hat{x}'\|} \cosh\left\{\int_0^d \mu(b+\zeta'e,c+\zeta'f)d\zeta' + \int_0^{d'} \mu(b+\zeta'e,c+\zeta'f)d\zeta'\right\}, \tag{3.86}$$

and d, d', b, c, e, f are given by Eqs. (3.28) - (3.33).

PROOF. The proof involves doing similar calculations to that given for the attenuated Radon transform in Theorem 3.3. ||

The kernel function for the modified attenuated Radon transform has a simpler expression than does the attenuated Radon transform given in Eq. (3.27). This is due to the parity relationship in the argument of the exponential function for the attenuation function a (i.e., $\exp\{\int_0^\zeta \mu(\zeta',\xi,\theta)d\zeta'\} = \exp\{-\int_0^\zeta \mu(\zeta',\xi,\theta+\pi)d\zeta'\}$).

The integrals in the argument of the hyperbolic cosine function in Eq. (3.86) are line integrals from the point (b,c) to $\hat{x}$ and $\hat{x}'$, respectively, in the direction of the unit vector (e,f). These points and vectors are illustrated in Fig. 3.6.

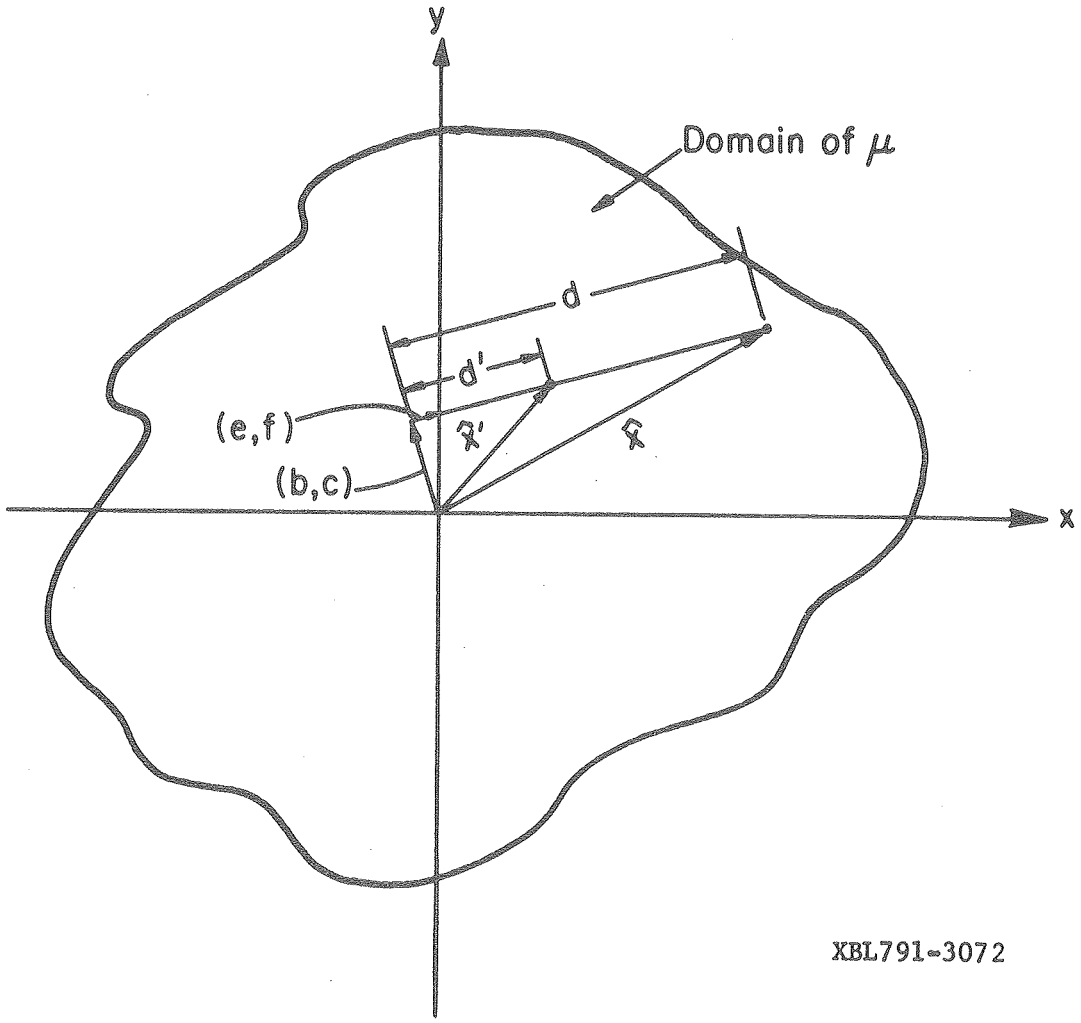

Figure 3.6. The integrals in the argument of the hyperbolic cosine of Eq. (3.86) are line integrals from the point (b,c) to the points $\hat{x}$ and $\hat{x}'$. The distances in the direction of the unit vector (e,f) from the point (b,c) to the points $\hat{x}$ and $\hat{x}'$ are equal to d and d', respectively.

THEOREM 3.21. For the back-projection operator B_μ defined by Eq. (3.83), the operator $B_\mu A_\mu : \rho \to \beta$ maps ρ into β where β is given by Eq. (3.84) with the kernel given by

$$K(x',y'|x,y) = \frac{2}{\|\hat{x}-\hat{x}'\|} \cosh\left\{\int_{d'}^{d} \mu(b+\zeta' e,\ c+\zeta' f)\ d\zeta'\right\} \tag{3.87}$$

and d, d', b, c, e, f are given by Eqs. (3.28) - (3.33).

PROOF. The proof involves doing similar calculations as those given for the attenuated Radon transform in Theorem 3.4. ||

The kernel function for the attenuated Radon transform given in Theorem 3.4 is precisely the same as that given above for the modified attenuated Radon transform.

3.5.3 The Composite of the Back-Projection and Projection Operators

The operator $A_\mu A_\mu^*$ is a one-to-one and onto mapping of $N(A_\mu^*)^\perp$ onto itself if $R(A_\mu)$ is closed. For the modified attenuated Radon transform A_μ, the operator $A_\mu A_\mu^*$: $p \to g$ is given by

$$g(\xi,\theta) = \iint p(\xi',\theta')\ I(\xi,\theta|\xi',\theta')d\xi'd\theta' \tag{3.88}$$

where the kernel I is given by the following theorem.

THEOREM 3.22. For the modified attenuated Radon transform $A_\mu : L^2(\mathbb{R}^2,W) \to L^2(\mathbb{C},w)$ defined by Eq. (3.75) and the adjoint operator A_μ^* defined by Eq. (3.81), the operator $A_\mu A_\mu^*$: $p \to g$ maps p into g where g is given by Eq. (3.88) with the kernel I given by

$$I(\xi,\theta|\xi',\theta') = \frac{\tilde{I}(\xi,\theta|\xi',\theta')\ w(\xi',\theta')}{W\left(\frac{\xi'\cos\theta-\xi\cos\theta'}{\sin(\theta-\theta')}\ ,\ \frac{\xi'\sin\theta-\xi\sin\theta'}{\sin(\theta-\theta')}\right)}$$

where

$$\tilde{I}(\xi,\theta|\xi',\theta') = \frac{1}{|\sin(\theta-\theta')|}\ \exp\left[\int_0^{\zeta_0}\mu(-\xi\sin\theta+\zeta\cos\theta,\xi\cos\theta+\zeta\sin\theta)d\zeta\right.$$

$$\left.+\int_0^{\zeta_0'}\mu(-\xi'\sin\theta'+\zeta'\cos\theta',\ \xi'\cos\theta'+\zeta'\sin\theta')d\zeta'\right] \qquad (3.89)$$

and

$$\zeta_0 = \xi\cot(\theta'-\theta) - \xi'\csc(\theta'-\theta) \qquad (3.90)$$

$$\zeta_0' \quad \xi\csc(\theta'-\theta) - \xi'\cot(\theta'-\theta) \qquad (3.91)$$

PROOF. The proof involves doing similar calculations as those given for the attenuated Radon transform in Theorem 3.5. ‖

The points ζ_0 and ζ_0' one illustrated in Fig. 3.5.

3.5.4 Constant Attenuation Coefficient

For constant attenuation coefficient, the attenuation function a in Eq. (3.74b) reduces to

$$a(x,y,\xi,\theta) = \exp[\mu(x\cos\theta + y\sin\theta)]\ . \qquad (3.92)$$

and the mapping $A_\mu:\rho \to p$ given by Eq. (3.75a) reduces to

$$p(\xi,\theta) = \iint\rho(x,y)\ \exp[\mu(x\cos\theta+y\sin\theta)]\ \delta(\xi+x\sin\theta-y\cos\theta)dxdy \qquad (3.93)$$

where μ is the constant attenuation coefficient.

The following are equivalent definitions for the constant attenuated Radon transform:

$$1.\quad p(\xi,\theta) = \int \rho(-\xi\sin\theta+\zeta\cos\theta,\ \xi\cos\theta+\zeta\sin\theta)e^{\mu\zeta}\,d\zeta \tag{3.93a}$$

$$2.\quad p(\xi,\theta) = \int_{r=|\xi|}^{\infty} \left[\rho\{r,\theta+\pi/2+\cos^{-1}(\xi/r)\}e^{-\mu\sqrt{r^2-\xi^2}} + \rho\{r,\theta+\pi/2-\cos^{-1}(\xi/r)\}\ e^{\mu\sqrt{r^2-\xi^2}}\right]\frac{rdr}{\sqrt{r^2-\xi^2}} \tag{3.93b}$$

$$3.\quad p(\xi,\theta) = \int\rho(\hat{x})\ e^{\mu\langle\underset{\sim}{\theta}^{\perp},\hat{x}\rangle}\ \delta\{\xi - \langle\underset{\sim}{\theta},\hat{x}\rangle\}\,d\hat{x} \tag{3.93c}$$

where

$$\underset{\sim}{\theta} = (-\sin\theta,\ \cos\theta)$$
$$\underset{\sim}{\theta}^{\perp} = (\cos\theta,\ \sin\theta)$$
$$\hat{x} = (x,y)$$

and $\langle\underset{\sim}{\theta},\hat{x}\rangle$ denotes the inner product.

$$4.\quad p(\xi,\theta) = \int\rho(\xi\underset{\sim}{\theta}+\zeta\underset{\sim}{\theta}^{\perp})e^{\mu\zeta}\,d\zeta \tag{3.93d}$$

3.5.4.1 Examples

Example 1. If we expanded $\rho(x,y)$ in a Fourier series

$$\rho(x,y) = \sum_n \rho_n(r)\ e^{in\theta}\ , \tag{3.94}$$

then the projection function for the constant attenuated Radon transform has the equation

$$p(\xi,\theta) = \sum_n \sigma_n(\xi)\, e^{in(\theta+\pi/2)} \tag{3.95}$$

where $\sigma_n(\xi)$ has the following equivalent expressions:

$$\text{a)}\quad \sigma_n(\xi) = 2 \int_{r=|\xi|}^{\infty} \rho_n(r) \left\{ T_n(\xi/r)\, \cosh(\mu\sqrt{r^2-\xi^2}\,) - i\sqrt{1 - T_n^2(\xi/r)}\, \sinh(\mu\sqrt{r^2-\xi^2}\,) \right\} \frac{r\, dr}{\sqrt{r^2-\xi^2}} \tag{3.96}$$

$$\text{b)}\quad \sigma_n(\xi) = 2 \int_{r=|\xi|}^{\infty} \rho_n(r)\, T_n(\xi/r)\, \cosh(\mu\sqrt{r^2-\xi^2})\, \frac{r\, dr}{\sqrt{r^2-\xi^2}}$$

$$- 2i \int_{r=|\xi|}^{\infty} \rho_n(r)\, U_{n-1}(\xi/r)\, \sinh(\mu\sqrt{r^2-\xi^2})\, \frac{r\, dr}{\sqrt{r^2-\xi^2}} \tag{3.97}$$

$$\text{c)}\quad \sigma_n(\xi) = 2 \int_{r=|\xi|}^{\infty} \rho_n(r) \cosh\left[\mu\sqrt{r^2-\xi^2} - in \cos^{-1}(\xi/r) \right] \frac{r\, dr}{\sqrt{r^2-\xi^2}} \tag{3.98}$$

where $T_n(x)$ and $U_n(x)$ are the Tchebycheff polynomials of the first and second kind, respectively. For variable attenuation distributions Ansari and Wee (1977) have shown that σ_n can be represented as a Voltera integral equation of the first kind with a singular kernel.

We will use the expression given in Eq. (3.93b) for the constant attenuated Radon transform to show these results. Substituting Eq. (3.94) into Eq. (3.93b) gives the following expressions:

$$p(\xi,\theta) = \int_{r=|\xi|}^{\infty} \left\{ \sum_n \rho_n(r)\, e^{in[\theta+\pi/2+\cos^{-1}(\xi/r)]}\, e^{-\mu\sqrt{r^2-\xi^2}} \right.$$

$$\left. + \sum_n \rho_n(r)\, e^{in[\theta+\pi/2-\cos^{-1}(\xi/r)]}\, e^{\mu\sqrt{r^2-\xi^2}} \right\} \frac{r\, dr}{\sqrt{r^2-\xi^2}}$$

$$= \int_{r=|\xi|}^{\infty} \left\{ \sum_n \rho_n(r) e^{in\pi/2} \left[\cos\{n\theta+n\cos^{-1}(\xi/r)\} + i\sin\{n\theta+n\cos^{-1}(\xi/r)\} \right] e^{-\mu\sqrt{r^2-\xi^2}} \right.$$

$$\left. + \sum_n \rho_n(r)\, e^{in\pi/2} \left[\cos\{n\theta-n\cos^{-1}(\xi/r)\} + i\sin\{n\theta-n\cos^{-1}(\xi/r)\} \right] e^{\mu\sqrt{r^2-\xi^2}} \right\} \frac{r\, dr}{\sqrt{r^2-\xi^2}}$$

$$= \int_{r=|\xi|}^{\infty} \left\{ \sum_n \rho_n(r)\, e^{in\pi/2} \left[\cos n\theta \cos\{n\cos^{-1}(\xi/r)\} - \sin n\theta \sin\{n \cos^{-1}(\xi/r)\} \right.\right.$$

$$\left. + i\sin n\theta \cos\{n\cos^{-1}(\xi/r)\} + i\sin\{\cos^{-1}(\xi/r)\}\cos n\theta \right] e^{-\mu\sqrt{r^2-\xi^2}}$$

$$+ \sum_n \rho_n(r)\, e^{in\pi/2} \left[\cos n\theta \cos\{n\cos^{-1}(\xi/r)\} + \sin n\theta \sin\{n\cos^{-1}(\xi/r)\} \right.$$

$$\left.\left. + i\sin n\theta \cos\{n\cos^{-1}(\xi/r)\} - i\sin\{n\cos^{-1}(\xi/r)\}\cos n\theta \right] e^{\mu\sqrt{r^2-\xi^2}} \right\} \frac{r\, dr}{\sqrt{r^2-\xi^2}}$$

$$= \int_{r=|\xi|}^{\infty} \left\{ \sum_n \rho_n(r) e^{in\pi/2} \left[2\cos n\theta \; T_n(\xi/r) \; \cosh(\mu\sqrt{r^2-\xi^2}) \right.\right.$$

$$+ 2i \sin n\theta \; T_n(\xi/r) \; \cosh(\mu\sqrt{r^2-\xi^2}) + 2 \sin n\theta \; \sin\{n\cos^{-1}(\xi/r)\}\sinh(\mu\sqrt{r^2-\xi^2})$$

$$\left.\left. - 2i \cos n\theta \; \sin\{n \cos^{-1}(\xi/r)\}\sinh(\mu\sqrt{r^2-\xi^2}) \right] \right\} \frac{r \, dr}{\sqrt{r^2-\xi^2}} \; .$$

Therefore

$$p(\xi,\theta) = \sum_n 2e^{in(\theta+\pi/2)} \int_{r=|\xi|}^{\infty} \rho_n(r) \left\{ T_n(\xi/r) \; \cosh(\mu\sqrt{r^2-\xi^2}) \right.$$

$$\left. - i\sqrt{1-T_n^2(\xi/r)} \; \sinh(\sqrt{r^2-\xi^2}) \right\} \frac{r \, dr}{\sqrt{r^2-\xi^2}} \; .$$

The expression in Eq. (3.97) follows immediately from the relation $U_{n-1}(x) = \sin(n \cos^{-1} x)/(1 - x^2)^{1/2}$, $0 < x < 1$. The expression in Eq. (3.98) follows immediately from the relations $\cosh(x+y) = \cosh x \cosh y + \sinh x \sinh y$ and $\cosh ix = \cos x$.

If we add projections 180° apart, we get $p(\xi,\theta) + p(-\xi,\theta+\pi) = \sum_n \tilde{\sigma}_n(\xi) \; e^{in(\theta+\pi/2)}$

where

$$\tilde{\sigma}_n(\xi) = 4 \int_{r=|\xi|}^{\infty} \rho_n(r) \; T_n(\xi/r) \; \cosh(\mu\sqrt{r^2-\xi^2}) \; \frac{r \, dr}{\sqrt{r^2-\xi^2}} \; .$$

Example 2. For the Hermite polynomials $H_m(x)$ and $H_n(y)$, the constant attenuated Radon transform of the function

$$\rho(x,y) = H_m(x)\, H_n(y)\, e^{-x^2-y^2} \tag{3.99}$$

is

$$p(\xi,\theta) =$$

$$\pi^{1/2} e^{-\xi^2} e^{\mu^2/4} \sum_{k=0}^{n} \sum_{\ell=0}^{m} (-1)^{m-\ell} \binom{n}{k}\binom{m}{\ell} H_{n+m-k-\ell}(\xi)\, \mu^{k+\ell} (\cos\theta)^{n-k+\ell} (\sin\theta)^{m-\ell+k}. \tag{3.100}$$

For $\theta=0$

$$p(\xi,\theta) = (-1)^m\ \pi^{1/2}\ e^{-\xi^2}\ e^{\mu^2/4}\ \mu^m\ H_n(\xi)$$

This is shown by substituting Eq. (3.99) into Eq. (3.93a) giving

$$p(\xi,\theta) = \int_{-\infty}^{\infty} H_m(-\xi\sin\theta+\zeta\cos\theta)\, H_n(\xi\cos\theta+\zeta\sin\theta) e^{-\xi^2-\zeta^2}\ e^{\mu\zeta}\ d\zeta.$$

Using the generating functions for the Hermite polynomials $H_m(x)$ and $H_n(y)$,

$$e^{-t^2+2tx} = \sum_{m=0}^{\infty} H_m(x)\ \frac{t^m}{m!}$$

$$e^{-s^2+2sy} = \sum_{n=0}^{\infty} H_n(y)\ \frac{s^n}{n!}\ ,$$

we obtain the expression

$$\sum_{m=0}^{\infty}\sum_{n=0}^{\infty} \frac{t^m}{m!}\frac{s^n}{n!} \int_{-\infty}^{\infty} H_m(-\xi\sin\theta+\zeta\cos\theta)\, H_n(\xi\cos\theta+\zeta\sin\theta) e^{-\xi^2-\zeta^2}\, e^{\mu\zeta}\, d\zeta$$

$$= \int_{-\infty}^{\infty} e^{-t^2+2t(-\xi\sin\theta+\zeta\cos\theta)}\, e^{-s^2+2s(\xi\cos\theta+\zeta\sin\theta)}\, e^{-\xi^2-\zeta^2}\, e^{\mu\zeta}\, d\zeta\ .$$

Collecting terms involving ζ and completing the square, we can rewrite the second integral so that

$$\sum_{m=0}^{\infty}\sum_{n=0}^{\infty} \frac{t^m}{m!}\ \frac{s^n}{n!}\ p(\xi,\theta) =$$

$$e^{-\xi^2}\ \exp[-t^2-s^2-2t\xi\sin\theta+2s\xi\cos\theta+(t\cos\theta+s\sin\theta+\mu/2)^2]$$

$$\times \int_{-\infty}^{\infty} \exp[-\zeta^2+2\zeta(t\cos\theta+s\sin\theta+\mu/2) - (t\cos\theta+s\sin\theta+\mu/2)^2]d\zeta$$

$$= \pi^{1/2}e^{-\xi^2}\ \exp[-t^2-s^2-2t\xi\sin\theta+2s\xi\cos\theta+(t\cos\theta+s\sin\theta+\mu/2)^2]$$

$$= \pi^{1/2}e^{-\xi^2}e^{\mu^2/4}\ \exp[-(-t\sin\theta+s\cos\theta)^2+2\xi(-t\sin\theta+s\cos\theta)]\exp[\mu(t\cos\theta+s\sin\theta)]$$

$$= \pi^{1/2}e^{-\xi^2}e^{\mu^2/4} \sum_{n=0}^{\infty} H_n(\xi)\ \frac{(-t\sin\theta+s\cos\theta)^n}{n!} \sum_{m=0}^{\infty} \mu^m\ \frac{(t\cos\theta+s\sin\theta)^m}{m!}$$

$$= \pi^{1/2}e^{-\xi^2}e^{\mu^2/4} \sum_{n=0}^{\infty} \frac{H_n(\xi)}{n!} \sum_{k=0}^{n} (-1)^k \binom{n}{k} s^{n-k}(\cos\theta)^{n-k}\ t^k(\sin\theta)^k$$

$$\times \sum_{m=0}^{\infty} \frac{\mu^m}{m!} \sum_{\ell=0}^{m} \binom{m}{\ell} s^{m-\ell}(\sin\theta)^{m-\ell}\ t^{\ell}(\cos\theta)^{\ell}\ .$$

If we let n-k = v, k = w, m-ℓ = a and ℓ = b we can rewrite

$$\sum_{m=0}^{\infty}\sum_{n=0}^{\infty} \frac{t^m}{m!} \frac{s^n}{n!} p(\xi,\theta) =$$

$$\pi^{1/2} e^{-\xi^2} e^{\mu^2/4} \sum_{v=0}^{\infty}\sum_{w=0}^{\infty}\sum_{a=0}^{\infty}\sum_{b=0}^{\infty} (-1)^w \frac{H_{v+w}(\xi)}{v!\ w!} \frac{\mu^{a+b}}{a!b!} s^{v+a} t^{w+b} (\cos\theta)^{v+b} (\sin\theta)^{w+a}.$$

Next make a change of variables v+a = p, w+b = q, a = c, b = d, then

$$\sum_{m=0}^{\infty}\sum_{n=0}^{\infty} \frac{t^m}{m!} \frac{s^n}{n!} p(\xi,\theta) =$$

$$\pi^{1/2} e^{-\xi^2} e^{\mu^2/4} \sum_{p=0}^{\infty}\sum_{q=0}^{\infty}\sum_{c=0}^{\infty}\sum_{d=0}^{\infty} (-1)^{q-d} \frac{H_{p+q-c-d}(\xi)}{(p-c)!(q-d)!c!d!} \times$$

$$\mu^{c+d} s^p t^q (\cos\theta)^{p-c+d} (\sin\theta)^{q-d+c} .$$

Equating the coefficients of $t^m s^n$ gives

$$\begin{aligned} & p(\xi,\theta) \\ &= \pi^{1/2} e^{-\xi^2} e^{\mu^2/4}\ n!\, m! \sum_{k=0}^{n}\sum_{\ell=0}^{m} (-1)^{m-\ell} \frac{H_{n+m-k-\ell}(\xi)\mu^{k+\ell}}{(n-k)!(m-\ell)!k!\ell!} \\ &\qquad \times (\cos\theta)^{n-k+\ell} (\sin\theta)^{m-\ell+k} \\ &= \pi^{1/2} e^{-\xi^2} e^{\mu^2/4} \sum_{k=0}^{n}\sum_{\ell=0}^{m} (-1)^{m-\ell} \binom{n}{k}\binom{m}{\ell} H_{n+m-k-\ell}(\xi)\ \mu^{k+\ell} \\ &\qquad \times (\cos\theta)^{n-k-\ell} (\sin\theta)^{m-\ell+k}. \end{aligned} \tag{3.100}$$

For $\theta = 0$ Eq. (3.100) reduces to

$$p(\xi,\theta) = (-1)^m \pi^{1/2} e^{-\xi^2} e^{\mu^2/4} \mu^m H_n(\xi).$$

The sum of projections 180° apart gives

$$p(\xi,\theta) + p(-\xi,\theta+\pi) = 2\pi^{1/2} e^{-\xi^2} e^{\mu^2/4} (-1)^m \sum_{k=0}^{n} \sum_{\ell=0}^{m} (-1)^{k+\ell} \binom{n}{k}\binom{m}{\ell}$$

$$\times H_{n+m-k-\ell}(\xi) \mu^{k+\ell} (\cos\theta)^{n-k+\ell} (\sin\theta)^{m-\ell+k} .$$

3.5.4.2 Properties

Theorems 3.23 - 3.25 will prove some properties for the modified attenuated Radon transform with constant attenuation which are similar to those proven by I. M. Gel'fand and co-workers (1966) for the Radon transform. These properties will be proven using the definition given in Eq (3.93c).

THEOREM 3.23. Let U be an orthogonal transformation. For constant attenuation the modified attenuated Radon transform of $\rho_U(\hat{x}) = \rho(U^T \hat{x})$ satisfies

$$A\{\rho_U(\hat{x}), \mu; \xi,\underset{\sim}{\theta}\} = A\{\rho(\hat{x}), \mu; \xi, U^T \underset{\sim}{\theta}\}.$$

PROOF. For constant attenuation the modified attenuated Radon transform operating on $\rho_U(\hat{x})$ gives

$$A\{\rho_U(\hat{x}), \mu;\xi,\underset{\sim}{\theta}\} = \int \rho(U^T \hat{x}) e^{\mu\langle \underset{\sim}{\theta}^{\perp},\hat{x}\rangle} \delta\{\xi - \langle \underset{\sim}{\theta},\hat{x}\rangle\} d\hat{x} .$$

Let $\hat{x} = U\hat{x}'$, then $\hat{x}' = U^T\hat{x}$ and

$$A\{\rho_U(\hat{x}),\mu;\xi,\underset{\sim}{\theta}\} = \int \rho(\hat{x}')e^{\mu\langle\underset{\sim}{\theta}^{\perp},U\hat{x}'\rangle}\ \delta\{\xi-\langle\underset{\sim}{\theta},U\hat{x}'\rangle\}|\det U|d\hat{x}' \ .$$

Since $\langle \hat{x}, U\hat{x}'\rangle = \langle U^T\hat{x}, \hat{x}'\rangle$ and for orthogonal matrices $|\det U| = 1$, we have

$$A\{\rho_U(\hat{x}),\mu;\xi,\underset{\sim}{\theta}\} = \int \rho(\hat{x}')\ e^{\mu\langle U^T\underset{\sim}{\theta}^{\perp},\hat{x}'\rangle}\ \delta\{\xi - \langle U^T\underset{\sim}{\theta}, \hat{x}'\rangle\}d\hat{x}' \ .$$

Since U is an orthogonal transformation, we know that $U^T\underset{\sim}{\theta}^{\perp} = (U^T\underset{\sim}{\theta})^{\perp}$. Therefore,

$$A\{\rho_U(\hat{x}),\mu;\xi,\underset{\sim}{\theta}\} = A\{\rho(\hat{x}),\mu;\xi,\ U^T\underset{\sim}{\theta}\}. \ \|$$

THEOREM 3.24. For constant attenuation the modified attenuated Radon transform of $\rho(\hat{x}+\hat{a})$ is

$$A\{\rho(\hat{x}+\hat{a}),\mu;\xi,\underset{\sim}{\theta}\} = A\{\rho(\hat{x}),\mu;\ \xi+\langle\underset{\sim}{\theta},\hat{a}\rangle,\ \underset{\sim}{\theta}\}\ e^{-\mu\langle\underset{\sim}{\theta}^{\perp},\hat{a}\rangle} \ .$$

PROOF. For constant attenuation the modified attenuated Radon transform of $\rho(\hat{x}+\hat{a})$ is

$$A\{\rho(\hat{x}+\hat{a}),\mu;\xi,\underset{\sim}{\theta}\} = \int \rho(\hat{x}+\hat{a})\ e^{\mu\langle\underset{\sim}{\theta}^{\perp},\hat{x}\rangle}\ \delta\{\xi-\langle\underset{\sim}{\theta},\hat{x}\rangle\}\ d\hat{x}.$$

The change of variables $\hat{x} = \hat{x}' - \hat{a}$ gives

$$A\{\rho(\hat{x}+\hat{a}),\mu;\ \xi,\underset{\sim}{\theta}\} = \int \rho(\hat{x}')e^{\mu\langle\underset{\sim}{\theta}^{\perp},\hat{x}'-\hat{a}\rangle}\ \delta\{\xi-\langle\underset{\sim}{\theta},\hat{x}'-\hat{a}\rangle\}\ d\hat{x}'$$

$$= \int \rho(\hat{x}')e^{\mu\langle\underset{\sim}{\theta}^{\perp},\hat{x}'\rangle}e^{-\mu\langle\underset{\sim}{\theta}^{\perp},\hat{a}\rangle}\ \delta\{\xi+\langle\underset{\sim}{\theta},\hat{a}\rangle-\langle\underset{\sim}{\theta},\hat{x}'\rangle\}\ d\hat{x}'$$

$$= A\{\rho(\hat{x}),\mu;\xi+\langle\underset{\sim}{\theta},\hat{x}\rangle,\ \underset{\sim}{\theta}\}\ e^{-\mu\langle\underset{\sim}{\theta},\hat{a}\rangle}\ .\ \|$$

THEOREM 3.25. For constant attenuation the modified attenuated Radon transform of the convolution

$$\rho(\hat{x}) = \int \omega(\hat{y})\ \beta(\hat{x}-\hat{y})\ d\hat{y}$$

is

$$A\{\rho(\hat{x}),\ \mu;\ \xi,\underset{\sim}{\theta}\} = \int p(\zeta,\theta)\ g(\xi-\zeta,\theta)\ d\zeta$$

where p and g are the modified attenuated Radon transform for constant attenuation of ω and β, respectively.

PROOF. For constant attenuation the modified attenuated Radon transform of $\rho(\hat{x})$ is

$$A\{\rho(\hat{x}),\mu;\xi,\underset{\sim}{\theta}\} = \iint \omega(\hat{y})\ \beta(\hat{x}-\hat{y})\ e^{\mu\langle\underset{\sim}{\theta}^{\perp},\hat{x}\rangle}\ \delta\{\xi-\langle\hat{x},\underset{\sim}{\theta}\rangle\}\ d\hat{y}\ d\hat{x}\ .$$

Let $\hat{z} = \hat{x}-\hat{y}$ and substituting for $\hat{x}$, we have

$$A\{\rho(\hat{x}),\mu;\xi,\underset{\sim}{\theta}\} = \iint \omega(\hat{y})\ \beta(\hat{z})\ e^{\mu\langle\underset{\sim}{\theta}^{\perp},\hat{z}+\hat{y}\rangle}\ \delta\{\xi-\langle\hat{z}+\hat{y},\underset{\sim}{\theta}\rangle\}\ d\hat{y}\ d\hat{z}\ .$$

$$= \int \omega(\hat{y}) \int \beta(\hat{z})\ e^{\mu\langle\underset{\sim}{\theta}^{\perp},\hat{z}\rangle}\ \delta\{\xi-\langle\hat{y},\underset{\sim}{\theta}\rangle-\langle\hat{z},\underset{\sim}{\theta}\rangle\}\ d\hat{z}\ e^{\mu\langle\underset{\sim}{\theta}^{\perp},\hat{y}\rangle}d\hat{y}$$

$$= \int \omega(\hat{y})\ g(\xi-\langle\hat{y},\underset{\sim}{\theta}\rangle,\theta)\ e^{\mu\langle\underset{\sim}{\theta}^{\perp},\hat{y}\rangle}\ d\hat{y}\ .$$

Using the delta function, this can be rewritten so that

$$A\{\rho(\hat{x}),\mu;\xi,\underset{\sim}{\theta}\} = \iint \omega(\hat{y})\, g(\xi-\zeta,\theta) e^{\mu\langle \underset{\sim}{\theta}^{\perp},\hat{y}\rangle}\, \delta\{\zeta - \langle \hat{y},\underset{\sim}{\theta}\rangle\}\, d\hat{y}\, d\zeta$$

$$= \int p(\zeta,\theta)\, g(\xi-\zeta,\theta)\, d\zeta. \quad \|$$

The differentiability property which holds for the Radon transform (Gel'fand et. al., 1966) does not hold for the modified Radon transform for constant attenuation. Also the result given in Theorem 3.23 is weaker than for the Radon transform which only requires that U be non-singular.

The adjoint transform $A_\mu^* : L^2(\mathbb{C},w) \to L^2(\mathbb{R}^2,W)$ for constant attenuation μ is defined by

$$(A_\mu^* g)(x,y) = \frac{1}{W(x,y)} \int_0^{2\pi} g(-x\sin\theta+y\cos\theta,\theta) e^{\mu x\cos\theta+\mu y\sin\theta} w(-x\sin\theta+y\cos\theta,\theta)\, d\theta. \tag{3.101}$$

This follows immediately from Eq. (3.81) for the modified attenuated Radon transform. For constant attenuation the back-projection operator $\mathcal{B}_\mu$ which operates on $L^2(\mathbb{C},w)$ is given by

$$(\mathcal{B}_\mu\, p)(x,y) = \int_0^{2\pi} p(-x\sin\theta+y\cos\theta,\theta) e^{-\mu x\cos\theta-\mu y\sin\theta}\, d\theta \ . \tag{3.102}$$

THEOREM 3.26. For constant attenuation coefficient and $w(\xi,\theta)$ independent of θ and satisfying $w(\xi) = w(-\xi)$, the operator $A_\mu^* A_\mu : \rho \to \beta$ maps ρ into β where β is given by Eq. (3.84) with the kernel K given by

$$K(x',y'|x,y) = \frac{\widetilde{K}(x',y'|x,y)}{W(x',y')} \quad w\left(\frac{xy'-yx'}{\|\hat{x}-\hat{x}'\|}\right)$$

where

$$\widetilde{K}(x',y'|x,y) = \frac{2}{\|\hat{x}-\hat{x}'\|} \cosh\left\{\frac{\mu[(x^2-x'^2)+(y^2-y'^2)]}{\|\hat{x}-\hat{x}'\|}\right\} . \quad (3.103)$$

PROOF. This follows immediately from Theorem 3.20 when we set $\mu(b+\zeta'e,\ c+\zeta'f)$ to a constant μ. ||

Note that for both the variable and constant attenuation, the operator $A_\mu^* A_\mu$ cannot be represented as a convolution unless $\mu = 0$ everywhere.

THEOREM 3.27. For constant attenuation coefficient, the operator $B_\mu A_\mu : \rho \to \beta$ maps ρ into β where β is given by Eq. (3.84) with the kernel $K(x',y'|x,y)$ given by

$$K(x',y'|x,y) = \frac{2}{\|\hat{x}-\hat{x}'\|} \cosh\left(\mu\|\hat{x}-\hat{x}'\|\right), \quad (3.104)$$

PROOF. This follows immediately from Theorem 3.21 when we set $\mu(b+\zeta'e,\ c+\zeta'f)$ to a constant μ. ||

The result in Theorem 3.27 implies that the linear operation of the composition of projecting and back-projecting for constant attenuation is shift invariant; thus the operation can be characterized by the convolution equation

$$\beta(x',y') = \int_{-\infty}^{\infty}\int_{-\infty}^{\infty} \rho(x,y)\ K(x'-x,\ y'-y)dxdy$$

where

$$K(x,y) = \frac{2}{\|\hat{x}\|}\ \cosh(\mu\|\hat{x}\|).$$

For $\mu=0$, the image $\rho(x,y)$ can be reconstructed from the back-projection image $\beta(x,y)$ using the expression

$$\rho(x,y) = \mathcal{F}_2^{-1}\ \{\mathcal{F}_2\ [\beta(x,y)]/\mathcal{F}_2\ [K(x,y)]\}\ .$$

This is the filter of the back-projection algorithm described in Section 2.2.6. However, for attenuation coefficients $\mu > 0$ the Fourier transform of $K(x,y)$ does not exist. Therefore this algorithm is not appropriate for the back-projection operator $\mathcal{B}_\mu$ given by Eq. (3.102).

THEOREM 3.28. For constant attenuation coefficient, the operator $A_\mu A_\mu^*: p \to g$ maps p into g where g is given by Eq. (3.88) with the kernel $\mathcal{I}(\xi,\theta|\xi',\theta')$ given by

$$\mathcal{I}(\xi,\theta|\xi',\theta') = \frac{\tilde{\mathcal{I}}(\xi,\theta|\xi',\theta')\ w(\xi',\theta')}{W\left(\frac{\xi'\cos\theta-\xi\cos\theta'}{\sin(\theta-\theta')},\ \frac{\xi'\sin\theta-\xi\sin\theta'}{\sin(\theta-\theta')}\right)}$$

where

$$\tilde{\mathcal{I}}(\xi,\theta|\xi',\theta') = \frac{1}{|\sin(\theta-\theta')|}\ \exp\left[\mu(\xi-\xi')\ \frac{(\cos(\theta'-\theta)+1)}{\sin(\theta'-\theta)}\right]. \quad (3.105)$$

PROOF. This follows immediately from Theorem 3.22 when we set the distribution of attenuation coefficients to a constant μ. ||

3.5.4.3 Convolution Result for Constant Attenuation

The convolution result due to Tretiak and Delaney (1978) gives an inverse relationship for the constant attenuated Radon transform:

$$\hat{\rho}(x,y) = \int_0^{2\pi} \int_{-\infty}^{\infty} c_\mu(-x\sin\theta+y\cos\theta-t)\ p(t,\theta)dt\ \exp[-\mu x\cos\theta-\mu y\sin\theta]d\theta \tag{3.106}$$

where $c_\mu(t)$ is a function which is convolved with the data before back-projecting and $p(t,\theta)$ are projection data given by Eq. (3.93). The subscript μ is used to indicate that the convolution function is a function of the attenuation coefficient. Chapter 5 investigates some methods for evaluating the convolution function $c_\mu(t)$.

The following theorem states that the reconstructed image $\hat{\rho}(x,y)$ given in Eq. (3.106) is equal to the convolution of the original image with the attenuated back-projection of the convolution function c_μ.

THEOREM 3.29. For constant attenuation coefficient μ the reconstructed image $\hat{\rho}$ given by Eq. (3.106) can be represented by the expression

$$\hat{\rho}(x,y) = \mathcal{B}_\mu\{c_\mu\} \ ** \ \rho(x,y) \tag{3.107}$$

where ** denotes the two-dimensional convolution of the true distribution ρ with the back-projection operator given by Eq. (3.102) acting

on the convolution function c_μ.

PROOF. Substituting Eq. (3.93) into Eq. (3.106) gives the expression for the estimated reconstruction

$$\hat{\rho}(x,y) = \int_0^{2\pi} \int_{-\infty}^{\infty} c_\mu(y\cos\theta - x\sin\theta - t) \iint_{\mathbb{R}^2} \rho(x',y') \exp[\mu(x'\cos\theta + y'\sin\theta)]$$

$$x\delta(t + x'\sin\theta - y'\cos\theta)\, dx'dy'dt \exp[-\mu x\cos\theta - \mu y\sin\theta]\, d\theta \ .$$

Integrating first with respect to t, we have

$$\hat{\rho}(x,y) = \iint_{\mathbb{R}^2} \int_0^{2\pi} c_\mu(-(x-x')\sin\theta + (y-y')\cos\theta)$$

$$\times \exp[-\mu(x-x')\cos\theta - \mu(y-y')\sin\theta]d\theta\ \rho(x',y')dx'dy'$$

Let

$$\mathcal{B}_\mu\{c_\mu\} = \int_0^{2\pi} c_\mu(-x\sin\theta + y\cos\theta) \exp[-\mu x\cos\theta - \mu y\sin\theta]d\theta,$$

then

$$\hat{\rho}(x,y) = \mathcal{B}_\mu\{c_\mu\} \ ** \ \rho(x,y) \ . \quad \|$$

3.5.4.4 Fourier Space Result for Constant Attenuation

An inversion relationship due to Bellini and co-workers (1979) involves first taking the Fourier transform of the projection data and then interpolating in Fourier space:

$$\rho(r,\phi) = \int_0^{\pi} \int_{-\infty}^{\infty} \tilde{p}(\sqrt{R^2 + \mu^2/4\pi^2}\ ,\ \theta + i\ \sinh^{-1}(\mu/2\pi R)) e^{2\pi i R r \sin(\phi-\theta)}\ |R|dR\ d\theta \tag{3.108}$$

where $\tilde{p}(R,\theta) = \mathcal{F}_1\{p(\xi,\theta)\}$ are the one-dimensional Fourier transforms of the modified attenuated projection data p for constant attenuation coefficient (Eq. 3.93). This result is proven in the following theorem.

THEOREM 3.30. For constant attenuation, the projection $p(\xi,\theta) = (A_\mu\rho)(\xi,\theta)$ given by Eq. (3.93) satisfies Eq. (3.108).

PROOF. First Fourier transforming the projections [Eq. (3.93)] and changing to polar coordinates gives

$$\tilde{p}(R',\theta') = \iiint \rho(r',\phi')\exp[\mu r'\cos(\theta'-\phi')]\delta(\xi+r'\sin(\theta'-\phi')) \times r'dr'd\phi'e^{-2\pi iR'\xi}d\xi .$$

Interchanging the order of integration and integrating over the variable ξ gives

$$\tilde{p}(R',\theta') = \iint \rho(r',\phi')\exp[\mu r'\cos(\theta'-\phi')]\exp[2\pi iR'r'\sin(\theta'-\phi')]r'dr'd\phi'.$$

Substituting the expressions $R' = \sqrt{R^2+\mu^2/4\pi^2}$ and $\theta' = \theta+i\sinh^{-1}(\mu/2\pi R)$ gives

$$\tilde{p}(\sqrt{R^2+\mu^2/4\pi^2}\ ,\ \theta+i\sinh^{-1}(\mu/2\pi R)) = \iint \rho(r',\phi')\exp(r'z)r'dr'd\phi' \tag{3.109}$$

where

$$z = \mu\cos(\theta+i\sinh^{-1}(\mu/2\pi R)-\phi') + 2\pi i\sqrt{R^2+\mu^2/4\pi^2}\sin(\theta+i\sinh^{-1}(\mu/2\pi R)-\phi').$$

Using the identities for the sum of angles gives

$$z = \mu\cos(\theta-\phi')\cos(i\sinh^{-1}(\mu/2\pi R)) - \mu\sin(i\sinh^{-1}(\mu(2\pi R))\sin(\theta-\phi')$$
$$+ 2\pi i\sqrt{R^2+\mu^2/4\pi^2}\sin(\theta-\phi')\cos(i\sinh^{-1}(\mu/2\pi R))$$
$$+ 2\pi i\sqrt{R^2+\mu^2/4\pi^2}\cos(\theta-\phi')\sin(i\sinh^{-1}(\mu/2\pi R)). \qquad (3.110)$$

Substituting the relationships:

$$\cos(i\sinh^{-1}(\mu/2\pi R)) = \frac{\sqrt{4\pi^2R^2+\mu^2}}{2\pi R}$$

$$\sin(i\sinh^{-1}(\mu/2\pi R)) = \frac{i\mu}{2\pi R}$$

into Eq. (3.110) gives

$$z = \mu\cos(\theta-\phi')\frac{\sqrt{4\pi^2R^2+\mu^2}}{2\pi R} - \mu\sin(\theta-\phi')\frac{i\mu}{2\pi R}$$
$$+ 2\pi i\sqrt{R^2+\mu^2/4\pi^2}\sin(\theta-\phi')\frac{\sqrt{4\pi^2R^2+\mu^2}}{2\pi R}$$
$$+ 2\pi i\sqrt{R^2+\mu^2/4\pi^2}\cos(\theta-\phi')\frac{i\mu}{2\pi R}$$
$$= 2\pi i\, R\sin(\theta-\phi').$$

Therefore Eq. (3.109) can be written as

$$\tilde{p}(\sqrt{R^2+\mu^2/4\pi^2},\ \theta+i\sinh^{-1}(\mu/2\pi R)) = \iint \rho(r',\phi')\exp[i2\pi r'R\sin(\theta-\phi')]$$
$$\times\quad r'dr'd\phi'.$$

Integrating $\tilde{p}$ over R and Θ as shown in Eq. (3.108) gives

$$\int_0^{\pi}\int_{-\infty}^{\infty} \tilde{p}(\sqrt{R^2+\mu^2/4\pi^2},\ \theta + i\ \sinh^{-1}(\mu/2\pi R))\ \exp[2\pi i R r\ \sin(\phi-\theta)]|R|dR\ d\theta$$

$$= \int_0^{\pi}\int_{-\infty}^{\infty}\iint_{\mathbb{R}^2} \rho(r',\phi')\ \exp[i2\pi r'R\ \sin(\theta-\phi')]r'dr'd\phi'\ \exp[2\pi i R r\ \sin(\phi-\theta)]$$

$$\times\ |R|dR\ d\theta\ . \qquad (3.111)$$

Interchanging the order of integration gives just the inverse two-dimensional Fourier transform of $\exp[i2\pi r'R\ \sin(\theta-\phi')]$ which is just the two-dimensional delta function $\delta(x-x')\delta(y-y')$. Thus Eq. (3.111) reduces to the convolution of $\rho(x,y)$ with $\delta(x-x')\delta(y-y')$:

$$\int_0^{\pi}\int_{-\infty}^{\infty} \tilde{p}(\sqrt{R^2+\mu^2/4\pi^2},\ \theta + i\ \sinh^{-1}(\mu/2\pi R))\ \exp[2\pi i R r\ \sin(\phi-\theta)]|R|dR\ d\theta$$

$$= \iint_{\mathbb{R}^2} \rho(x',y')\ \delta(x-x')\ \delta(y-y')\ dx'\ dy' = \rho(x,y).\ \|$$

An algorithm for implementing Eq. (3.108) is described in [Bellini et al., 1979 a,b]. If the projection data are rotationally invariant then we get a much simpler result.

COROLLARY 3.30.1. If $p(\xi,\theta) = p(\xi)$ for all θ the concentration distribution $\rho(r,\phi)$ is given by

$$\rho(r,\phi) = \int_0^{\pi}\int_{-\infty}^{\infty} \tilde{p}(\sqrt{R^2+\mu^2/4\pi^2},\ \theta)\ |R|dRd\theta. \qquad (3.112)$$

PROOF. For rotationally invariant projection data $\tilde{p}(R,\theta) = \tilde{p}(R,\theta+i\omega)$ for all ω. ‖

4. ITERATIVE METHODS FOR VARIABLE ATTENUATION COEFFICIENTS

4.1 Introduction

The practical implementation of inverting the attenuated Radon transform given in Eq. (1.1) requires that the relationship between the unknowns representing the distribution of the concentration of radionuclide and the observed projection values be put into a form which is tractable for digital computer processing. Therefore, the continuous transforms discussed in Chapter 3 are reduced to discrete linear transforms which are used in a matrix equation to represent data measured at discrete angular and lateral sampling. The solution to this matrix equation is determined by iterative methods.

A complete description of the discrete attenuated Radon transform involves obtaining projection data from a transmission experiment. The reconstruction of the transmission data is used as a priori information for the attenuation factors in the equations used to model the emission projection data. A major concern in our study of the discrete attenuated Radon transform is how the magnitudes of the attenuation coefficients affect the rate of convergence for the iterative methods and how they amplify the statistical fluctuacions of the measured data in the reconstructed image.

For a study of a particular organ such as the heart, the physician has at his disposal various radiopharmaceuticals and various radionuclides: ^{99m}Tc - stannous pyrophosphate, ^{99m}Tc - tetracycline,

^{99m}Tc - glucoheptonate (140 keV) which have an increased uptake in myocardial infarcts; and rubidium - 81 (446 keV), potassium - 43 (373 keV), cessium - 129 (372 keV), thallium - 201 (80 keV) which have a decreased uptake in myocardial infarcts. These tracers are usually evaluated based on the specificity of the tracer to the myocardium for the desired pathological study so that there is sufficient contrast between the myocardium and surrounding tissue such as the liver. They are also evaluated based on the camera system's ability to sufficiently collimate high energy photons for isotopes such as Cs-129 or eliminate the Compton scattered photons by energy selection for low energy radionuclide such as ^{99m}Tc. Our analysis shows that these tracers must also be evaluated based on the iterative algorithms' ability to accurately reconstruct the true concentration distribution in light of the increased statistical uncertainty for large attenuation experienced by low energy radionuclides such as Tl-201.

In the sections which follow we discuss in detail the development of the linear equations for the least-squares problem using the theorems in Chapter 3, the iterative algorithms for reconstructing large systems of linear equations, and the statistical aspects of reconstructing noisy transmission and emission data.

4.2 Basis Functions

The concentration function ρ and the attenuation function μ are real valued functions of position. In order to represent these functions by a digital computer, one must sample the continuous distribution by a finite array of numbers, called samples. These

samples should be chosen so that the distribution can be reconstructed with small errors.

We consider the samples as coefficients of an expansion of basis functions for the continuous distribution. There are many collections of basis functions which can be used; however, the choice depends on the errors incurred not only by the numerical approximation of taking only a finite number of terms in the series expansion, but also the amplification of statistical noise and the efficiency of calculating the continuous distribution.

In this chapter we will consider an orthonormal basis which is a set of characteristic functions defined over rectangular pixels. Suppose that the region $\mathbb{D}$ as shown in Fig. 4.1 is divided into disjoint rectangular regions called pixels for i=1,..., M and j=1,..., N:

$$D_{ij} = \{(x,y) \mid a(2i-M-2)/2 \leq x < a(2i-M)/2,\ b(2j-N-2)/2 \leq y < b(2j-N)/2\}$$

where a is the width and b is the height of the rectangular pixel D_{ij}. Later we will show reconstruction results for square pixels (a=b) but for the present we will keep the discussion more general. Over these rectangular regions we define the orthonormal basis as

$$\chi_{ij}(x,y) = \begin{cases} \left(\frac{1}{ab}\right)^{1/2} & \text{if } (x,y) \in D_{ij} \\ 0 & \text{otherwise} \end{cases} . \qquad (4.1)$$

Using these basis functions, we can expand the function ρ as

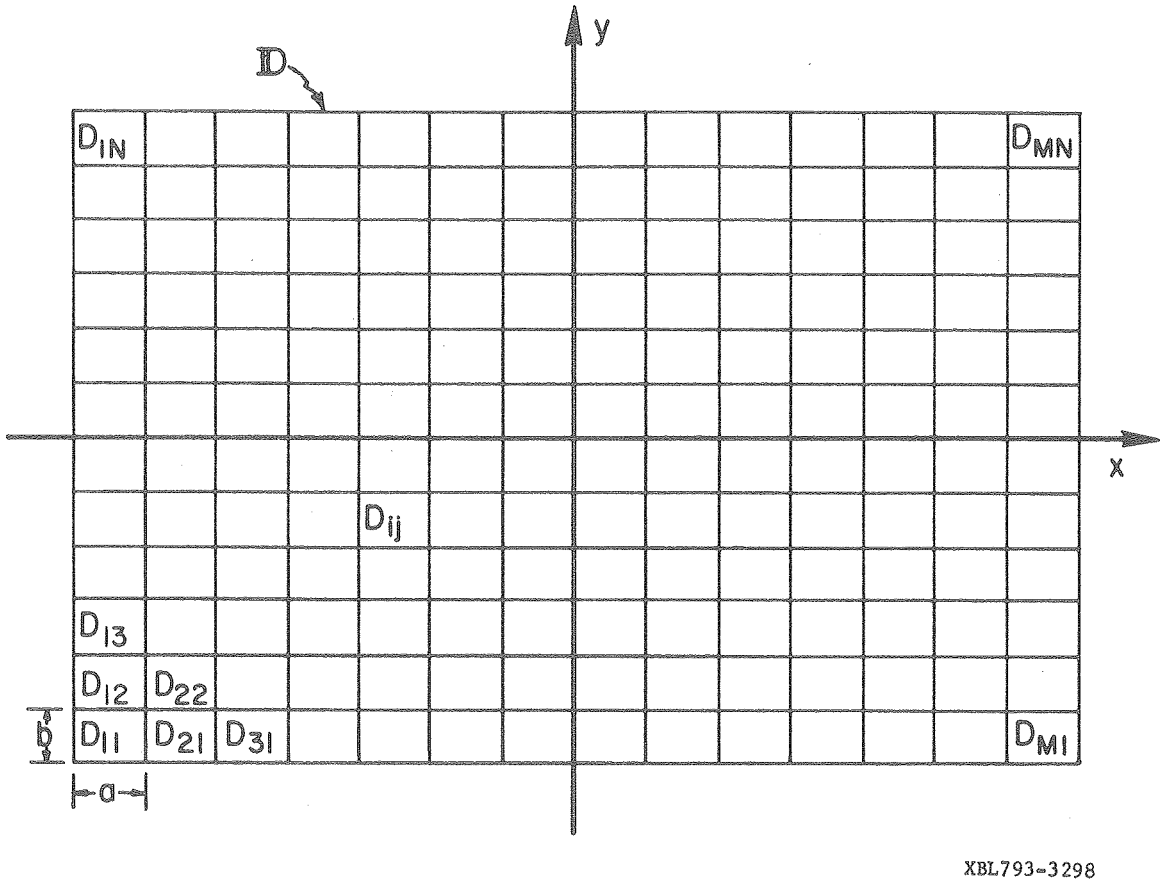

Figure 4.1. The rectangular region 𝔻 is divided up into disjoint rectangular pixels D_{ij} with width a and height b.

$$\rho(x,y) = \sum_{i=1}^{M} \sum_{j=1}^{N} \rho_{ij}\, \chi_{ij}(x,y) \ , \qquad (4.2)$$

where

$$\rho_{ij} = \left(\frac{1}{ab}\right)^{1/2} \int_{\frac{a(2i-M-2)}{2}}^{\frac{a(2i-M)}{2}} \int_{\frac{b(2j-N-2)}{2}}^{\frac{b(2j-N)}{2}} \rho(x,y)\,dx\,dy \ . \qquad (4.3)$$

The coefficients ρ_{ij} are the average value of the concentration over the rectangular region D_{ij}.

The basis $\{\chi_{ij}\}$ given by Eq. (4.1) is referred to by Rosenfeld and Kak (1976) as standard sampling and is chosen primarily due to its computational efficiency. The disadvantage of choosing these basis functions is that the approximate function ρ can have sharp boundaries (see Gordon and Herman, 1974; and Herman, Lent, and Rowland, 1973). Thus the number of pixels must be chosen large enough so that it is a good approximation even for a smoothly varying function. A generalization of standard sampling is the finite element approach (Strang and Fix, 1973) which uses basis functions that are piece-wise linear polynomials in two variables whose supports are polygons which possibly overlap. Other possible basis functions include Fourier and Bessel functions.

4.3 Projection of the Basis Functions

The evaluation of the attenuated Radon transform of the basis functions χ_{ij} is simplified if we consider the attenuated Radon transform of χ_D which is the characteristic function of a rectangle D with sides a and b positioned at the center of rotation as shown in Fig. 4.2.

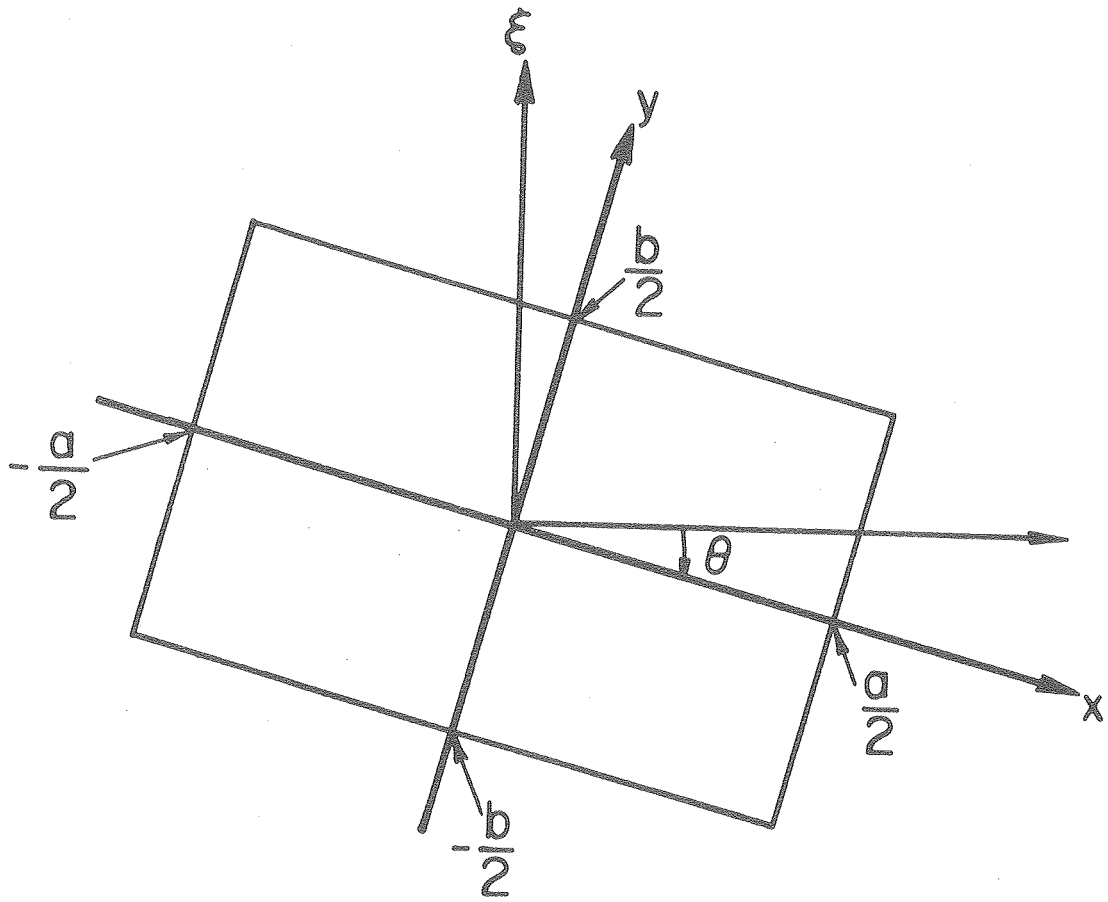

XBL789-3564

Figure 4.2. The rectangular region D with sides a and b is positioned at the center of rotation and rotates with the xy-coordinate system.

Then one can obtain the corresponding transforms of χ_{ij} using the shift properties given in Theorems 3.1 and 3.18 for the attenuated and modified attenuated Radon transforms, respectively.

4.3.1 The Attenuated Radon Transform

The attenuated Radon transform A_μ of the characteristic function χ_D with $\mu(x,y)$ equal to a constant μ for all $(x,y) \in D$ and zero otherwise is given by $A_\mu : \chi_D \to A\{\chi_D(x,y),\ \mu\chi_D(x,y);\ \xi,\theta\}$ where

$$A\{\chi_D(x,y),\ \mu\chi_D(x,y);\ \xi,\theta\} =$$

$$\begin{cases} 0 & \text{if } \frac{a}{2}|\sin\theta| + \frac{b}{2}|\cos\theta| < \xi \\ \frac{1}{\mu}\left\{1 - \exp\left[-\mu\left(\frac{a/2\,|\sin\theta| + b/2\,|\cos\theta| - \xi}{|\cos\theta|\,|\sin\theta|}\right)\right]\right\} & \text{if } \left|\frac{a}{2}|\sin\theta| - \frac{b}{2}|\cos\theta|\right| \le \xi < \frac{a}{2}|\sin\theta| + \frac{b}{2}|\cos\theta| \\ \frac{1}{\mu}\left\{1 - \exp\left[-\mu\,\frac{a}{|\cos\theta|}\right]\right\} & \text{if } \frac{a}{2}|\sin\theta| - \frac{b}{2}|\cos\theta| \le \xi < -\frac{a}{2}|\sin\theta| + \frac{b}{2}|\cos\theta| \\ \frac{1}{\mu}\left\{1 - \exp\left[-\mu\,\frac{b}{|\sin\theta|}\right]\right\} & \text{if } -\frac{a}{2}|\sin\theta| + \frac{b}{2}|\cos\theta| \le \xi < \frac{a}{2}|\sin\theta| - \frac{b}{2}|\cos\theta| \\ \frac{1}{\mu}\left\{1 - \exp\left[-\mu\left(\frac{a/2\,|\sin\theta| + b/2\,|\cos\theta| + \xi}{|\cos\theta|\,|\sin\theta|}\right)\right]\right\} & \text{if } -\frac{a}{2}|\sin\theta| - \frac{b}{2}|\cos\theta| \le \xi < \left|\frac{a}{2}|\sin\theta| - \frac{b}{2}|\cos\theta|\right| \\ 0 & \text{if } \xi < -\frac{a}{2}|\sin\theta| - \frac{b}{2}|\cos\theta| \end{cases} \tag{4.4}$$

Figure 4.3 gives a plot of Eq. (4.4) for attenuation coefficients $\mu = 0,\ .15,$ and 2 pixel^{-1} at $\theta = 30°$ with $a = b = 1$.

If we let μ go to zero in Eq. (4.4) we get the expression for the Radon transform of the characteristic function $\chi_D(x,y)$ (See Eggermont, 1975):

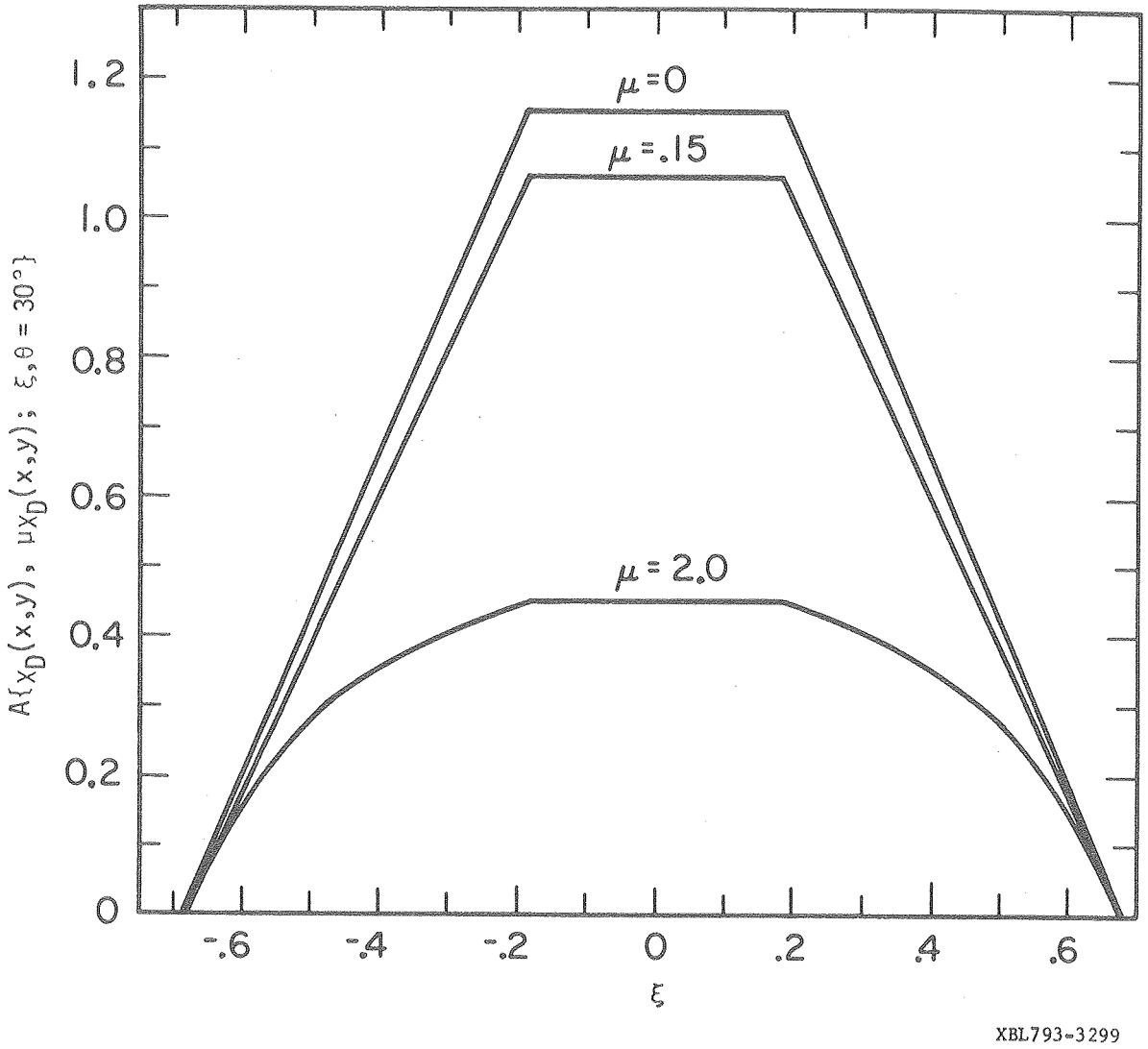

Figure 4.3. Plot of the attenuated Radon transform at θ=30° of the characteristic function χ_D with a = b = 1. The general expression for the transform is given in Eq. (4.4).

$$\mathcal{R}\{\chi_D(x,y);\ \xi,\theta\} =$$

$$\begin{cases} 0 & \text{if } \frac{a}{2}|\sin\theta| + \frac{b}{2}|\cos\theta| < \xi \\ \dfrac{a/2\,|\sin\theta| + b/2\,|\cos\theta| - \xi}{|\cos\theta|\,|\sin\theta|} & \text{if } \left|\frac{a}{2}|\sin\theta| - \frac{b}{2}|\cos\theta|\right| \le \xi < \frac{a}{2}|\sin\theta| + \frac{b}{2}|\cos\theta| \\ \dfrac{a}{|\cos\theta|} & \text{if } \frac{a}{2}|\sin\theta| - \frac{b}{2}|\cos\theta| \le \xi < \frac{-a}{2}|\sin\theta| + \frac{b}{2}|\cos\theta| \\ \dfrac{b}{|\sin\theta|} & \text{if } \frac{-a}{2}|\sin\theta| + \frac{b}{2}|\cos\theta| \le \xi < \frac{a}{2}|\sin\theta| - \frac{b}{2}|\cos\theta| \\ \dfrac{a/2\,|\sin\theta| + b/2\,|\cos\theta| + \xi}{|\cos\theta|\,|\sin\theta|} & \text{if } \frac{-a}{2}|\sin\theta| - \frac{b}{2}|\cos\theta| \le \xi < \left|\frac{a}{2}|\sin\theta| - \frac{b}{2}|\cos\theta|\right| \\ 0 & \text{if } \xi < -\frac{a}{2}|\sin\theta| - \frac{b}{2}|\cos\theta| \end{cases} \tag{4.5}$$

Equation (4.5) is plotted in Fig. 4.4.

Using the shift property given by Theorem 3.1, the attenuated Radon transform, $A\{\chi_{ij}(x,y),\ \mu_{ij}\chi_{ij}(x,y);\ \xi,\theta\}$, of the basis functions $\chi_{ij}(x,y) = \chi_D(x - a(2i-M-1)/2,\ y - b(2j-N-1)/2$ is given by

$$A\{\chi_{ij}(x,y),\ \mu_{ij}\chi_{ij}(x,y);\ \xi,\theta\} = A\{\chi_D(x,y),\ \mu_{ij}\chi_D(x,y);\ \xi',\theta\}$$

where $\xi' = \xi + [a(2i-M-1)/2]\sin\theta - [b(2j-N-1)/2]\cos\theta$. This gives

$$A\{\chi_{ij}(x,y),\ \mu_{ij}\ \chi_{ij}(x,y);\ \xi,\theta\} =$$

$$\begin{cases} 0 & \text{if } \frac{a}{2}|\sin\theta| + \frac{b}{2}|\cos\theta| < \xi + [a(2i-M-1)/2]\sin\theta - [b(2j-N-1)/2]\cos\theta \\ \dfrac{1}{\mu_{ij}}\left\{1 - \exp\left[-\mu_{ij}\left(\dfrac{a/2\,|\sin\theta| + b/2\,|\cos\theta| - \xi}{|\cos\theta|\,|\sin\theta|}\right)\right]\right\} & \text{if } \left|\frac{a}{2}|\sin\theta| - \frac{b}{2}|\cos\theta|\right| \le \xi + [a(2i-M-1)/2]\sin\theta - [b(2j-N-1)/2]\cos\theta < -\frac{a}{2}|\sin\theta| + \frac{b}{2}|\cos\theta| \\ \dfrac{1}{\mu_{ij}}\left\{1 - \exp\left[-\mu_{ij}\,\dfrac{a}{|\cos\theta|}\right]\right\} & \text{if } \frac{a}{2}|\sin\theta| - \frac{b}{2}|\cos\theta| \le \xi + [a(2i-M-1)/2]\sin\theta - [b(2j-N-1)/2]\cos\theta < -\frac{a}{2}|\sin\theta| + \frac{b}{2}|\cos\theta| \\ \dfrac{1}{\mu_{ij}}\left\{1 - \exp\left[-\mu_{ij}\,\dfrac{b}{|\sin\theta|}\right]\right\} & \text{if } -\frac{a}{2}|\sin\theta| + \frac{b}{2}|\cos\theta| \le \xi + [a(2i-M-1)/2]\sin\theta - [b(2j-N-1)/2]\cos\theta < \frac{a}{2}|\sin\theta| - \frac{b}{2}|\cos\theta| \\ \dfrac{1}{\mu_{ij}}\left\{1 - \exp\left[-\mu_{ij}\left(\dfrac{a/2\,|\sin\theta| + b/2\,|\cos\theta| + \xi}{|\cos\theta|\,|\sin\theta|}\right)\right]\right\} & \text{if } -\frac{a}{2}|\sin\theta| - \frac{b}{2}|\cos\theta| \le \xi + [a(2i-M-1)/2]\sin\theta - [b(2j-N-1)/2]\cos\theta < \left|\frac{a}{2}|\sin\theta| - \frac{b}{2}|\cos\theta|\right| \\ 0 & \text{if } \xi + [a(2i-M-1)/2]\sin\theta - [b(2j-N-1)/2]\cos\theta < -\frac{a}{2}|\sin\theta| - \frac{b}{2}|\cos\theta| \end{cases} \tag{4.6}$$

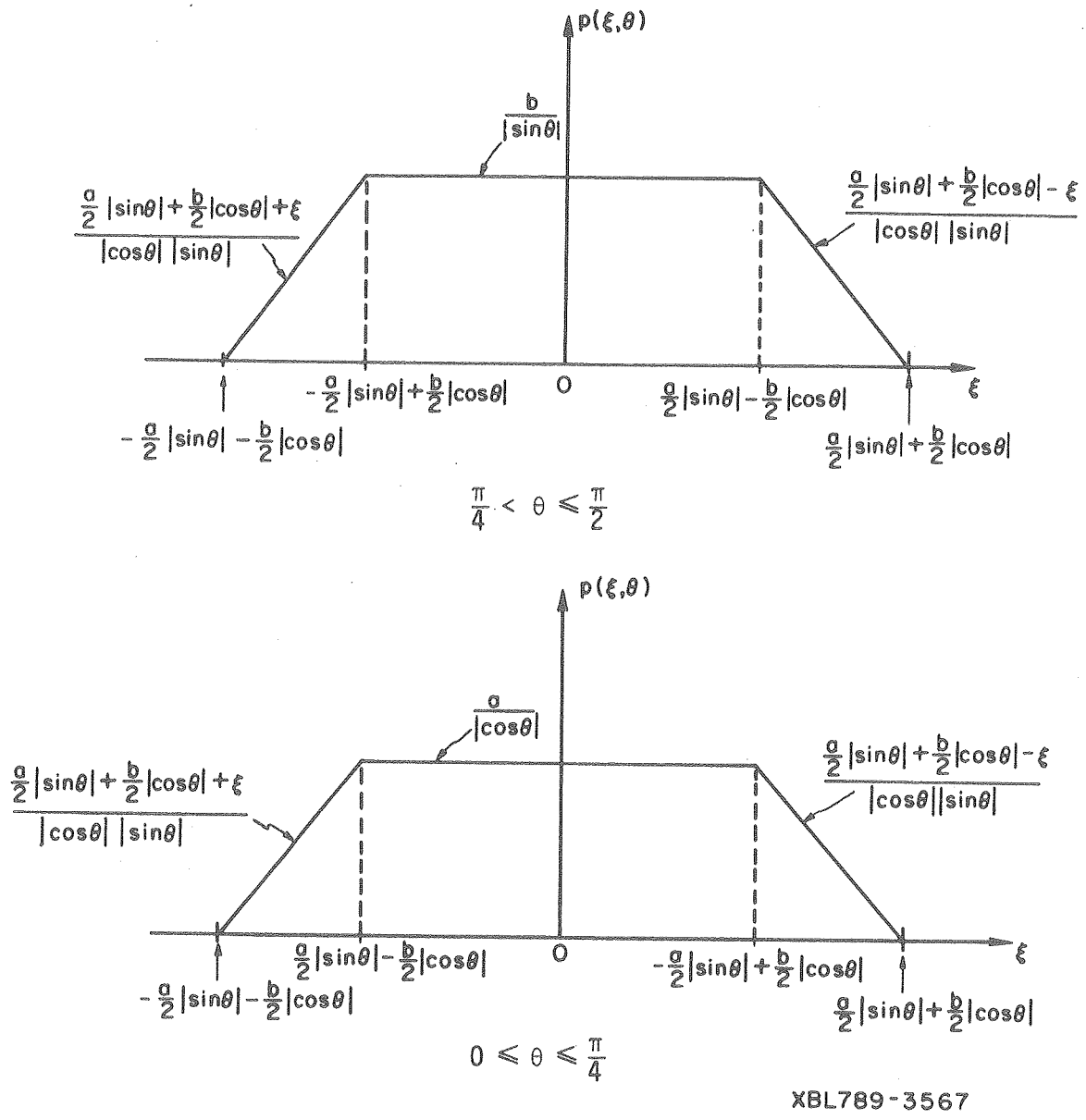

Figure 4.4. Plot of the Radon transform of the characteristic function χ_D. The top figure is a plot of Eq. (4.5) for angles $\pi/4 < \theta \leq \pi/2$ and the bottom figure is for angles $0 \leq \theta \leq \pi/4$.

4.3.2 The Modified Attenuated Radon Transform

The modified attenuated Radon transform A_μ of the characteristic function χ_D with $\mu(x,y)$ equal to a constant μ for all $(x,y) \in D$ and zero otherwise is given by $A_\mu : \chi_D \to A\{\chi_D(x,y),\ \mu\chi_D(x,y);\ \xi,\theta\}$ where

$A\{\chi_D(x,y),\ \mu\chi_D(x,y);\ \xi,\theta\} =$

$$\begin{cases} 0 & \text{if } \frac{a}{2}|\sin\theta| + \frac{b}{2}|\cos\theta| < \xi \\ \frac{1}{\mu}\left\{\exp\left[-\mu\left(\frac{\xi\,|\cos\theta| - b/2)}{|\sin\theta|}\right)\right] - \exp\left[-\mu\left(\frac{-\xi\,|\sin\theta| + a/2}{|\cos\theta|}\right)\right]\right\} & \text{if } \left|\frac{a}{2}|\sin\theta| - \frac{b}{2}|\cos\theta|\right| \le \xi < \frac{a}{2}|\sin\theta| + \frac{b}{2}|\cos\theta| \\ \frac{1}{\mu}\left\{\exp\left[-\mu\left(\frac{-\xi\,|\sin\theta| - a/2}{|\cos\theta|}\right)\right] - \exp\left[-\mu\left(\frac{-\xi\,|\sin\theta| + a/2}{|\cos\theta|}\right)\right]\right\} & \text{if } \frac{a}{2}|\sin\theta| - \frac{b}{2}|\cos\theta| \le \xi < -\frac{a}{2}|\sin\theta| + \frac{b}{2}|\cos\theta| \\ \frac{1}{\mu}\left\{\exp\left[-\mu\left(\frac{\xi\,|\cos\theta| - b/2)}{|\sin\theta|}\right)\right] - \exp\left[-\mu\left(\frac{\xi\,|\cos\theta| + b/2}{|\sin\theta|}\right)\right]\right\} & \text{if } -\frac{a}{2}|\sin\theta| + \frac{b}{2}|\cos\theta| \le \xi < \frac{a}{2}|\sin\theta| - \frac{b}{2}|\cos\theta| \\ \frac{1}{\mu}\left\{\exp\left[-\mu\left(\frac{-\xi\,|\sin\theta| - a/2}{|\cos\theta|}\right)\right] - \exp\left[-\mu\left(\frac{\xi\,|\cos\theta| + b/2}{|\sin\theta|}\right)\right]\right\} & \text{if } -\frac{a}{2}|\sin\theta| - \frac{b}{2}|\cos\theta| \le \xi < \left|\frac{a}{2}|\sin\theta| - \frac{b}{2}|\cos\theta|\right| \\ 0 & \text{if } \xi < -\frac{a}{2}|\sin\theta| - \frac{b}{2}|\cos\theta| \end{cases} \tag{4.7}$$

Using the shift property given by Theorem 3.18, the modified attenuated Radon transform, $A\{\chi_{ij}(x,y),\ \mu_{ij}\chi_{ij}(x,y);\ \xi,\theta\}$, of the basis functions $\chi_{ij}(x,y)$ is given by

$$A\{\chi_{ij}(x,y),\ \mu_{ij}\chi_{ij}(x,y);\ \xi,\theta\} = A\{\chi_D(x,y),\ \mu_{ij}\chi_D(x,y);\ \xi',\theta\}\ \exp\left[\int_0^{\zeta'} \mu_{ij}\chi_D(-\xi'\sin\theta+\zeta\cos\theta,\ \xi'\cos\theta+\zeta\sin\theta)\,d\zeta\right] \tag{4.8}$$

where $\xi' = \xi + [a(2i-M-1)/2]\sin\theta - [b(2j-N-1)/2]\cos\theta$ and $\zeta' = -[a(2i-M-1)/2]\cos\theta - [b(2j-N-1)/2]\sin\theta$. Note that for the modified attenuated Radon transform the shift results in an extra exponential factor.

4.4 Projection of the Radionuclide Distribution

With the preliminary results given in Sections 4.2 and 4.3, we can now obtain an explicit expression for the attenuated Radon transform of the radionuclide distribution

$$\rho(x,y) = \sum_{i=1}^{M} \sum_{j=1}^{N} \rho_{ij}\, \chi_{ij}(x,y) \ , \tag{4.9}$$

with an attenuation distribution given by

$$\mu(x,y) = \sum_{m=1}^{M} \sum_{n=1}^{N} \mu_{mn}\, \chi_{mn}(x,y) \ . \tag{4.10}$$

If we let $s_{ij}(\xi,\theta)$ be the attenuated Radon transform of $\chi_{ij}(x,y)$ [i.e., $s_{ij}(\xi,\theta) = A\{\chi_{ij}(x,y), \mu(x,y); \xi,\theta\}$], then we have

$$p_\gamma(\xi,\theta) = \sum_{i=1}^{M} \sum_{j=1}^{N} \rho_{ij}\, s_{ij}(\xi,\theta) \tag{4.11}$$

where

$$s_{ij}(\xi,\theta) = \int_{\alpha}^{\beta} \chi_{ij}(-\xi\sin\theta+\zeta\cos\theta,\ \xi\cos\theta+\zeta\sin\theta)$$

$$\times \exp\left[-\int_{\zeta}^{\infty} \mu(-\xi\sin\theta+\zeta'\cos\theta,\ \xi\cos\theta+\zeta'\sin\theta)d\zeta'\right]d\zeta \ . \tag{4.12}$$

The lower limit α and the upper limit β for the integral in Eq. (4.12) are the intersections of the line $\xi = -x\sin\theta+y\cos\theta$ with the rectangular support D_{ij} of the characteristic function χ_{ij} (Fig. 4.5). Substituting the expansion for $\mu(x,y)$ given in Eq. (4.10) we obtain

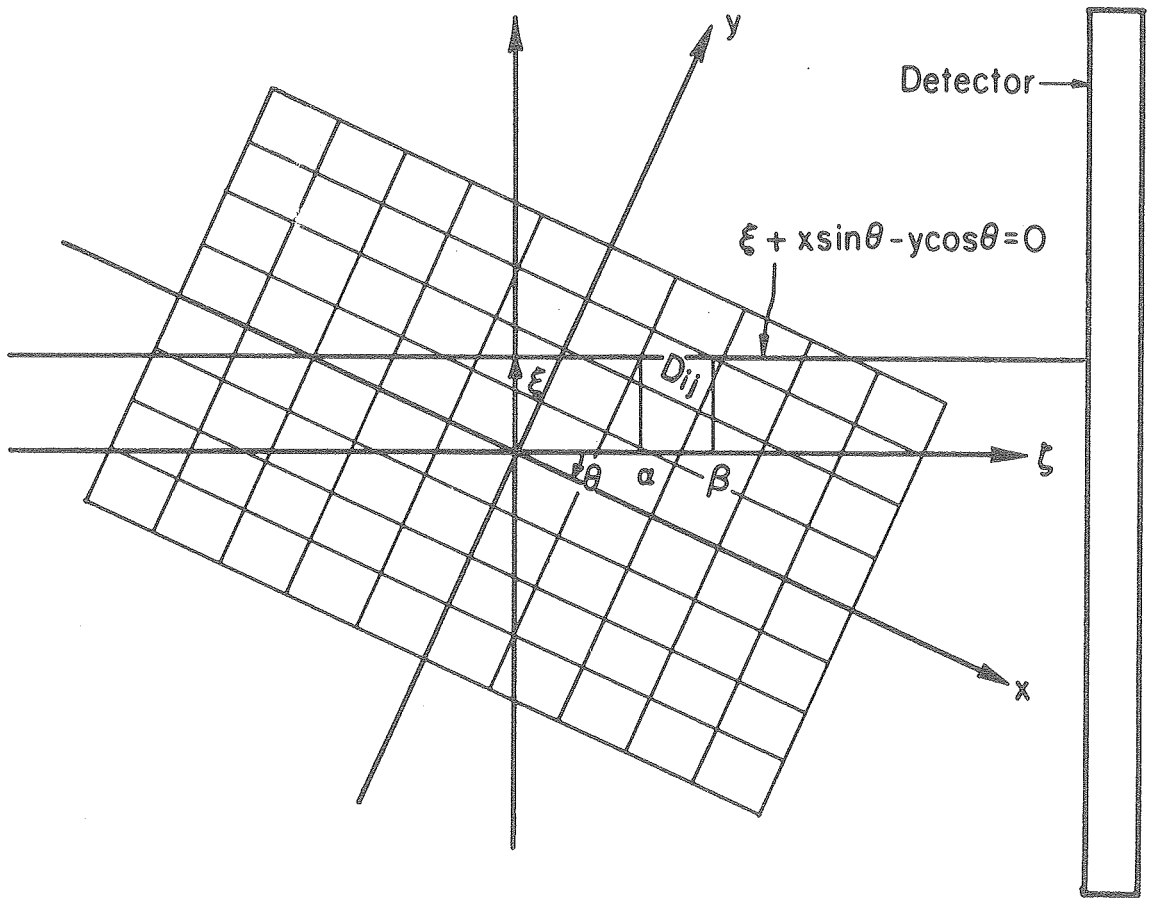

XBL793-3297

Figure 4.5. For the angle θ and lateral sampling ξ, the attenuated Radon transform of the basis function χ_{ij} with support D_{ij} is the integral between α and β of χ_{ij} modified by the integral of the attenuation coefficient distribution $\mu(x,y)$ along the line $\xi+x\sin\theta-y\cos\theta = 0$ as given by Eq. (4.12).

$$s_{ij}(\xi,\theta) = \int_{\alpha}^{\beta} \chi_{ij}(-\xi\sin\theta+\zeta\cos\theta,\ \xi\cos\theta+\zeta\sin\theta)$$

$$\times \exp\left[-\mu_{ij}\int_{\alpha}^{\beta} \chi_{ij}(-\xi\sin\theta+\zeta'\cos\theta,\ \xi\cos\theta+\zeta'\sin\theta)d\zeta'\right] d\zeta$$

$$\times \exp\left[-\sum_{m}\sum_{\substack{n \\ (m,n)\in E_{ij}}} \mu_{mn}\,\mathcal{R}\{\chi_{mn}(x,y);\ \xi,\theta\}\right] \qquad (4.13)$$

where $\mathcal{R}\{\chi_{mn}(x,y);\ \xi,\theta\}$ is the Radon transform of $\chi_{mn}(x,y)$ and

$$E_{ij} = \{(m,n)\,|\,m\cos\theta + n\sin\theta > \frac{a(2i-M-1)}{2}\cos\theta + \frac{b(2j-N-1)}{2}\sin\theta\}. \qquad (4.14)$$

The integral of the basis function χ_{ij} in Eq. (4.13) is just the attenuated Radon transform $A\{\chi_{ij}(x,y),\ \mu_{ij}\chi_{ij}(x,y);\ \xi,\theta\}$ given by Eq. (4.6). Therefore we can simplify the expression for s_{ij}:

$$s_{ij}(\xi,\theta) = A\{\chi_{ij}(x,y),\ \mu_{ij}\ \chi_{ij}(x,y);\xi,\theta\}\ \exp\left[-\sum_{m}\sum_{\substack{n \\ (m,n)\in E_{ij}}} \mu_{mn}\mathcal{R}\{\chi_{mn}(x,y);\xi,\theta\}\right]. \qquad (4.15)$$

Likewise the modified attenuated Radon transform of Eq. (4.9) for an attenuation distribution given by Eq. (4.10) satisfies

$$p\ (\xi,\theta) = \sum_{i=1}^{M}\ \sum_{j=1}^{N} \rho_{ij}\ s_{ij}(\xi,\theta) \qquad (4.16)$$

where

$$\delta_{ij}(\xi,\theta) = A\{\chi_{ij}(x,y),\ \mu_{ij}\chi_{ij}(x,y);\xi,\theta\}$$
$$\times \exp\left[-\sum_{m=0}^{M}\sum_{n=0}^{N}\mu_{mn}\int_{0}^{\alpha}\chi_{mn}(-\xi\sin\theta+\zeta'\cos\theta,\ \xi\cos\theta+\zeta'\sin\theta)d\zeta'\right] \tag{4.17}$$

and $A\{\chi_{ij}(x,y),\ \mu_{ij}\ \chi_{ij}(x,y);\xi,\theta\}$ is given by Eq. (4.8). The expression for the argument in the exponential of Eq. (4.17) is not expressed in terms of Radon transforms of pixels as is done in Eq. (4.15), because if one analyzes Fig. 4.5, one can see that at $\zeta = 0$ the axis intersects the line $\xi+x\sin\theta-y\cos\theta = 0$ in the interior of a pixel and, therefore, the line integral over this pixel is only a partial Radon transform of the characteristic function for that pixel.

4.5 Formulation of the Reconstruction Problem as a Solution to a Set of Linear Equations

If the projections given by Eq. (4.11) or Eq. (4.16) are sampled for a finite number of angles θ_ℓ $\ell = 1,\ldots,L$ and a finite number of points ξ_k, $k=1,\ldots,K$ for each angle, then the reconstruction of the radionuclide distribution is the solution to the following system of equations

$$\sum_{i=1}^{M}\sum_{j=1}^{N}\rho_{ij}\ s_{ij}(\xi_k,\theta_\ell) = p_\gamma(\xi_k,\theta_\ell),\ k=1,\ldots,K;\ \ell=1,\ldots,L \tag{4.18}$$

for attenuated data and

$$\sum_{i=1}^{M}\sum_{j=1}^{N}\rho_{ij}\ \delta_{ij}\ (\xi_k,\theta_\ell) = p(\xi_k,\theta_\ell),\ k=1,\ldots,K;\ \ell=1,\ldots,L \tag{4.19}$$

for modified attenuated projections. The samples $p(\xi_k,\theta_\ell)$ for the modified attenuated Radon transform is obtained by dividing the projections $p_\gamma(\xi_k,\theta_\ell)$ by $G_\mu(\xi_k,\theta_\ell)$ in Eq. (3.72) representing the attenuation between the central axis (ζ=0) and the detector . In order to simplify notation, Eq. (4.18) and (4.19) can be rewritten in matrix form by resorting to a lexicographic or stacked notation which contracts the double indices (i,j) and (k,ℓ) to single indices i' and k', respectively. Thus

$$A\rho = P \tag{4.20}$$

and

$$A\rho = P \tag{4.21}$$

where A and A are KL × MN matrices with elements $a_{i'k'} = s_{ij}(\xi_k,\theta_\ell)$ or $\delta_{ij}(\xi_k,\theta_\ell)$ such that $i' = (j-1) \times M + i$ and $k' = (\ell-1) \times K + k$. The vector ρ has elements $\rho_{i'} = \rho_{ij}$, and P and P are vectors with elements $p_{k'} = p_{km}$ and $p_{k'} = p_{km}$, respectively.

Through the remainder of this chapter we will be primarly concern with the matrix operator A and its elements $s_{ij}(\xi_k,\theta_\ell)$. An approximation of $s_{ij}(\xi_k,\theta_\ell)$ is used in solving Eq. (4.18) by the computer. The attenuation factor for the pixel D_{ij} is evaluated only from the center point (a[2i-M-1]/2, b[2j-N-1]/2) in the direction of $\underset{\sim}{\theta}_\ell^\perp = (\cos\theta_\ell, \sin\theta_\ell)$ instead of evaluating the Radon transform of the entire pixel as done in Eq. (4.15). This gives the following approximation to s_{ij}:

$$s_{ij}(\xi_k,\theta_\ell) \approx \mathcal{R}\{\chi_{ij}(x,y);\ \xi_k,\theta_\ell\}\ \exp[-\mu_{ij}\ \mathcal{R}\{\chi_{ij}(x,y);\xi_{ij},\theta_\ell\}/2]$$

$$\times \exp\left[-\sum_{\substack{m\\(m,n)\in E_{ij}}}\sum_{n} \mu_{mn}\ \mathcal{R}\{\chi_{mn}(x,y);\ \xi_{ij},\ \theta_\ell\}\right] \tag{4.22}$$

where $\xi_{ij} = -[a(2i-M-1)\ \sin\theta_\ell]/2 + [b(2j-N-1)\ \cos\theta_\ell]/2$ is the lateral sampling for a ray passing through the center of the pixel. This approximation is useful for computer applications since it reduces storage requirements.

The estimate $\hat{\rho}$ for the radionuclide distribution minimizes the least-squares function

$$\chi^2(\rho) = (A\rho - P)^T\ \Phi^{-1}\ (A\rho - P) \tag{4.23}$$

where Φ is the covariance matrix for the data and is a symmetric positive semidefinite matrix. The estimate is given by the following two equivalent forms

$$\hat{\rho} = (\Phi^{-1/2}\ A)^G\ \Phi^{-1/2}\ P \tag{4.24}$$

$$\hat{\rho} = (A^T\ \Phi^{-1}\ A)^G\ A^T\ \Phi^{-1}\ P \tag{4.25}$$

where G denotes the Moore-Penrose generalized inverse (see Boullion and Odell, 1971; and Ben-Israel and Greville, 1974).

The least-squares solution $\hat{\rho}$ is the best approximate solution to the system of equations

$$\Phi^{-1/2}\ A\rho = \Phi^{-1/2}\ P\ . \tag{4.26}$$

and $\hat{\rho}$ is the best approximate solution of Eq. (4.26) if and only if $\hat{\rho}$ is a best approximate solution of

$$A^T\ \Phi^{-1}\ A\rho = A^T\ \Phi^{-1}\ P\ . \tag{4.27}$$

The system given in Eq. (4.26) can be described using the following terminology:

1) Overdetermined and Underdetermined Systems - An overdetermined system implies that the number of equations is greater than the number of unknowns, i.e. $KL > MN$. An underdetermined system implies that the number of equations is less than the number of unknowns, i.e. $KL < MN$.

2) Consistent and Inconsistent Systems - A consistent system implies that the vector $\Phi^{-1/2} P$ is in the range of the matrix operator $\Phi^{-1/2}A$. For an inconsistent system the vector $\Phi^{-1/2}P$ is not in the range of the matrix operator $\Phi^{-1/2}A$.

3) Full Column Rank - The columns of the matrix operator $\Phi^{-1/2}A$ forms a linearly independent set of vectors. Also the null space of the operator $\Phi^{-1/2}A$ contains only the zero vector.

The solution to these systems are as follows:

1) Overdetermined, Consistent, Full Column Rank

$$\hat{\rho} = (A^T \Phi^{-1} A)^{-1} A^T \Phi^{-1} P$$

$$\chi^2(\hat{\rho}) = 0$$

2) Overdetermined, Consistent, Not Full Column Rank

$$\hat{\rho} = (\Phi^{-1/2}A)^G \Phi^{-1/2} P$$

$$\chi^2(\hat{\rho}) = 0$$

3) Overdetermined, Inconsistent, Full Column Rank

$$\hat{\rho} = (A^T \Phi^{-1} A)^{-1} A^T \Phi^{-1} P$$

$$\chi^2(\hat{\rho}) > 0$$

4) Overdetermined, Inconsistent, Not Full Column Rank

$$\hat{\rho} = (\Phi^{-1/2} A)^G \Phi^{-1/2} P$$

$$\chi^2(\hat{\rho}) > 0$$

5) Underdetermined, Consistent

$$\hat{\rho} = (\Phi^{-1/2} A)^G \Phi^{-1/2} P$$

$$\chi^2(\hat{\rho}) = 0$$

6) Underdetermined, Inconsistent

$$\hat{\rho} = (\Phi^{-1/2} A)^G \Phi^{-1/2} P$$

$$\chi^2(\hat{\rho}) > 0 \ .$$

In most cases the data collected from any patient study requires the determination of a best solution to an inconsistent system of linear equations. The inconsistency in the data comes from such physical factors as statistical noise in the data, inadequacy of the model, and patient movement.

The dimensions of the matrix A are too large in all practical applications so that at the present the solution to the best estimate $\hat{\rho}$ can-

not be found by inverting a matrix and determining a solution using Eqs. (4.24) or (4.25). Therefore, we must resort to iterative methods to minimize the χ^2 function in Eq. (4.23). These methods will be discussed in Section 4.7 but first we will investigate some of the properties of discrete attenuated projection operators A and A.

4.6 Properties of the Discrete Attenuated Projection Operators

The attenuated projection operators A and A are members of the space $L(\mathbb{R}^{MN}, \mathbb{R}^{KL})$ of linear operators which map the finite dimensional Hilbert space $\mathbb{R}^{MN}$ into the finite dimensional Hilbert space $\mathbb{R}^{KL}$. The space $L(\mathbb{R}^{MN}, \mathbb{R}^{KL})$ is a normed linear space with respect to the norm defined by

$$\|A\| = \sup_{\|\rho\| = 1} \|A\rho\| \tag{4.28}$$

where $A \in L(\mathbb{R}^{MN}, \mathbb{R}^{KL})$ and

$$\begin{aligned} \|\rho\| &= \left(\sum_{i=1}^{MN} \rho_i^2 \right)^{1/2} \qquad \rho \in \mathbb{R}^{MN} \\ \|p\| &= \left(\sum_{i=1}^{KL} p_i^2 \right)^{1/2} \qquad p \in \mathbb{R}^{KL}, \; p = A\rho. \end{aligned} \tag{4.29}$$

The discrete attenuated projection operators A and A are nonnegative operators (i.e. $A \geq 0$). Properties for these types of operators are discussed in (Marek, 1970; Vandergraft, 1968; Varga, 1962). In this discussion the pertinent results for nonnegative matrices will be discussed as they apply to the composite of the projection and transpose operations.

The solution to the reconstruction problem for attenuated data as formulated in Eq. (4.27) for $\Phi = I$ requires determining the inverse of the matrix $A^T A$ restricted to the range of A^T. The Rayleigh quotient $q(\rho)$ for the operator A^TA is defined by the expression

$$q(\rho) = \frac{\langle \rho, A^TA\rho \rangle}{\langle \rho,\rho \rangle} . \tag{4.30}$$

The minimum and maximum eigenvalues λ_N and λ_1 of A^TA are the minimum and maximum of the Rayleigh quotient (Bellman, 1970):

$$\lambda_1 = \max_{\rho} \frac{\langle \rho, A^TA\rho \rangle}{\langle \rho, \rho \rangle} \tag{4.31}$$

$$\lambda_N = \min_{\rho} \frac{\langle \rho, A^TA\rho \rangle}{\langle \rho, \rho \rangle} \tag{4.32}$$

where $\lambda_1 \geqslant \lambda_2 \geqslant \lambda_3 \geqslant \ldots . \geqslant \lambda_N$ are the eigenvalues of the linear operator A^TA. One can show that the norm of A given by Eq. (4.28) is equal to the square root of the maximum eigenvalue of A^TA; that is, $\| A \| = (\lambda_1)^{1/2}$ (p.41, Ortega and Rheinboldt, 1970).

The properties of A^TA are summarized as follows:

1. A^TA is symmetric.
2. A^TA is normal (i.e. A^TA commutes with its transpose).
3. A^TA is positive semidefinite.
4. The eigenvalues of A^TA are real and $\geqslant 0$. A^TA is positive definite if all eigenvalues are nonzero.

5. $A^TA = V\Lambda^T\Lambda V^T$ and $AA^T = U\Lambda\Lambda^TU^T$ where V and U are orthogonal matrices and Λ is a diagonal matrix with the square root ($\lambda_i^{1/2}$) of the common nonzero eigenvalues of A^TA and AA^T.
6. A^TA is a nonnegative matrix (i.e. all its elements are greater than or equal to zero).
7. If sufficient angular sampling is taken, than A^TA is a positive matrix and has a unique eigenvalue which has the greatest absolute value. This eigenvalue is positive and simple, and its associated eigenvector may be taken to be positive. (A simple eigenvalue means that the eigenvalue is real and has a multiplicity of 1.) This implies that the spectral radius $r(A^TA) = \max_i |\lambda_i|$ is a simple eigenvalue of A^TA.

These properties are developed and discussed in (Bellman, 1970). The result given in 7. is known as the Perron theorem (Perron, 1907). Bounds for the unique largest eigenvalue are given by Minc (1970).

The result in 5. means that A^TA and AA^T have a decomposition in terms of their common spectrum. Decomposing A^TA and AA^T leads to a singular value decomposition of the projection operator A:

$$A = \sum_{i=1}^{R} \lambda_i^{1/2} U_i V_i^T , \qquad (4.33)$$

where R is the rank of the matrix A, U_i and V_i are the eigenvectors of AA^T and A^TA, respectively, and λ_i are the corresponding eigenvalues. The outer product $U_iV_i^T$ is an KL × MN matrix and the matrices U(KL × KL) and V(MN × MN) with columns composed of the vectors U_i and V_i, respectively, are orthogonal. The generalized inverse of the matrix A has a similar

decomposition, namely

$$A^G = \sum_{i=1}^{R} \lambda_i^{-1/2} V_i U_i^T . \qquad (4.34)$$

One can show that this satisfies the Moore-Penrose properties for the generalized inverse of the attenuated projection operator A.

The spectrum of A^TA was investigated for attenuation coefficients μ=0, .0958, .15, .18 pixel^{-1} and are shown graphically in Fig. 4.6. The 64 eigenvalues of the matrix A^TA were evaluated for attenuation projection operators A which operate on an 8×8 transverse section image conveniently giving projections at 72 angles equally spaced over 360°. The matrix elements $s_{ij}(\xi_k,\theta_\ell)$ of A were evaluated for an attenuator which was constant throughout the 8×8 transverse section. Instead of using line lengths as in Eq. (4.22) the projection of the basis functions χ_{ij} were evaluated using ray factors (Huesman et al., 1977) by replacing $\mathcal{R}\{\chi_{ij}(x,y); \xi_k,\theta_\ell\}$ with the area that the ray (k,ℓ) intersects the pixel (i,j). The curves in Fig. 4.6 which decrease monotonically from left to right are the eigenvalues λ of A^TA, and the curves which increase monotonically from left to right are the reciprocals of the eigenvalues. The minimum and maximum values for λ and $1/\lambda$ and the condition numbers for A^TA are summarized in Table 4.1 (condition number = $\lambda_{max}/\lambda_{min}$).

Analyzing Fig. 4.6 and Table 4.1, it is obvious that the maximum eigenvalue for A decreases as the attenuation coefficient increases. Also the trace of A^TA which is proportional to the area under the curves for λ in Fig. 4.6, decreases as the attenuation coefficient

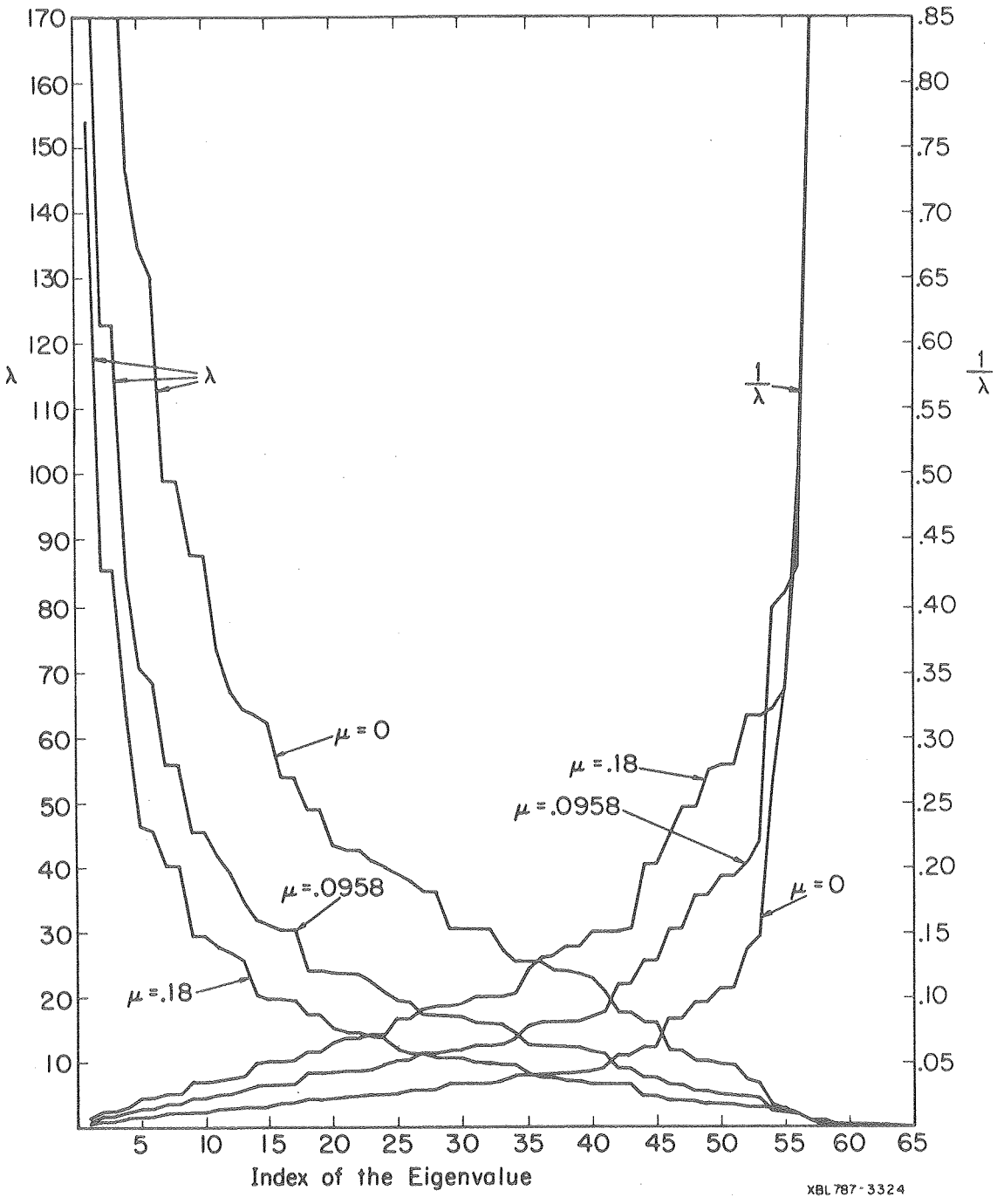

Figure 4.6. The curves which decrease from left to right are the 64 eigenvalues (λ) of A^TA where the operator A operates on an 8×8 transverse section giving projections of 72 angles equally spaced over 360°. The curves which increase from left to right are the eigenvalues of $(A^TA)^{-1}$ equal to $1/\lambda$. The units for μ are $pixel^{-1}$.

Table 4.1. The minimum and maximum eigenvalues of A^TA and $(A^TA)^{-1}$ and the condition number of A^TA. The operator A operates on an 8×8 transverse section giving projections of 72 angles equally spaced over 360°. The total spectrum for μ=0, .0958 and .18 are plotted in Fig. 4.6.

$\mu(\text{pixel}^{-1})$	λ_{min}	λ_{max}	$1/\lambda_{min}$	$1/\lambda_{max}$	Condition No.
0	.0121	551	82.6	.00181	45537
.075	.0564	308	17.7	.00325	5460
.0958	.0731	266	13.7	.00376	3638
.150	.106	185	9.4	.00541	1745
.180	.116	154	8.6	.00649	1327

increases. These observations are stated precisely in the following theorem.

THEOREM 4.1. For the discrete attenuated Radon transforms A_1 and A_2 with the attenuation distributions satisfying $\mu_1(x,y) > \mu_2(x,y)$ for all $(x,y) \in \mathbb{R}^2$, the following are true:

a) The maximum eigenvalues of $A_1^T A_1$ and $A_2^T A_2$ satisfy $\lambda_{max,1} < \lambda_{max,2}$.

b) The traces of $A_1^T A_1$ and $A_2^T A_2$ satisfy $tr(A_1^T A_1) < tr(A_2^T A_2)$.

PROOF. We first evaluate the element $c_{i'j'}$ of the matrix $A^T A$ using Eq. (4.15) and $k' = (\ell-1)K+k$, $i' = (j-1)M+i$, $j' = (q-1)M+p$:

$$
\begin{aligned}
c_{i'j'} &= \sum_{k'} a_{k'i'} a_{k'j'} \\
&= \sum_{k} \sum_{\ell} s_{ij}(\xi_k,\theta_\ell)\, s_{pq}(\xi_k,\theta_\ell) \\
&= \sum_{k} \sum_{\ell} A\{\chi_{ij}(x,y), \mu_{ij}\chi_{ij}(x,y); \xi_k,\theta_\ell\} \exp\Big[- \sum_{(m,n)\in E_{ij}} \sum_{m} \sum_{n} \mu_{mn} \mathcal{R}\{\chi_{mn}(x,y);\xi_k,\theta_\ell\}\Big] \\
&\quad \times A\{\chi_{pq}(x,y), \mu_{pq}\chi_{pq}(x,y); \xi_k,\theta_\ell\} \exp\Big[- \sum_{(m,n)\in E_{pq}} \sum_{m} \sum_{n} \mu_{mn} \mathcal{R}\{\chi_{mn}(x,y);\xi_k,\theta_\ell\}\Big].
\end{aligned}
\tag{4.35}
$$

a) From the expression for $c_{i'j'}$ in Eq. (4.35) it is easy to see that if $\mu_1 > \mu_2$, then the elements $c_{ij,1}$ of $A_1^T A_1$ and $c_{ij,2}$ of $A_2^T A_2$ satisfy $c_{ij,1} < c_{ij,2}$. Therefore

$$\| A_1^T A_1 \rho \| = \left[\sum_i \left(\sum_k c_{ik,1} \rho_k \right)^2 \right]^{1/2} < \left[\sum_i \left(\sum_k c_{ik,2} \rho_k \right)^2 \right]^{1/2} = \| A_2^T A_2 \| ,$$

and $$\lambda_{max,1} = \sup_{\|\rho\|=1} \| A_1^T A_1 \rho \| < \sup_{\|\rho\|=1} \| A_2^T A_2 \rho \| = \lambda_{max,2} .$$

b) The trace of the matrix $A^T A$ is equal to

$$tr(A^T A) = \sum_{i=1}^{MN} c_{i'i'} . \qquad (4.36)$$

It is clear from Eq. (4.35) that as the attenuation coefficient increases, the exponential factors will decrease. Therefore we see from Eq. (4.36) if $\mu_1 > \mu_2$ then $tr(A_1^T A_1) < tr(A_2^T A_2)$. ||

The proofs for the trace and the maximum eigenvalue of $A^T A$ in Theorem 4.1 were straightforward. Theorems relating the variation in the minimum eigenvalue, the condition number, and the trace of the inverse of $A^T A$ to the increase in attenuation coefficient are difficult to state precisely and prove. Therefore the computer was used to determine the eigenvalues for attenuated projection operators which operate on 8×8, 10×10, and 12×12 transverse section arrays conveniently giving in each case projections at 72 angles equally spaced over 360°. In Tables 4.2, 4.3, and 4.4 the matrix elements $s_{ij}(\xi_k, \theta_\ell)$ of A were evaluated using Eq. (4.22) for an attenuator which was constant throughout; whereas in Tables 4.5, 4.6, and 4.7 the line length weighting represented by $\mathcal{R}\{\chi_{ij}(x,y); \xi_k, \theta_\ell\}$ in Eq. (4.22) was replaced by ray factors. In both cases the projection bin width and the pixel

Table 4.2. For attenuation coefficients between 0 and .60 pixel^{-1}, the minimum and maximum eigenvalues, the condition number, the trace, and the trace of the inverse of the matrix A^TA are evaluated for attenuated projection operators A which operate on an 8×8 transverse section giving 72 projections equally spaced over 360°. The matrix elements for A were evaluated using Eq. (4.22) which weights by line lengths the pixel's contribution to the projection. Both the maximum eigenvalue and trace (A^TA) decrease monotonically with an increase in the attenuation coefficient. The maximum shown for λ_{min} is at μ = .18, and the minimum shown for the condition number and trace $[(A^TA)^{-1}]$ is at μ = .38 and μ = .10, respectively.

μ	λ_{min}	λ_{max}	Condition Number	Trace(A^TA)	Trace$[(A^TA)^{-1}]$
0	.234	557	2384.4	4376.3	8.33
.02	.222	474	2129.3	3774.1	9.03
.04	.240	405	1690.3	3284.2	8.90
.06	.266	348	1309.7	2882.6	8.57
.08	.292	301	1029.4	2550.8	8.32
.10	.315	261	828.4	2274.5	8.20
.12	.334	228	683.1	2042.6	8.22
.14	.347	200	576.7	1846.4	8.37
.16	.354	176	497.6	1679.3	8.62
.18	.357	156	438.0	1535.8	8.97
.20	.355	139	392.6	1411.8	9.42
.22	.348	125	357.9	1303.8	9.97
.24	.338	112	331.3	1209.1	10.62
.26	.326	101	310.9	1125.7	11.37
.28	.311	92.0	295.5	1051.7	12.24
.30	.295	83.9	284.2	985.7	13.24
.32	.278	76.8	276.4	926.4	14.38
.34	.260	70.6	271.4	873.1	15.67
.36	.242	65.1	269.0	824.8	17.13
.38	.224	60.3	268.9	780.9	18.79
.40	.207	56.1	271.0	740.8	20.66
.42	.190	52.3	275.1	704.1	22.79
.44	.174	48.9	281.2	670.3	25.19
.46	.159	45.9	289.3	639.1	27.91
.48	.144	43.2	299.5	610.2	30.99
.50	.131	40.7	311.7	583.4	34.48
.52	.118	38.5	326.2	558.5	38.44
.54	.106	36.5	343.1	535.2	42.92
.56	.0956	34.7	362.5	513.5	48.02
.58	.0858	33.0	384.6	493.1	53.81
.60	.0768	31.5	409.8	473.9	60.40

Table 4.3. The same as Table 4.2 except the attenuated projection operators A operate on a 10×10 transverse section giving 72 projection angles equally spaced over 360°. The maximum shown for λ_{min} is at μ = .12, .14, and the minimum shown for the condition number and trace $[(A^TA)^{-1}]$ is at μ = .28 and μ = 0, respectively.

μ	λ_{min}	λ_{max}	Condition Number	Trace(A^TA)	Trace$[(A^TA)^{-1}]$
0	.206	696	3384.4	6868.5	11.81
.02	.190	569	2990.6	5722.0	13.08
.04	.202	469	2323.5	4834.8	13.02
.06	.219	390	1777.9	4139.7	12.82
.08	.235	327	1392.6	3588.5	12.86
.10	.245	276	1125.3	3146.1	13.14
.12	.251	235	937.7	2786.6	13.67
.14	.251	202	804.4	2491.1	14.43
.16	.247	175	708.4	2245.5	15.43
.18	.238	152	639.1	2039.0	16.66
.20	.227	134	589.3	1863.8	18.16
.22	.214	119	554.2	1713.5	19.94
.24	.200	106	530.7	1583.6	22.05
.26	.184	95.2	516.6	1470.3	24.52
.28	.169	86.1	510.5	1370.6	27.42
.30	.153	78.3	511.4	1282.4	30.81
.32	.138	71.6	518.7	1203.8	34.76
.34	.124	65.9	532.2	1133.4	39.39
.36	.110	60.9	551.9	1069.8	44.80
.38	.0978	56.5	577.9	1012.3	51.12
.40	.0864	52.7	610.6	959.8	58.52
.42	.0759	49.4	650.4	911.9	67.18
.44	.0664	46.4	698.1	867.9	77.35
.46	.0579	43.7	754.6	827.4	89.28
.48	.0503	41.3	820.8	789.9	103.30
.50	.0436	39.1	898.3	755.1	119.80
.52	.0376	37.2	988.5	722.9	139.23
.54	.0323	35.4	1093.3	692.7	162.14
.56	.0278	33.7	1214.8	664.6	189.18
.58	.0238	32.2	1355.8	638.2	221.13
.60	.0203	30.8	1519.2	613.4	258.92

Table 4.4. The same as Table 4.2 except the attenuated projection operators A operate on a 12×12 transverse section giving 72 projection angles equally spaced over 360°. The maximum shown for λ_{min} is at $\mu = .10$, and the minimum shown for the condition number and trace $[(A^TA)^{-1}]$ is at $\mu = .24$ and $\mu = 0$, respectively.

μ	λ_{min}	λ_{max}	Condition Number	Trace(A^TA)	Trace$[(A^TA)^{-1}]$
0	.185	835	4511.2	9753.4	16.88
.02	.167	656	3936.3	7845.8	18.53
.04	.417	522	3005.9	6438.0	18.41
.06	.184	420	2283.1	5381.0	18.55
.08	.191	342	1793.9	4573.5	19.15
.10	.192	282	1465.6	3946.0	20.22
.12	.189	235	1242.5	3450.2	21.75
.14	.182	198	1089.7	3052.1	23.76
.16	.172	169	985.4	2727.7	26.30
.18	.160	146	916.2	2459.5	29.44
.20	.146	127	873.4	2235.0	33.27
.22	.132	112	851.8	2044.7	37.91
.24	.118	99.8	847.7	1881.6	43.51
.26	.104	89.5	859.4	1740.5	50.27
.28	.0914	80.9	886.0	1617.3	58.42
.30	.0795	73.7	927.4	1508.8	68.25
.32	.0687	67.6	984.0	1412.5	80.13
.34	.0589	62.3	1057.3	1326.6	94.49
.36	.0503	57.8	1149.1	1249.4	111.89
.38	.0427	53.8	1261.8	1179.7	132.98
.40	.0360	50.4	1398.8	1116.4	158.61
.42	.0302	47.3	1564.2	1058.7	189.78
.44	.0253	44.6	1763.1	1005.9	227.76
.46	.0211	42.2	2001.8	957.3	274.10
.48	.0175	40.0	2288.2	912.5	330.73
.50	.0144	38.0	2631.8	871.1	400.03
.52	.0119	36.2	3044.4	832.6	484.93
.54	.00976	34.6	3540.1	796.8	589.11
.56	.00799	33.0	4136.6	763.4	717.09
.58	.00651	31.6	4855.2	732.1	874.49
.60	.00530	30.3	5722.1	702.8	1068.3

Table 4.5. For attenuation coefficients between 0 and .60 pixel^{-1}, the minimum and maximum eigenvalues, the condition number, the trace, and the trace of the inverse of the matrix A^TA are evaluated for attenuated projection operators A which operate on an 8×8 transverse section giving 72 projections equally spaced over 360°. The matrix elements for A used ray factors instead of line lengths by replacing $\mathcal{R}\{\chi_{ij}(x,y); \xi_k, \theta_\ell\}$ in Eq. (4.22) with the area that the ray (k,ℓ) intersects the pixel (i,j). The maximum shown for λ_{min} is at $\mu = .22$ and .24, and the minimum shown for the condition number and trace $[(A^TA)^{-1}]$ is at $\mu = .38$ and $\mu = .16$, respectively.

μ	λ_{min}	λ_{max}	Condition Number	Trace(A^TA)	Trace[$(A^TA)^{-1}$]
0	.0121	551	45537	3177.6	133.42
.02	.0162	468	28879	2739.2	104.19
.04	.0282	401	14195	2382.6	67.45
.06	.0439	344	7833.6	2089.9	49.31
.08	.0605	297	4909.0	1847.9	40.28
.10	.0763	258	3382.8	1646.2	35.48
.12	.0900	225	2499.4	1476.9	32.89
.14	.101	197	1946.6	1333.6	31.60
.16	.110	174	1579.9	1211.6	31.19
.18	.116	154	1325.8	1106.8	31.40
.20	.120	137	1143.8	1016.3	32.12
.22	.121	123	1010.3	937.5	33.28
.24	.121	110	910.9	868.6	34.83
.26	.119	99.6	836.2	807.8	36.78
.28	.116	90.4	780.1	754.0	39.13
.30	.112	82.4	738.5	706.0	41.89
.32	.106	75.4	708.5	663.0	45.09
.34	.101	69.2	688.1	624.3	48.77
.36	.0945	63.8	675.8	589.4	52.98
.38	.0881	59.1	670.6	557.6	57.77
.40	.0816	54.9	672.0	528.6	63.22
.42	.0752	51.1	679.4	502.1	69.40
.44	.0690	47.7	692.5	477.8	76.42
.46	.0629	44.7	711.4	455.3	84.37
.48	.0571	42.0	735.9	434.6	93.38
.50	.0516	39.6	766.3	415.3	103.60
.52	.0465	37.3	802.7	397.4	115.19
.54	.0418	35.3	845.6	380.8	128.35
.56	.0374	33.5	895.4	365.2	143.30
.58	.0334	31.8	952.5	350.6	160.29
.60	.0297	30.2	1017.8	336.9	179.61

Table 4.6. The same as Table 4.5 except the attenuated projection operators A operate on a 10×10 transverse section giving 72 projection angles equally spaced over 360°. The maximum shown for λ_{min} is at $\mu = .18$, and the minumum shown for the condition number and trace $[(A^TA)^{-1}]$ is at $\mu = .30$ and $\mu = .12$, respectively.

μ	λ_{min}	λ_{max}	Condition Number	Trace(A^TA)	Trace$[(A^TA)^{-1}]$
0	.0086	690	80639	4942.8	253.3
.02	.0127	565	44285	4115.5	162.81
.04	.0239	465	19467	3474.4	98.53
.06	.0371	386	10422	2971.6	73.39
.08	.0497	324	6515.7	2572.5	62.26
.10	.0603	273	4528.3	2251.9	57.14
.12	.0685	233	3394.0	1991.4	55.20
.14	.0741	200	2692.7	1777.3	55.28
.16	.0773	173	2234.3	1599.3	56.82
.18	.0782	150	1923.2	1449.8	59.60
.20	.0774	132	1707.4	1323.0	63.50
.22	.0752	117	1556.7	1214.5	68.52
.24	.0718	104	1453.0	1120.7	74.72
.26	.0676	93.6	1384.8	1039.0	82.20
.28	.0628	84.5	1345.0	967.3	91.14
.30	.0578	76.8	1329.1	903.9	101.71
.32	.0525	70.1	1334.4	847.5	114.18
.34	.0474	64.4	1359.5	797.0	128.85
.36	.0423	59.4	1404.1	751.5	146.11
.38	.0375	55.0	1468.5	710.4	166.38
.40	.0329	51.2	1553.6	673.0	190.23
.42	.0288	47.8	1661.3	638.9	218.30
.44	.0249	44.7	1793.5	607.6	251.36
.46	.0215	42.0	1953.4	578.8	290.35
.48	.0185	39.6	2144.4	552.2	336.39
.50	.0158	37.4	2370.9	527.6	390.81
.52	.0134	35.4	2638.2	504.7	455.24
.54	.0114	33.6	2952.7	483.4	531.61
.56	.0960	31.9	3322.1	463.5	622.25
.58	.0809	30.4	3755.3	444.8	729.97
.60	.0679	29.0	4263.3	427.4	858.16

Table 4.7. The same as Table 4.5 except the attenuated projection operators A operate on a 12×12 transverse section giving 72 projection angles equally spaced over 360°. The maximum shown for λ_{min} is at $\mu = .16$, and the minimum shown for the condition number and trace $[(A^TA)^{-1}]$ is at $\mu = .26$ and $\mu = .10$, respectively.

μ	λ_{min}	λ_{max}	Condition Number	Trace(A^TA)	Trace$[(A^TA)^{-1}]$
0	.00462	830	179850	7111.8	441.13
.02	.00966	653	67556	5720.0	233.53
.04	.0197	519	26302	4693.1	138.55
.06	.0307	418	13614	3922.2	105.47
.08	.0403	340	8442.5	3333.4	92.18
.10	.0475	280	5896.7	2876.1	87.57
.12	.0521	233	4480.6	2514.9	87.82
.14	.0543	197	3627.8	2225.1	91.43
.16	.0544	168	3088.7	1989.0	97.80
.18	.0529	145	2740.7	1794.1	106.79
.20	.0501	126	2518.5	1631.0	118.51
.22	.0466	111	2385.7	1492.8	133.25
.24	.0425	98.7	2321.5	1374.5	151.47
.26	.0382	88.4	2314.6	1272.3	173.79
.28	.0338	79.8	2359.6	1183.0	201.03
.30	.0296	72.6	2455.7	1104.4	234.21
.32	.0255	66.4	2605.4	1034.8	274.63
.34	.0217	61.1	2814.1	972.6	323.89
.36	.0183	56.5	3089.8	916.8	384.02
.38	.0153	52.5	3443.3	866.4	457.52
.40	.0126	49.0	3888.4	820.6	547.54
.42	.0103	45.9	4442.2	778.8	658.00
.44	.00842	43.2	5126.8	740.6	793.81
.46	.00682	40.7	5969.3	705.5	961.12
.48	.00549	38.5	7004.1	673.0	1167.6
.50	.00440	36.4	8273.8	643.0	1423.0
.52	.00352	34.6	9831.6	615.1	1739.4
.54	.00280	32.9	11744	589.1	2132.2
.56	.00222	31.3	14092	564.9	2620.5
.58	.00176	29.9	16979	542.2	3228.6
.60	.00139	28.6	20532	520.9	3987.2

width were equal.

In Tables 4.2, 4.3, and 4.4 the minimum eigenvalue λ_{min} increases to a maximum before it decreases monotonically as the attenuation coefficient increases. As the size of the transverse section increases, the attenuation coefficient at which the maximum is obtained decreases. The maximum is obtained at $\mu = .18$ for the 8×8 transverse section array, at $\mu = .12$ for 10×10, and $\mu = .10$ pixel^{-1} for 12×12. As the attenuation coefficient increases the condition number of A^TA decreases monotonically to a minimum before it begins to increase monotonically. As the size of the transverse section array increases the minimum is obtained at lower and lower attenuation coefficients. The minimum is obtained at $\mu = .38$, $\mu = .28$, and $\mu = .24$ pixel^{-1} for the 8×8, 10×10, and 12×12 transverse section arrays, respectively.

The trace of the inverse matrix is somewhat oscillatory at first before it increases monotonically. Again as the size of the transverse section increases, the oscillatory behavior terminates at lower and lower attenuation coefficients. Note that the termination is at much lower attenuation coefficients ($\mu = .10$, $\mu = .06$, and $\mu = .04$ pixel^{-1} for 8×8, 10×10, and 12×12 transverse section arrays, respectively) than the maximum for λ_{min} or the minimum for the condition number. The trace of the inverse matrix is an important indicator of error propagation, since for equal statistical fluctuations in the projections, the average variance in the reconstruction is equal to $\sigma^2(\text{projection}) \times \text{trace}\,[(A^TA)^{-1}]/MN$. Therefore the tables indicate that as the

attenuation coefficient increases then so will the average variance. Note that the minimum of trace $[(A^TA)^{-1}]/MN$ for the 8×8 (MN=64), 10×10 (MN=100), and 12×12 (MN=144) arrays are all equal to .13.

The results given in Tables 4.5, 4.6, and 4.7 corresponding to replacing $\mathcal{R}\{\chi_{ij}(x,y);\xi_k,\theta_\ell\}$ with ray factors in Eq. (4.22), show a similar behavior; that is, as the attenuation coefficient increases the minimum eigenvalue increases to a maximum before it decreases monotonically and the condition number and trace $[(A^TA)^{-1}]$ both decrease to a minimum before monotonically increasing. Note that trace $[(A^TA)^{-1}]$ for the same size transverse section is larger weighting by ray factors than weighting by line lengths. This indicates that the average variance for the reconstructed image is larger using weights corresponding to ray factors than using line lengths.

4.7 Iterative Reconstruction Algorithms

Iterative methods are used to determine the minimum solution for the χ^2 function in Eq. (4.23). There are two principal types of iterative reconstruction procedures: (1) those which adjust the parameters that are involved in one or a small number of projection constraints at each iterative step--these are referred to as ART-type methods; and (2) those which adjust all the parameters based on information from all the projection samples at each iteration--these are referred to as SIRT-type methods.

An ART (for Algebraic Reconstruction Techniques) method was first proposed by Gordon, Bender, and Herman (1970). A tutorial on ART was later published by Gordon (1974) and a description of other types of ART methods along with optimization criteria and theorems on the convergence of the algorithms to optimum images was given by Herman and Lent (1976). A method for incorporating errors with the ART-type algorithms was described by Huebel and Lantz (1975). The ART-type algorithm was first suggested by Kaczmarz (1937). For the finite-dimensional case, the proof of convergence for consistent systems is given in (Durand, 1960; Tanabe, 1971; and Herman, Lent and Rowland, 1973). Convergence rates for this iterative procedure are analyzed by Hamaker and Solmon (1978).

SIRT (for Simultaneous Iterative Reconstruction Techniques) methods were first applied to reconstruction tomography by Goitein (1971) and Gilbert (1972). Later steepest descent methods and conjugate gradient methods were implemented by Huesman and co-workers (1977). A more recent paper about SIRT-type algorithms is by Lakashminarayanan and Lent (1979). These iterative schemes basically determine a direction q^n and a step length α^n for each iteration such that the new solution is given by

$$\rho^{n+1} = \rho^n + \alpha^n q^n . \tag{4.37}$$

The step length calculation α^n is determined so that $\chi^2(\rho^{n+1}) = \chi^2(\rho^n + \alpha^n q^n)$ is a minimum. It was shown in (Huesman et al., 1977) that Goitein's method is the same as a steepest descent method in a transformed space. In most cases, convergence of the iterative process

is accelerated by performing a scale change on the parameters. The scale change is given by

$$\rho' = D\rho \tag{4.38}$$

where D is a diagonal matrix with diagonal elements equal to

$$D_{ii} = \left[(A^T \Phi^{-1} A)_{ii}\right]^{1/2} . \tag{4.39}$$

The iterative stepping is performed on the transformed variables ρ' and the final reconstruction is obtained by the operation

$$\rho = D^{-1} \rho' . \tag{4.40}$$

This method of parameter scaling also improves the rate of convergence for the conjugate gradient method. The conjugate gradient method for solving a system of linear algebraic equations was originally developed by Hestenes and Stiefel (1952). Rates of convergence are discussed in Ortega and Rheinboldt (1970) and in Kammerer and Nashed (1972).

In the next three sections the gradient, conjugate gradient and ART-type algorithms are discussed as they apply to reconstructing attenuated data.

4.7.1. The Gradient Method

At a given point ρ^n the gradient method takes a step (i.e., $\rho^{n+1} = \rho^n + \alpha^n q^n$) in a direction q^n which is one half the negative of the gradient at ρ^n:

$$q^n = A^T\Phi^{-1} (P-A\rho^n). \tag{4.41}$$

This is a direction which gives the steepest descent of the χ^2 function -- thus such methods are commonly called steepest descent methods. The step length α^n in the direction of q^n is choosen so that $\chi^2(\rho^n + \alpha^n q^n)$ is a minimum:

$$\alpha^n = \langle q^n, q^n \rangle / \langle A^T\Phi^{-1}Aq^n, q^n \rangle \ . \tag{4.42}$$

The resulting algorithum is described as follows (Huesman et.al., 1977; Budinger et.al., 1979):

1. $q^o = A^T\Phi^{-1} P - A^T\Phi^{-1}A\rho^o = A^T\Phi^{-1}(P-A\rho^o)$
2. $\chi^2_o = (\rho^o)^T A^T\Phi^{-1} A\rho^o - 2(\rho^o)^T A^T\Phi^{-1}P + P^T\Phi^{-1}P$
3. $\beta^n = A^T\Phi^{-1}A\, q^n$
4. $\alpha^n = \langle q^n, q^n \rangle / \langle \beta^n, q^n \rangle$
5. $\rho^{n+1} = \rho^n + \alpha^n q^n$
6. $\chi^2_{n+1} = \chi^2_n - \alpha^n \langle q^n, q^n \rangle$
7. $q^{n+1} = q^n - \alpha^n\beta^n$
8. jump back to 3 .

Most of the computation time is expended in step 3 in calculating $A^T\Phi^{-1}Aq^n$. The computation time is cut in half by calculating this once and storing the result in β^n, which is then used in steps 4 and 7. The algorithm requires that memory is allocated for the vectors ρ^n, q^n, and β^n which are updated at each iteration.

4.7.2 The Conjugate Gradient Method

The conjugate gradient method improves the convergence of the iterative process. The direction of the first step q^0 is taken the same as the gradient method,

$$q^0 = r^0 = A^T\Phi^{-1} (P - A\rho^0)$$

$$\rho^1 = \rho^0 + \alpha^0 q^0 \quad . \tag{4.43}$$

The succeeding step directions are given by

$$q^n = r^n - \beta^n q^{n-1} \tag{4.44}$$

where

$$\beta^n = \langle r^n, A^T\Phi^{-1}A\, q^{n-1} \rangle / \langle q^{n-1}, A^T\Phi^{-1}A\, q^{n-1} \rangle \tag{4.45}$$

and where $r^n = A^T\Phi^{-1}(P-A\rho^n)$ is equal to one half the negative of the gradient. This gives an $A^T\Phi^{-1}A$- orthogonal set of vectors $\{q^1, \ldots q^n\}$; that is the inner product $\langle q^n, A^T\Phi A q^m \rangle = 0 \; \forall \; n \neq m$. The step length calculation α^n is given by Eq. (4.42). This gives a new estimate:

$$\rho^{n+1} = \rho^n + \alpha^n q^n \quad .$$

The following identities proven in (Hestenes and Stiefel, 1952; Hestenes, 1956; Ortega and Rheinboldt, 1970; Budinger et al., 1979)

$$\langle r^n, r^m \rangle = 0 \quad \text{for } m \neq n \tag{4.46}$$

$$\beta^{n+1} = \frac{-\| r^{n+1} \|^2}{\| r^n \|^2} \tag{4.47}$$

$$\alpha^n = \frac{\| r^n \|^2}{\langle r^n, A^T \Phi^{-1} A q^n \rangle} \tag{4.48}$$

$$r^{n+1} = r^n - \alpha^n A^T \Phi^{-1} A q^n \tag{4.49}$$

simplify the calculations which are given in the following algorithm

1. $r^0 = A^T \Phi^{-1} (P - A\rho^0)$
2. $\chi_0^2 = (\rho^0)^T A^T \Phi^{-1} A \rho^0 - 2(\rho^0)^T A^T \Phi^{-1} P + P^T \Phi^{-1} P$
3. $q^0 = 0$
4. $\beta^0 = 0$
5. $\beta^n = \beta^{n-1} \langle r^{n-1}, r^{n-1} \rangle$
6. $q^n = r^{n-1} - \beta^n q^{n-1}$
7. $\beta^n = -1/\langle r^{n-1}, r^{n-1} \rangle$
8. $\gamma^n = A^T \Phi^{-1} A q^n$
9. $\alpha^n = \langle r^{n-1}, r^{n-1} \rangle / \langle r^{n-1}, \gamma^n \rangle$
10. $\rho^n = \rho^{n-1} + \alpha^n q^n$
11. $\chi_n^2 = \chi_{n-1}^2 - \alpha^n \langle r^{n-1}, r^{n-1} \rangle$
12. $r^n = r^{n-1} - \alpha^n \gamma^n$
13. jump back to step 5 .

Most of the computation time is expended in step 8. The result for $A^T \Phi^{-1} A q^n$ is calculated once and stored in γ^n which is then used in steps 9 and 12. The algorithm requires that memory is allocated for the vectors ρ^n, r^n, q^n, and γ^n.

For a sequence $\{\rho^n\}$ which converges to ρ, Ortega and Rheinboldt (1970) define the factor $R_1\{\rho^n\}$ to be

$$R_1\{\rho^n\} = \lim_{n \to \infty} \sup \|\rho^n - \rho\|^{1/n}. \tag{4.50}$$

If $0 < R_1\{\rho^n\} < 1$, the convergence of $\{\rho^n\}$ to ρ is R - linear, while if $R_1 = 1$ or $R_1 = 0$ the convergence is R-sublinear or R-superlinear, respectively. Under conditions where the minimum of $\chi^2(\rho)$ in Eq. (4.23) has a unique solution it can be shown that the gradient algorithm is R-linear. Whereas the conjugate gradient algorithm converges to the solution of minimum norm in a finite number of steps. Therefore the conjugate gradient algorithm has a superlinear rate of convergence.

To test the convergence of the gradient and conjugate gradient methods, computer simulations were done that projected pseudo data of a 64×64 array containing a 60 pixel diameter disc of uniform concentration and uniform attenuator so that the measured projections were in the range of the discrete attenuated projection operator. The data were taken at 100 equal angles over 2π. The results at each iteration are shown in Table 4.8 for the conjugate gradient algorithm and in Table 4.9 for the gradient algorithm. Since the true solution was known, the difference between it and the solution at the nth iteration was tabulated along with the χ^2 at each iteration. For consistent data $\|\rho^n - \rho\|$ and the χ^2 function is guaranteed to converge to zero in 4096 steps for the conjugate gradient algorithm if one has perfect numerical accuracy. For the gradient algorithm convergence is guaranteed only as the number of iterations approach infinity. A comparison of the

Table 4.8. For μ=0, .001, .0958, .15, and .30 pixel^{-1}, the chi-square χ^2 in Eq. (4.23) with $\Phi = I$ and the difference between the true solution and that at the nth iteration is tabulated as a function of iteration for the conjugate gradient algorithm. The data were 100 true projections of ρ over 2π where ρ was a 60 pixel diameter disc of uniform emitter concentration and uniform attenuator in a 64×64 array.

CONJUGATE GRADIENT ALGORITHM

	μ = 0		μ = .001		μ = .0958		μ = .15		μ = .30	
Iteration	$\|\rho^n-\rho\|$	χ^2	$\|\rho^n-\rho\|$	χ^2	$\|\rho^n-\rho\|$	χ^2	$\|\rho^n-\rho\|$	χ^2	$\|\rho^n-\rho\|$	χ^2
0	3570	9.83×10^{10}	3570	9.58×10^{10}	3570	1.36×10^{10}	3570	6.54×10^{9}	3570	1.77×10^{9}
1	929	4.01×10^{8}	928	3.97×10^{8}	1560	1.03×10^{9}	2170	1.04×10^{9}	3010	5.42×10^{8}
2	549	1.18×10^{8}	532	1.07×10^{8}	328	1.30×10^{7}	933	6.38×10^{7}	2250	7.53×10^{7}
3	363	3.76×10^{7}	356	3.59×10^{7}	144	1.30×10^{6}	476	1.31×10^{7}	2010	3.83×10^{7}
4	236	1.07×10^{7}	234	1.04×10^{7}	121	6.43×10^{5}	379	7.24×10^{6}	1900	2.39×10^{7}
5	167	3.33×10^{6}	166	3.20×10^{6}	95.0	2.85×10^{5}	231	2.35×10^{6}	1780	1.72×10^{7}
6	126	1.25×10^{6}	125	1.20×10^{6}	74.0	1.09×10^{5}	173	8.87×10^{5}	1610	9.40×10^{6}
7	96.3	5.46×10^{5}	95.3	5.23×10^{5}	63.7	4.82×10^{4}	111	2.24×10^{5}	1480	6.57×10^{6}
8	81.9	3.29×10^{5}	81.0	3.13×10^{5}	55.1	2.43×10^{4}	90.5	1.20×10^{5}	1370	4.55×10^{6}
9	68.8	1.61×10^{5}	68.2	1.53×10^{5}	46.9	1.45×10^{4}	71.9	4.52×10^{4}	1280	3.30×10^{6}
10	58.9	8.25×10^{4}	60.2	9.40×10^{4}	42.3	1.07×10^{4}	65.2	2.56×10^{4}	1190	2.41×10^{6}
11	58.2	7.89×10^{4}	58.2	7.69×10^{4}	34.7	6.12×10^{3}	58.9	1.64×10^{4}	1110	1.83×10^{6}
12	51.5	5.19×10^{4}	51.3	5.02×10^{4}	33.3	5.50×10^{3}	52.9	9.97×10^{3}	1040	1.42×10^{6}
13	46.7	3.86×10^{4}	46.3	3.72×10^{4}	30.1	4.02×10^{3}	47.8	6.76×10^{3}	971	1.10×10^{6}
14	39.5	2.39×10^{4}	39.2	2.29×10^{4}	26.5	2.85×10^{3}	46.7	6.20×10^{3}	910	8.64×10^{5}
15	33.4	1.44×10^{4}	33.1	1.38×10^{4}	25.3	2.52×10^{3}	42.9	4.43×10^{3}	860	7.10×10^{5}
16	30.4	1.07×10^{4}	29.6	9.59×10^{3}	23.3	2.01×10^{3}	41.3	3.86×10^{3}	845	6.68×10^{5}
17	29.2	9.30×10^{3}	28.5	8.45×10^{3}	20.2	1.40×10^{3}	39.2	3.15×10^{3}	798	5.53×10^{5}
18	26.2	6.15×10^{3}	26.1	5.89×10^{3}	18.7	1.18×10^{3}	36.1	2.27×10^{3}	776	5.12×10^{5}
19	23.8	4.20×10^{3}	23.8	4.10×10^{3}	17.0	9.08×10^{2}	34.8	1.99×10^{3}	732	4.26×10^{5}
20	22.7	3.49×10^{3}	22.7	3.44×10^{3}	15.0	6.57×10^{2}	33.2	1.66×10^{3}	699	3.73×10^{5}
21	21.9	3.11×10^{3}	22.6	3.33×10^{3}	13.4	4.96×10^{2}	30.8	1.32×10^{3}	666	3.20×10^{5}
22	21.2	2.82×10^{3}	21.5	2.87×10^{3}	12.9	4.56×10^{2}	30.0	1.24×10^{3}	627	2.64×10^{5}
23	20.6	2.52×10^{3}	20.5	2.44×10^{3}	11.5	3.51×10^{2}	28.2	1.04×10^{3}	617	2.51×10^{5}
24	18.9	1.98×10^{3}	18.9	1.91×10^{3}	11.1	3.25×10^{2}	27.2	9.56×10^{2}	584	2.13×10^{5}
25	17.7	1.63×10^{3}	17.7	1.59×10^{3}	9.7	2.45×10^{2}	25.2	7.89×10^{2}	574	2.02×10^{5}
26	17.1	1.46×10^{3}	17.0	1.42×10^{3}	8.2	1.73×10^{2}	23.1	6.41×10^{2}	545	1.73×10^{5}
27	15.4	1.08×10^{3}	15.3	1.05×10^{3}	8.0	1.61×10^{2}	22.4	5.95×10^{2}	537	1.66×10^{5}
28	14.9	9.87×10^{3}	14.8	9.52×10^{2}	7.5	1.41×10^{2}	20.5	4.76×10^{2}	512	1.46×10^{5}
29	13.9	8.16×10^{3}	13.9	7.92×10^{2}	6.9	1.19×10^{2}	19.8	4.37×10^{2}	500	1.37×10^{5}
30	13.1	7.00×10^{3}	13.0	6.68×10^{2}	6.1	9.06×10^{1}	18.1	3.50×10^{2}	472	1.18×10^{5}

XBL794-3391

Table 4.9. For $\mu = 0$, .001, .0958, .15, and .30 pixel^{-1}, the chi-square χ^2 in Eq. (4.23) with $\Phi = I$ and the difference between the true solution and that at the nth iteration is tabulated as a function of iteration for the gradient algorithm. The data were 100 true projections of ρ over 2π where ρ was a 60 pixel diameter disc of uniform emitter concentration and uniform attenuator in a 64×64 array.

GRADIENT ALGORITHM

	$\mu = 0$		$\mu = .001$		$\mu = .0958$		$\mu = .15$		$\mu = .30$	
Iteration	$\|\rho^n-\rho\|$	χ^2	$\|\rho^n-\rho\|$	χ^2	$\|\rho^n-\rho\|$	χ^2	$\|\rho^n-\rho\|$	χ^2	$\|\rho^n-\rho\|$	χ^2
0	3570	9.83×10^{10}	3570	9.58×10^{10}	3570	1.36×10^{10}	3570	6.54×10^{9}	3570	1.77×10^{9}
1	929	4.01×10^{8}	928	3.97×10^{8}	1560	1.03×10^{9}	2170	1.04×10^{9}	3010	5.42×10^{8}
2	550	1.18×10^{8}	533	1.08×10^{8}	429	8.95×10^{7}	1100	2.10×10^{8}	2430	2.04×10^{8}
3	461	6.58×10^{7}	447	6.14×10^{7}	329	1.65×10^{7}	948	7.68×10^{7}	2320	1.04×10^{8}
4	440	5.24×10^{7}	428	4.84×10^{7}	226	6.17×10^{6}	710	3.88×10^{7}	2150	6.40×10^{7}
5	392	4.23×10^{7}	379	3.87×10^{7}	205	3.88×10^{6}	653	2.53×10^{7}	2100	4.63×10^{7}
6	376	3.46×10^{7}	363	3.14×10^{7}	170	2.53×10^{6}	525	1.71×10^{7}	2000	3.57×10^{7}
7	338	2.85×10^{7}	325	2.56×10^{7}	158	1.72×10^{6}	490	1.20×10^{7}	1970	2.92×10^{7}
8	326	2.36×10^{7}	314	2.11×10^{7}	137	1.21×10^{6}	406	8.69×10^{6}	1900	2.45×10^{7}
9	296	1.97×10^{7}	284	1.75×10^{7}	130	8.76×10^{5}	382	6.42×10^{6}	1880	2.12×10^{7}
10	286	1.65×10^{7}	275	1.46×10^{7}	117	6.54×10^{5}	323	4.82×10^{6}	1820	1.86×10^{7}
11	263	1.39×10^{7}	251	1.22×10^{7}	112	5.04×10^{5}	306	3.67×10^{6}	1800	1.65×10^{7}
12	255	1.18×10^{7}	244	1.03×10^{7}	103	3.97×10^{5}	264	2.83×10^{6}	1750	1.48×10^{7}
13	235	1.01×10^{7}	225	8.78×10^{6}	99.8	3.20×10^{5}	251	2.21×10^{6}	1740	1.34×10^{7}
14	229	8.64×10^{6}	219	7.50×10^{6}	93.0	2.63×10^{5}	220	1.75×10^{6}	1690	1.23×10^{7}
15	213	7.45×10^{6}	204	6.45×10^{6}	90.6	2.19×10^{5}	211	1.39×10^{6}	1680	1.13×10^{7}
16	208	6.46×10^{6}	199	5.57×10^{6}	85.4	1.85×10^{5}	186	1.12×10^{6}	1640	1.04×10^{7}
17	195	5.63×10^{6}	186	4.48×10^{6}	83.5	1.58×10^{5}	180	9.06×10^{5}	1630	9.67×10^{6}
18	191	4.92×10^{6}	182	4.23×10^{6}	79.4	1.36×10^{5}	161	7.40×10^{5}	1600	9.01×10^{6}
19	180	4.33×10^{6}	172	3.71×10^{6}	77.9	1.18×10^{5}	156	6.09×10^{5}	1590	8.42×10^{6}
20	176	3.82×10^{6}	168	3.28×10^{6}	74.5	1.04×10^{5}	141	5.05×10^{5}	1560	7.90×10^{6}
21	167	3.39×10^{6}	159	2.90×10^{6}	73.3	9.13×10^{4}	137	4.21×10^{5}	1550	7.43×10^{6}
22	164	3.02×10^{6}	157	2.58×10^{6}	70.5	8.10×10^{4}	126	3.54×10^{5}	1530	7.01×10^{6}
23	156	2.70×10^{6}	149	2.31×10^{6}	69.5	7.23×10^{4}	122	2.99×10^{5}	1520	6.63×10^{6}
24	153	2.43×10^{6}	147	2.07×10^{6}	67.2	6.48×10^{4}	113	2.54×10^{5}	1490	6.28×10^{6}
25	146	2.19×10^{6}	140	1.87×10^{6}	66.3	5.85×10^{4}	111	2.17×10^{5}	1490	5.97×10^{6}
26	144	1.98×10^{6}	138	1.69×10^{6}	64.3	5.30×10^{4}	103	1.86×10^{5}	1460	5.68×10^{6}
27	138	1.80×10^{6}	132	1.54×10^{6}	63.6	4.83×10^{4}	101	1.61×10^{5}	1460	5.41×10^{6}
28	136	1.63×10^{6}	131	1.40×10^{6}	61.9	4.42×10^{4}	95.2	1.40×10^{5}	1430	5.17×10^{6}
29	131	1.49×10^{6}	126	1.28×10^{6}	61.3	4.06×10^{4}	93.4	1.22×10^{5}	1430	4.94×10^{6}
30	129	1.37×10^{6}	124	1.17×10^{6}	59.7	3.75×10^{4}	88.5	1.06×10^{5}	1410	4.73×10^{6}

XBL794-3390

rate of convergence for the conjugate gradient and gradient algorithms is shown in Fig. 4.7.

The data in Tables 4.8 and 4.9 indicate that the rate of convergence at least for the first thirty iterations decreases as the attenuation coefficient increases above $\mu = .0958$ (see also Fig. 4.7). The rate of convergence for $\mu = .0958$ is better than $\mu = .001$ and $\mu = 0$ and it seems to decrease as you approach zero. It appears that there is an attenuation coefficient μ^* at which there is an optimum rate of convergence at least for the first thirty iterations so that as you decrease or increase μ the rate of convergences decreases.

4.7.3 The ART Method

The ART algorithm determines the solution to a consistent system of equations

$$A\rho = P \ . \tag{4.20}$$

At the nth iteration the solution vector ρ^n satisfies the equation

$$\langle a_j, \rho^n \rangle = p_j - r_j^n \tag{4.51}$$

where a_j is the j th row of the matrix A, p_j is the j th projection sample, and r_j^n is the residual in the j th projection. A new solution to ρ is determined by solving the equation

$$\langle a_j, \rho^n + q^n \rangle = p_j \tag{4.52}$$

for q^n. Combining Eqs. (4.51) and (4.52) gives

$$\langle a_j, q^n \rangle = r_j^n \ . \tag{4.53}$$

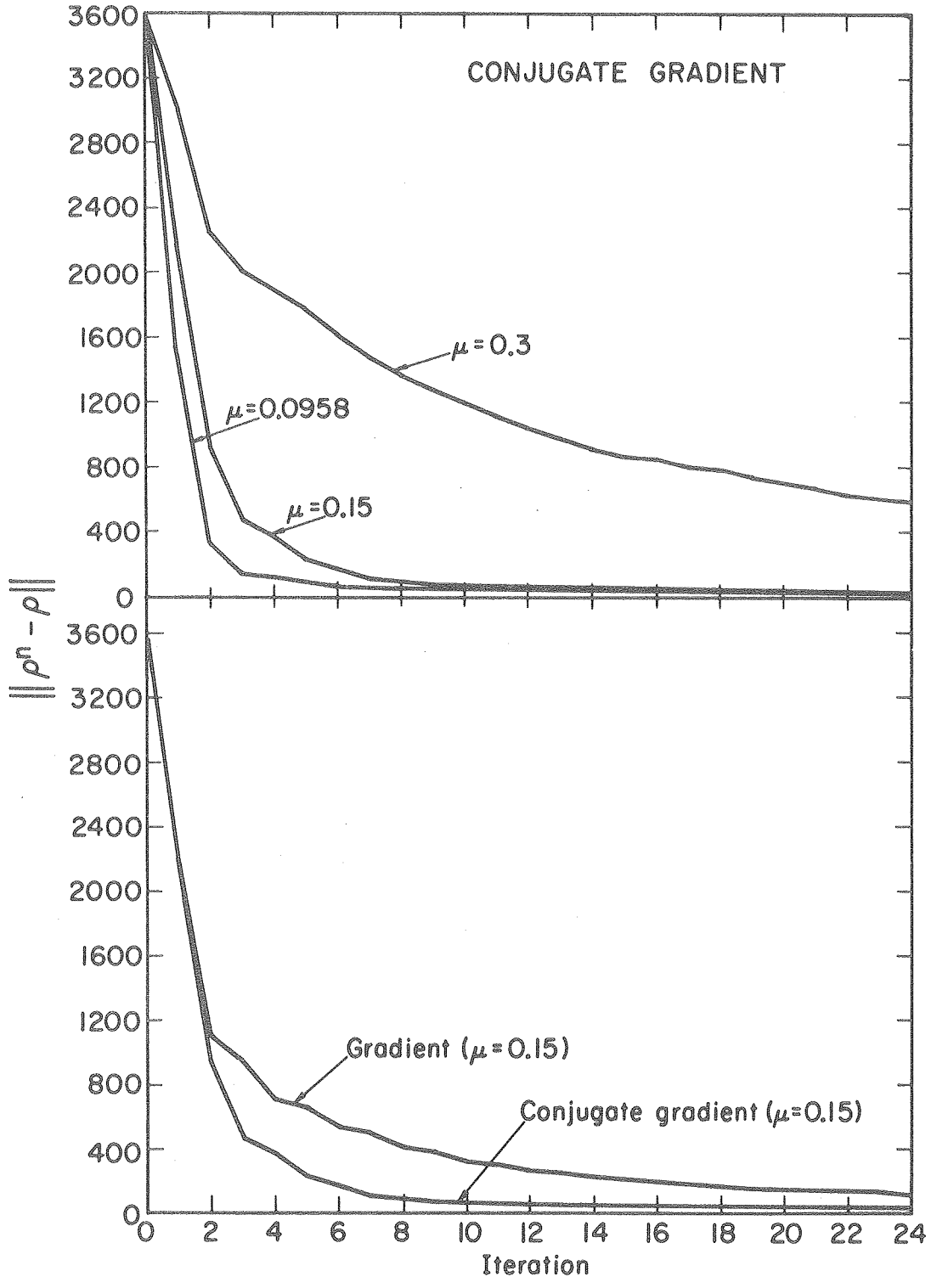

XBL793-3300

Figure 4.7. The top graph compares the convergence of the conjugate gradient algorithm for attenuation coefficients .0958, .15, and .30 pixel^{-1}. The bottom graph compares the convergence of the gradient and conjugate gradient algorithms for $\mu = .15$ pixel^{-1}. In all cases the data were 100 true projections of ρ taken over 2π where ρ was a 60 pixel diameter disc of uniform emitter concentration and uniform attenuator in a 64×64 array.

The solution for q^n satisfies

$$q^n = a_j^G r_j^n \tag{4.54}$$

where a_j^G denotes the generalized inverse of the row matrix a_j. The generalized inverse of a_j is easily calculated and is given by

$$a_j^G = \frac{1}{\| a_j \|^2} a_j^T . \tag{4.55}$$

The new solution for ρ is given by

$$\rho^{n+1} = \rho^n + q^n \tag{4.56}$$

For a given ρ, the operator $P_{\mu,j}$ at the nth iteration is given by

$$P_{\mu,j} \rho' = \rho' + a_j^G a_j(\rho-\rho') \tag{4.57}$$

where $j = n \bmod KL+1$, K is the number of projection bins, and L is the number of angles. For the discrete case the operator $P_{\mu,\theta}$ in Corollary 3.12.1 is the product of the individual projections $P_{\mu,j}$ which corresponds to the projection bins at the angle θ; that is,

$$P_{\mu,\theta} = \prod_{j=K_1(\theta)}^{K_2(\theta)} P_{\mu,j}$$

where $K_1(\theta)$ and $K_2(\theta)$ are the minimum and maximum index for j corresponding to the first and the last projection bin at the angle θ.

The ART algorithm is summarized in the following steps. Let KL be the total number of projection samples for all angles, then

1. Choose ρ^0
2. $j = n \bmod KL + 1$
3. $r_j^n = p_j - \langle a_j, \rho^n \rangle$
4. $q^n = r_j^n \, a_j^T / \|a_j\|^2$
5. $\rho^{n+1} = \rho^n + q^n$
6. jump back to 2 .

The vector q^n will be zero except for a very few pixels which intersect the jth ray.

If the projections P have statistical fluctuations, then it is highly likely that Eq. (4.20) is inconsistent. In this case Eq. (4.20) is augmented to include errors giving

$$\begin{aligned} A\rho + E &= P \\ A^T E &= 0 \end{aligned} \tag{4.58}$$

where the zero matrix 0 indicates that the back-projection of the errors E are constrained to be zero (Huebel and Lantz, 1975). The solution ρ and E to the new matrix equation

$$\begin{pmatrix} A & I \\ 0 & A^T \end{pmatrix} \begin{pmatrix} \rho \\ E \end{pmatrix} = \begin{pmatrix} P \\ 0 \end{pmatrix} \tag{4.59}$$

is determined by the ART algorithm described above:

1. Choose ρ^0, E^0

2. $j = n \bmod (KL + MN) + 1$

3. if $1 \leq j \leq KL$ then

$$r_j^n = p_j - \langle a_j, \rho^n \rangle - e_j^n$$

if $KL + 1 \leq j \leq KL + MN$ then $j' = KL + MN - j$ and

$$r_j^n = - \langle (a^T)_{j'}, E^n \rangle$$

4. if $1 \leq j \leq KL$ then

$$q^n = r_j^n \, a_j^T / (\| a_j \|^2 + 1)$$

$$v_j^n = r_j^n / (\| a_j \|^2 + 1), \quad v_i^n = 0 \quad i = 1, \ldots, KL \; i \neq j$$

if $KL + 1 \leq j \leq KL + MN$ then $j' = KL + MN - j$ and

$$q^n = 0$$

$$v^n = r_j^n \, (a^T)_{j'}^T / \| (a^T)_{j'} \|^2$$

5. $\rho^{n+1} = \rho^n + q^n$

$$E^{n+1} = E^n + v^n$$

6. jump back to 2 .

The $(a^T)_j$ denotes the jth row of the matrix A^T.

If the initial solution is chosen to be zero then both algorithms converge to the minimum norm solution (Tanabe, 1971). Hamaker and Solmon (1978) have shown that the rates of convergence depend on the angle between the projections, the order in which the angles are chosen for the succeeding iterations, and the choice of the initial solution.

4.8. Emission and Transmission Noise Propagation in Emission Computed Tomography

The algorithm illustrated in Fig. 4.8 can be used to reconstruct radionuclide distributions from projection data which have been attenuated by a variable attenuation coefficient. A transmission reconstruction is first done to accurately determine the attenuation coefficients. Then the factors $s_{ij}(\xi_k, \theta_\ell)$ are evaluated using either Eq. (4.15) or Eq. (4.22). The radionuclide distribution is then reconstructed using an iterative algorithm to fit the emission projection data to the projections given by the discrete attenuated transform in Eq. (4.20).

This method of attenuation correction requires two reconstructions: one for the transmission data to obtain the attenuation coefficients and one for the emission data to obtain the final reconstruction. Errors in the reconstruction of the attenuation coefficients will increase the errors in the emission reconstruction. These errors in the emission reconstruction are the result of noise propagated from three sources: 1) statistical fluctuations in emission data, 2) statistical fluctuations in the incident transmission beam, and 3) statistical fluctuations in the emerging transmission beam. In the sections to follow we will first define some statistical concepts and then analyze the emission and transmission noise propagation for the algorithm in Fig. 4.8.

4.8.1 Definitions for the Statistical Aspects of the Attenuated Reconstruction Problem

In the previous sections, we have been discussing the deterministic problem of reconstructing attenuated projection data. However, by the

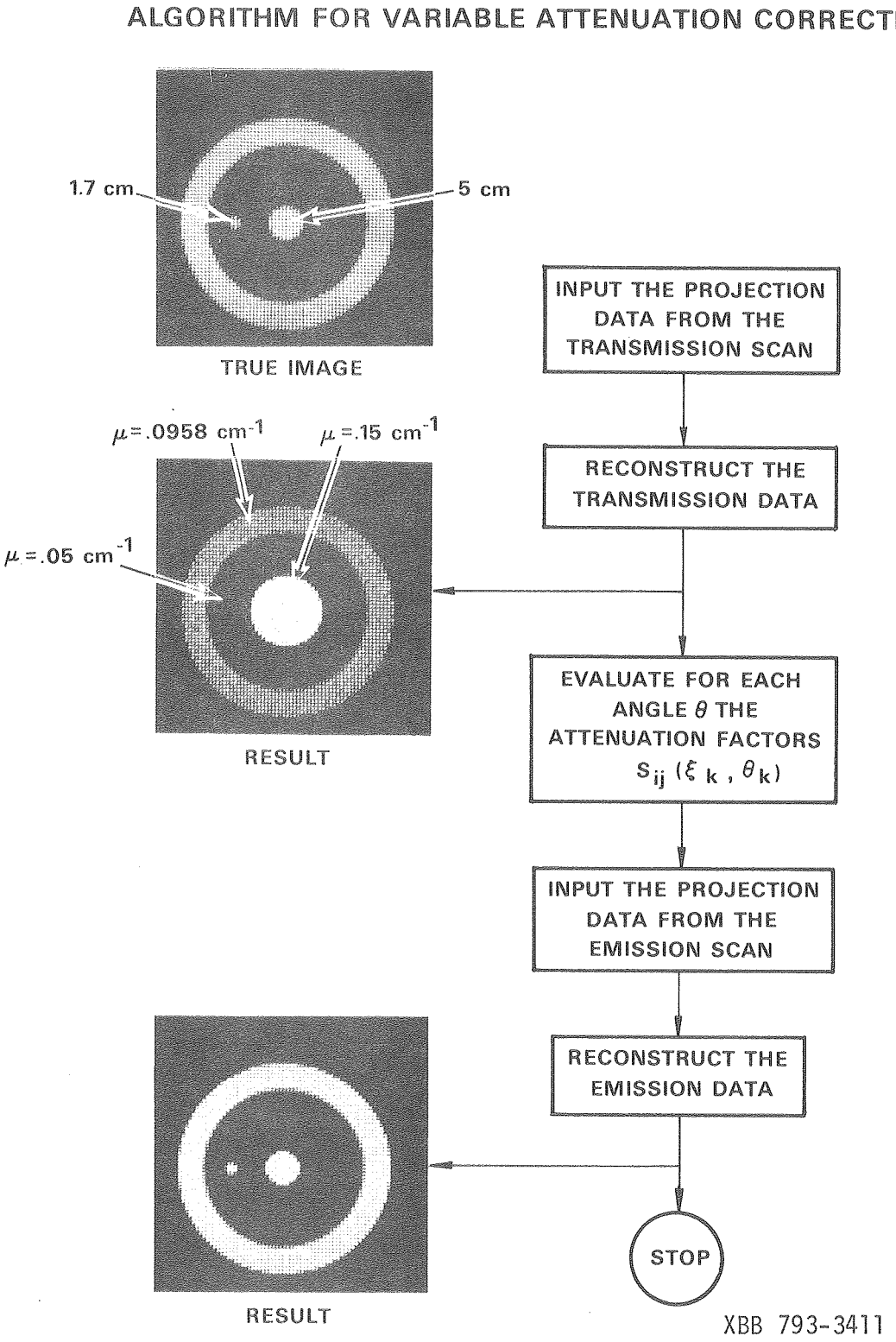

Figure 4.8. Algorithm for reconstructing emission data attenuated by a variable attenuation coefficient. Transmission data is reconstructed in order to determine the actual attenuation factors $s_{ij}(\xi_k,\theta_\ell)$ in Eq. (4.15) or Eq. (4.22). The emission reconstruction uses these factors to compensate for attenuation.

statistical nature of the measured projections, the reconstructed image represents one possible outcome of a random stochastic process. A stochastic process is a function of a one-dimensional subset S of the real numbers so that for every element of S there exists a set of possible outcomes defined by a probability density function. When the dimensionality of S is two or greater, the random process is called a random field (Rosenfeld and Kak, 1976). The family of reconstructions $\rho(x,y) = \rho(\hat{x})$ is a random field with probability distribution function

$$\Phi_\rho(z_1,z_2,\ldots,z_n;\ \hat{x}_1,\hat{x}_2,\ldots,\hat{x}_n) = \text{Prob}\{\rho(\hat{x}_1)\leqslant z_1,\ \rho(\hat{x}_2)\leqslant z_2,\ldots,\rho(\hat{x}_n)\leqslant z_n\} \tag{4.60}$$

The random field $\rho(\hat{x})$ is a random variable for every $\hat{x}$ in the xy-plane. Thus the probability density function given by $f_\rho(z;\hat{x}) = d(\Phi_\rho(z;\hat{x}))/dz$ and its expected value

$$m_\rho(\hat{x}) = E\{\rho(\hat{x})\} = \int_{-\infty}^{\infty} z\ f_\rho(z;\hat{x})dz \tag{4.61}$$

is a function of $\hat{x}$. This expectation is called the mean of the random field ρ at $\hat{x}$. Other important concepts which describe a random process are as follows (Rosenfeld and Kak, 1976)

Autocorrelation -

$$R_{\rho\rho}(\hat{x}_1,\hat{x}_2) = E\{\rho(\hat{x}_1)\,\rho(\hat{x}_2)\} = \iint z_1 z_2\ f_\rho(z_1,z_2;\hat{x}_1,\hat{x}_2)dz_1dz_2 \tag{4.62}$$

Autocovariance -

$$C_{\rho\rho}(\hat{x}_1,\hat{x}_2) = E\{[\rho(\hat{x}_1) - m_\rho(\hat{x}_1)]\,[\rho(\hat{x}_2) - m_\rho(\hat{x}_2)]\}$$
$$= R_{\rho\rho}(\hat{x}_1,\hat{x}_2) - m_\rho(\hat{x}_1)\, m_\rho(\hat{x}_2) \tag{4.63}$$

Cross correlation of two random fields ρ and μ -

$$C_{\rho\mu}(\hat{x}_1,\hat{x}_2) = E\{[\rho(\hat{x}_1) - m_\rho(\hat{x}_1)]\,[\mu(\hat{x}_2) - m_\mu(\hat{x}_2)]\}$$
$$= R_{\rho\mu}(\hat{x}_1,\hat{x}_2) - m_\rho(\hat{x}_1)\, m_\mu(\hat{x}_2)\,. \tag{4.64}$$

The variance of the random field ρ at $\hat{x}$ is $\sigma^2_\rho(\hat{x}) = C_{\rho\rho}(\hat{x},\hat{x})$. Two random fields ρ and μ are uncorrelated if $C_{\rho\mu}(\hat{x}_1,\hat{x}_2) = 0$ for all $\hat{x}_1$, $\hat{x}_2$. This implies that $E\{\rho(\hat{x}_1)\,\mu(\hat{x}_2)\} = E\{\rho(\hat{x}_1)\}\,E\{\mu(\hat{x}_2)\}$. Two random fields ρ and μ are called orthogonal if $R_{\rho\mu}(\hat{x}_1,\hat{x}_2) = 0$.

The random field is homogeneous if the mean value function in Eq. (4.61) is constant (i.e., $m_\rho(\hat{x}) = m$ for all $\hat{x}$) and the autocorrelation function is translation invariant:

$$R_{\rho\rho}(\hat{x}_1,\hat{x}_2) = R_{\rho\rho}(\hat{x}_1-\hat{x}_2)\,. \tag{4.65}$$

In Eq. (4.65) the expression for Eq. (4.62) has been reduced from an expression in four variables to an expression in two variables, which are the coordinates of the difference vector. This allows us to redefine the autocorrelation function:

$$R_{\rho\rho}(\alpha,\beta) = E\{\rho(x,y)\;\rho(x+\alpha,\, y+\beta)\}\,.$$

A homogeneous random field is a generalization of the one-dimensional wide sense stochastic process for higher dimension and is referred to as a wide-sense stationary random process. If the autocorrelation function is only a function of the distance between the two vectors (i.e. $R_{\rho\rho}(\hat{x}_1,\hat{x}_2) = R_{\rho\rho}(|\hat{x}_1 - \hat{x}_2|)$) then the random field is homogeneous and isotropic.

The spectral density $S_{\rho\rho}(u,v)$ of a homogeneous random field $\rho(\hat{x})$ is the Fourier transform of its autocorrelation

$$S_{\rho\rho}(\hat{w}) = \iint R_{\rho\rho}(\hat{x})\ e^{-j2\pi\langle\hat{x},\hat{w}\rangle}\ d\hat{x}\ . \tag{4.66}$$

Up to now we have been defining the mean, autocorrelation, etc. of a random field which are called ensemble averages. In the case of a homogeneous random field, one may ask if it is possible to take just one sample of the random field (i.e. perform one reconstruction) and then infer what the mean and autocorrelation are for a large sample of random fields by taking spatial averages:

$$\overline{\rho} = \lim_{\mathcal{A}\to\infty} \frac{1}{\mathcal{A}} \iint_{\Omega} \rho(x,y)\ dxdy \tag{4.67}$$

$$R(\alpha,\beta) = \lim_{\mathcal{A}\to\infty} \frac{1}{\mathcal{A}} \iint_{\Omega} \rho(x,y)\ \rho(x+\alpha,\ y+\beta)\ dxdy \tag{4.68}$$

where $\mathcal{A}$ is the area of a region Ω of the xy-plane and by $\lim_{\mathcal{A}\to\infty}$ is meant a limiting process which tends to include the entire xy-plane. Since ρ is a random variable, likewise both $\overline{\rho}$ and $R(\alpha,\beta)$ are random

variables. The homogeneous random field is called ergodic with respect to the mean if $\bar{\rho}$ is constant for all possible outcomes of ρ and equal to $m_\rho(\hat{x}) = m$. Likewise it is ergodic with respect to the autocorrelation if $R(\alpha,\beta)$ is constant at each (α,β) for all possible outcomes of ρ and this constant value is equal to $R_{\rho\rho}(\alpha,\beta)$. For a homogeneous random field a sufficient condition for the sample means to be ergodic is that $R_{\rho\rho}(\alpha,\beta) \to 0$ as $\alpha \to \infty$ and $\beta \to \infty$ (Parzen, 1962).

Single-photon emission computed tomograms are not ergodic processes with respect to the mean or autocorrelation nor are they homogeneous random fields. The salt and pepper effect illustrated in Fig. 4.9 is more evident in the center and decreases toward the outer portion of the disc. Therefore the variance in each picture value is not the same, which implies that the autocorrelation is not space invariant. This is not the situation in transmission computed tomography where the autocorrelation function is for all practical purposes isotropic (Snyder and Cox, 1977).

4.8.2 Optimal Sampling

If a random field $\rho(x,y)$ is expanded in terms of the orthonormal basis functions ψ_{ij},

$$\rho(x,y) = \sum_{i=1}^{M} \sum_{j=1}^{N} \rho_{ij}\, \psi_{ij}(x,y) \ ,$$

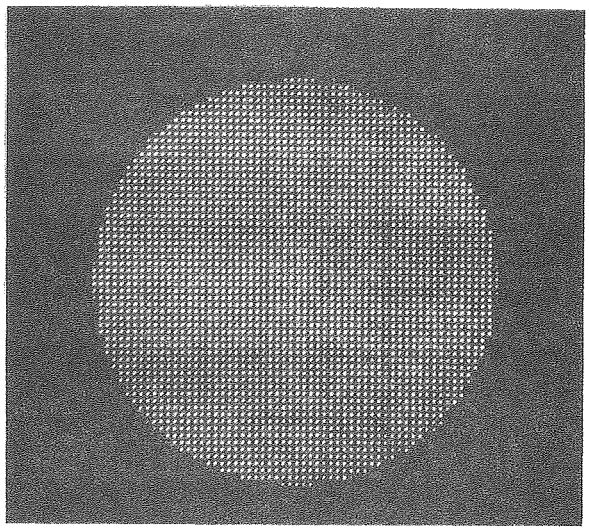

ORIGINAL PHANTOM

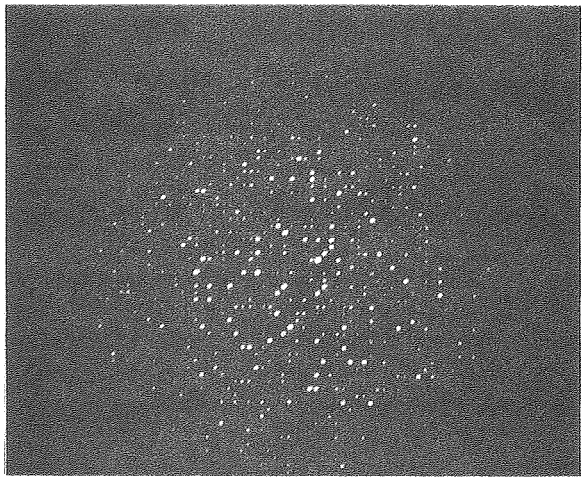

RECONSTRUCTED IMAGE

XBB 793-3410

Figure 4.9. Reconstruction of emission data with Poisson statistics results in larger variations in the center of the disc than toward the edge. This means that emission computed tomograms are not homogeneous random fields.

then the coefficients ρ_{ij} are random variables. The sampling error is the mean square error averaged over all the distributions ρ in the random field:

$$\varepsilon^2 = E\left\{\iint_{\Omega} |\rho(x,y) - \sum_{i=1}^{M}\sum_{j=1}^{N} \rho_{ij}\ \psi_{ij}(x,y)|^2\ dxdy\right\}$$

$$= \int_{\Omega} R_{\rho\rho}(\hat{x},\hat{x})d\hat{x} - \sum_{i=1}^{M}\sum_{j=1}^{N} \iint_{\Omega\ \Omega} R_{\rho\rho}(\hat{x},\hat{x}') \tag{4.69}$$

$$\times \psi_{ij}(\hat{x})\ \psi_{ij}(\hat{x}')\ d\hat{x}\ d\hat{x}' \ .$$

If ρ is a homogeneous random field then $R_{\rho\rho}(\hat{x},\hat{x}) = R_{\rho\rho}(0,0)$ and $R_{\rho\rho}(\hat{x},\hat{x}') = R_{\rho\rho}(x\text{-}x',\ y\text{-}y')$, allowing us to simplify Eq. (4.69):

$$\varepsilon^2 = \mathcal{A}\ R_{\rho\rho}(0,0) - \sum_{i=1}^{M}\sum_{j=1}^{N} \iint_{\Omega\ \Omega} R_{\rho\rho}(x\text{-}x',\ y\text{-}y')$$

$$\times \psi_{ij}(x,y)\ \psi_{ij}(x',y')\ dxdy\ dx'dy' \tag{4.70}$$

where $\mathcal{A}$ is the area of Ω.

The optimal sampling of a random field in ECT is the set of orthogonal functions $\psi_{ij}(x,y)$ which for every M and N yields a minimum value for the sampling error ε^2 in Eq. (4.69). In TCT if the random field is homogeneous then the optimal set of orthogonal functions minimize Eq. (4.70). Since $R_{\rho\rho}(0,0)$ is independent of the choice of the basis, the sampling error is minimized when the second term in Eq. (4.70) is maximized for the functions $\psi_{ij}(x,y)$ subject to the orthonormality condition. It has been shown by Brown (1960) that the

optimal set of basis functions are the eigenfunctions of the following integral operator:

$$\iint_{\Omega} R_{\rho\rho}(x,y,x',y')\ \psi(x',y')\ dx'dy' = \lambda\psi(x,y)\ . \qquad (4.71)$$

In order to solve Eq. (4.71) the autocovariance function must be known, and if known the solution for the eigenfunction can present an insurmountable mathematical challenge. Synder and Cox (1977) have pointed out that when the area $\mathcal{A}$ is large compared to the spatial variations of $\rho(x,y)$ and the autocorrelation function $R_{\rho\rho}(\hat{x}, \hat{x}')$ is a function only of the distance between $\hat{x}$ and $\hat{x}'$, then sampling with Bessel functions is the optimal choice of basis functions. However for the attenuated reconstruction problem it is not clear what the optimal choice of basis functions is. Standard sampling given by Eq. (4.1) was chosen, primarily for computational efficiency since computer codes can be written which are very fast in comparison with any other sampling scheme (Huesman, Gullberg, Greenberg, Budinger, 1977).

4.8.3 The Autocovariance Matrix

For the least-squares solution given by Eq. (4.25) the autocovariance function $C_{\rho\rho}(\hat{x}, \hat{x}')$ is estimated by the covariance matrix

$$\mathrm{Cov}(\rho) = (A^T \Phi^{-1} A)^G\ , \qquad (4.72)$$

where Φ is the data covariance matrix. Choosing Φ as a weighting matrix yields a minimum error covariance matrix (Deutsch, 1965).

The average variance over the reconstructed image is equal to the trace of $\mathrm{Cov}(\rho)$ divided by MN:

$$\text{Average variance} = \frac{\text{trace}(\mathrm{Cov}(\rho))}{MN} = \frac{1}{MN} \sum_{i=1}^{MN} \frac{1}{\lambda_i}$$

where λ_i are the eigenvalues of $A^T \Phi^{-1} A$. The results in Tables 4.2-4.7 indicate that for $\Phi = \sigma^2 I$ (i.e. equal projection errors) in Eq. (4.72) the average variance will increase as the attenuation coefficient increases.

The calculation of the covariance matrix is virtually impossible for the large dimension of $(A^T \Phi^{-1} A)$ which occurs in reconstruction tomography. However the effects of a finite number of projection angles and finite lateral sampling on the propagation of satistical errors in transverse section reconstruction was analyzed by Huesman (1977) for the unattenuated problem using the sampling in [Eq. (4.1)]. For this case the reconstructed intensities ρ_j satisfy

$$\rho_j = \sum_{k=1}^{KL} p_k \sum_{i=1}^{MN} M_{ji}^{-1} a_{ik} \tag{4.73}$$

where a_{ij} is an element of $A^T \Phi^{-1}$ and M_{ji}^{-1} is an element of the inverse or generalized inverse of $M = (A^T \Phi^{-1} A)$ and $\mu = 0$. The variance of ρ_j is the diagonal elements of $\mathrm{Cov}(\rho)$ in Eq. (4.72):

$$\sigma^2(\rho_j) = M_{jj}^{-1} . \tag{4.74}$$

If D is the diameter of the reconstruction region, a = b = d is the pixel size and $\sigma(p_i) = \text{const} = \sigma_\rho$, then for the case when D/d is large with 1.5 D/d angles and a sampling interval of about .5 d,

$$M_{jj}^{-1} = 1.59 \frac{D\sigma_\rho^2}{MNd^3} .$$

This gives a measure of the propagation of errors since M_{jj}^{-1} cannot be evaluated directly for large dimensional matrices.

For the attenuated reconstruction problem M_{jj}^{-1} will vary depending on the attenuation distribution. Also if the attenuation coefficients are determined from a transmission study M_{jj}^{-1} will be a random variable and it is not correct to use Eq. (4.74) to calculate the variance of ρ_j. In this case the variance of ρ_j is

$$\sigma^2(\rho_j) = \sum_{k=1}^{KL} \left\{ \sigma^2(p_k) \left(\sum_{i=1}^{MN} \sigma^2(M_{ji}^{-1} a_{ik}) \right) + \sigma^2(p_k) \left(\sum_{i=1}^{MN} E(M_{ji}^{-1} a_{ik}) \right)^2 + E(p_k)^2 \left(\sum_{i=1}^{MN} \sigma^2(M_{ji}^{-1} a_{ik}) \right) \right\} . \tag{4.75}$$

where it is assumed that $M_{ji}^{-1} a_{ik}$ and p_k are independent. This presents a serious mathematical problem--in order to evaluate the variance of ρ_j one must know both $\sigma^2(M_{ji}^{-1} a_{ik})$ and $E(M_{ji}^{-1} a_{ik})$ for all i,j,k. Here again the elements of M^{-1} cannot be evaluated for the large matrices that one experiences in computed tomography.

4.8.4 Measure of Percent Root-Mean-Square Uncertainty from Simulated Projection Data

An approach to estimating the propagation of errors in single-photon ECT which does not require inverting a matrix is to reconstruct simulated projection data with noise using an iterative algorithm. If the simulation is done many times then the sample mean and sample variance can be evaluated for each pixel value. However, this can be costly in terms of computer time. If the picture function is approximately an ergodic process with respect to the mean and with respect to the autocorrelation function, then one can use Eqs. (4.67) and (4.68) as an estimate of the sample mean and sample autocorrelation. In the discrete case these equations reduce to the following spatial averages for the mean and variance:

$$\bar{\rho} = \sum_{i,j\in\Omega} \frac{\rho_{ij}}{N} \tag{4.76}$$

$$\sigma^2(\rho) = \sum_{i,j\in\Omega} \frac{(\rho_{ij} - \bar{\rho})^2}{N - 1} \tag{4.77}$$

where N is the number of pixels sampled for the region Ω.

Circular discs of 60 and 40 pixels in diameter were chosen to simulate the propagation of errors. The 60 and 40 pixel diameter discs were reconstructed in a circular image array with 64 and 44 pixels across, respectively. The reconstruction procedure as outlined in Fig. 4.8 involved first reconstructing simulated transmission data, then evaluating the attenuation factors, and then reconstructing

simulated emission data. The attenuation coefficients were reconstructed from transmission data at 100 and 70 projection angles over 180° and the emission concentration were reconstructed from 200 and 140 projection angles over 360° for the 60 and 40 pixel diameter discs, respectively. The projections had bin sizes .66 that of the pixel size in order to conform to the correct reconstruction criterion (Huesman, 1977).

The projection data were evaluated using analytically calculated line integrals that did not involve subdividing the discs into pixels. For the transmission data, the true projection data are

$$p_{k\theta} = \int \mu(-\xi_k \sin\theta + z\cos\theta,\ \xi_k \cos\theta + z\sin\theta)dz. \tag{4.78}$$

If the incident number of photons per projection bin for the transmission beam is I_o, then the number of transmitted photons $I_{k\theta}$ is given by

$$I_{k\theta} = I_o \exp(-p_{k\theta}) \ . \tag{4.79}$$

Noise was added to the true projections $p_{k\theta}$ by generating Poisson random variates $\tilde{I}_o$ and $\tilde{I}_{k\theta}$ with variances equal to $\sqrt{I_o}$ and $\sqrt{I_{k\theta}}$ respectively. Then the random variate $\tilde{p}_{k\theta}$ was evaluated using

$$\tilde{p}_{k\theta} = \ln(\tilde{I}_o/\tilde{I}_{k\theta}). \tag{4.80}$$

The errors in $\tilde{p}_{k\theta}$ propagated in this way are approximately equal to

$$\sigma(\tilde{p}_{k\theta}) = \sqrt{1/\tilde{I}_o + 1/\tilde{I}_{k\theta}} \quad . \tag{4.81}$$

Likewise the emission data had Poisson noise added with errors equal to the square root of the measured analytically calculated line integrals:

$$\sigma(\tilde{p}_{k\theta}) = \sqrt{p_{k\theta}} \quad . \tag{4.82}$$

The data were calculated for various attenuation coefficients and counting statistics.

These data were reconstructed by minimizing the least-squares function in Eq. (4.23) weighted by the errors given in Eq. (4.81) for the transmission data and Eq. (4.82) for the emission data using Goitein's iterative relaxation method (Goitein, 1971) modified for conjugate gradient stepping to improve convergence. The iterative procedure was terminated after 30 iterations. In the case of the 40 pixel diameter disc the transmission data were reconstructed using a convolution algorithm. Selected examples of the reconstructions are shown in Fig. 4.10 of a 40 pixel diameter disc for various emission statistics and attenuation coefficients with transmission statistics of I_o = 1000 photons per projection bin.

The results of the simulations were evaluated based on the percent root-mean-square (% RMS) uncertainty for pixel values within the circular discs and are tabulated in Tables 4.10 and 4.11. The % RMS uncertainty was calculated from the equation

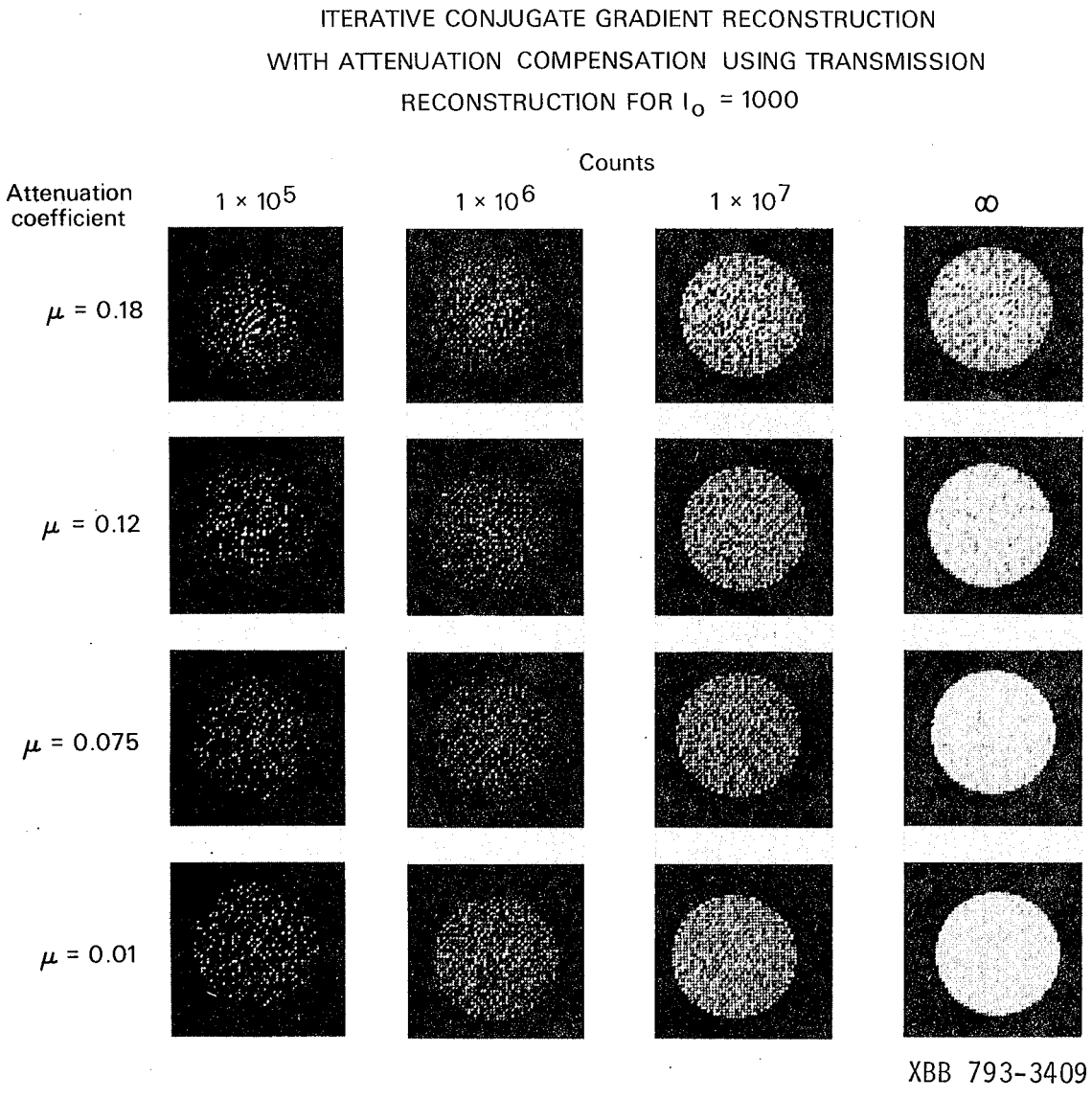

Figure 4.10. Reconstructions of a 40 pixel diameter disc using 30 iterations of the conjugate gradient algorithm applied to 140 equally spaced Poisson distributed projections between 0 and 2π. The attenuation factors were evaluated from a transmission reconstruction using the convolution algorithm applied to 70 projection angles between 0 and π with 1000 Poisson distributed incident photons per projection ray.

Table 4.10. The %RMS as a function of emission and transmission statistics and attenuation coefficient. The %RMS is given for the reconstruction of a circular disc 60 pixels in diameter (30 cm). The transmission data were reconstructed from 100 projection angles over 180° and the emission data were reconstructed from 200 projection angles over 360° with 100 bins per projection. The projections had bin sizes .66 that of the pixel size. The emission data were compensated for attenuation by using the reconstructed transmission attenuation coefficients. The total incident photons are equivalent to the following number of photons per projection ray I_0: 9×10^7 - I_0 = 9900, 7.9×10^7 - I_0 = 8690 and 3.7×10^7 - I_0 = 4070.

	Transmission		Emission	
Attenuation Coefficients (cm^{-1})	Total Photons Incident/Transmitted	%RMS	Total Photons Reconstructed/Measured	%RMS
.15	$9.0 \times 10^7/5.1 \times 10^6$	10.9	$8.5 \times 10^6/2.3 \times 10^6$	41.6
.15	$9.0 \times 10^8/5.1 \times 10^7$	4.3	$8.5 \times 10^6/2.3 \times 10^6$	41.2
.15	∞	---	$8.5 \times 10^6/2.3 \times 10^6$	41.8
.15	$9.0 \times 10^7/5.1 \times 10^6$	10.9	$8.5 \times 10^7/2.3 \times 10^7$	16.6
.15	$9.0 \times 10^8/5.1 \times 10^7$	4.3	$8.5 \times 10^7/2.3 \times 10^7$	15.3
.15	∞	---	$8.5 \times 10^7/2.3 \times 10^7$	14.8
.0958	$7.9 \times 10^7/1.1 \times 10^7$	8.98	$6.1 \times 10^6/2.3 \times 10^6$	32.1
.0958	$7.9 \times 10^8/1.1 \times 10^8$	3.6	$6.1 \times 10^6/2.3 \times 10^6$	31.9
.0958	∞	---	$6.1 \times 10^6/2.3 \times 10^6$	32.6
.0958	$7.9 \times 10^7/1.1 \times 10^7$	8.98	$6.1 \times 10^7/2.3 \times 10^7$	12.7
.0958	$7.9 \times 10^8/1.1 \times 10^8$	3.6	$6.1 \times 10^7/2.3 \times 10^7$	11.8
.0958	∞	---	$6.1 \times 10^7/2.3 \times 10^7$	11.3
.0958	$3.7 \times 10^7/5.0 \times 10^6$	12.9	$6.1 \times 10^6/2.3 \times 10^6$	32.4
.0958	$3.7 \times 10^8/5.0 \times 10^7$	4.6	$6.1 \times 10^6/2.3 \times 10^6$	31.9
.0958	∞	---	$6.1 \times 10^6/2.3 \times 10^6$	32.6
.0958	$3.7 \times 10^7/5.0 \times 10^6$	12.9	$6.1 \times 10^7/2.3 \times 10^7$	13.6
.0958	$3.7 \times 10^8/5.0 \times 10^7$	4.6	$6.1 \times 10^7/2.3 \times 10^7$	11.9
.0958	∞	---	$6.1 \times 10^7/2.3 \times 10^7$	11.3

XBL794-3388

Table 4.11. The %RMS uncertainty as a function of emission counting statistics and attenuation coefficients. The %RMS is given for the reconstruction of a circular disc 40 pixels in diameter (20 cm) from 140 projection angles over 360°. The projection data for various statistics were attenuated assuming a constant attenuation coefficient over the circular disc. The counts represent the total measured counts for all 140 projection angles. In compensating for attenuation, it was assumed that the transmission data had no errors for $I_0 = \infty$. For $I_0 = 1000$ the incident transmission beam is Poisson distributed with a mean and variance equal to 1000. The %RMS uncertainty for the transmission reconstruction is given in the column next to the attenuation coefficients.

		Counts						
μ cm^{-1}	%RMS	1×10^5	5×10^5	1×10^6	5×10^6	1×10^7	5×10^7	∞
		Transmission - $I_0 = \infty$						
.18		96.6	43.5	32.4	16.3	12.9	9.8	4.7
.15		91.5	41.5	29.3	14.2	11.2	8.6	3.9
.12		86.9	39.1	27.2	13.5	10.3	7.4	3.3
.0958		90.0	40.5	27.8	13.2	10.0	6.8	2.9
.075		89.6	40.2	26.9	12.9	9.8	6.5	2.7
.05		85.6	38.4	27.6	13.4	10.0	6.1	2.6
.01		87.7	39.5	26.6	12.5	9.3	5.8	2.5
0		85.0	38.1	26.5	13.4	9.8	6.0	2.5
		Transmission - $I_0 = 1000$						
.18	17.3	99.1	46.3	33.8	18.8	16.7	13.8	12.0
.15	14.9	94.7	41.9	30.7	16.6	14.2	11.5	9.8
.12	15.3	85.1	41.0	29.8	15.5	13.5	11.1	8.4
.0958	15.7	93.2	40.6	27.5	15.1	12.5	9.8	7.6
.075	16.7	90.1	40.7	29.3	14.8	12.0	9.2	7.3
.05	22.4	87.6	39.9	26.9	14.2	12.1	8.8	6.6
.01	85.5	90.1	39.4	27.4	13.5	10.6	7.8	5.8
0	765.0	85.0	40.4	28.0	12.9	10.1	6.1	3.9

XBL794-3387

$$\%\text{RMS uncertainty} = \frac{100\ \sigma(\rho)}{\bar{\rho}} \tag{4.83}$$

where $\bar{\rho}$ and $\sigma^2(\rho)$ are given by Eqs. (4.76) and (4.77), respectively.

The tables show that errors in the attenuation coefficients increase the %RMS uncertainty in the emission reconstruction. An example of the amplification of these errors for the 30 cm (60 pixel) diameter disc with attenuation coefficient $\mu = .15\ cm^{-1}$ is extracted from Table 4.10 and is tabulated below for emission statistics of 20 million photons:

Transmission data	%RMS in the Emission Reconstruction
∞	14.8
5×10^7	15.3
5×10^6	16.6

These data indicate that as you decrease the transmission photons the errors in the emission reconstruction increase.

The influence of the transmission errors on the emission reconstruction is not as significant when emission statistics are poor as when they are good. This is illustrated in the following two examples.

Example 1. For a 30 cm disc with $\mu = .15\ cm^{-1}$, we see from Table 4.10

	Transmission Photons				
Emission Photons	5×10^6		5×10^7		
2.3×10^6	41.6	-	41.2	=	.4
2.3×10^7	16.6	-	15.3	=	1.3

Thus at 2.3×10^6 emission photons there is a difference of .4 in the %RMS uncertainty going from 5×10^6 to 5×10^7 transmission photons; whereas at 2.3×10^7 emission photons there is a difference of 1.3.

Example 2. For a 20 cm disc with $\mu = .18\ cm^{-1}$, we see from Table 4.11

	Transmission Photons				
Emission Photons	3.7×10^5		∞		
5×10^5	46.3	-	43.5	=	2.8
5×10^7	13.8	-	9.8	=	4.0

where for $I_0 = 1000$ the total number of transmitted photons is 3.7×10^5.

The size of the disc influences the % RMS uncertainty. For the 20 cm diameter disc, with $\mu = .15\ cm^{-1}$, transmitted photons = 5.2×10^5 ($I_0 = 1000$), and emission photons = 1×10^6, the % RMS uncertainty equals 30.7; whereas for the 30 cm diameter disc, with $\mu = .15\ cm^{-1}$, transmitted photons = 5.1×10^6, and emission photons = 2.3×10^6 the % RMS uncertainty equals 41.6. Even with better transmission and emission statistics for the 30 cm disc, the reconstructed 20 cm disc had a better % RMS uncertainty. This same result was reported for simulations with unattenuated data (Budinger et al., 1978). It was found that for an equal number of recorded events the uncertainties were reduced when the activity was concentrated in a smaller portion of the field.

The % RMS uncertainty in the transmission results decrease with an increase in the incident and transmitted photons. Note in Table 4.10 that when the attenuation coefficient decreases from .15 to .0958 and the total incident photons decrease from 9.0×10^7 to 7.9×10^7,

the transmitted photons increase and the %RMS uncertainty decreases. However, as is shown in the second grouping for $\mu = .0958$, when the transmitted photons are kept constant (5×10^6), the incident photons decrease by almost a factor of 3 going from $\mu = .15$ cm^{-1} to $\mu = .0958$ cm^{-1} and the %RMS uncertainty increases. Remember that the errors on the projections are a function of both the incident photons and the measured photons as given by $\sigma(\text{projection}) = [\sigma(\text{Incident})^{-1} + \sigma(\text{measured})^{-1}]^{1/2}$.

The results of the transmission reconstruction for the 20 cm diameter disc in Table 4.11 indicate that the %RMS uncertainty given by Eq. (4.83) becomes large as $\mu \to 0$ because the standard error given in the numertor of Eq. (4.83) does not go to zero as fast as the estimate of the mean in the denominator. Therefore there are two things influencing the %RMS uncertainty for the transmission data: (1) for a constant number of incident photons I_0, lowering the attenuation coefficient increases the transmitted data resulting in smaller errors (Eq. (4.81)) in the projection data given by Eq. (4.80); (2) however at the same time the numerator in Eq. (4.83) does not decrease as fast as the denominator, thus increasing the %RMS uncertainty as the attenuation coefficient decreases.

Table 4.11 indicates that for the same transmission and emission statistics, increasing the attenuation coefficients results in higher %RMS uncertainty. This observation is similar to the results in Tables 4.2 - 4.7 which indicate that the trace $[(A^TA)^{-1}]/MN$ which is a measure of variance for projections with equal errors, increases

as the attenuation coefficient increases.

4.9 Applications

Single-photon ECT with attenuation compensation has been applied to both human and canine studies using various radionuclide (Budinger, Cahoon, Derenzo, et al., 1977). The ability to image a particular organ depends on the ability of the organ to take up the radionuclide compared to the surrounding tissue, the energy of the emitted photon, and the measured statistics for both the emission and transmission studies. For example, the use of radionuclides for myocardial imaging generally give a low target to nontarget contrast ratio. For high energy radionuclides such as potassium-43, rubidium-82, rubidium-81 and -82m, and cesium-129, fewer photons are attenuated as compared with Tl-201 and Cs-131, however the contribution of activity from back muscles and lungs tends to wash out the image on projection (Budinger and Rollo, 1977). The anterior myocardium is well visualized using lower energy radionuclides such as cesium-131 and thallium-201; however photons from the posterior myocardial wall are greatly attenuated and quantitation of septal and posterior wall defects is seriously limited. The fundamental problem is not so much the specificity of uptake of radionuclide in the organ versus uptake in the contiguous tissues, but the physical properties of the radionuclide which one can equate to attenuation coefficients which in turn dictate the required statistics to insure a desired %RMS uncertainty.

Results from a study showing abnormal accumulation of isotope in two tumors in a 50 year old woman are shown in Fig. 4.11. This study

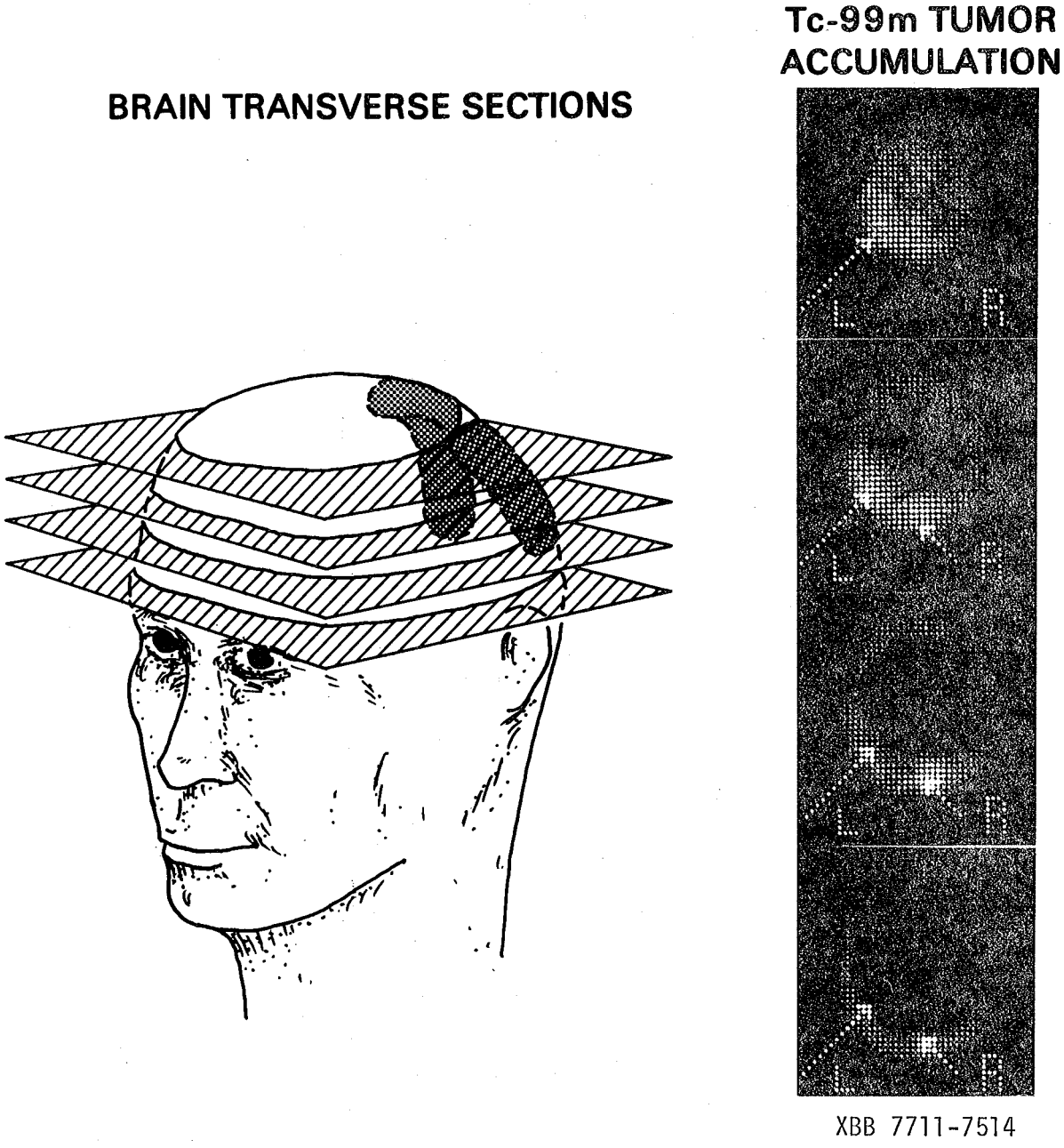

Figure 4.11. Transverse sections showing abnormal accumulation in the head of a 50-year-old patient using ^{99m}Tc-pertechnetate and 36 views. The measured number of emission events for each section are (from bottom to top) 220582, 251213, 265286, and 222584, respectively.

was done one hour after injection of 15 mCi of ^{99m}Tc-pertechnetate (140 keV). Normal brain tissue is either relatively or completely impermeable to the passage of most radionuclides from the blood. In contrast, brain tumors are much more permeable than normal brain and this results in a significantly higher relative concentration of radioactivity in the tumor. For the study shown in Fig. 4.11, the projection data were collected in 10 degree increments over 360° which gave approximately 240,000 counts per slice. The attenuation coefficient was assumed to be constant. Table 4.5 indicates that for perfect transmission statistics the percent root-mean-square uncertainty is between 91.5% and 41.5% for attenuation coefficient $\mu = .15\ cm^{-1}$ and emission counts of 2.5×10^5. This means that the tumors which have a contrast of 2 to 1 can be seen, but the boundary of the tumors are hard to delineate.

Potassium and potassium analogs such as cesium have a high affinity to the heart because of the high muscular and nerve activity. Transverse section images of ^{129}Cs in the human myocardium are shown in Fig. 4.12 for a patient who previously had four myocardial infarctions. The study was done by taking views at 20° increments. A transverse section reconstruction of attenuation coefficients was performed first in order to correct for attenuation in the emission reconstruction. Section 4 shows a paucity of uptake in the posterior wall and septum consistant with electrocardiographic findings. The left myocardial wall, septum, and right ventricular myocardium are recognizable. The dome of the liver is seen in sections 2 and 3 as would be expected,

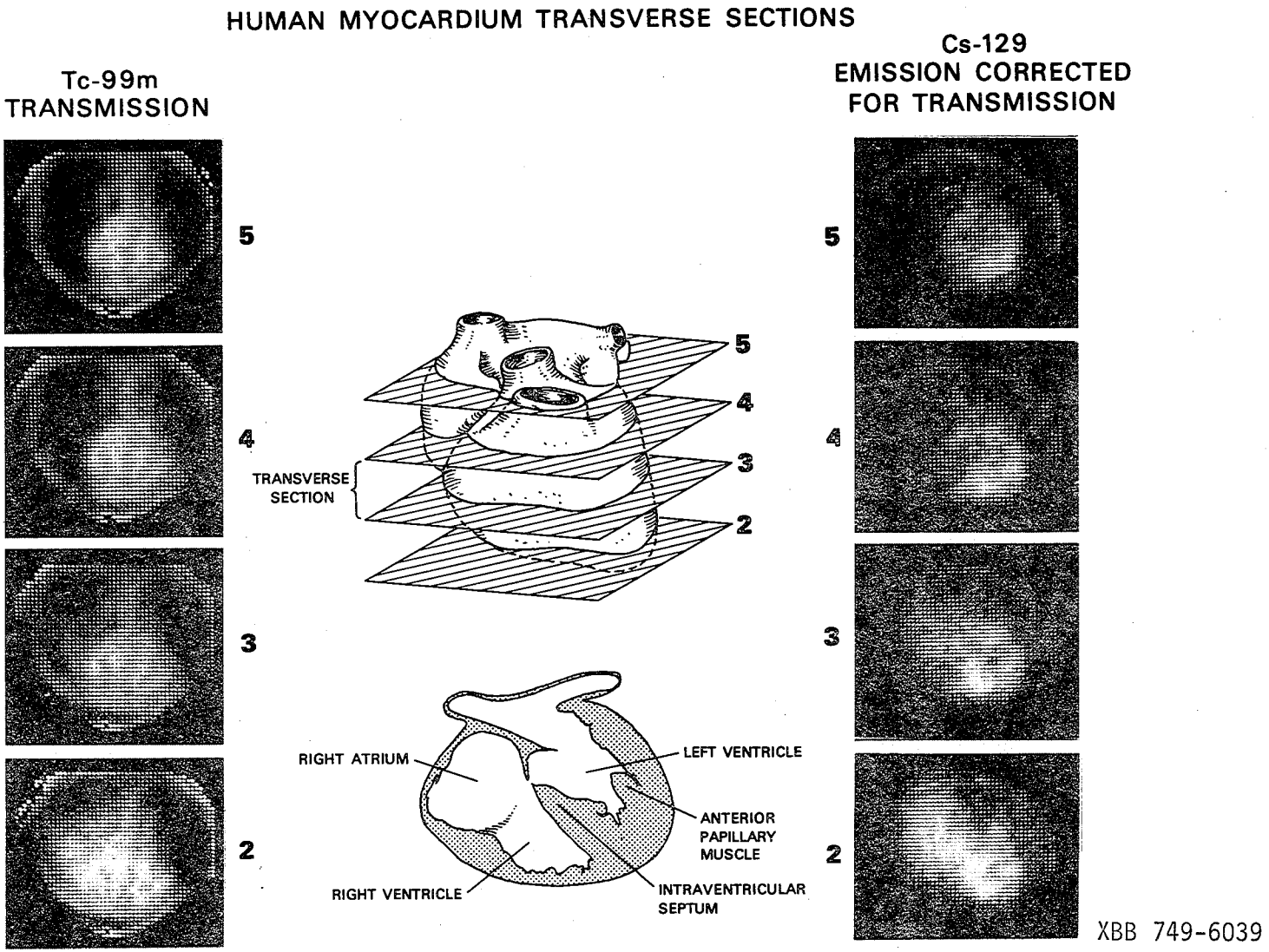

Figure 4.12. Transmission and emission transverse sections of the thorax in a 60-year-old patient with four myocardial infarctions. Septal activity normal, but anterolateral activity low. The measured number of emission events are Plane 2-247903, Plane 3-233989, Plane 4-220230, Plane 5-205529. The incident number of photons per projection bin (I_o) for the transmission study are Plane 2-3558, Plane 3-3801, Plane 4-3942, Plane 5-3822.

since the liver accumulates cesium and potassium analogs with about the same avidity as the heart. In order to obtain the correct attenuation coefficients for Cs-129 (375 keV-48%), the results of the transmission study using Tc-99m (140 keV) were extrapolated using the curve in Fig. 2.4 so that the attenuation coefficients corresponded to the 375 keV photons emitted from Cs-129. This means in tissue the attenuation coefficient is approximately .11 cm^{-1}. The transmission study in Fig. 4.12 would have a somewhat higher %RMS, probably about 15%, for an incident number of photons I_o of almost 4,000 per projection bin than the 8.98% in Table 4.10 for μ = .0958 cm^{-1} and total incident photons of 7.9×10^7 ($I_o = 8690$). The approximate number of 2.5×10^5 emission events for the sections in Fig. 4.12 were much less than the 2.3×10^5 emission events given in Table 4.10. Therefore one would guess that the %RMS error in the emission images of Fig. 4.12 could be as high as 50%.

When injected intravenously, selenomethionine is rapidly removed from the blood and is utilized in protein synthesis. The isotope will eventually reappear in the form of plasma proteins. The selenomethionine concentration in muscle is much lower than in the thyroid, parathyroid, or blood because of the slow rate of turnover of muscle protein. A study shown in Fig. 4.13 was done on a dog to see how well ^{75}Se-selonomethionine (136 keV-57%, 265 keV-60%) is taken up in the heart. On the left are two transverse sections demonstrating the position of the heart in the chest with sufficient resolution to show the esophagus. The accumulation of ^{75}Se in the myocardium is shown on the right. The results in Table 4.11 indicate that the %RMS

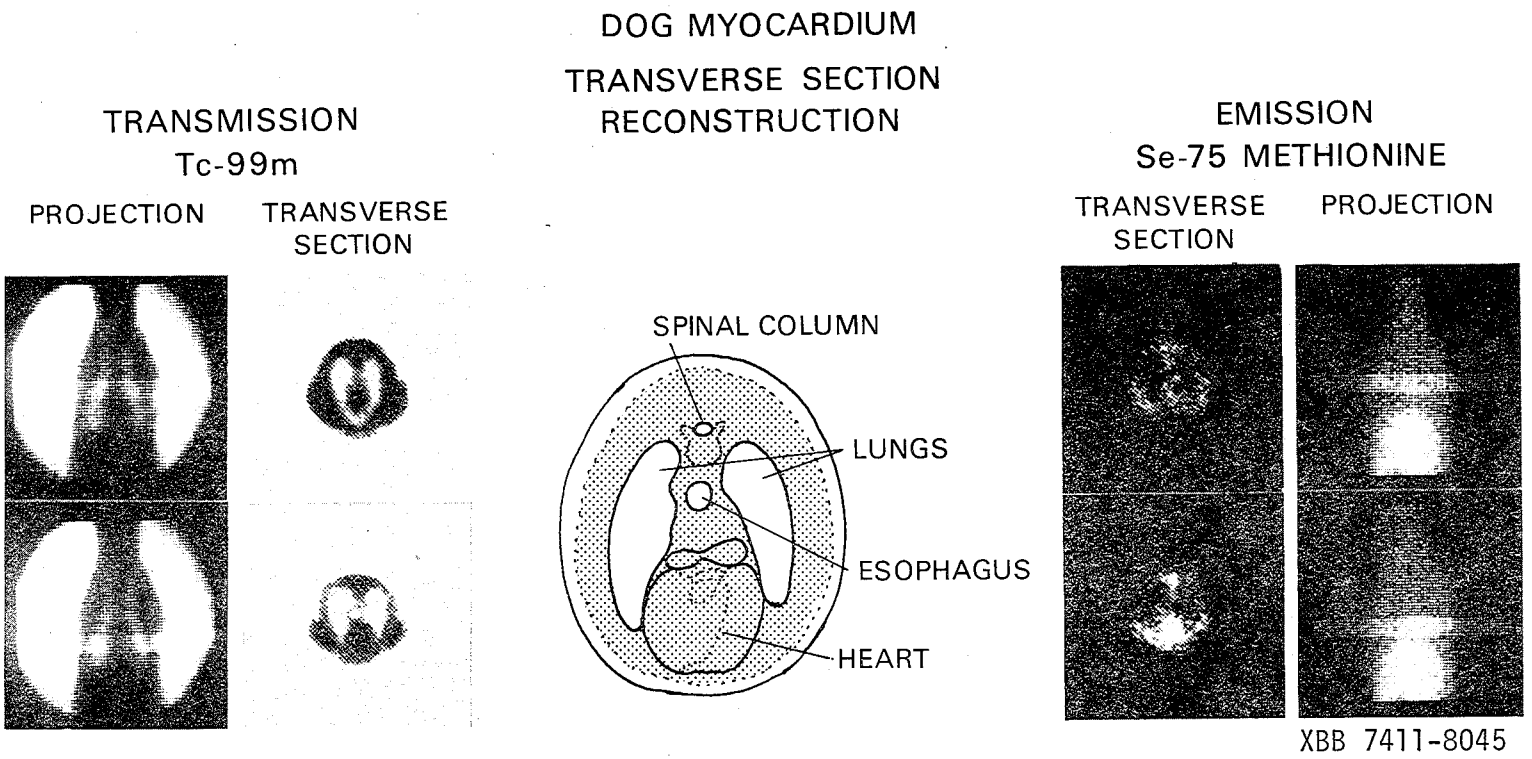

Figure 4.13. At the right accumulation of ^{75}Se-selenomethionine is seen in the dog myocardium after intravenous injection of 750 μCi. These cross-sectional images were reconstructed from 36 projections over 360° with a total of 128103 events for the bottom image and 113092 for the top image. The transmission study shown on the left was performed using an 8-mCi point source of ^{99m}Tc, three meters from the subject (see Fig. 2.12). This gave an incident number of photons per projection bin (I_0) for each of the 18 projections over 180° of 4449 for the bottom cross section and 4730 for the top cross section. The light bands across the projection images indicate the level for the transverse sections.

uncertainty for 10^5 counts with I_0 = 1000 is approximately 90%. Since the target is not distributed over a 20 cm disc as was simulated in Table 4.11 the results in (Budinger et al., 1978) would indicate that the %RMS uncertainty is better than 90% when the activity is concentrated in a smaller portion of the field.

The accumulation of ^{99m}Tc-sulfur colloid in the liver and spleen is shown in the transverse sections of Fig. 4.14. The Kupffer cells of the liver which function to remove foreign substances from the blood accumulate the labeled sulfur granules of 1 μm in diameter. (See also Fig. 1.2 and discussion in Chapter 1.) The better the liver is functioning, the more ^{99m}Tc attached to sulfur colloid will be available for imaging; that is, the functioning liver becomes labeled. The time required to reach a steady state accumulation is 3 to 5 minutes, and the time during which the distribution of concentration remains constant is 30 minutes or longer. The results in Table 4.10 indicate that the %RMS uncertainty for a uniform distribution of 2.3×10^6 counts in a 30 cm disc is approximately 41%. The results in Table 1 of (Budinger et al., 1978) indicate that the %RMS uncertainty is better than this (maybe as good as 20%) since the liver and spleen concentrate the isotope in approximately 30% of the field.

Figure 4.14. Accumulation of ^{99m}Tc-sulfur colloid in transverse sections of the liver and spleen are shown both with and without attenuation correction using the transmission reconstruction of the attenuation coefficients. In 72 projections over 360° the emission events in each transverse section totaled from bottom to top - 4.10×10^6, 4.58×10^6, 3.56×10^6, 2.69×10^6, 1.69×10^6 and $.81\times10^6$ events. The incident number of photons per projection bin (I_o) for the transmission study is from bottom to top - 1556, 1616, 1611, 1575, 1534, 1492, and 1396.

HUMAN MYOCARDIUM, LIVER,
SPLEEN TRANSVERSE SECTIONS

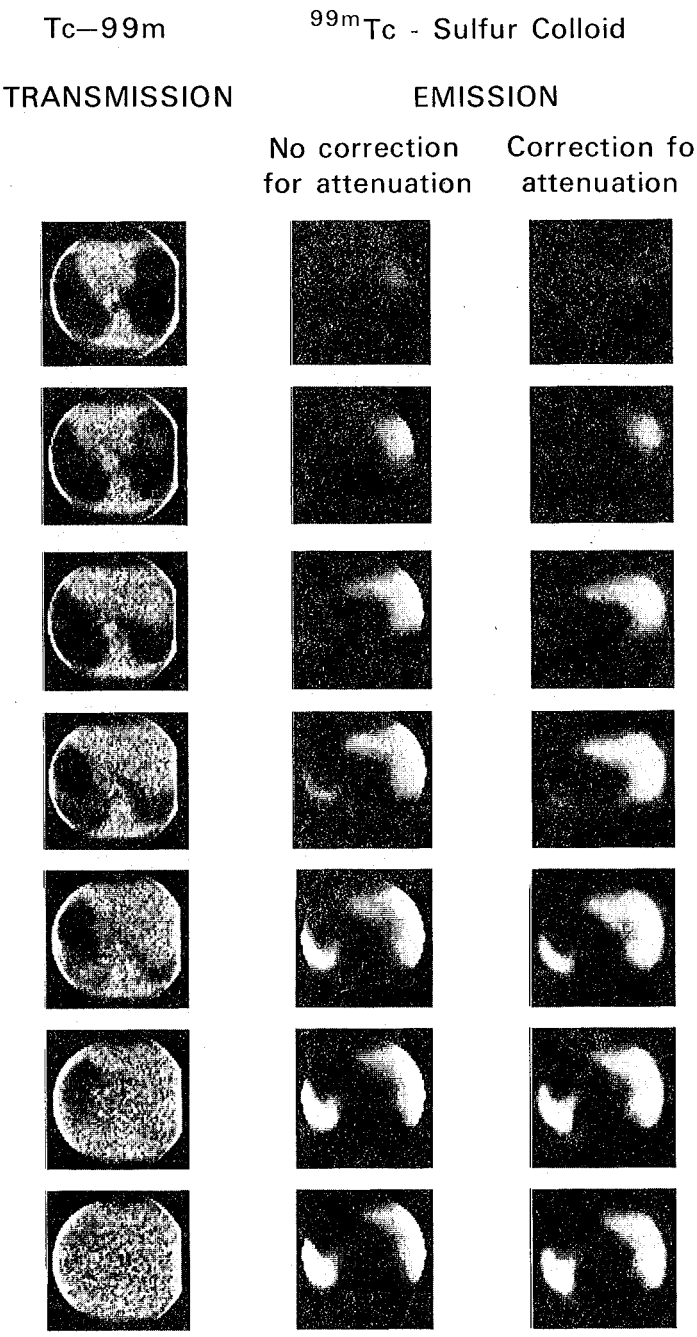

Figure 4.14.

5. THE CONVOLUTION METHOD FOR CONSTANT ATTENUATION

5.1 Introduction

The convolution algorithm proposed by Tretiak and Delaney (1978) for attenuation compensation in single-photon emission computed tomography is a very appealing approach for reconstructing projection data attenuated by a constant attenuation coefficient. The convolution algorithm given in Eq. (2.11) is now used in most commercial x-ray scanners and positron emission tomographic systems because of its computational efficiency and because it requires very little computer memory. Closed form expressions for two important convolution functions used in these systems were developed by Ramachandran and Lakshminarayanan (1971) and Shepp and Logan (1974). For the case of constant attenuation the convolution function does not have a simple closed form expression. However, convolvers can be evaluated using least-squares and power series expansion methods, or window functions can be designed for filtering the projections in frequency space which is an equivalent operation to convolution in real space. The reconstruction results presented in this chapter indicate that in the case of constant attenuation, attenuation can be compensated for in emission computed tomography using an attenuation dependent convolver which reconstructs the transverse section reliably and requires little computer memory and very little computer time.

The reconstruction of projection data which has been attenuated by a constant attenuation coefficient μ is performed by first modifying the projection data at the angle θ and lateral sampling ξ using

Eq. (3.76) so that they conform to projections represented by the modified attenuated Radon transform:

$$p(\xi,\theta) = \int \rho(\hat{x})\, e^{\mu\langle \hat{x}, \underset{\sim}{\theta}^{\perp} \rangle}\, \delta(\xi - \langle \hat{x}, \underset{\sim}{\theta} \rangle) d\hat{x}\ , \qquad (3.93c)$$

where ρ is the transverse section tomogram and $\langle \hat{x}, \underset{\sim}{\theta} \rangle$ and $\langle \hat{x}, \underset{\sim}{\theta}^{\perp} \rangle$ denotes the dot product between the position vector $\hat{x} = (x,y)$ and the vectors $\underset{\sim}{\theta} = (-\sin\theta, \cos\theta)$ and $\underset{\sim}{\theta}^{\perp} = (\cos\theta, \sin\theta)$, respectively. After this modification, the convolution is performed with a convolver c_μ which has been previously determined for a particular attenuation coefficient μ so that the attenuated back-projection of the convolver,

$$h(\hat{x}) = \int_0^{2\pi} c_\mu(\langle \hat{x}, \underset{\sim}{\theta} \rangle)\, e^{-\mu\langle \hat{x}, \underset{\sim}{\theta}^{\perp} \rangle}\, d\theta, \qquad (5.1)$$

is equal to a desired point response function h. The filtered projections are then back-projected using the attenuated back-projection operator given in Eq. (3.102). This algorithm gives a reconstructed image $\hat{\rho}$ which can be represented for continuous data sampling by the formula

$$\hat{\rho}(\hat{x}) = \int_0^{2\pi} \int_{-\infty}^{\infty} c_\mu(\langle \hat{x}, \underset{\sim}{\theta} \rangle - \xi)\ p(\xi,\theta) d\xi\, e^{-\mu\langle \hat{x}, \underset{\sim}{\theta}^{\perp} \rangle}\, d\theta. \qquad (3.106)$$

We see from Theorem 3.29 that under ideal conditions (continuous angular sampling and infinite data statistics) one would like to choose the convolution function c_μ so that its back-projection h given in Eq. (5.1) is a delta function. However in practical applications with

finite data samples over a finite number of projections, the discrete back-projection of c_μ can only approximate a delta function. In this case, the function h is referred to as the point spread function of the reconstruction procedure. Convolvers with point spread functions which closely approximate a delta function give very good spatial resolution but tend to amplify statistical fluctuations in the data so that contrast resolution deteriorates.

If the point spread function is isotropic, for example, it may be represented as a Gaussian; then for continuous sampling, the convolution function c_μ corresponding to this type of point spread function is the solution to the integral equation

$$h(r) = \int_0^{2\pi} c_\mu(r\sin\theta)\, \exp[-\mu r\cos\theta]\, d\theta. \tag{5.2}$$

For $\mu = 0$, Eq. (5.2) is known as the Schlömilch's integral equation (Whittaker and Watson, 1962), and if h(r) has a continuous derivative, $c(\xi)$ is given by

$$c(\xi) = \frac{h(0)}{2\pi} + \frac{\xi}{2\pi} \int_0^{\pi/2} h'(\xi\sin\theta)\, d\theta\ . \tag{5.3}$$

Tanaka and Iinuma (1975, 1976) evaluated Eq. (5.3) for a Gaussian point spread function h.

A convolution function c_μ is a solution to Eq. (5.1) if and only if c_μ is a solution to the operator equation

$$A_\mu h = A_\mu A_\mu^* c_\mu \tag{5.4}$$

Using Theorem 3.28, we can express this operator equation for weights $W(x,y) = w(\xi,\theta) = 1$ as the integral equation

$$(A_\mu h)(\xi,\theta) = \iint c_\mu(\xi',\theta') \frac{1}{|\sin(\theta-\theta')|} \times \exp\left[\mu(\xi-\xi') \frac{\cos(\theta'-\theta) + 1}{\sin(\theta'-\theta)}\right] d\xi' d\theta'. \quad (5.5)$$

Davison and Grünbaum (1979) used an eigenvalue decomposition of the operator $A_\mu A_\mu^*$ to solve for $c_\mu(\xi',\theta')$ for various point spread functions h. Convolvers were evaluated for both equal angular sampling over π and for limited angular sampling. With attenuation (i.e., $\mu \neq 0$) the operator $A_\mu A_\mu^*$ does not have an obvious singular value decomposition which can be expressed as a closed form solution.

In this chapter we will first look at least-squares methods for solving Eq. (5.1) which give a discrete convolution function and then look at methods which give an analytical solution to Eq. (5.1). A statistical analysis will show that the percent root-mean-square uncertainty increases with an increase in attenuation and increases with a decrease in total measured photons.

5.2 Convolvers Evaluated Using Least-Squares

The point response function h in Eq. (5.1) can be expanded using the basis functions given in Eq. (4.1):

$$h(\hat{x}) = \sum_{i=1}^{M} \sum_{j=1}^{N} h_{ij}\, \chi_{ij}(\hat{x}) \,. \quad (5.6)$$

For finite angular sampling Eq. (5.1) reduces to

$$h(\hat{x}) = \sum_m c_\mu(\langle \hat{x}, \underset{\sim}{\theta}_m \rangle) e^{-\mu \langle \hat{x}, \theta_m^{\perp} \rangle} \quad . \tag{5.7}$$

If we sample h at $\hat{x}_{ij} \in$ domain χ_{ij} then we see from Eq. (5.6) that one obtains the following system of equations

$$h_{ij} = \sum_m c_\mu(\langle \hat{x}_{ij}, \underset{\sim}{\theta}_m \rangle) e^{-\mu \langle \hat{x}_{ij}, \underset{\sim}{\theta}_m^{\perp} \rangle} \quad . \tag{5.8}$$

The convolution function $c_\mu(\langle \hat{x}_{ij}, \underset{\sim}{\theta}_m \rangle)$ can be expressed as the linear interpolated value between discrete samples of c_μ

$$c_\mu(\langle \hat{x}_{ij}, \underset{\sim}{\theta}_m \rangle) = c_k f + (1-f)\, c_{k+1} \quad , \tag{5.9}$$

where $k = \text{INT}[\langle \hat{x}_{ij}, \underset{\sim}{\theta}_m \rangle]$ (INT [Z] meaning the smallest integer less than or equal to Z) and $f(\langle \hat{x}_{ij}, \underset{\sim}{\theta}_m \rangle) = \langle x_{ij}, \underset{\sim}{\theta}_m \rangle - k+1$. For $\mu=0$ and for the Shepp and Logan convolver (Shepp and Logan, 1974), Eq. (5.9) is an exact representation of the continuous convolution function. The Shepp and Logan convolver was designed to be piece-wise linear.

Equation (5.8) can be rewritten as

$$h_{ij} = \sum_m [c_k\, f(\langle \hat{x}_{ij}, \underset{\sim}{\theta}_m \rangle) + (1-f(\langle \hat{x}_{ij}, \underset{\sim}{\theta}_m \rangle))\, c_{k+1}]\, e^{-\mu \langle \hat{x}_{ij}, \underset{\sim}{\theta}_m^{\perp} \rangle} \tag{5.10}$$

which reduces to

$$h_{ij} = \sum_m \sum_k A_{ij}^{km}\, c_k \tag{5.11}$$

where A_{ij}^{km} is either one of the factors $f(\langle \hat{x}_{ij}, \underset{\sim}{\theta}_m \rangle)$ or $(1-f(\langle \hat{x}_{ij}, \underset{\sim}{\theta}_m \rangle))$ or zero. Equation (5.11) can be represented in matrix notation

$$A^T C = H \tag{5.12}$$

where the MN×KL matrix A^T is a discrete back-projection operator, the KL×1 matrix C is the convolver and the MN×1 matrix H is the point spread function. The notation A is used to denote that this is a modified attenuated projection operator. Therefore we see from Eq. (5.12) that the convolver C can be chosen such that the back-projection of C fits some desired point spread function in a least-squares sense.

The matrices A and C in Eq. (5.12) can be partitioned:

$$(A_1^T \; A_2^T \; \cdots \; A_L^T) \begin{pmatrix} C_1 \\ C_2 \\ \vdots \\ C_L \end{pmatrix} = H \tag{5.13}$$

where the MN×K matrices A_ℓ^T are the back-projectors for each angle and the K×1 matrices C_ℓ are the convolution functions for each angle. If we assume that the convolution functions are equal for each angle, i.e. $C_\ell = C$ for $\ell=1, \ldots, L$, then one can rewrite Eq. (5.13) as

$$\left(\sum_{\ell=1}^{L} A_\ell^T \right) C = H \tag{5.14}$$

where the matrix in parentheses is an MN×K matrix. We can now partition C and rewrite Eq. (5.14) as

$$\left(\sum_{\ell=1}^{L} A_\ell^T \right) \begin{pmatrix} C_1 \\ C_0 \\ C_1 \end{pmatrix} = H \tag{5.15}$$

where C_0 is the central element of the convolver and the (K-1)/2×1 matrix C_1 contains the other elements of the convolver which is symmetric about C_0. Now the matrix representing the sum of the individual

back-projectors for each angle can be rewritten as

$$\left(\sum_{\ell=1}^{L} A_\ell^T\right) = \left(\sum_{\ell=1}^{L} \left(A_{\ell 1}^T \; A_{\ell 0}^T \; A_{\ell 2}^T\right)\right) \tag{5.16}$$

where $A_{\ell 1}^T$ and $A_{\ell 2}^T$ are MN×(K-1)/2 matrices and $A_{\ell 0}^T$ is a MN×1 matrix. Substituting Eq. (5.16) into Eq. (5.15) gives

$$\sum_{\ell=1}^{L} \left(A_{\ell 0}^T \left(A_{\ell 1}^T + A_{\ell 2}^T\right)\right)\begin{pmatrix} C_0 \\ C_1 \end{pmatrix} = H . \tag{5.17}$$

The system of equations in Eq. (5.12) has now been reduced so that there are (K-1)/2+1 unknowns to solve for.

The solution to Eq. (5.17) is

$$\begin{pmatrix} C_0 \\ C_1 \end{pmatrix} = (M^T M)^G M^T H \tag{5.18}$$

where

$$M = \sum_{\ell=1}^{L} \left[A_{\ell 0}^T \left(A_{\ell 1}^T + A_{\ell 2}^T\right)\right] , \tag{5.19}$$

and $(M^T M)^G$ denotes the generalized inverse. Examining $M^T M$, we see that it can be expressed as

$$M^T M = \left\{\sum_{\ell=1}^{L} \left[A_{\ell 0}^T \left(A_{\ell 1}^T + A_{\ell 2}^T\right)\right]\right\}^T \sum_{\ell=1}^{L} \left[A_{\ell 0}^T \left(A_{\ell 1}^T + A_{\ell 2}^T\right)\right] \tag{5.20}$$

$$M^T M = \begin{bmatrix} \overbrace{\sum_{n,m} A_{n0}\, A_{m0}^T}^{1\times 1} & \overbrace{\sum_{n,m} A_{n0}\left(A_{m1}^T + A_{m2}^T\right)}^{1\times(K-1)/2} \\ \underbrace{\sum_{n,m}\left(A_{n1} + A_{n2}\right) A_{m0}^T}_{(K-1)/2\times 1} & \underbrace{\sum_{n,m}\left(A_{n1} + A_{n2}\right)\left(A_{m1}^T + A_{m2}^T\right)}_{(K-1)/2\times(K-1)/2} \end{bmatrix} . \qquad (5.21)$$

$1\times N \quad 1\times N$ (over the first column) and $N\times 1$ (over the second term of the first column); $1\times N \quad N\times(K-1)/2$ (over the second column) and $N\times(K-1)/2$ (over the second term of the second column).

Therefore the evaluation of the convolver requires determining the generalized inverse of a $[1+(K-1)/2] \times [1+(K-1)/2]$ matrix. For example, if $K = 129$, this would be a 65×65 matrix.

Using Eq. (5.18) the convolvers tabulated in Table 5.1 were determined for various attenuation coefficients. The back-projection of these convolvers approximated in a least-squares sense the point spread function H which is equal to the unattenuated back-projection of the convolution function given by Ramachandran and Lakshminarayanan (1971) with the exception of $\mu = .15^*$ pixel^{-1} in which the point response was the back-projection of a Shepp and Logan convolver (1974). The point response functions were determined by back-projecting over 2π, 360 equal projections representing the appropriate convolvers into a 64×64 array using Eq. (2.4).

A plot of the estimated convolvers is given in Fig. 5.1 and a plot of their corresponding Fourier transform is given in Fig. 5.2. The Fourier transform of the convolvers for low attenuation coefficients (μ = .075 and .0958 pixel^{-1}) is very close to a ramp function

Table 5.1. Convolvers for constant attenuation coefficient determined from Eq. (5.18). The point response function was determined by back-projecting over 2π, 360 equal projections of the Ramachandran and Lakshminarayanan convolution function with the exception of $\mu = .15^*$ pixel^{-1} in which the point response was the back-projection of a Shepp and Logan convolver.

	Attenuation Coefficient				
	.075	.0958	.15	.15*	.18
0	7.83×10^{-1}	7.75×10^{-1}	5.47×10^{-1}	4.55×10^{-1}	2.40×10^{-1}
1	-3.17×10^{-1}	-3.11×10^{-1}	-1.57×10^{-1}	-1.00×10^{-1}	-1.14×10^{-2}
2	-1.33×10^{-3}	-4.31×10^{-3}	-4.89×10^{-2}	-6.11×10^{-2}	-2.62×10^{-2}
3	-3.54×10^{-2}	-3.45×10^{-2}	-2.71×10^{-2}	-2.41×10^{-2}	-3.43×10^{-2}
4	-9.09×10^{-4}	-2.59×10^{-3}	-2.75×10^{-2}	-2.73×10^{-2}	-3.49×10^{-2}
5	-1.28×10^{-2}	-1.16×10^{-2}	1.98×10^{-2}	1.62×10^{-2}	8.24×10^{-3}
6	-5.83×10^{-4}	-1.63×10^{-3}	-2.60×10^{-2}	-2.49×10^{-2}	-2.06×10^{-2}
7	-7.04×10^{-3}	-7.14×10^{-3}	5.71×10^{-3}	7.83×10^{-3}	1.23×10^{-2}
8	-2.24×10^{-4}	-5.55×10^{-4}	-6.73×10^{-3}	-1.02×10^{-2}	-6.70×10^{-3}
9	-4.14×10^{-3}	-3.41×10^{-3}	9.12×10^{-3}	9.04×10^{-3}	-2.74×10^{-3}
10	-7.30×10^{-4}	-2.58×10^{-3}	-3.33×10^{-2}	-2.77×10^{-2}	-2.77×10^{-2}
11	-2.88×10^{-3}	-1.54×10^{-3}	2.26×10^{-2}	1.77×10^{-2}	1.53×10^{-2}
12	-9.35×10^{-4}	-2.64×10^{-3}	-1.48×10^{-2}	-1.18×10^{-2}	2.76×10^{-3}
13	-1.74×10^{-3}	-3.66×10^{-4}	1.59×10^{-2}	1.19×10^{-2}	8.27×10^{-3}
14	-3.27×10^{-4}	-1.06×10^{-3}	-9.65×10^{-3}	-7.96×10^{-2}	-8.40×10^{-3}
15	-1.71×10^{-3}	-2.16×10^{-3}	-1.29×10^{-2}	-9.54×10^{-3}	-1.45×10^{-2}
16	-1.55×10^{-4}	8.98×10^{-4}	1.69×10^{-2}	1.12×10^{-2}	-1.43×10^{-2}
17	-1.49×10^{-3}	-2.40×10^{-3}	-2.88×10^{-3}	-3.96×10^{-4}	5.50×10^{-3}
18	-5.93×10^{-4}	-5.13×10^{-4}	-1.09×10^{-2}	-9.48×10^{-3}	-1.66×10^{-2}
19	-9.62×10^{-4}	-1.06×10^{-3}	2.41×10^{-3}	1.95×10^{-3}	4.90×10^{-3}
20	-2.11×10^{-4}	4.00×10^{-5}	8.94×10^{-3}	7.99×10^{-3}	1.26×10^{-2}
21	-7.73×10^{-4}	-3.77×10^{-4}	-6.34×10^{-4}	-1.54×10^{-3}	1.11×10^{-4}
22	-1.08×10^{-3}	-2.06×10^{-3}	-1.03×10^{-2}	-7.99×10^{-3}	-1.10×10^{-2}

TABLE 5.1 (Cont'd)

CONVOLVERS FOR CONSTANT ATTENUATION COEFFICIENT

	Attenuation Coefficient				
	.075	.0958	.15	.15*	.18
23	-1.20×10^{-3}	-1.34×10^{-3}	4.24×10^{-3}	4.40×10^{-3}	9.65×10^{-3}
24	1.81×10^{-4}	8.84×10^{-4}	2.66×10^{-3}	7.60×10^{-4}	-1.03×10^{-2}
25	-6.88×10^{-4}	-9.10×10^{-4}	-7.48×10^{-3}	-4.75×10^{-3}	1.36×10^{-3}
26	9.31×10^{-4}	2.52×10^{-3}	2.15×10^{-2}	1.75×10^{-2}	2.73×10^{-2}
27	-6.94×10^{-4}	-1.02×10^{-3}	-1.17×10^{-2}	-9.67×10^{-3}	-2.28×10^{-2}
28	1.50×10^{-3}	3.51×10^{-3}	1.78×10^{-2}	1.38×10^{-2}	2.33×10^{-2}
29	-1.57×10^{-3}	-2.96×10^{-3}	-1.86×10^{-2}	-1.30×10^{-2}	-2.50×10^{-2}
30	-6.91×10^{-4}	-8.21×10^{-4}	6.68×10^{-3}	4.07×10^{-3}	1.51×10^{-2}
31	2.60×10^{-4}	9.44×10^{-4}	7.42×10^{-4}	2.43×10^{-3}	-1.49×10^{-3}
32	-8.76×10^{-4}	-1.43×10^{-3}	-4.54×10^{-3}	-5.66×10^{-3}	-6.81×10^{-3}
33	3.04×10^{-3}	6.76×10^{-3}	2.33×10^{-2}	1.90×10^{-2}	1.63×10^{-2}
34	-2.33×10^{-3}	-4.73×10^{-3}	-1.69×10^{-2}	-1.22×10^{-2}	-7.15×10^{-3}
35	9.43×10^{-4}	2.04×10^{-3}	-1.86×10^{-3}	-3.58×10^{-3}	-1.58×10^{-2}
36	-2.16×10^{-3}	-4.26×10^{-3}	-1.35×10^{-2}	-5.94×10^{-2}	-3.31×10^{-3}
37	2.09×10^{-4}	5.83×10^{-4}	-1.93×10^{-3}	-6.95×10^{-3}	-1.29×10^{-2}
38	5.62×10^{-3}	1.33×10^{-2}	6.77×10^{-2}	5.23×10^{-2}	8.65×10^{-2}
39	-1.09×10^{-2}	-2.53×10^{-2}	-8.17×10^{-2}	-4.42×10^{-2}	-2.72×10^{-2}
40	4.65×10^{-3}	1.09×10^{-2}	-6.23×10^{-2}	-7.90×10^{-2}	-2.37×10^{-1}
41	4.74×10^{-3}	1.26×10^{-2}	2.08×10^{-1}	1.78×10^{-1}	3.95×10^{-1}
42	-1.73×10^{-2}	-4.28×10^{-2}	-3.18×10^{-1}	-2.42×10^{-1}	-3.83×10^{-1}
43	1.45×10^{-2}	3.75×10^{-2}	2.06×10^{-1}	1.46×10^{-1}	7.55×10^{-2}
44	-4.54×10^{-2}	-1.12×10^{-1}	-4.14×10^{-1}	-2.66×10^{-1}	2.78×10^{-1}
45	-3.72×10^{-5}	-9.02×10^{-5}	-3.12×10^{-4}	-2.02×10^{-4}	1.85×10^{-4}

XBL794-3386

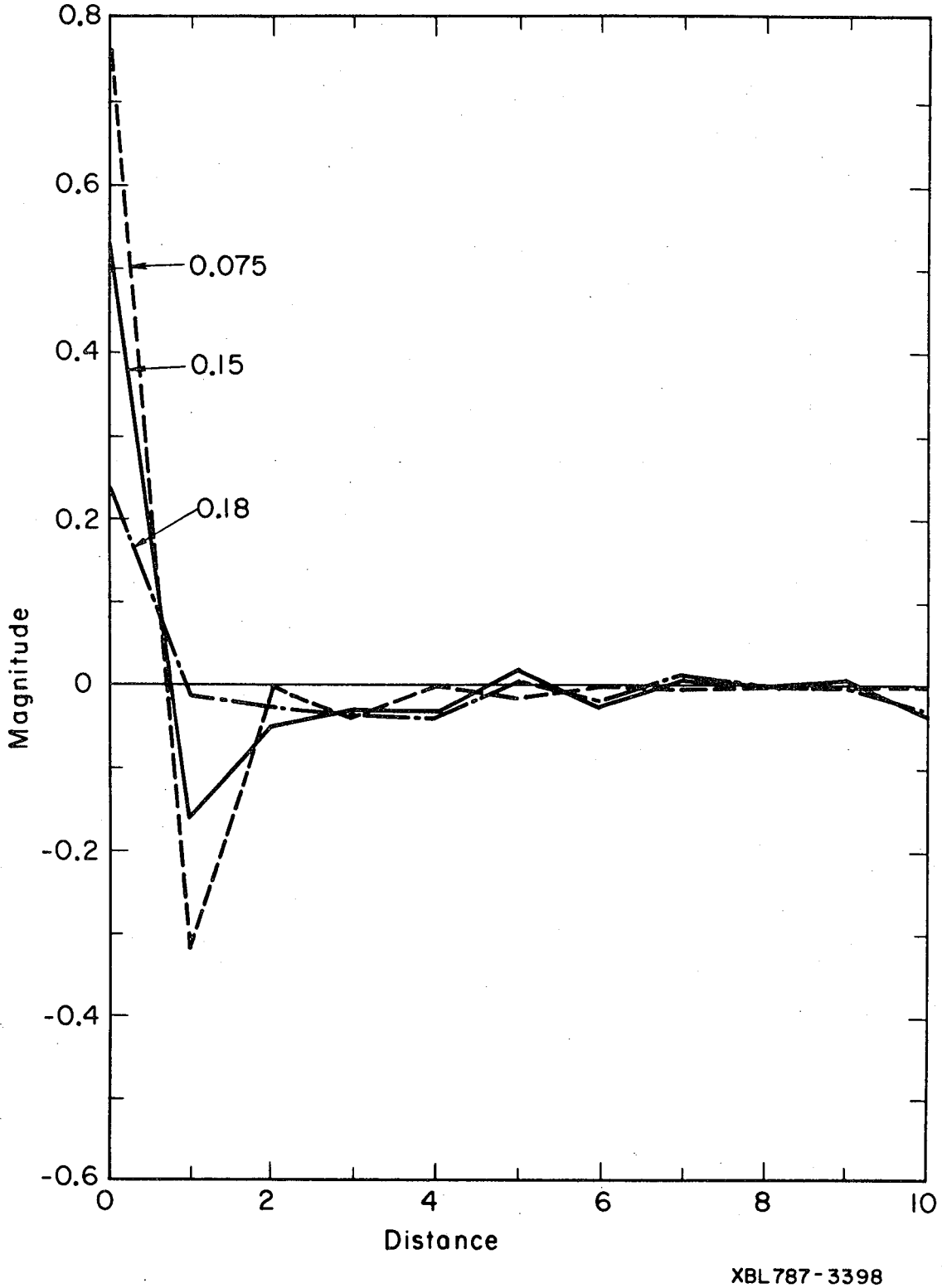

Figure 5.1. Convolvers tabulated in Table 5.1 for attenuation coefficients of μ = .075, .15, and .18 pixel^{-1}

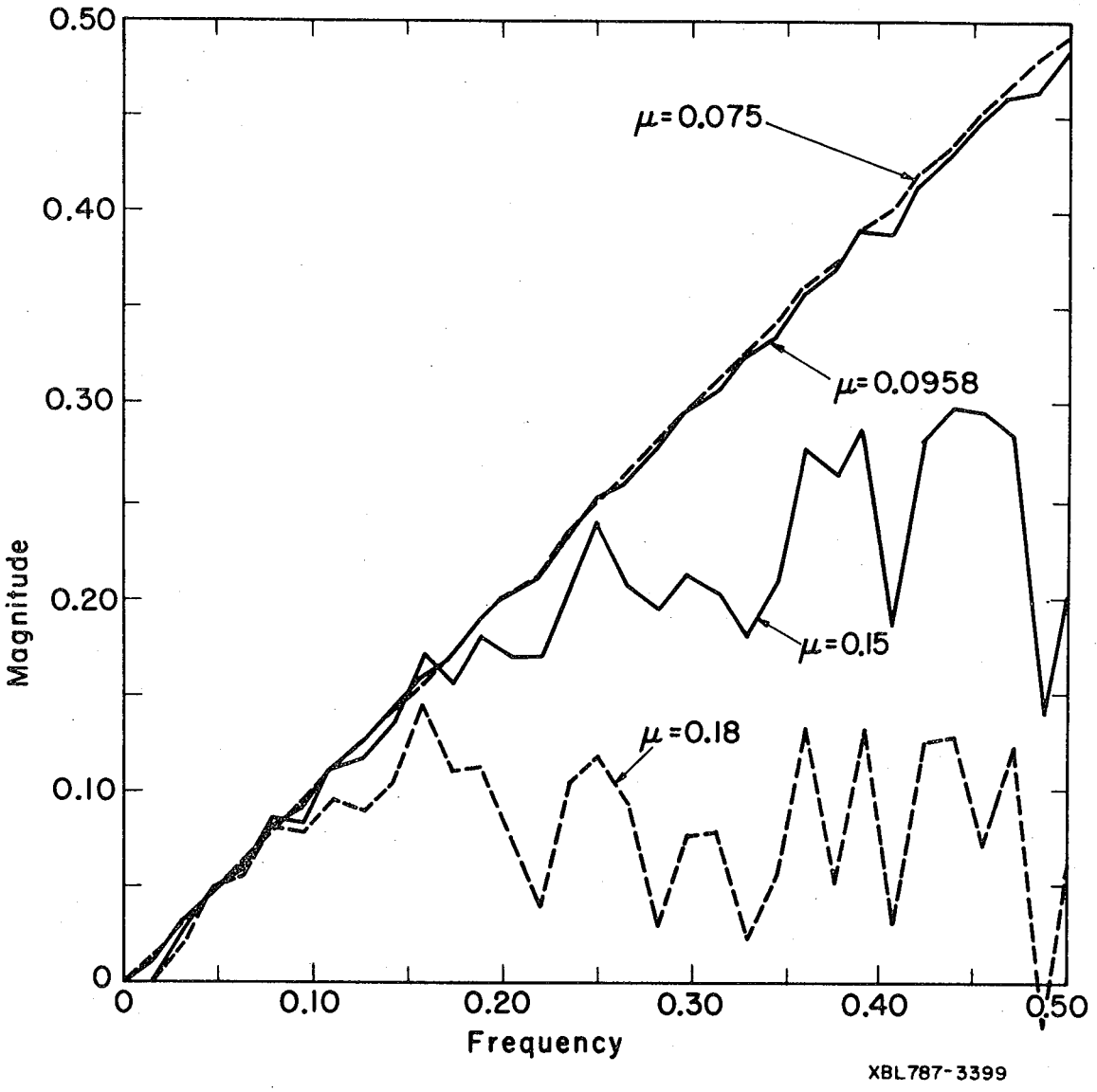

Figure 5.2. The Fourier transform of the convolution functions given in Figure 5.1 and Table 5.1 for μ = .075, .0958, .15, and .18 pixel^{-1}.

which is equal to the Fourier transform of the Ramachandran and Lakshminarayanan convolution function. For higher attenuation coefficients such as $\mu = .15$ pixel^{-1} and .18 pixel^{-1}, the filters oscillate considerably and in particular at low frequencies bend away from the ramp function and approach zero. This is consistent with the result given in Eq. (3.108) which indicates the projection data attenuated by a constant attenuation coefficient has no useful information for frequencies less than $\mu/2\pi$ cycles per projection bin. Figure 5.2 shows that for frequencies between $\mu/2\pi$ and approximately .15 cycles per projection bin, all the filters approximate a ramp, suggesting that these intermediate frequencies are not affected by attenuation, whereas the higher frequencies are distorted.

Figure 5.3 gives the reconstruction of a 30 pixel diameter phantom using the convolvers in Table 5.1 applied to 360 equally spaced projections between 0 and 2π. The resolution deteriorates as the attenuation coefficient increases. The reason for this becomes more evident if one analyzes the width of the central window of the convolvers plotted in Figure 5.1. As the attenuation coefficient increases, the central window becomes wider--this is noticeably so for $\mu = .18$ pixel^{-1}.

5.3 Convolvers Evaluated Using Power Series

In the previous section we obtained a convolution function which was piece-wise linear and thus needed only to determine the function at discrete points. To obtain a continuous varying convolution function which is not necessarily piece-wise linear, we can expand both the convolution function c_μ and point response function h in Eq. (5.1) in

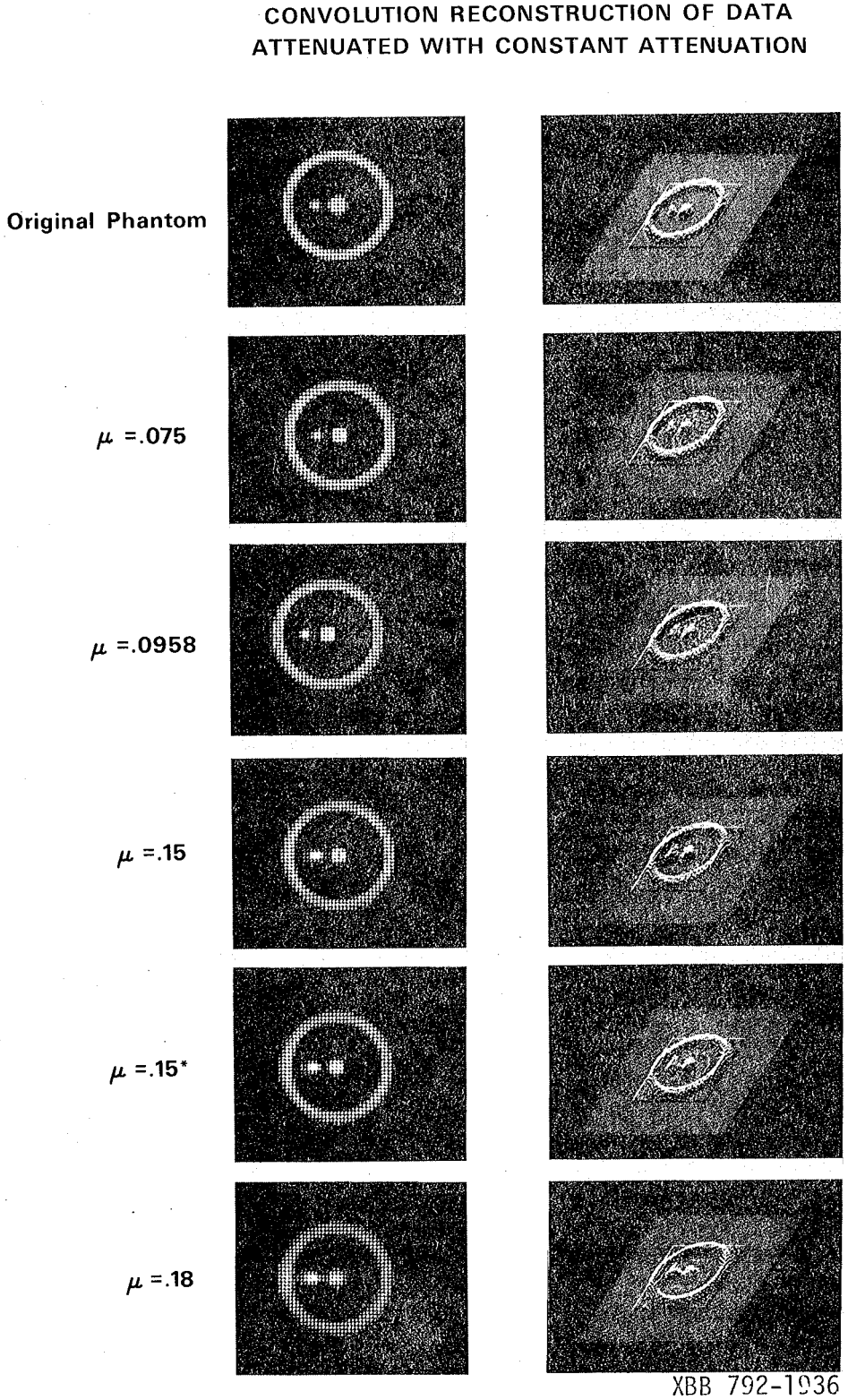

Figure 5.3. Reconstructions of a 30 pixel diameter phantom using the convolution algorithm (Eq. (3.106)) applied to 360 equally spaced projections between 0 and 2π. The convolution functions for μ = .075, .0958, .15, .15*, .18 pixel^{-1} are tabulated in Table 5.1.

terms of a power series and by equating coefficients obtain a power series solution for c_μ (Miller, 1979).

As an example, take a point response function h which is equal to a Gaussian ($h(r) = \frac{1}{\delta^2} e^{-\pi r^2/\delta^2}$). The solution to the equation

$$\frac{1}{\delta^2} e^{-\pi r^2/\delta^2} = \int_0^{2\pi} c_\mu(r\sin\theta) e^{-\mu r\cos\theta} \, d\theta \tag{5.22}$$

is

$$c_\mu(\xi) = a_0 + a_2\xi^2 + a_4\xi^4 + \ldots + a_{2n}\xi^{2n} + \ldots \tag{5.23}$$

where the first four coefficients are given by

$$a_0 = 1/(2\pi\delta^2)$$

$$a_2 = \frac{-1}{\delta^4} \left[1 + (\mu\delta)^2/(4\pi)\right]$$

$$a_4 = \frac{2\pi}{3\delta^6} \left[1 + (\mu\delta)^2/(4\pi) + (\mu\delta)^4/(32\pi^2)\right]$$

$$a_6 = \frac{-4\pi^2}{15\delta^8} \left[1 + (\mu\delta)^2/(4\pi) + (\mu\delta)^4/(32\pi^2) + (\mu\delta)^6/(384\pi^3)\right]$$

In general,

$$a_{2n} = B(2n)\{c_0 + c_2(\mu\delta)^2/\pi + c_4(\mu\delta)^4/\pi^2 + c_6(\mu\delta)^6/\pi^3 + \ldots + c_{2n}(\mu\delta)^{2n}/\pi^n\} \tag{5.24}$$

where

$$B(2n) = \frac{(-1)^n}{2\pi} \frac{2\cdot 4\cdot \ldots \cdot 2n}{1\cdot 3\cdot 5\cdot \ldots \cdot (2n-1)} \frac{\pi^n}{n!\ \delta^{2n+2}} \tag{5.25}$$

and

$$c_{2n} = (-1)^{n-1}\left\{\frac{B(2n-2)\ \delta^{2n}\ n!}{\pi^{n-1}\ 2!}\int_0^{2\pi}\cos^2\theta\ \sin^{2n-2}\theta d\theta\ c_{2n-2}\right.$$

$$+\frac{B(2n-4)\delta^{2n-2}\ n!}{\pi^{n-2}\ 4!}\int_0^{2\pi}\cos^4\theta\ \sin^{2n-4}\theta d\theta\ c_{2n-4}+..$$

$$.....+\frac{B(4)\delta^6\ n!}{\pi^2(2n-4)!}\int_0^{2\pi}\cos^{2n-4}\theta\ \sin^4\theta\ d\theta\ c_4$$

$$+\frac{B(2)\ \delta^4\ n!}{\pi(2n-2)!}\int_0^{2\pi}\cos^{2n-2}\theta\ \sin^2\theta\ d\theta\ c_2$$

$$\left.+\frac{B(0)\delta^2 n!}{(2n)!}\int_0^{2\pi}\cos^{2n}\theta d\theta\ c_o\right\} \qquad (5.26)$$

Evaluating the integrals involving products of sines and cosines gives

$$c_{2n} = \frac{1}{\Gamma(1/2)}\left\{\frac{\Gamma(3/2)}{2!}c_{2n-2} - \frac{\Gamma(5/2)}{4!}c_{2n-4} + \frac{\Gamma(7/2)}{6!}\ c_{2n-6}\right.$$

$$\left.+\ ...\ +(-1)^{n-1}\frac{\Gamma(n-\frac{3}{2})}{(2n-4)!}c_4 + (-1)^n\frac{\Gamma(n-\frac{1}{2})}{(2n-2)!}c_2 + (-1)^{n+1}\frac{\Gamma(n+\frac{1}{2})}{(2n)!}c_0\right\}$$

$$= \frac{1}{2^2\ 1!}\ c_{2n-2} - \frac{1}{2^4\ 2!}\ c_{2n-4} + \frac{1}{2^6\ 3!}\ c_{2n-6}$$

$$+\ ...\ +\frac{(-1)^{n-1}}{2^{2n-4}(n-2)!}c_4 + \frac{(-1)^n}{2^{2n-2}(n-1)!}c_2 + \frac{(-1)^{n+1}}{2^{2n}\ n!}\ c_o \qquad (5.27)$$

Thus for the parameter δ, the convolution function c_μ is given by Eqs. (5.23), (5.24), (5.25) and (5.27).

The full-width at half maximum (FWHM) of the point response function is related to the parameter δ by the equation

$$\delta^2 = \frac{\pi(\text{FWHM})^2}{4\ln 2} \quad .$$

This gives a Gaussian function which has an area equal to 1. The spatial resolution of the reconstruction will improve with a narrowing of FWHM, but the noise amplification will increase. Therefore FWHM must be choosen based on the statistical fluctuations in the data and the resolution requirements for the reconstructed image.

5.4 Fourier Space Filters

Due to the convolution theorem the convolution algorithm can be implemented either by convolving the projection data with a convolution function in real space or by multiplying the Fourier transform of the projection data by an appropriate filter in frequency space. Applying the convolution theorem to Eq. (3.106), the reconstruction of modified attenuated projection data for a constant attenuation is given by

$$\rho(\hat{x}) = \int_0^{2\pi} \int_{-\infty}^{\infty} \tilde{c}_\mu(R)\, \tilde{p}(R,\theta)\, e^{2\pi i R \langle \hat{x},\underset{\sim}{\theta} \rangle}\, dR\, e^{-\mu \langle \hat{x},\underset{\sim}{\theta}^{\perp} \rangle}\, d\theta \qquad (5.28)$$

and is implemented digitally by the back-projection of filtered projection algorithm described in Section 2.2.4. The steps of this algorithm can be symbolized as:

$$\hat{\rho} = \mathcal{B}_\mu \{ \mathcal{F}_1^{-1} [\tilde{c}_\mu \mathcal{F}_1(p)] \} \tag{5.29}$$

where $\mathcal{F}_1$ denotes the one-dimensional Fourier transform and $\mathcal{B}_\mu$ denotes the attenuated back-projection operator given by Eq. (3.102).

This algorithm can be developed with various options for frequency space filters which lends itself to easily changing the noise propagation vs. resolution properties of the convolution kernel. One can improve the resolution by changing the filter shape, but the noise amplification will increase. Alternatively, one can suppress noise; however, this noise suppression will come at the cost of resolution. Fourier space filtering also has the advantage in that the computational method for reconstructing is more efficient using the Fast Fourier Transform than convolving in real space.

The back-projection of the filtered projection algorithm has been implemented in the RECLBL Library (Huesman et al., 1977) for unattenuated data with filter functions equal to the product of a window function w(R) and the absolute value of the frequency:

$$\tilde{c}(R) = |R| \; w(R) \; . \tag{5.30}$$

Window functions such as the Butterworth, Hann, Hamming, Parzen or a rectangular window have different resolution and noise amplification characteristics. The width of these windows is measured as the distance between the closest zeros on each side of the central lobe of the inverse Fourier transform of the window function. Ideally, for good resolution,

the window function should have a central lobe that is tall and narrow. The side lobes for the inverse Fourier transform of the window function gives rises to the Gibbs phenomenon, which is observed as artifacts that are contamination from adjacent parts of the reconstruction. These side lobes can amplify statistical fluctuations in the data if the lobes and data fluctuations are in resonance.

For constant attenuation, window functions can be designed which reconstruct the emission distribution with good resolution. These window functions must be designed not only to give a narrow central window to insure adequate resolution but must be able to deconvolve the effects of attenuation and leave the required spatial frequencies which will reconstitute the image when back-projected using the attenuated back-projection operator (Eq. 3.102).

It has been proven by Tretiak and Metz (1979) that for constant attenuation, window functions can be designed for continuous sampling which reconstruct the emission distribution with a desired spatial resolution. If we take the Fourier inverse of Eq. (5.30) and substitute it into Eq. (5.2) we see that the point spread function can be represented in terms of the window function w(R):

$$h(r) = \int_0^{2\pi} \int_{-\infty}^{\infty} |R|\, w(R) e^{2\pi i R r \sin\theta} dR\, e^{-\mu r \cos\theta} d\theta \,. \qquad (5.31)$$

Rewritting Eq. (5.31) so that the first integration is with respect to θ, we have

$$h(r) = \int_{-\infty}^{\infty} |R|\, w(R) \int_0^{2\pi} e^{2\pi i R r \sin\theta - \mu r \cos\theta}\, d\theta dR \,. \qquad (5.32)$$

Integrating over θ gives

$$h(r) = 2\pi \int_{-\infty}^{\infty} |R|\, w(R)\, J_0(2\pi r \sqrt{R^2 - \mu^2/4\pi^2}\,)\, dR \qquad (5.33)$$

where J_0 is the zeroth order Bessel function.

If the window function is chosen so that w(R) is zero for $|R| < \mu/2\pi$ and $w(-R) = w(R)$ for $|R| > \mu/2\pi$, we can rewrite Eq. (5.33):

$$h(r) = 2\pi \int_{\mu/2\pi}^{\infty} 2R\, w(R)\, J_0(2\pi r \sqrt{R^2 - \mu^2/4\pi^2})\, dR. \qquad (5.34)$$

Making the change of variables $s = \sqrt{R^2 - \mu^2/4\pi^2}$ gives

$$h(r) = 2\pi \int_{0}^{\infty} 2w([s^2 + \mu^2/4\pi^2]^{1/2})\, J_0(2\pi rs)\, sds\ . \qquad (5.35)$$

Therefore we see that the point response is equal to the Hankel transform of $2w([s^2 + \mu^2/4\pi^2]^{1/2})$, where the Hankel transform is $H\{f;r\} = 2\pi \int_0^\infty f(s) \times J_0(2\pi rs)sds$ (Bracewell, 1965).

5.4.1 Rectangular Window

One window function which is of particular interest is a rectangular window function given by

$$w(R) = \begin{cases} 1 & \text{if } \mu/2\pi \leqslant |R| \leqslant \frac{1}{2} \\ 0 & \text{otherwise .} \end{cases} \qquad (5.36)$$

Note that as $\mu \to 0$ $|R|w(R)$ becomes the ramp filter which is equivalent to the convolution function due to Ramachandran and Lakshminarayanan

(1971) and Bracewell and Riddle (1967). If we substitute $[s^2 + \mu^2/4\pi^2]^{1/2}$ into w(R) we obtain

$$w(s) = \begin{cases} 1 & \text{if } 0 \leq |s| \leq \frac{1}{2}\left[1 - \mu^2/\pi^2\right]^{1/2} \\ 0 & \text{otherwise .} \end{cases} \tag{5.37}$$

Taking the Hankel transform of w(s) gives a point response function

$$h(r) = \left[1 - \mu^2/\pi^2\right]^{1/2} \frac{J_1(\pi[1 - \mu^2/\pi^2]^{1/2} r)}{r} \tag{5.38}$$

where J_1 is the first order Bessel function. We see from Eq. (5.38) that the width of the impulse response deteriorates as the attenuation coefficient increases. Note also that for attenuation coefficients greater than π, the image cannot be restored.

If instead of Eq. (5.36) the rectangular window function is

$$w(R) = \begin{cases} 1 & \text{if } \mu/2\pi \leq |R| \leq \frac{1}{2}\left[1 + \mu^2/\pi^2\right]^{1/2} \\ 0 & \text{otherwise ,} \end{cases} \tag{5.39}$$

then substituting $[s^2 + \mu^2/4\pi^2]^{1/2}$ for R, w obtain

$$w(s) = \begin{cases} 1 & \text{if } 0 \leq |s| \leq \frac{1}{2} \\ 0 & \text{otherwise .} \end{cases} \tag{5.40}$$

Taking the Hankel transform gives a point response function

$$h(r) = \frac{J_1(\pi r)}{r} \quad . \tag{5.41}$$

In order to obtain a fixed point response function for all μ the rectangular window function w(R) must vary as a function of μ as given

in Eq. (5.39). However when we implement the filtering procedure digitally using the Fast Fourier Transform, we obtain a maximum frequency of 1/2 cycle per projection bin. Equation (5.39) tells us that in order to use a rectangular window with a fixed point response function for all μ, we need to sample the projection data more frequently than a projection bin.

5.4.2 Gaussian Window

To improve the resolution of the reconstructed image a Gaussian window function can be used

$$w(R) = \begin{cases} \exp[-\pi(R^2 - \mu^2/4\pi^2)/\delta^2] & \text{if } \mu/2\pi \leq |R| \\ 0 & \text{otherwise .} \end{cases} \tag{5.42}$$

If we substitute $[s^2 + \mu^2/4\pi^2]^{1/2}$ into w(R), then the Hankel transform of w(s) gives a point response function

$$h(r) = \frac{1}{\delta^2} \; e^{-\pi r^2/\delta^2} \; . \tag{5.43}$$

The window function given by Eq. (5.42) insures that the point response remains constant for all attenuation coefficients. Digitally implementing Eq. (5.42) zeros all frequencies greater than 1/2 cycle per projection bin which causes the point spread function to deteriorate with increase in attenuation.

5.5 Noise Propagation in the Convolution Method for Constant Attenuation

In contrast to the variable attenuation situation where errors in the reconstructed image are the result of statistical fluctuations in

the transmission and emission data, the noise propagated by the convolution algorithm with constant attenuation is the result of statistical fluctuations only in the emission data. If these fluctuations are statistically independent and Poisson distributed, the estimate of the variance and mean for each projection random variable is the projection value measured:

$$E\{p_\gamma(\xi,\theta)\} = p_\gamma(\xi,\theta) \ , \tag{5.44}$$

$$\sigma^2\{p_\gamma(\xi,\theta)\} = p_\gamma(\xi,\theta) \ . \tag{5.45}$$

Using Eq. (3.76), the estimate for the mean and variance for the modified projections given by Eq. (3.93c) are

$$E\{p(\xi,\theta)\} = p_\gamma(\xi,\theta)/G_\mu(\xi,\theta) \ , \tag{5.46}$$

$$\sigma^2\{p(\xi,\theta)\} = p_\gamma(\xi,\theta)/[G_\mu(\xi,\theta)]^2 \ , \tag{5.47}$$

where $G_\mu(\xi,\theta)$ is the exponential factor given by Eq. (3.72).

5.5.1 Statistical Aspects of the Convolution Algorithm

Errors in the reconstructed image are more easily analyzed for the convolution algorithm than for the iterative methods discussed in Chapter 4. Using Eq. (3.106), one can express the mean value function for the reconstructed image as

$$m_\rho(\hat{x}) = \mathcal{B}_\mu\{c_\mu(\xi) * E[p(\xi,\theta)]\} \tag{5.48}$$

where $\mathcal{B}_\mu$ is the back-projection operator given by Eq. (3.102) and $p(\xi,\theta)$ are the modified projections. Substituting Eq. (5.46) into (5.48) gives an expression of the mean value function $m_\rho(\hat{x})$ in terms of the measured projections--

$$m_\rho(\hat{x}) = \mathcal{B}_\mu\{c_\mu(\xi) * [p_\gamma(\xi,\theta)/G_\mu(\xi,\theta)]\} \tag{5.49}$$

The variance in the reconstructed image is given by the equation

$$\sigma_\rho^2(\hat{x}) = E\{[\rho(\hat{x}) - E[\rho(\hat{x})]]^2\} \ . \tag{5.50}$$

Barrett and co-workers (1976) have shown for independent projection samples that Eq. (5.50) reduces to

$$\sigma_\rho^2(\hat{x}) = \mathcal{B}_{2\mu}\{c_\mu^2(\xi) * \sigma^2[p(\xi,\theta)]\} \ . \tag{5.51}$$

To express this in terms of the measured data $p_\gamma(\xi,\theta)$, we use Eq. (5.47) and obtain

$$\sigma_\rho^2(\hat{x}) = \mathcal{B}_{2\mu}\{c_\mu(\xi)^2 * [p_\gamma(\xi,\theta)/(G_\mu(\xi,\theta))^2]\} \ . \tag{5.52}$$

The percent root-mean-square uncertainty defined as

$$\%\text{RMS uncertainty} = \frac{100\{\sigma_\rho^2(\hat{x})\}^{1/2}}{m_\rho(\hat{x})} \ , \tag{5.53}$$

can be expressed in terms of the measured projections $p_\gamma(\xi,\theta)$ by substituting Eqs. (5.49) and (5.52) into Eq. (5.53) -

$$\% \text{ RMS} = \frac{100[\mathcal{B}_\mu\{c_\mu(\xi)^2 * [p_\gamma(\xi,\theta)/(G_\mu(\xi,\theta))^2]\}]^{1/2}}{\mathcal{B}_\mu\{c_\mu(\xi) * [p_\gamma(\xi,\theta)/G_\mu(\xi,\theta)]\}} \quad . \tag{5.54}$$

Note that the % RMS is a function of position in the transverse section.

The autocovariance function,

$$C_{\rho\rho}(\hat{x}_1,\hat{x}_2) = E\{[\rho(\hat{x}_1) - m_\rho(\hat{x}_1)][\rho(\hat{x}_2) - m_\rho(\hat{x}_2)]\} \quad , \tag{5.55}$$

gives a measure of the "texture" of the reconstructed noise (Metz and Beck, 1974). One can show that

$$C_{\rho\rho}(\hat{x}_1,\hat{x}_2) = \iint c_\mu(\langle \hat{x}_1,\underset{\sim}{\theta}\rangle - \xi)\ e^{-\mu\langle \hat{x}_1,\underset{\sim}{\theta}^\perp\rangle}$$

$$\times\ c_\mu(\langle \hat{x}_2,\underset{\sim}{\theta}\rangle - \xi)\ e^{-\mu\langle \hat{x}_2,\underset{\sim}{\theta}^\perp\rangle}\ \sigma^2\{p(\xi,\theta)\}\ d\xi d\theta \quad . \tag{5.56}$$

A covariance function which decreases rapidly to zero as the distance between points increases indicates that the reconstruction values are relatively independent except at small distances; whereas, a covariance function which decreases slowly would indicate that the reconstruction values have correlations of greater extent. A positive covariance indicates that the errors for the two points $\hat{x}_1$ and $\hat{x}_2$ are likely to be of the same sign. Negative covariance indicates that the errors are of the opposite sign and the reconstruction values have positive to negative fluctuations at the two points about their own mean value. Note that when $\hat{x}_1 = \hat{x}_2$ in Eq. (5.56), the autocovariance reduces to the variance given by Eq. (5.51). For stationary random processes, the covariance function depends only on the distance between the two

points $\hat{x}_1$ and $\hat{x}_2$; however, this is not the case in emission computed tomography.

5.5.1.1 Point Source Image

For a point source image, one can easily evaluate the mean, the variance, and the covariance functions. Using Eq. (3.73) the projection of a point source $\rho(x,y) = \delta(x-x_0)\,\delta(y-y_0)$ is

$$p_\gamma(\xi,\theta) = G_\mu(\xi,\theta)\, e^{\mu\langle \hat{x}_0, \underset{\sim}{\theta}^\perp\rangle}\, \delta(\xi - \langle \hat{x}_0, \underset{\sim}{\theta}\rangle) \,. \tag{5.57}$$

Substituting this into Eq. (5.49) and using the definition of the back-projection operator given by Eq. (3.102), gives

$$\begin{aligned} m_\rho(\hat{x}) &= \mathcal{B}_\mu \{c_\mu(\xi) * [e^{\mu\langle \hat{x}_0, \underset{\sim}{\theta}^\perp\rangle}\, \delta(\xi - \langle \hat{x}_0, \underset{\sim}{\theta}\rangle)]\} \\ &= \int_0^{2\pi} c_\mu[\langle \hat{x}-\hat{x}_0, \underset{\sim}{\theta}\rangle]\, e^{-\mu\langle \hat{x}-\hat{x}_0, \underset{\sim}{\theta}^\perp\rangle}\, d\theta \,. \end{aligned} \tag{5.58}$$

Note that if $x_0 = y_0 = 0$ this is just the point response function h given by Eq. (5.1) which should be very close to a delta function.

Likewise substituting the projection of a point source [Eq. (5.57)] into Eq. (5.52) gives the variance function

$$\sigma_\rho^2(\hat{x}) = \int_0^{2\pi} c_\mu^2[\langle \hat{x}-\hat{x}_0, \underset{\sim}{\theta}\rangle]/G_\mu(\langle \hat{x}_0, \underset{\sim}{\theta}\rangle, \theta)\, e^{-2\mu\langle \hat{x}-\hat{x}_0, \underset{\sim}{\theta}^\perp\rangle}\, d\theta \,. \tag{5.59}$$

If $x_0 = y_0 = 0$, the variance is just the back-projection of the square of the convolution function divided by the exponential factor $G_\mu(0,\theta)$.

Thus the average value given by Eq. (5.58) is very local; whereas, the variance function has a much larger extent. From the plots of the convolution functions given in Fig. 5.2, one might expect that the variances will decrease due to the depressed side lobes as the attenuation coefficient increases. However, the exponential factor in Eq. (5.59) tends to dominate and negates any noise suppression of the side lobes in the convolution function.

For a point source image using Eq. (5.56) the autocovariance function is given by

$$C_{\rho\rho}(\hat{x}_1,\hat{x}_2) = \int_0^{2\pi} c_\mu[\langle \hat{x}_1-\hat{x}_0,\underset{\sim}{\theta}\rangle]\; c_\mu[\langle \hat{x}_2-\hat{x}_0,\underset{\sim}{\theta}\rangle]/G_\mu(\langle \hat{x}_0,\theta\rangle,\theta)$$

$$\times\; e^{-\mu\langle \hat{x}_1+\hat{x}_2-\hat{x}_0,\underset{\sim}{\theta}^{\perp}\rangle}\; d\theta\,. \tag{5.60}$$

5.5.1.2 Circular Disc

For a circular disc the measured projections are

$$p_\gamma(\xi,\theta) = \begin{cases} G_\mu(\xi,\theta)\;\dfrac{2}{\pi R^2}\,\dfrac{C}{\mu}\,\sinh[\mu(R^2-\xi^2)^{1/2}] & |\xi|\leq R \\ 0 & \text{otherwise} \end{cases} \tag{5.61}$$

where $G_\mu(\xi,\theta)$ as defined in Eq. (3.72) is $G_\mu(\xi,\theta) = \exp[-\mu(R^2-\xi^2)^{1/2}]$ and C is the total emitted photons over the disc. Using Eqs (5.49) and (3.102), the mean value function is

$$m_\rho(\hat{x}) = \frac{2C}{\pi R^2 \mu}\;\; \mathcal{B}_\mu\{c_\mu(\xi) * \sinh[\mu(R^2-\xi^2)^{1/2}]\}\,. \tag{5.62}$$

Using Eq. (5.52) the variance function is given by

$$\sigma_\rho^2(\hat{x}) = \frac{2C}{\pi R^2 \mu} B_{2\mu}(c_\mu^2(\xi) * \{\sinh[\mu(R^2-\xi^2)^{1/2}] \exp[\mu(R^2-\xi^2)^{1/2}]\}). \quad (5.63)$$

For a circular disc the % RMS defined by Eq. (5.53) is given by

$$\% \text{ RMS} = \left(\frac{A}{C}\right)^{1/2} \quad (5.64)$$

where A represents the remaining factors (factors not including C) after dividing Eq. (5.63) by the square of Eq. (5.62) and multiplying by 10^4. We see that the square of the %RMS is inversely proportional to the total emitted photons. Since the emitted photons and measured photons are related by a constant attenuation factor which is independent of C, we are assured that Eq. (5.64) is also a correct formulation if we interpret C to mean total measured photons.

5.5.2 Measure of Percent Root-Mean-Square Uncertainty for Simulated Projection Data

A circular disc of 30 pixels in diameter were chosen to simulate the propagation of errors for the convolution algorithm. The disc was reconstructed from 360 projection angles over 360°. The projections had bin sizes equal to the pixel size. The projection data were evaluated using analytically calculated line integrals and adding Poisson noise with mean and variance equal to the measured line integral. The projection data were then modified as given by

Eq. (3.76). This modification in essence factored from the data the attenuation measured between the central axis and the edge of the disc.

These data, which conformed to the projections given by Eq. (3.93c), were reconstructed using the convolution algorithm given by Eq. (3.106) for attenuation coefficients equal to .075, .0958, .15, .18 pixel^{-1}. For each attenuation coefficient, the projection data were convolved with the corresponding convolvers given in Table 5.1 before back-projecting. The results for total measured photons of 5×10^5, 1×10^6, 5×10^6, 1×10^7 and ∞ are shown in Fig. 5.4. The convolvers for the higher attenuation coefficients amplify the noise at low statistics resulting in reconstruction artifacts.

The %RMS uncertainty was evaluated using Eqs. (4.76), (4.77), and (4.83) for the reconstructions in Fig. 5.4 and tabulated in Table 5.2. The results indicate that the %RMS uncertainty decreases with an increase in the total measured photons for each attenuation coefficient. The %RMS uncertainty increases with an increase in the attenuation coefficient for the same measured photons. The convolver for μ = .15* was evaluated by a least-squares fit of the attenuated back-projection of a convolver with a point response function equal to the unattenuated back-projection (Eq. (2.4)) of a Shepp and Logan convolver. Using this convolver does not amplify the noise as much as the convolver fitted for μ = .15 pixel^{-1} to the point response function which was the back-projection of the Ramachandran and Lakshminarayanan convolver. The variation in the reconstructed image for perfect data (counts = ∞) are less than 5%; however, the image was thresholded so that the

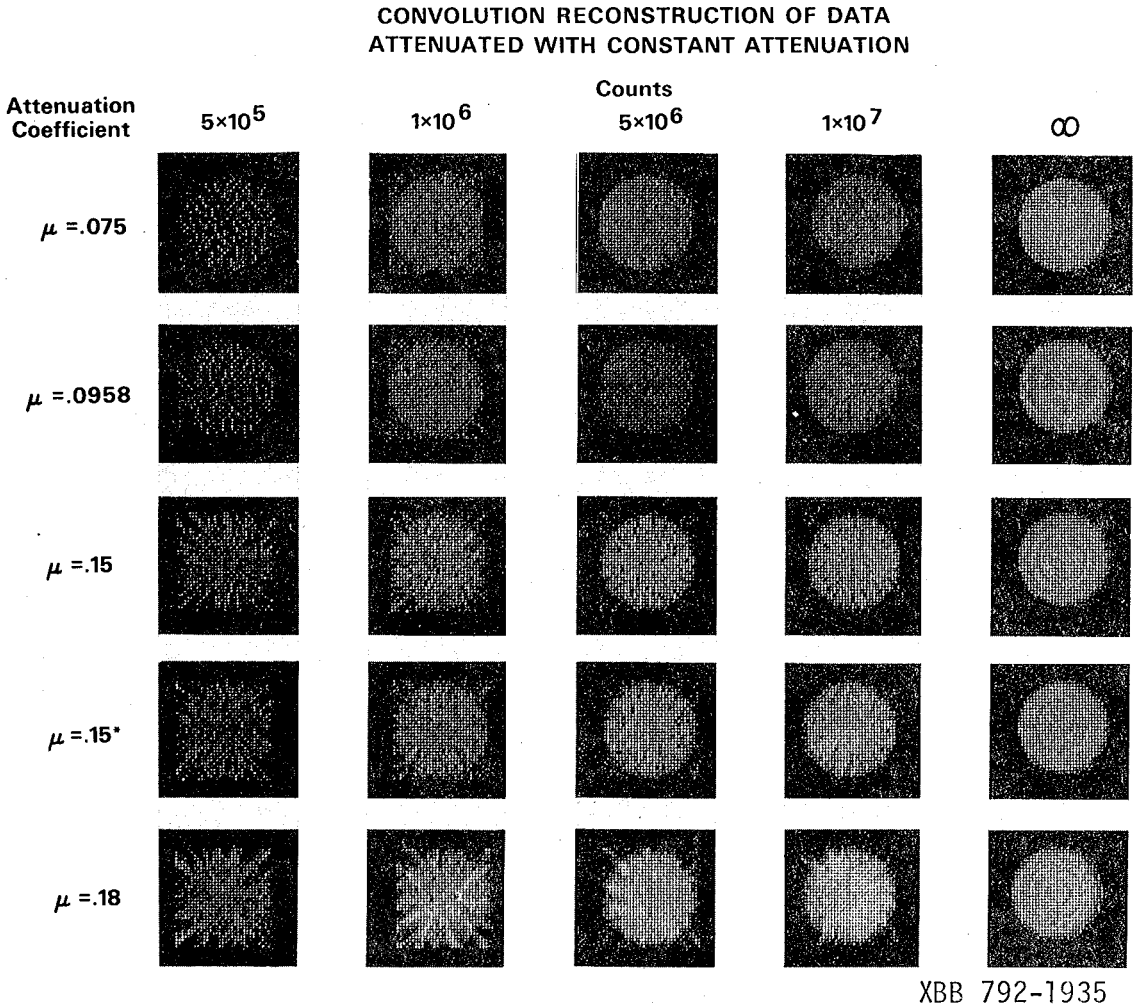

Figure 5.4. Reconstructions of a 30 pixel diameter disc using the convolution algorithm applied to 360 equally spaced Poisson distributed projections between 0 and 2π. The convolution functions for μ = .075, .0958, .15, .15*, .18 pixel^{-1} are tabulated in Table 5.1.

Table 5.2. The percent root-mean-square uncertainty as a function of emission statistics and attenuation coefficient for the reconstruction of a circular disc 30 pixels in diameter from 360 projection angles over 360° using the convolution algorithm. The convolvers for μ = .075, .0958, .15, .15* and .18 pixel^{-1} are tabulated in Table 5.1. The counts represent the total measured counts for all 360 projections.

Attenuation Coefficient (pixel^{-1})	Emission Counts				
	5×10^5	1×10^6	5×10^6	1×10^7	∞
0	12.2	8.5	3.9	2.9	0.9
.075	18.9	13.9	6.2	4.2	1.1
.0958	24.2	18.1	8.1	5.8	1.4
.15	50.1	34.0	13.8	10.7	3.3
.15*	37.7	25.8	13.5	9.1	2.9
.18	35.3	29.2	13.3	9.9	4.6

resulting structure could be analyzed.

Fitting the data tabulated in Table 5.2 to Eq. (5.64) gives the following values for the constant A:

$$1.82 \times 10^8 - \mu = .075$$
$$3.00 \times 10^8 - \mu = .0958$$
$$1.23 \times 10^9 - \mu = .15$$
$$7.03 \times 10^8 - \mu = .15^*$$
$$6.71 \times 10^8 - \mu = .18$$

Note that the constant A is dependent on the attenuation coefficient μ. From the mean value function $m_\rho(\hat{x})$ in Eq. (5.62) and the variance function $\sigma^2_\rho(\hat{x})$ in Eq. (5.63) it is not obvious how the %RMS varies with μ since these functions depend in a more complicated way on μ than does the total counts C.

6. CONCLUSION

This thesis developed the theory and reconstruction methods for single-photon emission computed tomography. Reconstruction methods for variable attenuation coefficient involve iterative techniques of implementing a generalized inverse of the discrete attenuated Radon transform. Methods for constant attenuation coefficient involve convolution methods that give an estimate of the inverse of the modified attenuated Radon transform when applied to appropriately modified projection data. The rates of convergence for the iterative algorithms and the amplification of statistical errors for both the iterative and convolution methods are a function of the magnitude of the attenuation coefficient.

The mathematical aspects of single-photon ECT were investigated for both the attenuated Radon transform (A_μ: $\rho \to p_\gamma$) -

$$p_\gamma(\xi,\theta) = \int \rho(\hat{x}) \exp\left\{ - \int_{\langle \hat{x}', \underset{\sim}{\theta}^\perp \rangle \geq \langle \hat{x}, \underset{\sim}{\theta}^\perp \rangle} \mu(\hat{x}')\, \delta(\xi - \langle x', \underset{\sim}{\theta} \rangle) d\hat{x}' \right\} \delta(\xi - \langle \hat{x}, \underset{\sim}{\theta} \rangle) d\hat{x} \tag{1.1}$$

and the modified attenuated Radon transform (A_μ: $\rho \to p$) -

$$p(\xi,\theta) = \int \rho(\hat{x}) \exp\left\{ - \int_{0 \leq \langle \hat{x}', \theta^\perp \rangle \leq \langle \hat{x}, \theta^\perp \rangle} \mu(\hat{x}')\, \delta(\xi - \langle \hat{x}', \underset{\sim}{\theta} \rangle) dx' \right\} \delta(\xi - \langle \hat{x}, \underset{\sim}{\theta} \rangle) d\hat{x}.$$

where $p(\xi,\theta)$ is obtained from $p_\gamma(\xi,\theta)$ using Eq. (3.76). The advantages and disadvantages of these two transforms are as follows:

1) The kernel for the integral operator, $A_\mu^* A_\mu$, has a simpler expression (Theorem 3.20) than does the attenuated Radon transform

(Theorem 3.3); whereas the kernel expressions for $B_\mu A_\mu$ (Theorem 3.4) and $\mathcal{B}_\mu A_\mu$ (Theorem 3.21) are identical, and the kernels for $A_\mu A_\mu^*$ (Theorem 3.5) and $A_\mu A_\mu^*$ (Theorem 3.22) differ only in the limits of integration for the integrals in the exponential arguments.

2) The shift properties for the modified attenuated Radon transforms are complicated by an extra exponential attenuation factor for the projections of the unshifted concentration function ρ (Theorems 3.18 and 3.19) which is not present for the attenuated Radon transform (Theorems 3.1 and 3.2). This factor and the fact that the central axis most often intersects the projection ray in the interior of a pixel makes the attenuation factors (Eq. (4.17)) for the modified attenuated Radon transform less efficient to calculate than the attenuation factors for the attenuated Radon transform (Eq. (4.15)). However, one may want to use the discrete modified attenuated Radon transform A to solve the reconstruction problem if it has better numerical stability; that is, the condition number of the matrix A is greater than the discrete attenuated Radon transform A for the same attenuation distribution. This has not yet been confirmed.

3) The major application of the modified attenuated Radon transform is for constant attenuation coefficient in which estimates for the inverse of the modified attenuated Radon transform can be evaluated either by: a) a convolution approach which involves convolving in real space (Eq. (3.106)) or equivalently filtering in frequency space (Eq. (5.28)); or b) interpolating in frequency space which yields Fourier transforms of unattenuated projections (Theorem 3.30).

The theorems and mathematical structure developed for the attenuated Radon transform and the modified attenuated Radon transform point

to the fact that with properly chosen weight functions, there exist eigenfunctions for $A_\mu A_\mu^*$, $A_\mu^* A_\mu$, $A_\mu A_\mu^*$ and $A_\mu^* A_\mu$. However, explicit expressions for these eigenfunctions have not been developed for even the simplest case of constant attenuation. For the Radon transform the eigenfunctions of $\mathcal{R}^*\mathcal{R}$ have been expressed analytically and analyzed by various authors (Maldonado, 1965; Maldonado and Olsen, 1965; Marr, 1974; Zeitler, 1974; Eggermont, 1975; Miller, 1978). The eigenfunctions of $\mathcal{R}\mathcal{R}^*$ have been developed for various weight functions by Davison and Grünbaum (1979).

Inversion of the discrete attenuated Radon transform requires using iterative algorithms to reconstruct projection data attenuated by a variable attenuation coefficient. These algorithms converge with acceptable errors within 15 iterations for most radionuclides used in nuclear medicine. Simulations have shown that the rate of convergence decreases as the magnitude of the attenuation coefficient increases above $\mu = .19\ cm^{-1}$ for a 30 cm diameter disc, so that at $\mu = .60\ cm^{-1}$ the result does not converge to an acceptable error criterion even after 30 iterations. This means that energies of photons emitted in tissue of less than 22 keV should not be used in single-photon ECT. The isotope of ^{131}Cs has a very low energy photon of 34.5 keV (x-rays of xenon) which has an attenuation coefficient of $.27\ cm^{-1}$ in tissue. This isotope can be used for reconstructing transverse sections of the body in most areas where there is solid tissue; however, the presence of bone may yield artifacts due to the photoelectric absorption of calcium leading to an attenuation coefficient of $1.3\ cm^{-1}$. The same scenario can be given for iodine-125 which emits a 27 keV photon with an

attenuation coefficient of $\mu = .45\ cm^{-1}$ in tissue. Isotopes of Tl-201 (73-80 keV, $\mu = .18\ cm^{-1}$), Tc-99m (140 keV, $\mu = .15\ cm^{-1}$), Se-75 (136 keV, $\mu = .15\ cm^{-1}$, 57%; 265 keV, $\mu = .125\ cm^{-1}$, 60%), and Cs-129 (375 keV, $\mu = .11\ cm^{-1}$, 48%) have been used for ECT with good contrast and spatial resolution.

In contrast to the detrimental effects of high attenuation coefficients, low attenuation coefficients actually improve convergence and the condition number of the discrete attenuated Radon transform. It is believed the reason there is an improvement in the rate of convergence for increased attenuation coefficients using the iterative methods is due to the existence of more independent equations. For example, data measured 180° apart give independent linear equations with attenuation, whereas the coefficients of the equations for 180° conjugate views are identical with no attenuation. However for high attenuation coefficients, the added information of independent samples for conjugate views is dominated by the increased sensitivity of the problem (increase in the condition number) as the attenuation coefficient increases. The point at which increase in attenuation stops being an advantage in iteratively reconstructing a circular disc is dependent on the product of attenuation coefficient with the object size. As the size of the object increases the minimum of the condition number is obtained at lower attenuation coefficients.

The rate of convergence is a deterministic factor of the discrete attenuated transform, whereas trace $[(A^TA)^{-1}]$ is a stochastic factor that measures the amplification of statistical errors. For equal errors on the projections and infinite transmission statistics,

the average variance is given by {trace $[(A^TA)^{-1}]$/ no. of pixels} $\times \sigma^2$ (projection value). For a uniform source distributed in a circular attenuator the projections are nearly constant (Fig. 2.9). Thus the errors on the projections of the disc are almost equal assuming Poisson statistics. The spectra for discrete attenuated projection operators operating on 8 x 8, 10 x 10, and 12 x 12 transverse sections indicate that the errors as measured by tr $[(A^TA)^{-1}]$ increase almost monotonically as the attenuation coefficient increases. These results agree with numerical simulations of objects having diameters of 30 and 40 pixels. These results showed that the % RMS uncertainty increased with attenuation coefficient. In summary, the rate of convergence for the first 30 iterations improves with an increase in attenuation coefficient to a maximum, then decreases; however, with the increase in attenuation coefficient the statistical variation of the solution increases.

With the doses of radiopharmaceuticals used presently in nuclear medicine, the %RMS uncertainty in the reconstructed image ranges between 50 and 20%. Using Tc-99m as a brain scanning agent the reconstructed %RMS uncertainty can be no better than 9.8%, even with infinite statistics if the attenuation coefficients are determined from a transmission experiment with I_o = 1000 (4.2×10^6 total photons) incident photons per projection ray (Table 4.11). The data indicate that changes in the transmission statistics result in larger improvement in the % RMS uncertainty for high than low emission statistics. For positron emission computed tomography a similar conclusion can be drawn as shown analytically below. For a fixed attenuation coefficient and a disc with

radius R, the functional relationship for the % RMS uncertainty is (Gullberg and Huesman, 1979):

$$\% \text{ RMS (Positron)} = \left(\frac{K_1}{C} + \frac{K_2}{I_0} \right)^{1/2},$$

where C is the total number of emission events and I_0 is the number of incident transmission photons per projection ray. The partial derivative of the % RMS uncertainty with respect to I_0 is

$$\frac{\partial(\% \text{ RMS})}{\partial I_0} = - \frac{K_2}{2I_0^2} \frac{1}{(K_1/C + K_2/I_0)^{1/2}},$$

which shows that as the emission counts C increase, the rate of change of the %RMS uncertainty with respect to I_0 increases. This means that if one is not able to obtain high statistics for the emission study, then not much improvement can be expected for a transmission study with high statistics. For constant attenuation the analysis of errors is much simpler because it is not complicated by the statistical errors of a transmission study.

There are three methods for determining convolvers for constant attenuation: (1) optimum least-squares approach; (2) series expansion method that fits the back-projection of the convolution to a desired point spread function; and (3) optimum window functions for filtering the data in frequency space. The filter functions are zero for frequencies less than $\mu/2\pi$ (see Eq. (5.35)). This is consistent with the interpolation result given in Eq. (3.108) where frequencies less than $\mu/2\pi$ cycles per projection bin are not used to evaluate the Fourier

transform of unattenuated projections. All frequencies greater than .5 cycles per projection bin are zeroed by digital implementation of filtering. This suggests that data attenuated by a constant attenuation coefficient greater than π cycles per projection bin cannot be reconstructed (i.e., $\mu/2\pi$ must be less than .5). Preliminary simulations show that the upper bound of $\mu/2\pi = 0.5$ is much more restrictive. Thus filtering and convolution procedures cannot reconstruct attenuated projections for attenuation coefficients higher than $\mu = .20\ cm^{-1}$ for a 30 cm disc with diameter of 60 resolution elements. In this respect the filtering or convolution methods are inferior to iterative algorithms which can accurately reconstruct a 30 cm disc with an attenuation coefficient $\mu = .30\ cm^{-1}$. This may be due to the fact that iterative methods can simultaneously make adjustments in the solution based on information obtained from all the projections, whereas the convolution methods modify only one projection at a time. The convolution method is much faster and is adequate for reconstructing transverse sections of the head using radionuclides such as ^{99m}Tc or ^{123}I.

ACKNOWLEDGEMENTS

The attenuated Radon transform was formulated to explain the artifacts observed in reconstructions of projection data for phantom studies directed by Professor Thomas Budinger. I am indebted to him for his direction and encouragement in this research, and appreciate his enthusiasm for science and his willingness to tackle difficult problems. The many comments and suggestions of Dr. Ronald Huesman were invaluable in preparing this thesis. The results for the single angle and N-fold attenuated projection operators were an extension of results for the Radon transform presented by Dr. Robert Marr in Professor Alberto Grünbaum's seminars on reconstruction tomography in the Fall of 1978. I am grateful to both Dr. Marr and Professor Grünbaum for the many discussions and answers to many of my questions. I want to thank Professor Robert Glaeser for his comments and also thank Professor Stanley Deans for the many stimulating discussions we had concerning aspects of the attenuated Radon transform.

Above all I appreciate the love and kindness of my wife Kathy, daughter Stacy, and son Trig who supported me and were very, very patient.

I am grateful to Bob Stevens for the preparation of the illustrations, to Alice Ramirez for typing the manuscript, and for the typing support of Mary Graham and Linda Lutgens.

This research was supported in part by the U.S. Department of Energy and the National Cancer Institute and the National Heart, Lung and Blood Institute.

BIBLIOGRAPHY

H. O. Anger, Survey of radioisotope cameras, ISA Trans. 5, 311-334, 1966a.

H. O. Anger, Sensitivity, resolution, and linearity of the scintillation camera, IEEE Trans. Nucl. Sci. NS-13, 380-392, 1966b.

H. O. Anger, The instruments of nuclear medicine: I, Hospital Practice 7, 45-54, 1972.

H. O. Anger, Multiple plane tomographic scanner, in Tomographic Imaging in Nuclear Medicine, G. S. Freedman, ed. (Society of Nuclear Medicine, New York, 1973), 2-15.

H. O. Anger, Tomography and other depth discrimination techniques, in Instrumentation in Nuclear Medicine, G. J. Hine and J. A. Sorenson, eds. (Academic Press, New York, 1974), Vol. 2, 61-100.

A. Ansari and W. G. Wee, Reconstruction for projection in the presence of distortion, in Proc. 1977 IEEE Conference on Decision and Control (IEEE, New Orleans, 1977), Vol. I, 361-366.

H. H. Barrett, S. K. Gordon, and R. S. Hershel, Statistical limitations in transaxial tomography, Comput. Biol. Med. 6, 307-323, 1976.

R. H. T. Bates and T. M. Peters, Towards improvements in tomography, New Zealand J. Sci. 14, 883-896, 1971.

S. Bellini, C. Cafforio, M. Piacentini, and F. Rocca, Design of a computerized emission tomographic system, Signal Processing (in press), 1979a.

S. Bellini, C. Cafforio, M. Piacentini, and F. Rocca, Compensation of tissue absorption in emission tomography, IEEE Trans. ASSP (in press), 1979b.

R. Bellman, Introduction to Matrix Analysis, McGraw-Hill, New York, 1970.

A. Ben-Israel and T. N. E. Greville, Generalized Inverses: Theory and Applications, John Wiley and Sons, New York, 1974.

T. L. Boullion and P. L. Odell, Generalized Inverse Matrices, John Wiley and Sons, New York, 1971.

A. R. Bowley, C. G. Taylor, D. A. Causer, D. C. Barber, W. I. Keyes, P. E. Undrill, J. R. Corfield, and J. R. Mallard, A radioisotope scanner for rectilinear, arc, transverse section and longitudinal section scanning: (ASS - The Aberdeen Section Scanner), Br. J. Radiology 46, 262-271, 1973.

R. N. Bracewell, The Fourier Transform and Its Applications, McGraw-Hill, New York, 1965.

R. N. Bracewell and A. C. Riddle, Inversion of fan-beam scans in radio astronomy, Astrophysics J. 150, 427-434, 1967.

R. A. Brooks and G. DiChiro, Principles of computer assisted tomography (CAT) in radiographic and radioisotopic imaging, Phys. Med. Biol. 21, 689-732, 1976.

J. L. Brown, Mean square truncation error in series expansion of random functions, J. SIAM 8, 28-32, 1960.

G. L. Brownell, J. A. Correia, and R. G. Zamenhof, Positron instrumentation, in Recent Advances in Nuclear Medicine, J. H. Lawrence and T. F. Budinger, eds. (Grune and Stratton, New York, 1978), Vol. 5, 1-49.

T. F. Budinger and G. T. Gullberg, Three-dimensional reconstruction in nuclear medicine emission imaging, IEEE Trans. Nucl. Sci. NS-21, 2-20, 1974.

T. F. Budinger and G. T. Gullberg, Transverse section reconstruction of gamma-ray emitting radionuclides in patients, in Reconstruction Tomography in Diagnostic Radiology and Nuclear Medicine, M. M. Ter-Pogossian, M. E. Phelps, G. L. Brownell, J. R. Cox, Jr., D. O. Davis, and R. G. Evans, eds. (University Park Press, Baltimore, 1977), 315-342.

T. F. Budinger, J. L. Cahoon, S. E. Derenzo, G. T. Gullberg, B. R. Moyer, and Y. Yano, Three dimensional imaging of the myocardium with radionuclides, Radiology 125, 433-439, 1977.

T. F. Budinger, S. E. Derenzo, G. T. Gullberg, W. L. Greenberg, and R. H. Huesman, Emission computer assisted tomography with single-photon and positron annihilation photon emitters, J. Comput. Assist. Tomogr. 1, 131-145, 1977.

T. F. Budinger and F. D. Rollo, Physics and instrumentation, Progress in Cardiovascular Diseases 20, 19-53, 1977.

T. F. Budinger, S. E. Derenzo, W. L. Greenberg, G. T. Gullberg, and R. H. Huesman, Quantitative potentials of dynamic emission computed tomography, J. Nucl. Med. 19, 309-315, 1978.

T. F. Budinger, G. T. Gullberg, and R. H. Huesman, Emission computed tomography, in Image Reconstruction from Projections: Implementation and Application, G. T. Herman, ed. (Springer-Verlag, New York, 1979), (in press).

Y. Censor, D. E. Gustafson, A. Lent, and H. Tuy, A new approach to the emission computerized tomography problem: Simultaneous calculation of attenuation and activity coefficients, in Proc. IEEE Workshop on Physics and Engineering in Computerized Tomography (Newport Beach, California, Jan. 17-19, 1979), IEEE Trans. Nucl. Sci. NS-26 (No. 2, Part 2), 2775-2779, 1979.

L. T. Chang, A method for attenuation correction in radionuclide computed tomography, IEEE Trans. Nucl. Sci. NS-25, 638-643, 1978.

M. E. Davison and F. A. Grünbaum, Convolution algorithms for arbitrary projection angles, in Proc. IEEE Workshop on Physics and Engineering in Computerized Tomography (Newport Beach, California, Jan. 17-19, 1979), IEEE Trans. Nucl. Sci. NS-26 (No. 2, Part 2), 2670-2673, 1979.

S. R. Deans, A unified Radon inversion formula, J. Math. Phys. 19, 2346-2349, 1978.

S. R. Deans, The Radon transform: some remarks and formulas for two dimensions, Lawrence Berkeley Laboratory Report LBL-5691, 1977.

S. E. Derenzo, T. F. Budinger, J. L. Cahoon, R. H. Huesman, and H. G. Jackson, High resolution computed tomography of positron emitters, IEEE Trans. Nucl. Sci. NS-24, 544-558, 1977.

R. Deutsch, Estimation Theory, Prentice-Hall, Englewood Cliffs, N. J., 1965.

E. L. Dobson and H. B. Jones, The behavior of intravenously injected particulate material: Its rate of disappearance from the blood stream as a measure of liver blood flow, Acta Med. Scand. 144, (Suppl. 273), 1-71, 1952.

N. Dunford and J. T. Schwartz, Linear Operators Part II: Spectral Theory - Self Adjoint Operators in Hilbert Space, Interscience Publishers, New York, 1963.

E. Durand, Solutions Numériques des Équations Algébrique, Tome II, p. 120, Masson, Paris, 1960.

P. P. B. Eggermont, Three-dimensional image reconstruction by means of two-dimensional Radon inversion, Technological University Eindhoven, Netherlands, Report No. T.H. - Report 75 - WSK-04, 1975.

I. M. Gel'fand, M. I. Graev, and N. Ya. Vilenkin, Generalized Functions: Volume 5 Integral Geometry and Representation Theory, Academic Press, New York, 1966.

S. Genna, S. C. Pang, and B. A. Burrows, Analysis of an arcuate gamma camera design for transaxial reconstruction, in International Symposium on Medical Radionuclide Imaging, (IAEA, Vienna, 1976), Vol. 1, 323-339.

P. Gilbert, Iterative methods for the reconstruction of three-dimensional objects from projections, J. Theor. Biol. 36, 105-117, 1972.

M. Goitein, Three-dimensional density reconstruction from a series of two-dimensional projections, Nucl. Instrum. Meth. 101, 509-518, 1971.

R. Gordon, R. Bender, and G. T. Herman, Algebraic reconstruction techniques (ART) for three-dimensional electron microscopy and x-ray photography, J. Theor. Biol. 29, 471-481, 1970.

R. Gordon, A tutorial on ART (Algebraic Reconstruction Techniques), IEEE Trans. Nucl. Sci. NS-21, 78-93, 1974.

R. Gordon and G. T. Herman, Three-dimensional reconstruction from projections: a review of algorithms, Int. Rev. Cytol. 38, 111-151, 1974.

G. T. Gullberg and R. H. Huesman, Emission and transmission noise propagation in positron emission computed tomography, J. Nucl. Med. (in press), 1979.

P. R. Halmos, Introduction to Hilbert Space and the Theory of Spectral Multiplicity, Chelsea, New York, 1951.

C. Hamaker and D. C. Solmon, The angles between the null spaces of x-rays, J. Math. Anal. and Appl. 62, 1-23, 1978.

G. T. Herman, A. Lent, and S. W. Rowland, ART: mathematics and applications (a report on the mathematical foundations and on the applicability to real data of the algebraic reconstruction techniques), J. Theor. Biol. 42, 1-32, 1973.

G. T. Herman and A. Lent, Iterative reconstruction algorithms, Comput. Biol. Med. 6, 273-294, 1976.

M. R. Hestenes and E. Stiefel, Methods of conjugate gradients for solving linear systems. J. Res. Nat. Bur. Standards Sect. B. 49, 409-436, 1952.

M. R. Hestenes, The conjugate-gradient method for solving linear systems, in Proc. Symposium on Applied Mathematics, Vol. VI, Numerical Analysis, (McGraw-Hill, New York, 1956), 83-102.

G. Hevesy, Adventures in Radioisotope Research; the Collected Papers of G. Hevesy, Permagon Press, London, 1962.

R. C. Hsieh and W. G. Wee, On methods of three-dimensional reconstruction from a set of radioisotope scintigrams, IEEE Trans. SMC-6(12), 854-862, 1976.

J. H. Hubbell and M. J. Berger, Photon Attenuation and Energy Absorption Coefficients Tabulations and Discussion, 2nd ed., U.S. Nat. Bur. Standards, Report 8681, 1966.

J. G. Huebel and B. Lantz, A converging algebraic image reconstruction technique incorporating a generalized error model, in Proc. Ninth Asilomar Conference on Circuits, Systems, and Computers (IEEE, Nov. 3-5, 1975), 571-576.

R. H. Huesman, The effects of a finite number of projection angles and finite lateral sampling of projections on the propagation of statistical errors in transverse section reconstruction, Phys. Med. Biol. 22, 511-521, 1977.

R. H. Huesman, G. T. Gullberg, W. L. Greenberg, and T. F. Budinger, RECLBL Library Users Manual--Donner Algorithms for Reconstruction Tomography, Tech. Rpt. PUB 214, Lawrence Berkeley Laboratory, 1977.

R. J. Jaszczak, P. H. Murphy, D. Huard, and J. A. Burdine, Radionuclide emission computed tomography of the head with ^{99m}Tc and a scintillation camera, J. Nucl. Med. 18, 373-380, 1977.

H. E. Johns and J. R. Cunningham, The Physics of Radiology, Thomas, Springfield, Illinois, 1974.

S. Kaczmarz, Angenäherte von Systemen linearer Gleichungen, Bull. Int. de l'Académie Polonaise des Sciences et des Lettres - Classe Des Sciences Mathématiques et Naturelles-Série A: Sciences Mathématiques, 355-357, 1937.

W. J. Kammerer and M. Z. Nashed, On the convergence of the conjugate gradient method for singular linear operator equations, SIAM J. Numer. Anal. 9, 165-181, 1972.

D. B. Kay and J. W. Keyes,Jr., First order corrections for absorbtion and resolution compensation in radionuclide Fourier tomography, J. Nucl. Med. 16, 540-541, 1975.

D. H. Keeling, A new approach to brain scanning, in Proc. Second Congress of the European Assoc. of Radiology, Amsterdam, 14-18 June 1971, (Excerpta Medica, Amsterdam, 1972), 572-577.

J. W. Keyes, Jr., N. Orlandea, W. J. Heetderks, P. F. Leonard, and W. L. Rogers, The Humongotron - a scintillation-camera transaxial tomograph, J. Nucl. Med. 18, 381-387, 1977.

A. Klug and R. A. Crowther, Three-dimensional image reconstruction from the viewpoint of information theory, Nature (London) 238, 435-440, 1972.

D. E. Kuhl and R. Q. Edwards, Image separation radioisotope scanning, Radiology 80, 653-661, 1963.

D. E. Kuhl and R. Q. Edwards, Cylindrical and section radioisotope scanning of the liver and brain, Radiology 83, 926-936, 1964.

D. E. Kuhl, F. W. Pitts, T. P. Sanders, and M. M. Mishkin, Transverse section and rectilinear brain scanning with ^{99m}Tc pertechnetate, Radiology 86, 822-829, 1966a.

D. E. Kuhl, F. W. Pitts, and S. H. Tucker, Brain scanning of children using body section techniques and pertechnetate ^{99m}Tc, Acta Radiol. 5, 843-854, 1966b.

D. E. Kuhl and R. Q. Edwards, Reorganizing data from transverse section scans of the brain using digital processing, Radiology 91, 975-983, 1968.

D. E. Kuhl and R. Q. Edwards, The Mark III scanner: a compact device for multiple-view and section scanning of the brain, Radiology 96, 563-570, 1970.

D. E. Kuhl, R. Q. Edwards, A. R. Ricci, M. Reivich, Quantitative section scanning using orthogonal tangent correction, J. Nucl. Med. 14, 196-200, 1973.

D. E. Kuhl, R. Q. Edwards, A. R. Ricci, R. J. Yacob, T. J. Mich, and A. Alavi, The Mark IV system for radionuclide computed tomography of the brain, Radiology 121, 405-413, 1976.

P. C. Lauterbur, Image formation by induced local interactions: examples employing nuclear magnetic resonance, Nature (London) 242, 190-191, 1973.

A. V. Lakshminarayanan and A. Lent, Methods of least squares and SIRT in reconstruction, J. Theor. Biol. 76, 267-295, 1979.

B. F. Logan and L. A. Shepp, Optimal reconstruction of a function from its projections, Duke Math. J. 42, 1975.

W. V. Lovitt, Linear Integral Equations, Dover Publications, New York, 1950.

D. Ludwig, The Radon transform on Euclidean space, Comm. Pure Appl. Math. 19, 49-81, 1966.

W. Magnus, F. Oberhettinger, and R. P. Soni, Formulas and Theorems for the Special Functions of Mathematical Physics, Springer-Verlag, New York, 1966.

C. D. Maldonado, Note on orthogonal polynomials which are "invariant in form" to rotations of axes, J. Math. Phys. 6, 1935-1938, 1965.

C. D. Maldonado and H. N. Olsen, New method for obtaining emission coefficients from emitted spectral intensities. Part II - Assymetrical sources, J. Optical Society of America 56, 1305-1313, 1966.

I. Marek, Frobenius theory of positive operators: comparison theorems and applications, SIAM J. Appl. Math. 19, 607-628, 1970.

R. B. Marr, On the reconstruction of a function on a circular domain from a sampling of its line integrals, J. Math. Anal. Appl. 45, 357-374, 1974.

R. B. Marr, On the inversion of sampled Radon transforms, to appear as a Brookhaven National Laboratory Report, 1979.

C. E. Metz and R. N. Beck, Quantitative effects of stationary linear image processing on noise and resolution of structure in radionuclide images, J. Nucl. Med. 15, 164-170, 1974.

K. Miller, An optimal method for the x-ray reconstruction problem, Amer. Math. Soc. Not. 25, A-161-162, January, 1978.

K. Miller, New results on reconstruction methods from x-ray projections, Math. 290 Lecture Notes, University of California, Berkeley, 1979.

H. Minc, On the maximal eigenvector of a positive matrix, SIAM J. Numer. Anal. 7, 424-427, 1970.

M. J. Myers, W. I. Keyes, and J. R. Mallard, An analysis of tomographic scanning systems, in Medical Radioisotopes Scintigraphy, (IAEA, Vienna, 1972), Vol. 1, 331-345.

F. Natterer, On the inversion of the attenuated Radon transform, Universität des Saarlandes, Saarbrucken, Report A 78/17, 1978.

J. M Ortega and W. C. Rheinboldt, Iterative Solution of Nonlinear Equations in Several Variables, Academic Press, New York, 1970.

A. Papoulis, Systems and Transforms with Applications in Optics, McGraw-Hill, New York, 1968.

E. Parzen, Stochastic Processes, Holden-Day, San Francisco, 1962.

O. Perron, Zur Theorie der Matrizen, Math. Ann. 64, 248-263, 1907.

I. G. Petrovskii, Lectures on the Theory of Integral Equations, Graylock Press, Rochester, New York, 1957.

M. E. Phelps, Emission computed tomography, Seminars in Nucl. Med. 7, 337-365, 1977.

J. Radon, Über die Bestimmung von Funktionen durch ihre integralwerte längs gewisser Mannigfaltigkeiten, Ber. Saechs. Akad. Wiss. Leipzig, Math.-Phys. Kl. 69, 262-277, 1917.

G. N. Ramachandran and A. V. Lakshminarayanan, Three-dimensional reconstruction from radiographs and electron micrographs: application of convolutions instead of Fourier transforms, Proc. Nat. Acad. Sci. U.S. 68, 2236-2240, 1971.

W. T. Reid, Generalized inverses of differential and integral operators, in Proceedings of the Symposium on Theory and Application of Generalized Inverses of Matrices, T. L. Boullion and P. L. Odell, eds. (Texas Technological College Mathematics Series, No. 4, Lubbock, 1968), 1-25.

S. W. Root, G. A. Andrews, R. M. Kniseley, and M. P. Tyor, The distribution and radiation effects of intravenously administered colloid Au-198 in man, Cancer 7, 856-866, 1954.

A. Rosenfeld and A. C. Kak, Digital Picture Processing, Academic Press, New York, 1976.

L. A. Shepp and B. F. Logan, The Fourier reconstruction of a head section, IEEE Trans. Nucl. Sci. NS-21, 21-43, 1974.

C. W. Sheppard, G. Jordan, and P. P. Hahn, Disappearance of isotopically labeled gold colloids from the circulation of the dog, Amer. J. Physiol. 164, 345-350, 1951.

J. R. Singer, NMR diffusion and flow measurements and an introduction to spin phase graphing, J. Physics. E. Sci. Instr. 11, 281-376, 1978.

G. F. Simmons, Introduction to Topology and Modern Analysis, McGraw-Hill, New York, 1963.

F. Smithies, Integral Equations, Cambridge University Press, Cambridge, England, 1958.

D. L. Snyder and J. R. Cox, Jr., An overview of reconstructive tomography and limitations imposed by a finite number of projections, in Reconstruction Tomography in Diagnositc Radiology and Nuclear Medicine, M. M. Ter-Pogossian, M. E. Phelps, G. L. Brownell, J. R. Cox, Jr., D. O. Davis, R. G. Evans, eds. (University Park Press, Baltimore, 1977), 3-32.

G. Strang and G. J. Fix, An Analysis of the Finite Element Method, Prentice-Hall, New York, 1973.

D. W. Sweeney and C. M. Vest, Reconstruction of three-dimensional refractive index fields from multidirectional interferometric data, Appl. Opt. 12, 2649-2664, 1973.

K. Tanabe, Projection method for solving a singular system of linear equations and its applications, Num. Math. 17, 203-214, 1971.

E. Tanaka, T. A. Iinuma, N. Nohara, T. Tomitani, and T. Shimizu, Multicrystal section imaging device and its data processing, in Proc. Thirteenth International Congress of Radiology, Madrid, 1973, (Excerpta Medica, Amsterdam, 1974), 314-324.

E. Tanaka and T. A. Iinuma, Correction functions for optimizing the reconstructed image in transverse section scan, Phys. Med. Biol. 20, 789-798, 1975.

E. Tanaka and T. A. Iinuma, Correction functions and statistical noises in transverse section picture reconstruction, Comput. Biol. Med. 6, 295-306, 1976.

A. E. Taylor, Introduction to Functional Analysis, John Wiley and Sons, New York, 1966.

M. M. Ter-Pogossian, Basic principles of computed axial tomography, Seminars in Nucl. Med. 7, 109-128, 1977.

C. A. Tobias, J. H. Lawrence, F. J. W. Roughton, W. S. Root, and M. I. Gregersen, The elimination of carbon monoxide from the human body with reference to the possible conversion of CO to CO_2, Am. J. Physiol. 145, 253-263, 1945.

A. E. Todd-Pokropek, The formation and display of section scans, in Proc. Second Congress of the European Assoc. of Radiology, Amsterdam, 14-18 June 1971, (Excerpta Medica, Amsterdam, 1972), 542-548.

O. J. Tretiak and P. Delaney, The exponential convolution algorithm for emission computed axial tomography, in Review of Information Processing in Medical Imaging (Proc. Fifth International Conference, Vanderbilt University, June 27-July 1, 1977), A. B. Brill and R. R. Price, eds. (Oak Ridge National Laboratory Report ORNL/BCTIC-2, 1978), 266-278.

O. J. Tretiak and C. Metz, The exponential Radon transform, (in press), 1979.

F. G. Tricomi, Integral Equations, Interscience Publishers, New York, 1965.

J. S. Vandergraft, Spectral properties of matrices which have invariant cones, SIAM J. Appl. Math. 16, 1208-1222, 1968.

R. S. Varga, Matrix Iterative Analysis, Prentice-Hall, Englewood Cliffs, N. J., 1962.

H. N. Wagner, Jr., Images of the future, J. Nucl. Med. 19, 599-605, 1978.

H. N. Wagner, Jr., (ed.), Principles of Nuclear Medicine, W. B. Saunders, Philadelphia, 1968.

T. E. Walters, W. Simon, D. A. Chesler, J. A. Correia, and S. J. Riederer, Radionuclide axial tomography with correction for internal absorption, in Information Processing in Scintigraphy, C. Raynaud and A. Todd-Pokropek, eds. (Comissariat à l'energie atomique, Orsay, France, 1976), 333-342.

E. T. Whittaker and G. N. Watson, A Course of Modern Analysis, Cambridge University Press, England (1927), 4th edition, 1962.

K. W. Weiler and G. Z. Seielstad, A model of the Crab Nebula derived from dual-frequency radio measurements, Astron. Astrophys. 21, 393-400, 1972.

K. Yosida, Functional Analysis, 4th edition, Springer-Verlag, New York, 1974.

E. Zeitler, The reconstruction of objects from their projections, OPTIK 39, 396-415, 1974.

U.S.GPO:1979-689-058(F)37